

Technische Universität München
Fachgebiet Strömungsmechanik

Direct and large-eddy simulation of supersonic turbulent flow in pipes, nozzles and diffusers

Somnath Ghosh

Vollständiger Abdruck der von der Fakultät für Maschinenwesen der Technischen Universität München zur Erlangung des akademischen Grades eines

Doktor-Ingenieurs

genehmigten Dissertation.

Vorsitzender: Univ.-Prof. Dr.-Ing. W. A. Wall

Prüfer der Dissertation:

1. Univ.-Prof. Dr.-Ing, Dr.-Ing. habil. R. Friedrich, i.R.
2. Univ.-Prof. Dr.-Ing. habil. N. A. Adams

Die Dissertation wurde am 13.11.2007 bei der Technischen Universität München eingereicht und durch die Fakultät für Maschinenwesen am 14.03.2008 angenommen.

Abstract

This thesis reports results from high order accurate direct and large-eddy simulations of supersonic turbulent flow in pipes, nozzles and diffusers with circular cross-section and isothermal walls. The focus is on compressibility effects.

In the first part of this thesis, we investigate compressibility effects in turbulent pipe flows by means of direct and large-eddy simulations at Mach numbers 0.3 and 1.5 and friction Reynolds numbers 214 and 245 respectively. The supersonic flow produces high dissipation rates in the near-wall region which results in a large temperature gradient in this region. Because of the isothermal wall, the mean temperature increases from the wall towards the core. There is a corresponding reduction in mean density because radial pressure gradients are negligible in this flow. The near-wall structures in the supersonic flow show increased streamwise coherence which is a result of an increase in the ratio of turbulence time scale to that of the mean shear because of the higher density gradients. Reynolds stress anisotropy is increased in the supersonic case. Streamwise stresses increase and the other components decrease. This is due to decreased pressure-strain correlations in the supersonic flow which has been shown in previous studies of supersonic channel flows to be an effect of reduced mean density.

In the second part of this study, effects of weak mean dilatation on the turbulence structure are explored with the help of DNS/LES by subjecting a supersonic turbulent pipe flow to weak favourable/adverse pressure gradients in a nozzle/diffuser. Expansion of the flow leads to dramatic reduction of turbulence intensities. An analysis of production terms in the Reynolds stress equations shows that although mean dilatation and extra strain rates have small sink effects, the mechanism of production due to shear is substantially affected by acceleration. The reason for this is the reduction of pressure-strain correlations due to acceleration. Analogous effects are observed in the flow through a diffuser. Here, the turbulence intensities are amplified. The increase in pressure-strain correlations is again the major cause of increase of turbulence production. The results form an extensive database suitable for turbulence modeling.

Acknowledgements

I am grateful to **Prof. Friedrich** for giving me the opportunity to work on a research theme which became more and more interesting as I progressed, and which holds promises for the future. He has always been a source of inspiration and was always approachable for questions and discussions.

I would also like to thank **Prof. J. Sesterhenn** for his valuable suggestions in the course of this work and for the basic version of the code used in our group.

Many helpful discussions with **Prof. J. Mathew** (who has been a well-wisher since my student years in IISC, Bangalore), during his visits to TUM are gratefully acknowledged.

Prof. S. Sarkar (UC, San Diego) has always been supportive of my work and I thank him for his encouragement.

I would like to express my gratitude to **Prof. N. Adams** for supporting my work and agreeing to be the second examiner of this thesis.

I must thank my ex-colleagues **Dr.-Ing. Holger Foyssi** and **Dr.-Ing. Johannes Kreuzinger** for their help and support during the first two years of this work.

Special thanks goes to my colleague **Dr.-Ing. Inga Mahle** for her moral support and companionship.

I thank all my other colleagues in our group for their companionship and help.

I thank my friends Kiran, Sabyasachi, Yadhu and Manish for the wonderful time I spent with them. They helped me a lot in going through the periods of frustration.

Without the excellent computing facilities provided by the Leibniz Rechenzentrum (LRZ), Munich and the supportive LRZ staff, it would have been impossible to perform the computations on which this thesis is based.

And, last but not the least, without the support of my parents and my brother (who are always with me despite being far away in India), this work would not have been possible.

Garching, November 2007

Somnath Ghosh

Contents

List of symbols	XI
1 Introduction	1
2 Mathematical and numerical considerations	5
2.1 Governing Equations	5
2.1.1 Cylindrical coordinates	6
2.1.2 Coordinates for nozzle/diffuser simulations	7
2.2 Spatial and temporal discretization	8
2.2.1 LES method	8
2.2.2 Axis singularity treatment	10
2.2.3 Parallelisation	11
2.2.4 Code coupling for nozzle/diffuser simulation	14
2.2.5 Boundary Conditions	14
2.2.6 Some definitions concerning statistics	16
3 Supersonic turbulent pipe flow	18
3.1 Introduction	18
3.2 Computational Details	19
3.3 DNS results	19
3.3.1 Time history	20
3.3.2 Energy spectra and two-point correlations	20
3.3.3 Instantaneous fields	22
3.3.4 Mean profiles	26
3.3.5 Turbulence statistics	37
3.3.6 Reynolds stress budgets	41
3.4 LES of supersonic turbulent pipe flow	55
3.5 Conclusions	57
4 Supersonic turbulent nozzle flow	64
4.1 Introduction	64
4.2 Computational details	65
4.3 Instantaneous fields	66
4.4 Azimuthal spectra	66
4.5 Mean Profiles	66
4.6 Rms profiles	71
4.7 Reynolds stresses	73
4.8 Reynolds stress budgets	80

4.9	Analysis of production terms	82
4.10	Conclusions	91
5	Supersonic turbulent diffuser flow	92
5.1	Introduction	92
5.2	Flow cases	93
5.3	Supersonic diffuser without shock train ($M_{in} = 1.8$)	93
5.3.1	Azimuthal spectra	94
5.3.2	Mean flow features	94
5.3.3	Rms profiles	98
5.3.4	Reynolds stresses	102
5.3.5	Reynolds stress budgets	104
5.4	Supersonic diffuser without shock train ($M_{in} = 2.5$)	116
5.4.1	Mean flow features	116
5.4.2	Turbulence statistics	117
5.5	Supersonic diffuser with shock train ($M_{in} = 1.5$)	121
5.5.1	Instantaneous fields	122
5.5.2	Mean Profiles	123
5.5.3	Rms profiles	127
5.5.4	Reynolds stresses	130
5.5.5	Aspects of TKE and Reynolds stress budgets	131
5.6	Conclusions	139
6	Summary and outlook	141

List of Figures

2.1	Sketch of the computational domain for the pipe flow.	7
2.2	Sketch of the computational domain for the nozzle flow.	8
2.3	Filter transfer functions for $\alpha = 0.2$: — G , - - - Q_N , . . . $Q_N * G$, -.- ($Q_N * G$) ² with $\alpha = 0.2$ and $N = 6$	10
2.4	Physical and computational domains	11
3.1	Time history of Re_τ for DNS $M = 0.3$	20
3.2	Streamwise energy spectra (a) in the near-wall ($y^* = 5$) region, and (b) in the core. —, $M=1.5$; - - -, $M=0.3$	21
3.3	Energy spectra in the near-wall ($y^* = 5$) region in the azimuthal direction. Line types as in fig. 3.2	22
3.4	Two-point correlation coefficients in streamwise direction (a) at $y^* = 5$, and (b) in the core ($r/R = 0.0075$). —, $M=1.5$; - - -, $M=0.3$	23
3.5	Two-point correlation coefficients in streamwise direction (a) at $y^* = 5$ and (b) in the core ($r/R = 0.0075$). —, $M=1.5$; - - -, $M=0.3$	23
3.6	Two-point correlation coefficients in streamwise direction (a) at $y^* = 5$ and (b) in the core ($r/R = 0.0075$). —, $M=1.5$; - - -, $M=0.3$	24
3.7	Two-point correlation coefficients in azimuthal direction at $y^* = 5$ using two different normalizations (a), (b). —, $M=1.5$; - - -, $M=0.3$	24
3.8	Two-point correlation coefficients in azimuthal direction at $y^* = 5$. —, $M=1.5$; - - -, $M=0.3$	25
3.9	Instantaneous axial (top), radial (bottom) velocity fluctuations in a (x, ϕ) - surface for $M = 0.3$ at $y^* = 5$. Red lines show positive fluctuations.	27
3.10	Instantaneous azimuthal velocity fluctuations in a (x, ϕ) -surface for $M =$ 0.3 at $y^* = 5$. Red lines show positive fluctuations.	28
3.11	Instantaneous axial (top), radial (bottom) velocity fluctuations in a (x, ϕ) - surface, for $M = 1.5$ at $y^* = 5$. Red lines show positive fluctuations.	29
3.12	Instantaneous azimuthal velocity fluctuations in (x, ϕ) -surface for $M = 1.5$ at $y^* = 5$. Red lines show positive fluctuations	30
3.13	Instantaneous axial, azimuthal and radial (top to bottom) velocity fluctu- ations in a (x, r) -plane for $M = 0.3$. Red lines show positive fluctuations.	30
3.14	Instantaneous axial, azimuthal and radial (top to bottom) velocity fluctu- ations in a (x, r) -plane for $M = 1.5$. Red lines show positive fluctuations.	31
3.15	Instantaneous axial (left) and radial (right) velocity fluctuations in (ϕ, r) - plane at $x/L_x = 0.5$ for $M = 1.5$. Red lines show positive fluctuations	31

3.16	Instantaneous azimuthal (left) velocity and pressure (right) fluctuations in (ϕ, r) -plane at $x/L_x = 0.5$ for $M = 1.5$. Red lines show positive fluctuations.	32
3.17	Mean temperature, density and pressure normalized with wall values. Solid line: $M=1.5$; Dashed line: $M=0.3$	32
3.18	Local mean Mach and friction Reynolds numbers. Solid line: $M=1.5$; Dashed line: $M=0.3$	33
3.19	Turbulent Mach number (M_t) and gradient Mach number (M_g). Line types as in fig. 3.17	33
3.20	Mean dilatation and solenoidal dissipation rate. Line types as in fig. 3.17	34
3.21	Compressible dissipation rate and pressure-dilatation correlation. Line types as in fig. 3.17	34
3.22	Viscosity transformed mean velocity, U_μ^+ for the two Mach numbers. Line types as in fig. 3.17	36
3.23	Van Driest transformed mean velocity, U_{VD}^+ . Solid line: $M=1.5$; dashed line: $M=0.3$. -.-.-, U_x^+ at $M=1.5$. Straight line: $u^+ = 2.5lny^+ + 5.5$	37
3.24	Mean velocity using scaling proposed by Brun <i>et al.</i> (2008). Solid line: $M=1.5$; dashed line: $M=0.3$. Straight line: $u^+ = 2.5lny^+ + 5.5$	38
3.25	Rms density and temperature fluctuations. Line types as in fig. 3.24	39
3.26	Pressure and total temperature fluctuations. Line types as in fig. 3.24	40
3.27	Correlations between pressure and density fluctuations; and between density and temperature fluctuations. Line types as in fig. 3.24	40
3.28	Left: Correlations between velocity and temperature fluctuations. Line types as in fig. 3.24; Right: MSRA (Gaviglio (1987)) for $M = 1.5$. solid line: DNS, dashed line: equation 3.9	41
3.29	Rms velocity fluctuations. Line types as in fig. 3.24	42
3.30	Rms velocity fluctuations using the scaling suggested by Brun <i>et al.</i> (2008). Line types as in fig. 3.24	42
3.31	Streamwise Reynolds stress plotted against the 'semi-local' wall-normal coordinate. Line types as in fig. 3.24	43
3.32	Azimuthal Reynolds stress plotted against the 'semi-local' wall-normal coordinate. Line types as in fig. 3.24	43
3.33	Radial Reynolds stress, plotted against the 'semi-local' wall-normal coordinate. Line types as in fig. 3.24	44
3.34	Reynolds shear stress, plotted against the 'semi-local' wall-normal coordinate. Line types as in fig. 3.24	44
3.35	Streamwise Reynolds stress, outer scaling. Line types as in fig. 3.24	45
3.36	Azimuthal Reynolds stress, outer scaling. Line types as in fig. 3.24	45
3.37	Radial Reynolds stress, outer scaling. Line types as in fig. 3.24	46
3.38	Reynolds shear stress, outer scaling. Line types as in fig. 3.24	46
3.39	Streamwise Reynolds stress balance scaled with $\tau_w u_m / R$ at $M=1.5$	51
3.40	Azimuthal Reynolds stress balance scaled with $\tau_w u_m / R$ at $M=1.5$. Line types as in fig. 3.39. Cylindrical coordinates redistribution term (CR) is negligibly small.	52

3.41	Radial Reynolds stress balance scaled with $\tau_w u_m / R$ at $M=1.5$. Line types as in 3.39 but velocity-pressure-gradient term is plotted instead of pressure-strain correlation. Cylindrical coordinates redistribution term (CR) shown by dashed line (- - -)	52
3.42	Reynolds shear stress balance scaled with $\tau_w u_m / R$ at $M=1.5$. Line types as in 3.39 but velocity-pressure-gradient term is plotted instead of pressure-strain correlation. Cylindrical coordinates redistribution term (CR) shown by dashed line (- - -)	53
3.43	Streamwise Reynolds stress production, viscous diffusion and dissipation scaled with $\tau_w^2 / \bar{\mu}$. Solid line $M=1.5$, dashed line $M=0.3$	53
3.44	Turbulent diffusion, pressure-strain and mass flux variation terms in streamwise Reynolds stress budget, scaled with $\tau_w^2 / \bar{\mu}$. Solid line $M=1.5$, dashed line $M=0.3$	54
3.45	Pressure-strain correlations and radial pressure diffusion at $M=1.5$ scaled with $\tau_w^2 / \bar{\mu}$. — streamwise; - - - azimuthal; -.- radial; pressure diffusion	54
3.46	Rms vorticity fluctuations at $M=1.5$: — streamwise; -.- radial; - - - - azimuthal	55
3.47	Instantaneous axial (top) and radial (bottom) velocity fluctuations in (x, r) plane for $M = 1.5$ at $y^* = 5$. Red lines show positive fluctuations	58
3.48	Instantaneous axial and radial velocity fluctuations in (x, r) -plane for $M = 1.5$. Red lines show positive fluctuations	59
3.49	Instantaneous axial and radial velocity fluctuations in (ϕ, r) - plane for $M = 1.5$. Red lines show positive fluctuations	59
3.50	Left: Streamwise energy spectra, averaged in the other directions for the three velocity components. Right: azimuthal spectra for the streamwise component, averaged in the streamwise direction at $y^* = 10$. Solid line: DNS, Dashed line: LES	60
3.51	Mean temperature, density and Van Driest transformed velocity at $M=1.5$. solid line: DNS; dashed line: LES. Straight line: $u^+ = 2.5 \ln y^+ + 5.5$	60
3.52	Density and temperature fluctuations. Line types as in fig. 3.51	61
3.53	Rms velocity fluctuations, semi-local scaling. Line types as in fig. 3.51	61
3.54	Streamwise Reynolds stress in outer scaling. Line types as in fig. 3.51	62
3.55	Reynolds shear stress in outer scaling. Line types as in fig. 3.51	62
3.56	Streamwise Reynolds stress production, viscous diffusion and dissipation terms at $M=1.5$, scaled with $\tau_w^2 / \bar{\mu}$. Lines: DNS; symbols: LES	63
3.57	Turbulent diffusion, pressure-strain and mass flux variation terms in the streamwise Reynolds stress balance at $M=1.5$, scaled with $\tau_w^2 / \bar{\mu}$. Lines: DNS; symbols: LES	63
4.1	Axial velocity fluctuations (DNS), normalized with $u_\tau(x/L = 0)$, in a (x, r) -plane of the nozzle.	66
4.2	Axial velocity fluctuations (DNS), normalized with $u_\tau(x/L = 0)$, in a (r, ϕ) -plane of the nozzle. Left: $x/L = 0.1$, right: $x/L = 0.5$	67

4.3	Axial velocity fluctuations (DNS), normalized with $u_\tau(x/L = 0)$, in a (r, ϕ) -plane at $x/L = 0.88$	67
4.4	Energy spectra (DNS) of axial velocity fluctuations in the near-wall region ($y^* = 10$) in the azimuthal direction. $x/L = \dots \dots 0.0$; — 0.25; - - - 0.5; -.-.- 0.8	68
4.5	Axial variation of Clauser parameter (β) and bulk velocity. $u_{b,o}$: bulk velocity at $x/L = 0$ (LES)	69
4.6	Centerline pressure, local Mach number, area distributions; Centerline density and temperature distributions from the LES. Subscript 'o' denotes values at $x/L = 0$. Dashed lines are the solutions of isentropic streamtube equations.	69
4.7	Centerline (solid line) and wall (dashed line) pressure and wall shear stress (LES) profiles.	70
4.8	Displacement (solid line), momentum thickness (dashed line) and Shape factor	71
4.9	Profiles of mean density, temperature, normalized with values at the wall, and dissipation rate of the mean flow. $x/L = \dots \dots 0.0$; — 0.45, -.-.- 0.8. Symbols represent DNS results at the corresponding x/L locations.	72
4.10	Solenoidal dissipation rate and mean dilatation. Line types as in fig. 4.9. Symbols represent DNS results at the corresponding x/L locations.	72
4.11	Extra strain rate versus wall shear rate and local Mach number. Line types as in fig. 4.9	73
4.12	Van Driest transformed mean velocity, rms density fluctuations. Line types as in fig. 4.9. Symbols represent DNS results at the corresponding x/L locations.	74
4.13	Rms temperature and pressure fluctuations. Line types as in fig. 4.9	74
4.14	Density-temperature and pressure-density correlations. Line types as in fig. 4.9	75
4.15	Velocity-temperature correlations, Turbulent Mach number. Line types as in fig. 4.9	75
4.16	Compressible dissipation rate and pressure-dilatation correlation (DNS). $\odot, x/L = 0$; $\times, x/L = 0.5$; $\nabla, x/L = 0.8$	76
4.17	Rms velocity fluctuations in 'semi-local', inner scaling. Line types as in fig. 4.9	76
4.18	Rms velocity fluctuations, 'semi-local', inner scaling. Line types as in fig. 4.9	77
4.19	Axial Reynolds stress in outer scaling. Line types as in fig. 4.9. Symbols represent DNS results.	78
4.20	Azimuthal Reynolds stress in outer scaling. Line types as in fig. 4.9. Symbols represent DNS results.	78
4.21	Radial Reynolds stress in outer scaling. Line types as in fig. 4.9. Symbols: DNS	79
4.22	Reynolds shear stress and total shear stress, outer scaling. Line types as in fig. 4.9. Symbols: DNS	79
4.23	Axial Reynolds stress budget (LES) at $x/L = 0.1$, scaled with local $\tau_w^2/\bar{\mu}$	83

4.24	Axial Reynolds stress budget at $x/L = 0.4$, scaled with local $\tau_w^2/\bar{\mu}$. Line types as in fig. 4.23	83
4.25	Axial Reynolds stress budget (LES) at $x/L = 0.65$, scaled with local $\tau_w^2/\bar{\mu}$. Line types as in fig. 4.23	84
4.26	Axial Reynolds stress budget (LES) at $x/L = 0.8$, scaled with local $\tau_w^2/\bar{\mu}$. Line types as in fig. 4.23	84
4.27	Terms in the TKE budget (LES) at $x/L = 0.4$, scaled with local $\tau_w^2/\bar{\mu}$. All line types as in fig. 4.23 except that for pressure-strain which here denotes pressure-dilatation correlations.	85
4.28	Terms in the TKE budget (LES) at $x/L = 0.65$, scaled with local $\tau_w^2/\bar{\mu}$. Line types as in fig. 4.27.	85
4.29	Production term of the axial Reynolds stress budget at $x/L = 0.1, 0.15, 0.45, 0.65, 0.8$ (from top to bottom of the figure) scaled by local $\tau_w^2/\bar{\mu}$ (LES)	87
4.30	Contributions to the production of the axial Reynolds stress in the nozzle at stations $x/L = 0.0$ (dashed line) and 0.45 (solid line). sh : mean shear, dil: mean dilatation, es: extra rate of strain. Lines: LES, symbols: DNS. All terms are normalized by $\tau_w^2/\bar{\mu}$	87
4.31	Contributions to the production of the Reynolds shear stress in the nozzle at stations $x/L = 0.0$ (dashed line), 0.45 (solid line). sh1: mean shear (<i>shear1</i>), dil: mean dilatation. Lines: LES, symbols: DNS. All terms are normalized by $\tau_w^2/\bar{\mu}$	88
4.32	Decomposition of the axial production terms at $x/L = 0.65$, mean shear; — mean dilatation; -.- extra strain rate (LES). All terms are normalized by $\tau_w^2/\bar{\mu}$	88
4.33	Decomposition of the axial production terms at $x/L = 0.8$, mean shear; — mean dilatation; -.- extra strain rate (LES). All terms are normalized by $\tau_w^2/\bar{\mu}$	89
4.34	Mean shear, rms pressure fluctuations. $x/L = \dots \dots 0.0$; — 0.45 , -.- 0.8 (LES)	89
4.35	Pressure-strain correlation Π_{xx} in the nozzle, x/L stations as in Figure 4.9. Lines: LES. Symbols: DNS. Terms are normalized by $\tau_w^2/\bar{\mu}$	90
4.36	Pressure-strain correlation Π_{rr} in the nozzle x/L stations as in Figure 4.9. Lines: LES. Symbols: DNS. Terms are normalized by $\tau_w^2/\bar{\mu}$	90
5.1	Axial velocity fluctuations (LES), normalized with $u_\tau(x/L = 0)$, in a (x, r) -plane. Flow is from left to right.	94
5.2	Energy spectra (LES) of axial velocity fluctuations in the near-wall region ($y^* = 10$) in the azimuthal direction. $x/L = \dots \dots 0.0$; — 0.25 ; — — 0.5 ; -.- 0.65	95
5.3	Axial variation of Clauser parameter (β) and bulk velocity. $u_{b,o}$: bulk velocity at $x/L = 0$	96
5.4	Left: Centerline pressure, local Mach number, and area distribution; Right: centerline density and temperature. Dashed lines are the solutions of isentropic streamtube equations. Subscript 'o' denotes values at $x/L = 0$	96

5.5	Left: Centerline (solid line) and wall (dashed line) pressure distribution. Right: Wall shear stress	97
5.6	Left: Displacement (solid line) and momentum thickness (dashed line). Right: Shape factor	97
5.7	Left: Mean density, temperature profiles. Right: Dissipation of the mean flow. $x/L = \dots \dots 0.0$; — 0.25; — — — 0.5; -.-.- 0.65	98
5.8	Solenoidal dissipation rate and mean dilatation. Line types as in fig. 5.7	99
5.9	Left: Extra strain rate normalized with wall shear at $x/L =$ — 0.3; -.-.- 0.5. Right: Local Mach number. Line types as in fig. 5.7	99
5.10	Van Driest transformed mean velocity, rms density fluctuations. Line types as in fig. 5.7. Dashed line in left figure: $u^+ = 2.5 \ln y^+ + 5.5$	100
5.11	Rms temperature and pressure fluctuations. Line types as in fig. 5.7	101
5.12	Density-temperature and pressure-density correlations. Line types as in fig. 5.7	101
5.13	Velocity-temperature correlations, Turbulent Mach number. Line types as in fig. 5.7	102
5.14	Compressible dissipation rate and pressure-dilatation correlation. Line types as in fig. 5.7	103
5.15	Rms velocity fluctuations, 'semi-local', inner scaling. $x/L = \dots \dots 0.0$; — 0.25; — — — 0.5; -.-.- 0.75	103
5.16	Rms velocity fluctuations, inner scaling. Line types as in fig. 5.15	104
5.17	Axial Reynolds stress, outer scaling. Line types as in fig. 5.15	105
5.18	Azimuthal Reynolds stress, outer scaling. Line types as in fig. 5.15	105
5.19	Radial Reynolds stress, outer scaling. Line types as in fig. 5.15	106
5.20	Reynolds shear stress and total shear stress, outer scaling. Line types as in fig. 5.15	106
5.21	Axial Reynolds stress budget at $x/L = 0.25$ scaled with local $\tau_w^2/\bar{\mu}$. P: Production TD: turbulent diffusion, MT: mean convection, VD: viscous diffusion, M: Mass flux variation, PS: Pressure-strain correlations, PD: Pressure diffusion, DS:viscous dissipation	107
5.22	Axial Reynolds stress budget at $x/L = 0.5$ scaled with local $\tau_w^2/\bar{\mu}$. Line types and abbreviations as in fig. 5.21	108
5.23	Axial Reynolds stress budget at $x/L = 0.75$ scaled with local $\tau_w^2/\bar{\mu}$. Line types and abbreviations as in fig. 5.21	108
5.24	Terms in the TKE budget at $x/L = 0.25$ scaled with local $\tau_w^2/\bar{\mu}$. All line types as in fig. 5.21 except that for pressure-strain which here denotes pressure-dilatation correlation.	109
5.25	Terms in the TKE budget at $x/L = 0.5$ scaled with local $\tau_w^2/\bar{\mu}$. All line types as in fig. 5.21 except that for pressure-strain which here denotes pressure-dilatation correlation.	110
5.26	Terms in the TKE budget at $x/L = 0.75$ scaled with local $\tau_w^2/\bar{\mu}$. Line types as in 5.24.	110
5.27	Axial production term scaled with local $\tau_w^2/\bar{\mu}$. Line types as in fig. 5.15	111

5.28	Decomposition of axial production term. $x/L = \dots \dots 0.0$; — 0.5 ; -.- 0.75 . sh: mean shear term; es: extra strain rate term; dil: mean dilatation term. All terms normalized with $\tau_w^2/\bar{\mu}$	112
5.29	Mean shear rate and Reynolds shear stress. $x/L = \dots \dots 0.0$; — 0.5 ; -.- 0.75	112
5.30	Decomposition of production terms in the Reynolds shear stress transport. $x/L = \dots \dots 0.0$; — 0.5 ; -.- 0.75 . All terms are normalized with $\tau_w^2/\bar{\mu}$	113
5.31	Comparison of pressure-strain correlation (PS) and decomposed production term in the radial Reynolds stress budget at $x/L = 0.5$. — PS; — — extra strain; -.- shear; $\dots \dots$ dilatation. All terms are normalized with $\tau_w^2/\bar{\mu}$	113
5.32	Rms pressure fluctuations. Line types as in 5.29	114
5.33	Axial pressure-strain correlations. Line types as in fig. 5.29. Terms are normalized with $\tau_w^2/\bar{\mu}$	114
5.34	Radial pressure-strain correlations. Line types as in fig. 5.29. Terms are normalized with $\tau_w^2/\bar{\mu}$	115
5.35	Centerline pressure, local Mach number and area; centerline density and temperature.	116
5.36	Left: Wall shear stress, Right: Displacement (solid line) and momentum thickness (dashed line).	117
5.37	Left: Mean density, temperature profiles. Right: Solenoidal dissipation rate. $x/L = \dots \dots 0.0$; — 0.25 ; — — 0.5 ; -.- 0.8	118
5.38	Left: Van Driest transformed mean velocity. Right: Local Mach number. Line types as in fig. 5.37. Dashed line in left figure: $u^+ = 2.5 \ln y^+ + 5.5$	118
5.39	Rms temperature and density fluctuations. Line types as in fig. 5.37	119
5.40	Axial Reynolds stress, outer scaling. Line types as in fig. 5.37	119
5.41	Axial production scaled with local $\tau_w^2/\bar{\mu}$. Line types as in fig. 5.37	120
5.42	Pressure-strain correlation scaled with local $\tau_w^2/\bar{\mu}$. Line types as in fig. 5.37	120
5.43	Decomposition of axial production term. $x/L = \dots \dots 0.0$; — 0.5 ; -.- 0.8 . sh: mean shear term; es: extra strain rate term; dil: mean dilatation term. Terms are normalized with $\tau_w^2/\bar{\mu}$	121
5.44	Instantaneous pressure in an (x, r) -plane containing the axis. Flow is from left to right.	122
5.45	Time trace of centerline and wall pressure at $x/L = 0.2$, downstream of the first shock. $u_{\tau,o}$ is the friction velocity at inlet to the diffuser, R is the radius at inlet.	123
5.46	Time trace of centerline and azimuthally averaged wall pressure at $x/L = 0.75$, in the mixing region.	124
5.47	Time trace of centerline Mach number $x/L = 0.2$ (left) and $x/L = 0.75$	124
5.48	Axial distribution of wall (dashed line), centerline (solid line) pressure and wall shear stress.	126
5.49	Axial distribution of centerline local Mach number, density and temperature. In the figure on the right, the solid line shows density and the dashed line shows temperature distributions.	126
5.50	Displacement and momentum thicknesses. Solid line: Shock train case; Dashed line: No shock train case (section 5.3)	127

5.51	Radial density, temperature and local Mach number distribution. $x/L =$ 0.0, — 0.15, — — 0.4, -.- 0.6	128
5.52	Van Driest transformed mean velocity. Line types as in fig. 5.51	128
5.53	Turbulent Mach number and rms pressure fluctuations. Line types as in fig. 5.51	129
5.54	Rms density and temperature fluctuations. Line types as in fig. 5.51	129
5.55	Solenoidal dissipation rate. Line types as in fig. 5.51	130
5.56	Pressure-dilatation correlation and compressible dissipation rate. Line types as in fig. 5.51	131
5.57	Axial Reynolds stress. Left: $x/L =$ 0.0; — 0.15; — — 0.25; -.- 0.3 Right: $x/L =$ — 0.4; — — 0.55; -.- 0.6	132
5.58	Azimuthal Reynolds stress. Line types as in fig. 5.57	132
5.59	Radial Reynolds stress. Line types as in fig. 5.57	133
5.60	Comparison of production (—), dissipation (... ..), pressure dilatation (- .-) terms in the TKE budget at $x/L=$ 0 (left) , 0.15 (right). Terms are normalized with $\tau_{w,o}^2/\bar{\mu}$	134
5.61	Comparison of production (—), dissipation (... ..), pressure dilatation (- .-) terms in the TKE budget at $x/L=$ 0.2 (left), 0.25 (right). Terms are normalized with $\tau_{w,o}^2/\bar{\mu}$	134
5.62	Comparison of production (—), dissipation (... ..), pressure dilatation (- .-) terms in the TKE budget at $x/L=$ 0.3 (left), 0.4 (right). Terms are normalized with $\tau_{w,o}^2/\bar{\mu}$	135
5.63	Comparison of production (—), dissipation (... ..), pressure dilatation (- .-) terms in the TKE budget at $x/L=$ 0.6 (left), 0.75 (right). Terms are normalized with $\tau_{w,o}^2/\bar{\mu}$	135
5.64	Axial production term : $x/L =$0.0, — 0.15, — — 0.25 for the figure on the left and $x/L =$0.3, — 0.4, — — 0.5 for the one on the right. Terms are normalized with $\tau_{w,o}^2/\bar{\mu}$	136
5.65	Decomposition of axial production term at $x/L =$ 0.15 (left), 0.25 (right). —, mean shear; mean dilatation; -.- extra strain rate. Terms are normalized with $\tau_{w,o}^2/\bar{\mu}$	136
5.66	Decomposition of axial production term at $x/L =$ 0.3 (left), 0.4 (right). Line types as in figure 5.65. Terms are normalized with $\tau_{w,o}^2/\bar{\mu}$	137
5.67	Left:Decomposition of axial production term at $x/L =$ 0.5. Line types as in figure 5.65. Terms are normalized with $\tau_{w,o}^2/\bar{\mu}$. Right: Mean shear at $x/L =$, 0.0; -.- 0.15; — 0.25; — — 0.5	137
5.68	Reynolds shear stress (left); Pressure-strain correlations (right). Line types as in figure 5.67 (right)	138

List of symbols

Latin symbols

C_p	Specific heat at constant pressure
C_v	Specific heat at constant volume
$c = \sqrt{\gamma RT}$	Speed of sound
$E_{u'_i u'_i}^* = \frac{E_{u'_i u'_i}}{(u_\tau^*)^2}$	Non-dimensional energy spectrum
\bar{f}	Reynolds average
$\tilde{f} = \overline{\rho f} / \bar{\rho}$	Favre or mass weighted average
f'	Reynolds fluctuation
f''	Favre fluctuation
h, s	Enthalpy, entropy
$k_x^* = k_x \bar{v} / u_\tau^*$	Non-dimensional wavenumber
l	Integral turbulent length scale in the direction of mean shear
$M = u_b / c_w$	Mach number = Bulk velocity/speed of sound at the wall
$\bar{M} = \bar{u} / \bar{c}$	Local Mach number
$M_{in} = (\bar{M})_c$	Centerline local Mach number of incoming flow
$M_t = u_{rms} / \bar{c}$	Turbulent Mach number
$M_g = Sl / \bar{c}$	Gradient Mach number
p	Pressure
Pr	Prandtl number
q	Heat flux according to Fourier's law
R	Gas constant per unit mass
r	Radial coordinate (local radius)
R	Radius
$Re_\tau = \frac{\rho_w u_\tau R}{\mu_w}$	Friction Reynolds number
$R_{u'u'}$	Two point correlation coefficient, $\frac{\overline{u'(x)u'(x+r)}}{u_{rms}(x)u_{rms}(x+r)}$
$R_{ab} = \frac{\overline{a'b'}}{a_{rms}b_{rms}}$	Single point correlation coefficient between a' and b'
$S = \frac{d\bar{U}}{dy}$	Mean shear rate
t	Time
T	Temperature
TKE	Turbulent kinetic energy

U_{VD}^+	Van Driest transformed mean velocity
u_x	Axial velocity
u_r	Radial velocity
u_ϕ	Azimuthal velocity
u_b	Bulk velocity
u^l	Contravariant velocity components
$u_\tau = \sqrt{ \tau_w /\rho_w}$	Friction velocity
$u_\tau^* = \sqrt{ \tau_w /\bar{\rho}}$	Semi-local friction velocity
(x, r, ϕ)	Axial, radial and azimuthal directions
$y/R = (1 - r/R)$	Normalized radial coordinate measured as distance from the wall
$y^+ = \frac{(R-r)u_\tau}{\nu_w}$	Coordinate in wall units measured as distance from the wall
$y^* = \frac{(R-r)u_\tau^*}{\bar{\nu}}$	Semi-local coordinate in the radial direction measured as distance from the wall

Greek symbols

$\nabla \cdot \vec{u}$	Divergence of \vec{u}
Ψ	Viscous dissipation rate
$\beta = \frac{\delta^*}{\tau_w} \frac{d\bar{p}}{dx}$	Clauser pressure gradient parameter
$\gamma = C_p/C_v$	Ratio of specific heats
δ^*	Displacement thickness
$\epsilon_d = 4/3 \bar{\mu} \overline{u'_{i,l} u'_{k,k}}$	Compressible or dilatational dissipation rate
$\epsilon_s = 1/2 \bar{\mu} \overline{\omega'_k \omega'_k}$	Solenoidal dissipation rate
θ	Momentum thickness
μ	Dynamic viscosity
ν	Kinematic viscosity
ρ	Density
τ	Viscous stress tensor
τ_w	Wall shear stress
ω	Vorticity tensor, $(u_{i,j} - u_{j,i})$
(ξ^1, ξ^2, ξ^3)	General non-orthogonal curvilinear coordinates

Superscripts

+	Normalization with ν_w and u_τ
*	Normalization with $\bar{\nu}$ and u_τ^*

Subscripts

c	Values at the centerline
w	Values at the wall
o	Stagnation (total) values for pipe flow; values at inlet for nozzle/diffuser flow

Chapter 1

Introduction

Compressible turbulence occurs in nature and in engineering applications. Recent evidences show that supersonic turbulence is important in star formation processes (Low & Klessen (2004)). In engineering applications, compressible turbulent flows occur in high speed flight as external flows over the fuselage or as internal flows in jet engines.

Kovaszny (1953) examined the linearized equations for compressible turbulence (at low rms Mach number) and showed the existence of three basic modes: acoustic, vorticity and entropy. In the absence of viscous effects and mean shear these modes are independent of each other. If viscous effects are taken into account, then coupling exists between the acoustics and entropy modes. If only mean shear is considered, then the vorticity and acoustic modes are coupled. In the presence of both mean shear and viscous effects, the three modes are coupled to each other (Blaisdell *et al.*, 1993). The coupling between the vorticity and acoustic modes in homogeneous shear flows makes them independent of initial conditions.

Sarkar *et al.* (1991) studied isotropic turbulence at low turbulent Mach numbers, M_t and showed that the acoustic mode can be effectively isolated. In such flows, the effects of compressibility on vorticity is much smaller than that on acoustics (dilatation). The analysis given in Sarkar *et al.* (1991) yields a parameter which represents the partition of internal and kinetic energy of the acoustic mode. It was shown that this parameter evolves to a constant value of unity which denotes a state of acoustic equilibrium i.e. the equipartition of kinetic and potential energies of the acoustic mode.

Homogeneous shear flows show inhibited shear layer growth rate (suppression of turbulence) at higher convective Mach numbers. Sarkar (1995) pointed out that the gradient Mach number, M_g (which is the ratio of an acoustic timescale to that of the mean shear) is a more important parameter than the turbulent Mach number, M_t (ratio of acoustic time scale to a turbulence time scale) as an indicator of compressibility effects. The lower value of M_g in supersonic turbulent boundary layers is responsible for lower intrinsic compressibility effects in such flows than in free shear layers. In this study it was also found that the reduced growth rate is due to reduced turbulence production and not due to effects of dilatation fluctuations. In case of high speed shear layers, Pantano & Sarkar (2002) relate this reduced production to reduced pressure-strain correlations as M_g increases. Reduced pressure-strain, reduced pressure fluctuations and suppression of turbulence levels with increasing Mach numbers have been observed before in plane mixing layers (Vreman

et al., 1996) and annular mixing layers (Freund *et al.*, 1997). The analysis of a wave equation for the pressure fluctuations by Pantano & Sarkar (2002) shows both M_g and M_t to be important parameters determining compressibility. The increase in the ratio of an acoustic time scale to a turbulent time scale at increasing Mach number inhibits the pressure-strain correlations by causing a time delay in the passage of pressure signals.

Based on experimental results, Morkovin (1964) concluded that the pressure fluctuations are negligible and the total temperature fluctuations are small in non-hypersonic boundary layers with adiabatic walls. He derived the following form of strong Reynolds analogy (SRA) for such flows:

$$\frac{T'}{\bar{T}} = -(\gamma - 1)M^2 \frac{u'}{\bar{u}}$$

Since the pressure fluctuations are negligible,

$$\frac{\rho'}{\bar{\rho}} \approx -\frac{T'}{\bar{T}} = (\gamma - 1)M^2 \frac{u'}{\bar{u}}$$

which means that density fluctuations are negligible as long as $(\gamma - 1)M^2$ remains small (non-hypersonic flow). These findings are known as ‘Morkovin’s hypothesis’ in the literature (Bradshaw, 1977). This means that the turbulence structure of non-hypersonic boundary layers is expected to follow closely that of low-speed boundary layers. In supersonic boundary layers as also in supersonic channel flows with heat transfer at the wall, total temperature fluctuations are not negligible and the SRA relation does not hold. The pressure fluctuations, however, remain negligible. Simulations of supersonic channel flows with isothermal walls show increased streamwise coherence (Coleman *et al.*, 1995) and increased Reynolds stress anisotropy at high Mach numbers Foysi *et al.* (2004). Dilatation fluctuations are found to be negligible up to $M = 3.5$. The increased coherence of streaky structures at higher Mach numbers was found (from the simulations of Coleman *et al.* (1995)) to be an effect of mean density variation. Foysi *et al.* (2004) found that the pressure-strain correlations are reduced at supersonic speeds leading to higher Reynolds stress anisotropy. Moreover, solving a Poisson equation for pressure fluctuations using Green’s functions (and not the wave equation as in shear layers) was found to be sufficient to match the DNS pressure-strain profiles. The observed change in pressure-strain correlations is attributed to changes in mean density. We expect similar effects in our supersonic pipe flow simulations.

However, Morkovin’s hypothesis does not cover flows which are under the influence of favourable and adverse longitudinal pressure gradients. It has been shown in experimental studies (Spina *et al.*, 1994) of supersonic boundary layers that acceleration/deceleration leads to decrease/increase of turbulence intensities. These changes in turbulence structure are far greater than those expected from the extra production terms in the Reynolds stress equations for such flows. The pressure-strain correlations might also play an important role in these flows. In this study, we intend to examine these effects by means of direct and large eddy simulations of supersonic nozzle and diffuser flows with fully developed supersonic pipe flow at inlet. The nozzle and the diffuser are designed in such a way as to produce weak, gradual acceleration and deceleration effects respectively.

Coleman & Mansour (1993) study effects of rapid spherical compression on compressible isotropic turbulence and observe high pressure-dilatation correlation at large compression rates. Effects of rapid axial compression on compressible, homogeneous turbulence have been studied by Cambon *et al.* (1993) using DNS. They found increased pressure-dilatation correlation at large compression speeds. However, its relative importance compared to the TKE production was found to become smaller with increasing compressibility (i.e. with increasing M_t). On the other hand, the pressure-strain correlation, which modifies the Reynolds stress anisotropy and hence TKE production, was found to be larger than the pressure-dilatation correlation over a wide range of Mach numbers and large compression speeds. Using DNS, Mahesh *et al.* (1996) study shock/shear flow interactions and show that the TKE evolution across the shock depends on the upstream anisotropy and the velocity-temperature correlations. Large amplification of TKE was observed when the upstream velocity-temperature correlation was negative. All the above-mentioned studies provide comparisons of DNS with rapid distortion theory (RDT).

However, we did not come across systematic studies of the effects of weak, distributed pressure gradients on compressible, turbulent boundary layers. Hence, it is our aim to contribute new findings about effects of weak, distributed dilatation on the turbulence structure in supersonic nozzles and diffusers using well-established and accurate numerical methods. The geometry is chosen in such a way as to ensure that an extended region of constant acceleration/deceleration exists.

We intend to find answers to the following questions in this study of nozzle and diffuser flows with weak, gradual expansion/compression:

- In what way is turbulence production modified in flows with weak mean dilatation?
- How important is the role of pressure-strain correlations in such flows?

Shock-turbulent boundary layer interaction is another important area of research in compressible boundary layers. These flows exhibit substantial effects of dilatation fluctuations at high shock intensities. For example, in the DNS of compressible ramp flow by Adams (2000) at incoming $M = 3$ the pressure-dilatation correlation at the shock-foot region is larger than the TKE production by a factor of 2. The oscillatory nature of the shock wave incursions into the boundary layer is of interest in such flows and investigations focus on the causes of such oscillations.

Shock trains in supersonic diffusers have been studied experimentally and using RANS in the past (Matsuo *et al.*, 1999). According to these studies, when the incoming Mach number exceeds 1.5, a series of weak shocks is produced instead of a single normal shock because of the presence of the near-wall viscous layer. Thus, the pressure rise in these flows occurs over a finite length of the diffuser. Time accurate data for such flows are necessary to study the oscillatory nature of the shock system and compressibility effects, in general.

We perform LES of a diffuser flow with incoming $M = 1.5$ where the flow is decelerated through a weak shock system. This flow shows intrinsic compressibility effects in the form of dilatation fluctuations. Effects on turbulence production are looked into in proper detail.

The present thesis is organised as follows:

Chapter 2 gives an overview of the numerical method used in this study. DNS and LES results of compressible turbulent pipe flow are presented in chapter 3 where the focus is on compressibility effects. In chapter 4, effects of weak mean expansion on turbulence structure in a supersonic nozzle are looked into. In the first part of Chapter 5, effects of weak mean compression in supersonic diffusers which in some sense are opposite to those of expansion in a nozzle are examined. The second part of chapter 5 investigates the dynamics of weak shock trains in a diffuser.

Chapter 2

Mathematical and numerical considerations

2.1 Governing Equations

Compressible flows up to low hypersonic Mach numbers, and sufficiently high Reynolds numbers so that the Knudsen numbers remain smaller than 10^{-2} , are known to obey laws of continuum mechanics. It is thus possible to describe such flows using conservation of mass, momentum and energy. A form of such equations in terms of primitive variables such as pressure, velocity and entropy in generalized non-orthogonal curvilinear coordinates as proposed by Sesterhenn (2001), are given below.

$$\begin{aligned}
 p_t &= -\frac{\rho c}{2} [X^+ + X^- + Y^+ + Y^- + Z^+ + Z^-] + \frac{p}{C_v} [s_t + X^s + Y^s + Z^s], \\
 u_t &= -\frac{\sqrt{g^{11}}}{2} [X^+ - X^-] - Y^u - \frac{g^{21}}{2\sqrt{g^{22}}} [Y^+ - Y^-] - Z^u - \frac{g^{31}}{2\sqrt{g^{33}}} [Z^+ - Z^-] \\
 &\quad + \frac{\xi_{,i}^1 \xi_{,j}^l}{\rho} \frac{\partial \tau_{ij}}{\partial \xi^l}, \\
 v_t &= -X^v - \frac{\sqrt{g^{22}}}{2} [Y^+ - Y^-] - Z^v - \frac{g^{12}}{2\sqrt{g^{11}}} [X^+ - X^-] - \frac{g^{32}}{2\sqrt{g^{33}}} [Z^+ - Z^-] \\
 &\quad + \frac{\xi_{,i}^2 \xi_{,j}^l}{\rho} \frac{\partial \tau_{ij}}{\partial \xi^l}, \\
 w_t &= -X^w - \frac{\sqrt{g^{33}}}{2} [Z^+ - Z^-] - Y^w - \frac{g^{23}}{2\sqrt{g^{22}}} [Y^+ - Y^-] - \frac{g^{13}}{2\sqrt{g^{11}}} [X^+ - X^-] \\
 &\quad + \frac{\xi_{,i}^3 \xi_{,j}^l}{\rho} \frac{\partial \tau_{ij}}{\partial \xi^l}, \\
 s_t &= -X^s - Y^s - Z^s + \frac{1}{\rho T} \left(-\xi_i^l \frac{\partial}{\partial \xi^l} \left(-\lambda \xi_i^l \frac{\partial T}{\partial \xi^l} \right) + \Psi \right). \tag{2.1}
 \end{aligned}$$

The above equations for the evolution of p, u, v, w and s , in which subscripts 't' denote partial derivatives with respect to time, can be solved along with an ideal gas equation

of state, $p = \rho RT$, with constant C_p, C_v and Prandtl number for simplest canonical compressible flows. The dynamic viscosity is assumed to vary with temperature according to Sutherland's law: $\mu \propto T^{0.7}$. X^\pm, Y^\pm, Z^\pm can be interpreted as acoustic waves propagating with velocities $u \pm \sqrt{g^{11}}c$, $v \pm \sqrt{g^{22}}c$, and $w \pm \sqrt{g^{33}}c$; X^s, Y^s, Z^s are entropy waves travelling with velocities u, v and w ; and $X^{v,w}, Y^{u,w}, Z^{u,v}$ are vorticity waves propagating with velocities u, v, w according as the superscripts:

$$\begin{aligned} X^\pm &\equiv (u \pm \sqrt{g^{11}}c) \left[\frac{p\xi}{\rho c} \pm \frac{u_\xi}{\sqrt{g^{11}}} \right], & X^s &\equiv us_\xi, & X^v &\equiv u \left(v_\xi - \frac{g^{12}}{g^{11}} u_\xi \right), \\ X^w &\equiv u \left(w_\xi - \frac{g^{13}}{g^{11}} u_\xi \right), & Y^\pm &\equiv (v \pm \sqrt{g^{22}}c) \left[\frac{p\eta}{\rho c} \pm \frac{v_\eta}{\sqrt{g^{22}}} \right], & Y^s &\equiv vs_\eta, \\ Y^u &\equiv v \left(u_\eta - \frac{g^{21}}{g^{22}} v_\eta \right), & Y^w &\equiv v \left(w_\eta - \frac{g^{23}}{g^{22}} v_\eta \right), & Z^\pm &\equiv (w \pm \sqrt{g^{33}}c) \left[\frac{p\zeta}{\rho c} \pm \frac{w_\zeta}{\sqrt{g^{33}}} \right], \\ & & Z^s &\equiv ws_\zeta, & Z^u &\equiv w \left(u_\zeta - \frac{g^{31}}{g^{33}} w_\zeta \right), & Z^v &\equiv w \left(v_\zeta - \frac{g^{32}}{g^{33}} w_\zeta \right). \end{aligned}$$

Although, three dimensional Euler equations do not admit simple wave solutions, a decomposition of the convective terms as shown above, provides ease of upwinding and implementation of boundary conditions in the corresponding coordinate directions. u, v, w are the velocities along coordinates $\xi^1 \equiv \xi, \xi^2 \equiv \eta, \xi^3 \equiv \zeta$. The viscous stress tensor and the dissipation rate read:

$$\tau_{ij} = 2\mu \left(s_{ij} - \frac{1}{3} s_{kk} \delta_{ij} \right), \quad s_{ij} = \frac{1}{2} \left(\frac{\partial u_i}{\partial x_j} + \frac{\partial u_j}{\partial x_i} \right), \quad \Psi = \tau_{ij} s_{ij}.$$

Here, bulk viscosity effects have been neglected.

$g^{lm} = \xi_{,i}^l \xi_{,i}^m$ and $\xi_{,i}^l$ are shorthands for $\frac{\partial \xi^l}{\partial x_i}$ such that $\frac{\partial}{\partial x_i} = \frac{\partial \xi^l}{\partial x_i} \frac{\partial}{\partial \xi^l}$ where x_i are cartesian coordinates.

Similarly, the contravariant velocities $u^1 \equiv u, u^2 \equiv v, u^3 \equiv w$ can be connected to the cartesian components through $u^l = \xi_{,i}^l u_i$. From now on, we will denote $\xi_{,i}^l$ by k_{li} .

The temporal changes of the cartesian velocity components can be written as:

$$\frac{\partial u_i}{\partial t} = \frac{\partial x_i}{\partial \xi^l} \frac{\partial u^l}{\partial t}.$$

2.1.1 Cylindrical coordinates

We introduce cylindrical coordinates for a domain of length L_x in the axial direction and of radius R as follows with the wall-normal tanh stretching taken into account:

$$x_1 = \xi L_x, \quad x_2 = \frac{\tanh \kappa \zeta}{\tanh \kappa} R \cos 2\pi\eta, \quad x_3 = \frac{\tanh \kappa \zeta}{\tanh \kappa} R \sin 2\pi\eta.$$

This is an orthogonal coordinate system where ξ, ζ, η vary uniformly from 0 to 1. Now, we just need the following connection coefficients between the cylindrical and cartesian

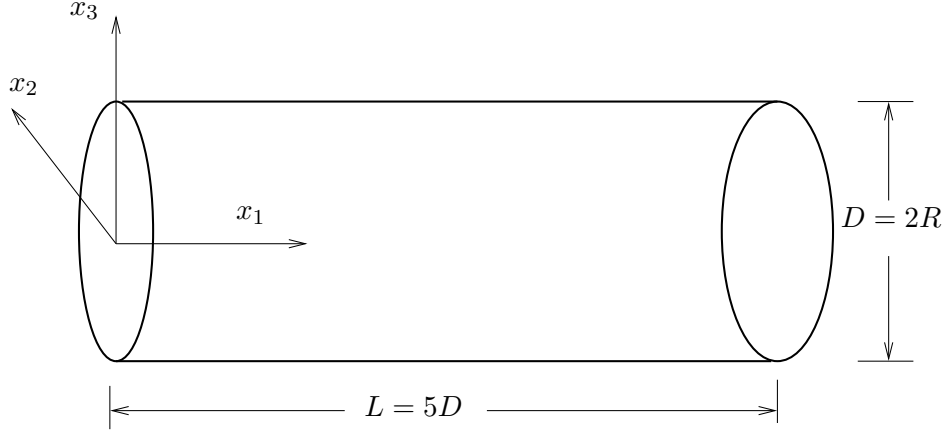


Figure 2.1: Sketch of the computational domain for the pipe flow.

coordinate systems.

$$k_{11} = \frac{1}{L_x}, \quad k_{22} = -\frac{\sin 2\pi\eta}{2\pi r}, \quad k_{23} = \frac{\cos 2\pi\eta}{2\pi r},$$

$$k_{32} = \frac{\cos 2\pi\eta \tanh \kappa \cosh^2 \kappa\zeta}{\kappa R}, \quad k_{33} = \frac{\sin 2\pi\eta \tanh \kappa \cosh^2 \kappa\zeta}{\kappa R}.$$

where $r = \frac{\tanh \kappa\zeta}{\tanh \kappa} R$.

All other k_{ij} are zero and hence only g^{ii} , $i=1,2,3$ are non-zero i.e. this coordinate system is orthogonal.

2.1.2 Coordinates for nozzle/diffuser simulations

The nozzle/diffuser configuration is computed in a nonorthogonal, quasi-cylindrical coordinate system where the radius is a function of the longitudinal coordinate as written below :

$$x_1 = \xi L_x, \quad x_2 = \frac{\tanh \kappa\zeta}{\tanh \kappa} f(\xi) \cos 2\pi\eta, \quad x_3 = \frac{\tanh \kappa\zeta}{\tanh \kappa} f(\xi) \sin 2\pi\eta.$$

The connection coefficients are

$$k_{11} = \frac{1}{L_x}, \quad k_{22} = -\frac{\sin 2\pi\eta}{2\pi r}, \quad k_{23} = \frac{\cos 2\pi\eta}{2\pi r}, \quad k_{31} = -\frac{\tanh \kappa\zeta f'(\xi) \cosh^2 \kappa\zeta}{L_x \kappa f(\xi)},$$

$$k_{32} = \frac{\cos 2\pi\eta \tanh \kappa \cosh^2 \kappa\zeta}{\kappa f(\xi)}, \quad k_{33} = \frac{\sin 2\pi\eta \tanh \kappa \cosh^2 \kappa\zeta}{\kappa f(\xi)}.$$

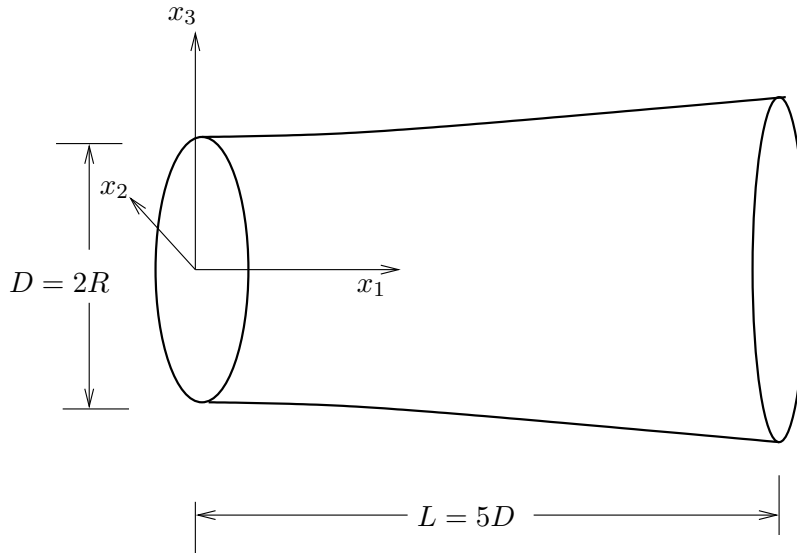


Figure 2.2: Sketch of the computational domain for the nozzle flow.

where $r = \frac{\tanh \kappa \zeta}{\tanh \kappa} f(\xi)$ and $f(\xi)$ is function defining the axial radius distribution. Such a system is nonorthogonal since g^{13} is nonzero along with g^{ii} , $i=1,2,3$.

$f(\xi)$ is determined in our flow cases using isentropic streamtube equations and specifying a pressure distribution ensuring that the flow goes through a region of constant pressure gradient.

2.2 Spatial and temporal discretization

The DNS results are obtained using 5th order compact upwind schemes (CULD, Adams & Shariff (1996)) for the convective terms and 6th order central schemes (Lele, 1992) for the molecular terms. Time advancement is done using the 3-stage, 3rd order low-storage Runge-Kutta algorithm of Williamson (1980). These schemes were used by Foyi *et al.* (2004) for supersonic channel simulations as well.

The LES results are obtained using 6th order central schemes (Lele, 1992) for both convective and molecular transport terms.

2.2.1 LES method

An explicit filtering variant (Mathew *et al.*, 2003) of the Approximate Deconvolution Method (Stolz *et al.*, 2001) is used for modelling the subgrid scale terms.

The method is explained below with the help of a 1-d nonlinear transport equation:

$$\frac{\partial u}{\partial t} + \frac{\partial f(u)}{\partial x} = 0.$$

LES implies low-pass filtering:

$$\bar{u} = G * u = \int G(x - x') u(x') dx', \quad (2.2)$$

which leads to the filtered transport equation:

$$\frac{\partial \bar{u}}{\partial t} + \frac{\partial f(\bar{u})}{\partial x} = \frac{\partial f(\bar{u})}{\partial x} - G * \frac{\partial f(u)}{\partial x}. \quad (2.3)$$

The approximate deconvolution procedure $u^* = Q_N * \bar{u}$ uses the approximate inverse $Q_N \approx G^{-1}$ computed using the Van Cittert series (Stolz *et al.*, 2001) truncated at $N = 6$:

$$Q_N = \sum_{n=0}^N (I - G)^n.$$

I being the identity operator. Equation (2.3) can now be written as,

$$\frac{\partial \bar{u}}{\partial t} + \frac{\partial f(\bar{u})}{\partial x} = \frac{\partial f(\bar{u})}{\partial x} - G * \frac{\partial f(u^*)}{\partial x} + G * \left[\frac{\partial f(u^*)}{\partial x} - \frac{\partial f(u)}{\partial x} \right], \quad (2.4)$$

where the last term in the bracket is unknown in an LES and has to be modeled. For a useful LES, the low wavenumber content of the deconvolved velocity field u^* should be close to that of u :

$$G * u^* \approx G * u = \bar{u}.$$

The model $u = u^*$ gives the LES equation,

$$\frac{\partial \bar{u}}{\partial t} + G * \frac{\partial f(u^*)}{\partial x} = 0.$$

The integration of this equation involves the following 3 steps:

deconvolution:	$u^{*(n)} = Q_N * \bar{u}^n$
integration:	$u^{*(n+1)} \leftarrow u^{*(n)}$
filtering:	$\bar{u}^{(n+1)} = G * u^{*(n+1)}$

In a simulation, step 1 follows step 3, so that both steps can be combined:

$$u^{*(n)} \leftarrow Q_N * G * u^{*(n)}.$$

Regularization by addition of artificial dissipation is seen to be necessary since the model problem (LES) does not include the dissipation scales. It is done in the ADM formulation of Adams & Leonard (1999) and subsequently by Stolz *et al.* (2001) by adding a term of the form $\chi(I - Q_N * G) * \bar{u}$ to the filtered equation. This can be interpreted as an additional filtering step and approximated by the filter $Q_N * G$ (Mathew *et al.*, 2003). Thus the procedure of deconvolution and regularization can be combined into a single step filtering with the filter $(Q_N * G)^2$.

Filters used

In the periodic directions, a one-parameter filter with the following transfer function (see Mathew *et al.* (2003)) is used as a primary filter(G),

$$\hat{G}(\omega) = \left(\alpha + \frac{1}{2}\right) \frac{1 + \cos \omega}{1 + 2\alpha \cos \omega}.$$

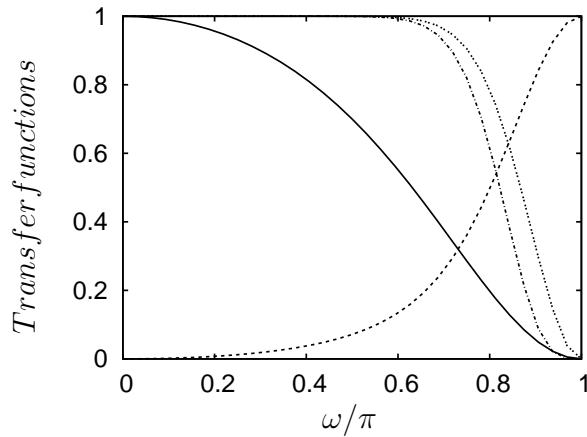


Figure 2.3: Filter transfer functions for $\alpha = 0.2$: — G , - - - Q_N , $Q_N * G$, -.-. $(Q_N * G)^2$ with $\alpha = 0.2$ and $N = 6$.

Figure 2.3 shows the transfer functions of the primary filter G , its approximate inverse Q_N and those of $Q_N * G$ and $(Q_N * G)^2$. $Q_N * G$ and $(Q_N * G)^2$ both decay smoothly to zero at high wavenumbers which is, of course, what we desire.

In the non-periodic directions explicit filters in physical space following Stolz (2000) are used for G . For symmetric filters (i.e. for interior points), G has a cutoff wavenumber $\omega_c \approx 0.63\pi$ on uniform meshes. It should be noted here that we use $Q_N * G$ in the non-periodic directions instead of $(Q_N * G)^2$ to avoid extra computation costs. $(Q_N * G)^2$ can always be interpreted as a filter F which has the desired transfer function.

2.2.2 Axis singularity treatment

The quality of high order accurate finite difference computations in cylindrical coordinates depends on the treatment of the singularity at the centerline. The axis singularity arises due to the presence of terms with $1/r$ factors in the governing equations. To avoid solving the governing equations at the axis, boundary conditions could be specified there, but this is not a recommended approach in computing turbulent flows. Freund *et al.* (1997) solved the equations at the centerline in cartesian coordinates in order to avoid the singularity. Another approach is to solve a modified set of governing equations which are not singular at the axis. One such approach has been recently proposed by Constantinescu & Lele (2002) which has been applied to study jet acoustics by LES. Careful implementation of this approach for compressible, fully developed, turbulent pipe flows by the author of this thesis led to stable DNS computations but there were non-physical grid-to-grid oscillations (two-delta or sawtooth waves) which called for the use of a high wavenumber cutoff filter which is not desirable in a DNS.

Instead, we refrain from solving the governing equations at the axis and stagger the grid points as in Mohseni & Colonius (2000) so that no grid point lies directly on the axis.

A new radial coordinate r_1 is defined such that

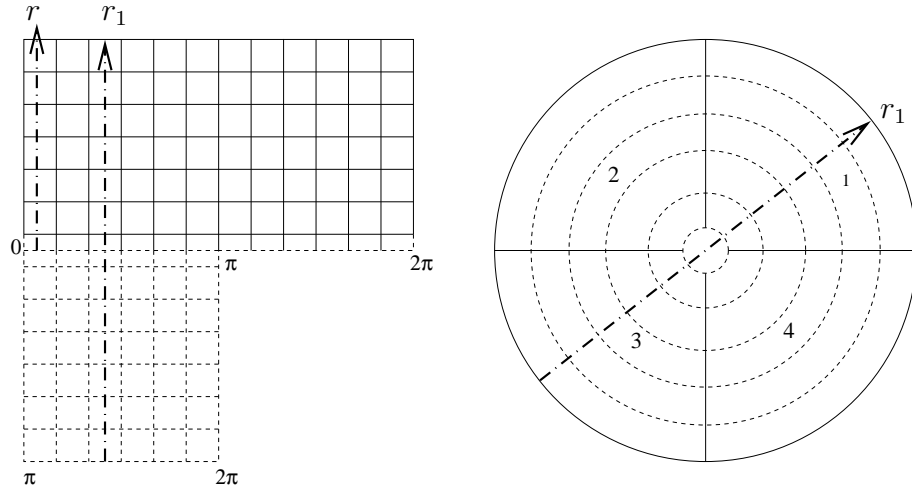


Figure 2.4: Physical and computational domains

$$r_1(r, \phi) = \begin{cases} r & \text{if } 0 \leq \phi \leq \pi \\ -r & \text{if } \pi < \phi < 2\pi \end{cases}$$

where $0 \leq r \leq R$. r_1 is discretized on a set of nodes $r_n = \frac{(2n+1)\Delta r}{2}$, $n = 0, 1, 2, \dots$ which avoids placing a grid-point on the axis. The radial derivative is now computed across a diameter. The sign of this derivative has to be carefully chosen depending on the azimuthal coordinate ϕ . An illustration of the physical and computational domains used for the radial derivative is shown in figure 2.4.

In order to get rid of the artificial time step constraint near the axis which arises due to the higher grid-point density there in the cylindrical coordinate system, spatial filtering is applied in this region ($0 < r/R < 0.05$) in the DNS using a $Q_N * G$ filter similar to that in figure 2.3 but with a higher cutoff wavenumber $\omega_c \approx 0.85\pi$.

2.2.3 Parallelisation

The code uses MPI routines for communication between processors. A pipelined Thomas algorithm involving the use of 'ghost' cells is used applied, for example, to solve tridiagonal systems in the periodic direction. Similar 'chained' algorithms are used for pentadiagonal systems as well. For the pipe flow simulations, the periodic streamwise and azimuthal directions are parallelised as described above. For the nozzle flow simulations, a transpose algorithm is used for computing the derivative in the non-periodic streamwise direction and the periodic direction is parallelised as in the pipe flow.

In all the computations, no parallelization is used in the radial direction. However, since we compute the radial derivative along a diameter we must also communicate between processors which are not neighbours. As illustrated on the right of figure 2.4, the domain for example is split into 4 processors in the azimuthal direction. So, to compute

$$\begin{aligned} u_1 &= b_1, v_1 = c_1/u_1, w_1 = h_1/u_1, \\ s_2 &= a_2, u_2 = b_2 - s_2v_1, \\ v_2 &= (c_2 - s_2w_1)/u_2, w_2 = h_2/u_2 \end{aligned}$$

and so on....

$$\begin{aligned} u_n &= b_n, v_n = a_n/u_n, w_n = f_n/u_n, \\ s_{n-1} &= c_{n-1}, u_{n-1} = b_{n-1} - s_{n-1}v_n, \\ v_{n-1} &= (a_{n-1} - s_{n-1}w_n)/u_{n-1}, w_{n-1} = f_{n-1}/u_{n-1} \end{aligned}$$

and so on....

Then, a forward sweep is carried out in each processor starting from the periphery towards the center in the following way. Compute z from

$$Tz = d,$$

$$\begin{aligned} z_1 &= d_1/u_1, z_2 = (d_2 - s_2z_1)/u_2, \\ z_i &= (d_i - s_iz_{i-1} - f_iz_{i-2})/u_i, i = 3, 4, \dots, q \end{aligned}$$

and

$$\begin{aligned} z_n &= d_n/u_n, z_{n-1} = (d_{n-1} - s_{n-1}z_n)/u_{n-1}, \\ z_i &= (d_i - s_iz_{i-1} - f_iz_{i-2})/u_i, i = n-2, n-3, \dots, q+1. \end{aligned}$$

Backward substitution starts using $Wx = z$ in each processor at the first few points near the center in the following way

$$\begin{aligned} x_{q-1} + v_{q-1}x_q + w_{q-1}x_{q+1} &= z_{q-1}, \\ x_q + v_qx_{q+1} + w_qx_{q+2} &= z_q, \\ w_{q+1}x_{q-1} + v_{q+1}x_q + x_{q+1} &= z_{q+1}, \\ w_{q+2}x_q + v_{q+1}x_{q+1} + x_{q+2} &= z_{q+2}. \end{aligned}$$

The above set of linear equations are solved using Cramer's rule.

Processor pairs 1,3 and 2,4 now exchange the following information which is stored in 'ghost' cells:

$$\begin{aligned} & z_{q-1}, z_q \\ & z_{q+1}, z_{q+2}. \end{aligned}$$

Backward substitution continues in each processor away from the centerline towards the periphery:

$$\begin{aligned} x_i &= z_i - v_ix_{i+1} - w_ix_{i+2}, i = q-2, q-3, \dots, 1 \\ x_i &= z_i - v_ix_{i-1} - w_ix_{i-2}, i = q+3, q+4, \dots, n \end{aligned}$$

Thus there is virtually no idle time for any processor except during the exchange of a small amount of data near the centerline.

This algorithm has proved to be accurate, efficient and stable in our DNS computations. The DNS code now performs at nearly 576 Mflops/core on the ALTIX 4700 at the Leibniz Rechenzentrum in Munich.

2.2.4 Code coupling for nozzle/diffuser simulation

The nozzle and diffuser simulations are performed using real-time DNS/LES data of fully developed supersonic pipe flow as inflow . This calls for a coupling of two different versions of the existing flow solver - one computing the pipe flow and the other computing the nozzle/diffuser flow, using basic MPI routines. Although coupling of two widely different existing CFD solvers is still challenging, the problem is simplified in our case by the fact that the two flow solvers to be coupled are very similar to each other. Thus addition of a few lines in each code is all we did to achieve our goal. The procedure is similar (but much simpler in our case) to that described in Schlueter *et al.* (2002).

The message passing between two separate flow solvers (peer-to-peer message passing) is very similar to the information exchange between processors in a parallel computation. `MPI_COMM_WORLD` is the communicator which is associated with all the processors in a computation started with: `mpirun N1 ./a.out : N2 ./b.out` where `N1`, `N2` are the number of processors used by the two solver executables `a.out` and `b.out` respectively. Using this communicator for message passing between flow solvers would result in confusion between the two codes. To avoid this, separate communicators should be used which will be associated with processors dedicated to each solver. This is done in our case using `MPI_COMM_SPLIT` on `MPI_COMM_WORLD` to group the processors of each solver and associate them with a new communicator (intra-communicator). Then message passing is possible between the processors in the intra-communicator and the remaining processors of `MPI_COMM_WORLD` which belong to the other flow solver. A special inter-communicator has to be constructed now, which achieves this. This is done using `MPI_INTERCOMM_CREATE` which is a communicator which facilitates message passing between the intra-communicator and `MPI_COMM_WORLD`. So, we see that two similar solvers can be connected easily by use of only two MPI functions, `MPI_COMM_SPLIT` and `MPI_INTERCOMM_CREATE`.

2.2.5 Boundary Conditions

Isothermal, no-slip Wall

The no-slip condition implies $\frac{\partial u_i}{\partial t} = 0$. The isothermal condition implies that $\frac{\partial T}{\partial t} = 0$ which is interpreted for the primitive variables p and ρ in the following manner.

Starting from a differential form of the Gibbs fundamental relation:

$$dh = C_p dT = T ds + \frac{1}{\rho} dp,$$

and introducing the thermal boundary condition gives:

$$\begin{aligned} \frac{\partial T}{\partial t} = 0 &= \frac{T}{C_p} \frac{\partial s}{\partial t} + \frac{1}{C_p \rho} \frac{\partial p}{\partial t} \\ \text{or, } \frac{\partial p}{\partial t} &= -\frac{p}{R} \frac{\partial s}{\partial t}. \end{aligned}$$

Now, from the first of eqn. (2.1) at the wall,

$$\frac{\partial p}{\partial t} = -\frac{\rho c}{2}[Z^+ + Z^-] + \frac{p}{C_v} \frac{\partial s}{\partial t},$$

where Z^\pm are the 'waves' normal to the wall, the expressions of which have been given before in this chapter.

Solving for $\frac{\partial p}{\partial t}$ and $\frac{\partial s}{\partial t}$ gives,

$$\begin{aligned} \frac{\partial p}{\partial t} &= -\frac{\rho c}{2\gamma}[Z^+ + Z^-], \\ \frac{\partial s}{\partial t} &= -\frac{R}{2c}[Z^+ + Z^-]. \end{aligned}$$

Z^\pm are computed values and the use of these results in a small temporal drift in wall temperature. To prevent this, the entropy at the wall is fixed at the beginning of every time integration sub-step according to:

$$s_w = C_v \ln\left(\frac{(RT_w)^\gamma}{p^{\gamma-1}}\right).$$

Inflow and Outflow conditions

Accuracy of DNS and LES of compressible flows strongly depends on the way the inflow and outflow are treated. Of particular importance is the treatment of acoustic waves which should have a possibility to exit the computational domain. For compressible wall-bounded flows, special treatments are needed for the viscous and heat conduction effects in the near-wall region.

Since the aim of our nozzle/diffuser simulations is to look at effects of acceleration/retardation on supersonic, fully-developed pipe flow we chose to simulate the supersonic pipe flow as a separate simulation using streamwise periodicity and to use the information from this simulation at the inflow of the nozzle/diffuser simulation at every time step i.e. the two simulations run simultaneously and use a global minimum time step. The coupling procedure described above is used.

Now, the inflow information could be the primitive variables p, u, v, w, s with either p or s unspecified to make the inflow transparent to the acoustics. This procedure, however, leads to instabilities since there is no distinction between boundary conditions on convective and viscous terms.

Instead, we choose to specify the inflow in terms of characteristics in the same spirit as Poinot & Lele (1992) which leads to stable computations with physically plausible results. In the supersonic region of the nozzle/diffuser inflow plane, we specify the incoming acoustic, vorticity and entropy waves X^+, X^-, X^v, X^w, X^s computed from the pipe flow simulation. In the subsonic region of the inflow, however, the outgoing acoustic wave X^- is not specified and this information comes from the region downstream of the inflow and thus facilitates removal of acoustics from the computational domain.

The transfer of the characteristics from the pipe flow to the nozzle/diffuser computations is, however, not enough for the Navier-Stokes equations. For the viscous terms, we

compute the second derivative in the streamwise direction using the primitive variables from both the computations, using ghost layers in the nozzle/diffuser computation at the inflow.

Outflow conditions are only required in the subsonic part of the outflow where information can travel upstream. Supersonic regions of the outflow get all the information from upstream and hence need no boundary condition. The subsonic partially nonreflecting outflow condition as in Poinso & Lele (1992) is used here. It consists in weakly specifying the pressure at the outflow by adding an extra forcing in the axial momentum equation. The extra information is the acoustic wave which enters the computational domain at the outflow and brings in information about the ambient pressure p_{inf} .

$$X^- = K(p - p_{inf})$$

Poinso & Lele (1992) provide a way to evaluate the constant K such that the imposed condition has only a weak influence on the flow,

$$K = \sigma(1 - M^2)c/L$$

where M is the maximum Mach number in the flow, L is a characteristic domain size, c is the speed of sound and σ is a constant. In our flow cases, M and c were taken as average quantities, L as the streamwise domain size and $\sigma = 0.25$. p_{inf} is taken to be constant along the radius in the subsonic regions. This is indeed close to the physics since we will see that in our nozzle and diffuser flows, the radial variation of pressure in the near-wall region is negligible. Extra conditions for the viscous terms are specified by setting to zero the axial derivatives of the transverse shear stresses and the heat flux through the outflow plane.

$$\frac{\partial \tau_{12}}{\partial x_1} = 0, \frac{\partial \tau_{13}}{\partial x_1} = 0, \frac{\partial q_1}{\partial x_1} = 0$$

where x_1 is a coordinate normal to the outflow plane.

We did not find it necessary to use absorbing layers (Hu (2004)) at the outflow which provide a mechanism to damp out acoustic waves and prevent spurious reflections back to the inflow. Since, we have an inflow which is partially transparent to acoustics waves, we do not need absorbing layers anywhere in the flow.

2.2.6 Some definitions concerning statistics

Its useful at this point to have a look at the definitions of certain statistical quantities in cylindrical coordinates. Any bulk quantity f_b (i.e. bulk velocity) is defined as:

$$f_b = \frac{2}{R^2} \int_0^R f r dr$$

where $f(r)$ is the velocity at radius r averaged over the homogeneous directions.

A displacement thickness (δ^*) which is a measure of the mass defect in the viscous sublayer is defined as:

$$\delta^*(2R - \delta^*) = 2 \int_0^R r \left(1 - \frac{u}{u_{cl}}\right) dr$$

Similarly a momentum thickness (θ) which is a measure of the momentum defect in the viscous sublayer is defined as:

$$\theta(2R - \theta) = 2 \int_0^R r \frac{u}{u_{cl}} \left(1 - \frac{u}{u_{cl}}\right) dr$$

Here $u(r)$ and u_{cl} are velocities at a radius r and at the centerline respectively, averaged over homogeneous directions.

Chapter 3

Supersonic turbulent pipe flow

3.1 Introduction

Turbulent flow through pipes with circular cross-section is common in numerous industrial applications. It is well-known that such flows through circular cross-sections show effects different from those through rectangular cross-sections. For example, experimental data (Zaman, 1999) indicate that a round jet spreads less rapidly than a plane jet. In case of internal flows, Patel & Head (1969) demonstrated that in an incompressible pipe flow, the mean velocity profile fails to conform to the accepted law of the wall although the channel flow profiles match the law at nearly the same Reynolds numbers based on the pipe radius and channel half-width, respectively. This was confirmed by two independent DNS of incompressible pipe flow (Eggels *et al.*, 1994). They compared their results with those from DNS of channel flow by Kim *et al.* (1987) and noted that the turbulence statistics appear to be less affected by the axisymmetric flow geometry. The wall-normal fluctuations in the pipe are altered due to a different 'splatting' mechanism close to the curved wall.

Besides the incompressible pipe flow with constant density, low Mach number pipe flows with strong heat transfer have been the focus of a number of studies by Satake *et al.* (2000), Xu *et al.* (2004) and Bae *et al.* (2006). These studies show that strong heating of the flow through heat transfer at the wall causes all turbulence intensities to decrease and lead to laminarization if the heating is strong enough.

Supersonic turbulent pipe flow is a canonical flow case which facilitates the investigation of compressibility effects in wall-bounded flows with circular cross-section since this flow is statistically steady when the wall is kept at a constant temperature. Complicating effects of shocks can be avoided by maintaining a balance between the mean pressure gradient driving the flow and the wall shear stress. This flow can be driven by a homogeneous body force instead of a weak pressure gradient (as in reality) balancing the friction at the wall, which enables the use of periodicity in the streamwise direction and hence avoids uncertainties caused by low order effects of inflow and outflow conditions in a compressible flow.

Supersonic plane channel flows have been studied by several groups in the recent past in order to ascertain compressibility effects in a wall-bounded flow (see Coleman *et al.* (1995), Foyi *et al.* (2004)). Coleman *et al.* (1995) were the first to report the

validity of Morkovin’s hypothesis (as formulated in the introduction of this thesis) in a supersonic channel flow with isothermal wall based on DNS up to a Mach number of 3. They note enhanced streamwise coherence of streaky structures in the near-wall region with increasing Mach number which was found to be due to mean property variations. Lechner *et al.* (2001) and Foysi *et al.* (2004) found an appreciable increase in anisotropy in their supersonic channel flow simulations compared to the incompressible case. This was shown to be an effect of mean property variations in the supersonic case, which modified the pressure-strain correlations (Foysi *et al.*, 2004) which are responsible for redistribution of fluctuating energy among the momentum components.

Now, flow through supersonic pipes with circular cross-section has never been simulated in the past because of uncertainties arising from the treatment of the axis singularity in a high accuracy, finite difference cylindrical coordinate framework as well as the general high computational costs involved in simulating a wall-bounded compressible flow using the full compressible Navier-Stokes equations.

In this study, fully converged statistics from DNS and LES of compressible turbulent pipe flow with isothermal wall are presented. While the DNS data may be used to test existing RANS models and develop more elaborate, second order models for compressible wall-bounded flows as well as a reference dataset for future LES computations, the LES results show the applicability of explicit filtering as a SGS modelling strategy. Since the LES have been carried out at sufficient resolution, the results may be used with confidence to validate SGS models and to develop reliable wall models for compressible LES simulations.

3.2 Computational Details

The flow and computational parameters are shown in Table 3.1. For the DNS, $256 \times 128 \times 91$ points were used in the streamwise, azimuthal and radial directions while the LES was carried out with $64 \times 64 \times 50$ points. Thus the LES uses 16 times coarser resolution than the DNS. The computational domain is $10R \times 2\pi R \times R$ where R is the pipe radius.

While the DNS computations are carried out at Mach numbers (ratio of bulk velocity to the speed of sound at wall temperature) of 0.3 and 1.5 in order to assess compressibility effects, LES computations correspond to the supersonic DNS in order to facilitate validation of the LES methodology. All computations are at constant Prandtl number, $Pr = 0.7$; specific heat ratio, $\gamma = 1.4$ and viscosity exponent, $n = 0.7$ (Sutherland’s law, $\mu \sim T^n$).

The starting field for the subsonic DNS was an incompressible fully-developed pipe flow field at $Re_\tau = 180$. Its use resulted in a shorter transient before the flow converged to the state $M = 0.3$ and $Re_\tau = 214$.

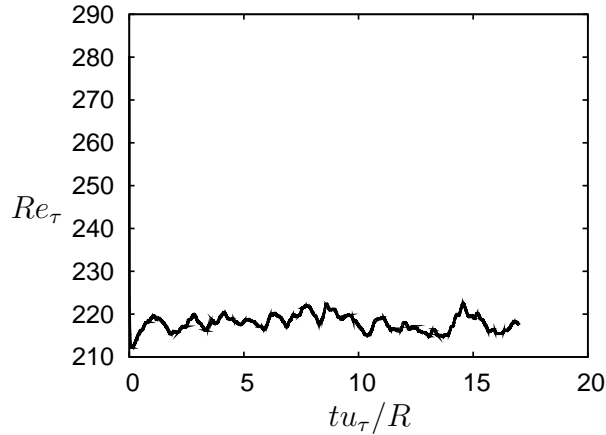
The DNS code performs at 576 Mflops/core on the SGI Altix 4700 at LRZ, Munich.

3.3 DNS results

In this section we present DNS results from the subsonic and supersonic flow cases which enables us to ascertain compressibility effects in turbulent pipe flows up to a low supersonic

Table 3.1: Flow and computation parameters

Case	Δx^+	$r\Delta\phi_{max}^+$	Δr_{min}^+	Δr_{max}^+	M	Re_τ	T_w
DNSM0.3	8.3	10.5	1.18	3.26	0.3	214	250
DNSM1.5	9.5	12.0	1.3	3.73	1.5	245	220
LESM1.5	38	21.2	2.5	6.79	1.5	244	220

Figure 3.1: Time history of Re_τ for DNS $M = 0.3$

limit ($M = 1.5$). We did not perform simulations with higher Mach numbers because of the huge computational effort involved. Since, near-wall statistics of pipe flow are qualitatively (and to a large extent, quantitatively) similar to those of channel flow, we expect to draw analogous conclusions as Coleman *et al.* (1995), Foysi *et al.* (2004) who did simulations up to $M = 3.5$.

3.3.1 Time history

The time development of Re_τ in the DNS of the subsonic flow is shown in figure 3.1 where the statistics are collected from $tu_\tau/R = 6$ onwards.

3.3.2 Energy spectra and two-point correlations

The turbulent kinetic energy spectra and the two-point correlations (TPC) are means to verify that the resolution and the domain sizes of the computations are properly chosen. The proper decay of the spectra at high wavenumbers indicates that the resolution is sufficient to resolve the small scales which arise as a consequence of the nonlinearity of the governing equations. The proper decay of the TPC indicates that the computational domain is big enough to capture the large scale flow structures.

Figure 3.2 shows the streamwise energy spectra of the individual velocity components in the near-wall as well as in the core region of the pipe. The spectra and the wavenumbers

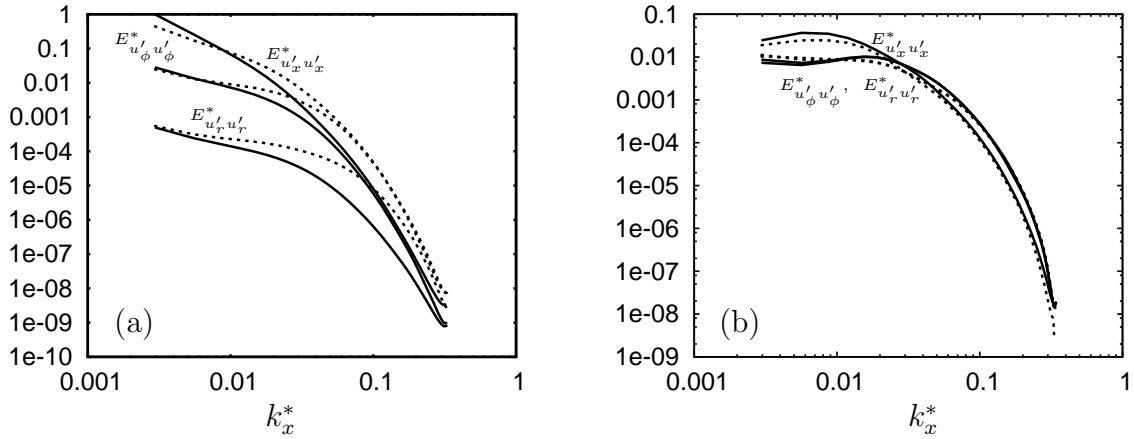


Figure 3.2: Streamwise energy spectra (a) in the near-wall ($y^* = 5$) region, and (b) in the core. —, $M=1.5$; - - -, $M=0.3$

are normalized using the semi-local friction velocity u_τ^* and the local kinematic viscosity $\bar{\nu}$ i.e. $E_{u'_i u'_i}^* = E_{u'_i u'_i} / (u_\tau^{*2})$ and $k_x^* = k_x \bar{\nu} / u_\tau^*$, where $u_\tau^* = \sqrt{|\tau_w| / \bar{\rho}}$. All the spectra decay satisfactorily by several orders of magnitude, although the low Reynolds number of the flow leads to deviations from the Kolmogorov $-5/3$ inertial subrange behaviour even in the core region where the turbulence is nearly isotropic. The highly anisotropic behaviour in the near-wall region compared to the core flow is clearly indicated in the spectra. In the near-wall region the spectra in the supersonic flow decay more rapidly compared to the subsonic flow i.e. the turbulence structure in the supersonic flow is altered and a different energy cascade results. Such effects are not seen in the core region. Obviously, the scaling used, works fine in the core region, but not in the near-wall region where viscous effects come into play besides mean density effects (mean property variations).

Due to the typical geometry of the flow and due to the cylindrical coordinate system, it makes little sense to look at the spectra in the azimuthal direction in the core region. Hence, only the spectra in the near-wall layer are shown (Figure 3.3) for this direction which again confirms the high degree of anisotropy in this layer and the role of mean property variations.

Two-point correlations of streamwise velocity fluctuations $R_{u'_x u'_x}$ (Figure 3.4) in the streamwise direction show a slower decay in the supersonic case in the near-wall region compared to the subsonic case. This indicates increased streamwise length scale associated with u_x in the streamwise direction and hence increased streamwise coherence in this region as has been observed in the previous studies by Coleman *et al.* (1995) and Foyi (2005). A similar slower decay of streamwise correlations is also observed for the azimuthal and radial components (Figures 3.5(a), 3.6(a)) which again confirms the increased near-wall streamwise coherence in the streamwise direction for the higher Mach number case. The fact that figures 3.5(b) and 3.6(b) show nearly identical results is not due to a mistake. In fact, incompressible DNS of pipe flow by Unger (1994) reveals the same result (fig. 5.40, page 101).

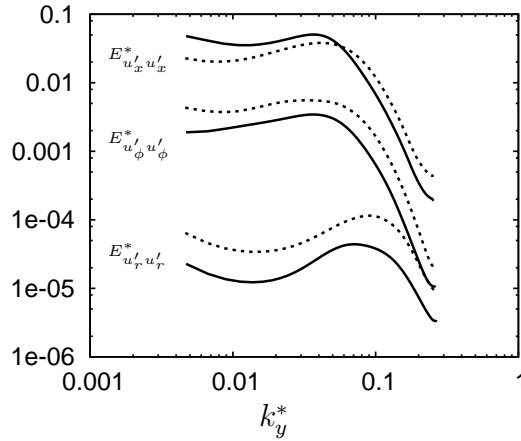


Figure 3.3: Energy spectra in the near-wall ($y^* = 5$) region in the azimuthal direction. Line types as in fig. 3.2

Streamwise elongated structures known as 'streaks' are a universal feature in the near-wall region of wall-bounded turbulent flows. They occur due to the high shear rate in this region and consist of alternate high-speed and low-speed regions. The high-speed regions are formed due to fluid from the outer layers coming into the wall layer leading to local acceleration, called a 'sweep' event. Low speed fluid from the near-wall layer is being constantly ejected into the layers above forming an 'ejection' event. These sweeps and ejections are primarily responsible for the radial transport of fluctuating streamwise momentum and hence the production of turbulent kinetic energy. Similar streaky structures have also been observed in homogeneous shear layers at shear rates comparable to those in the near-wall region of a channel flow (Lee *et al.* (1990)).

The location of the first minimum of the two-point correlation profiles of streamwise velocity fluctuations in the azimuthal direction indicates half the azimuthal spacing of the streaks. As shown in Figure 3.7, the first minimum of $R_{u'_x u'_x}$ in the supersonic case shows an appreciable shift towards the right. From this figure, we find that the non-dimensional streak spacing (normalized with u_τ^*/\bar{v}) increases from 100 in the subsonic flow to a value of 140 in the supersonic case. Foyasi *et al.* (2004) observed a similar behaviour in their supersonic channel simulations. Similar behaviour is also observed in the $R_{u'_\phi u'_\phi}$ profiles, but not in the $R_{u'_r u'_r}$ profiles (Figure 3.8).

Another consequence of the increased streamwise coherence in the supersonic pipe flow is the increased anisotropy in the buffer layer (to be shown later in this chapter) which leads to increased concentration of turbulent kinetic energy in the streamwise component.

3.3.3 Instantaneous fields

A look at the instantaneous fields, especially in the near-wall region is necessary in order to gain insight into the effects of mean property variation on the turbulence structure in this region and hence on the turbulence production mechanism.

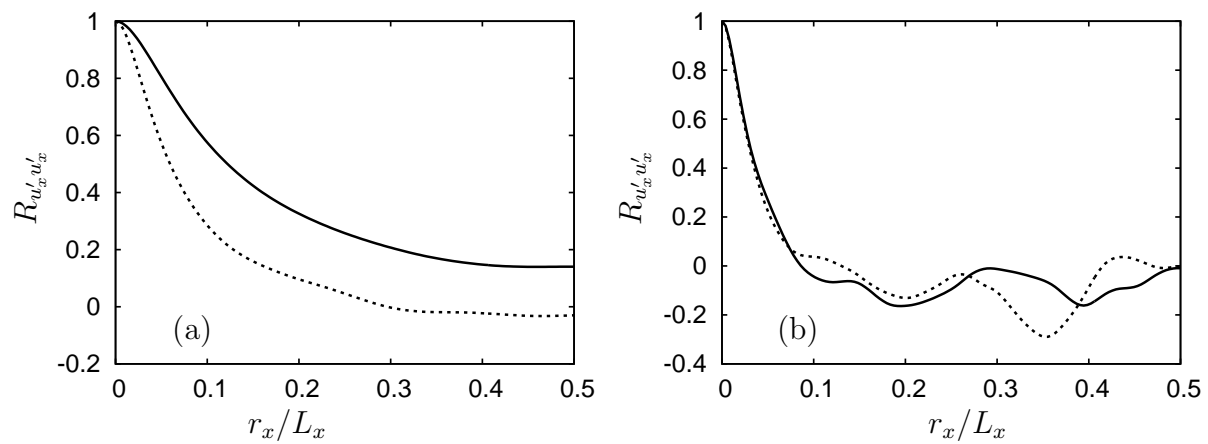


Figure 3.4: Two-point correlation coefficients in streamwise direction (a) at $y^* = 5$, and (b) in the core ($r/R = 0.0075$). —, $M=1.5$; - - -, $M=0.3$

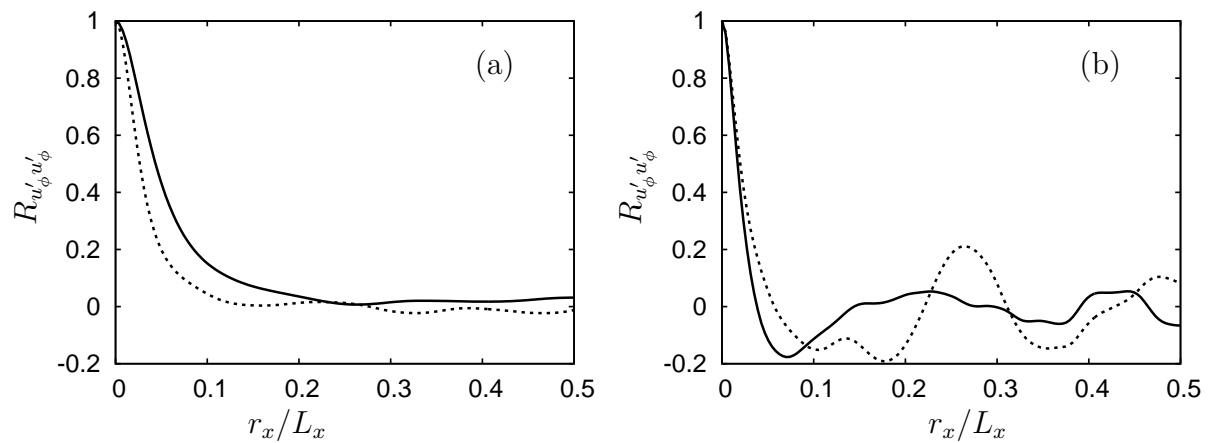


Figure 3.5: Two-point correlation coefficients in streamwise direction (a) at $y^* = 5$ and (b) in the core ($r/R = 0.0075$). —, $M=1.5$; - - -, $M=0.3$

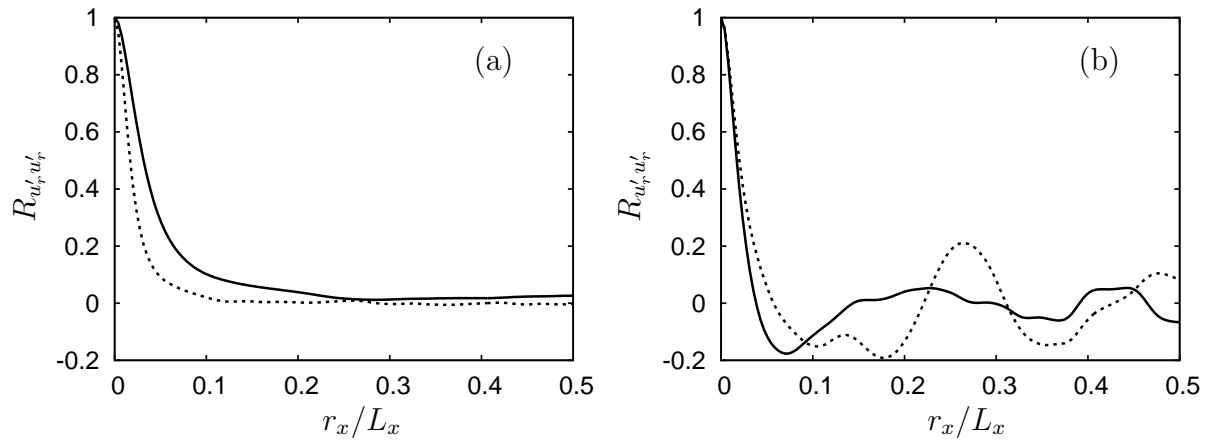


Figure 3.6: Two-point correlation coefficients in streamwise direction (a) at $y^* = 5$ and (b) in the core ($r/R = 0.0075$). —, $M=1.5$; - - -, $M=0.3$

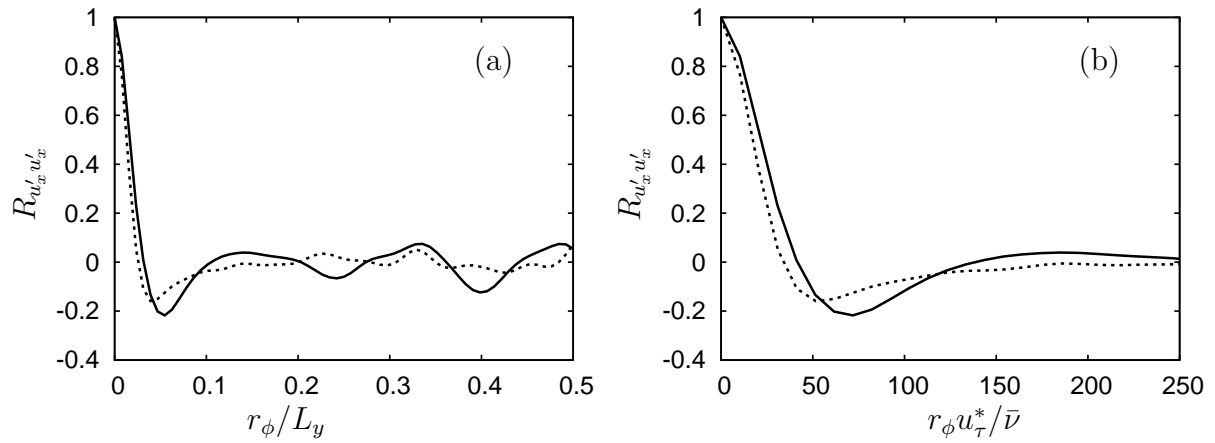


Figure 3.7: Two-point correlation coefficients in azimuthal direction at $y^* = 5$ using two different normalizations (a), (b). —, $M=1.5$; - - -, $M=0.3$

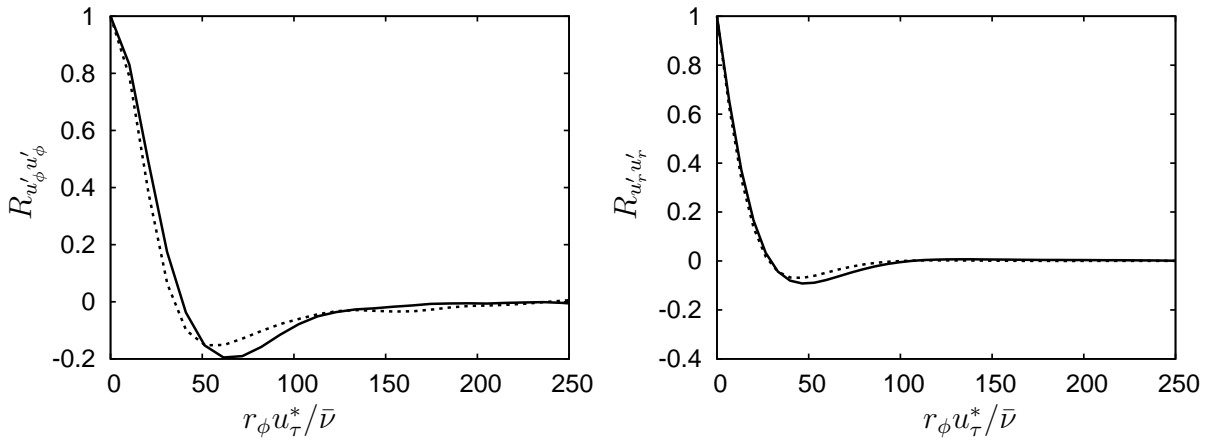


Figure 3.8: Two-point correlation coefficients in azimuthal direction at $y^* = 5$. —, $M=1.5$; - - -, $M=0.3$

We first look at contours of velocity fluctuations at $y^* = 5$ (where $y^* = yu_\tau^*/\bar{\nu}$) in a surface parallel to the wall. Since we use a cylindrical coordinate system, surfaces parallel to the wall are 'rolled out' for visualisation purposes. We see the expected 'streaky structures' in the streamwise velocity fluctuations with regions of 'high-speed' fluid (red contours) coming from a layer further away from the wall (sweep) and 'low-speed' fluid (blue contours) coming from a layer close to the wall (ejection). As seen from figures 3.9 and 3.11, the streamwise fluctuations definitely show more organisation in the supersonic case and the streak spacing is increased. The radial velocity fluctuations (figures 3.9, 3.11) have the spotty character also known from pressure fluctuations, show more organisation at the supersonic Mach number. The azimuthal velocity (figures 3.10, 3.12) fluctuations are also somewhat more organized in the supersonic case.

The elongation of the streamwise streaks can also be observed in a plane normal to the wall through the axis (Figures 3.13, 3.14). Here, the streamwise fluctuation plots indicate longer near-wall coherent structures. The inclination of the near-wall structures with respect to the wall depends on the mean shear rate. The azimuthal fluctuations in both cases show a preferred orientation (roughly 45 degrees). This was also noticed in incompressible pipe flow DNS of Unger (1994).

The abovementioned streak modification in the supersonic flow was shown to be an effect of mean property (density, viscosity) variations by Coleman *et al.* (1995). They performed simulations with artificial forcing of the energy equation such that the supersonic channel had a constant wall-normal mean temperature (and density) profile. This flow showed no streak modification in spite of the high Mach number. The variations of mean property lead to an increase in the ratio of the turbulence time scale to that of the mean shear and hence to enhancement of the streaky structures.

In the radial fluctuation plots (figures 3.13, 3.14), the blue regions indicate motion towards the center and red regions indicate motion towards the wall. Exact correspondence can be noticed between the streamwise and radial fluctuations, the low speed regions

in the streamwise plot correspond to motion away from the wall in the radial plots. It should be noted that in a cylindrical coordinate system, the azimuthal and radial velocity component switch signs across the centerline (Unger (1994)). This is clearly evident in the figures and is not an irregularity due to the axis singularity treatment.

A look at contours of streamwise and radial fluctuations in a plane normal to the axis and the wall ((ϕ, r) -plane) is now shown (figure 3.15). Here again we see the alternate high-speed and low-speed regions in the streamwise fluctuations and the corresponding regions in the radial component showing sweeps and ejections. The radial fluctuations underline definitive motions of the fluid from the core towards the wall and vice versa.

The azimuthal component (figure 3.16) in this plane should be viewed together with the radial and axial components which reveals the 'splatting' effect (Moin & Kim (1982)) close to the wall. The 'splatting' effect refers to the net energy transfer from the radial component to the wall-parallel components much like the impingement of a jet on a wall. Although, energy is also transferred from the azimuthal component to the radial component in the near-wall region, the net energy transfer is from the radial to the other components since the high speed fluid coming to the wall is more energetic than that leaving the viscous region near the wall towards the pipe center.

Both the plots of azimuthal and radial component in the (ϕ, r) -plane show the sign changes across the axis, resulting from the definition of these velocities in the cylindrical coordinate system. A plot of pressure fluctuations (fig. 3.16) is additionally shown in order to clarify that we do not have any problems whatsoever with the axis.

3.3.4 Mean profiles

The assumption of constant viscosity and density which holds in channel and pipe flows (without heat transfer at the walls) in the incompressible limit fails as the Mach number approaches the supersonic regime. Increased viscous dissipation in the near-wall region leads to strong gradients in mean temperature (and mean viscosity) - and hence in mean density since the mean pressure remains almost constant in the wall-normal direction (Figure 3.17) - which is obvious from averaged continuity and radial momentum equations after applying streamwise and azimuthal homogeneity. The use of an isothermal boundary condition at the wall in supersonic pipe flow in order to prevent 'choking' and to reach a statistically steady state thus leads to steep gradients in density and temperature close to the wall. Thus, instead of occurring near the wall as in the adiabatic wall case, the maxima of temperature and the minima of density occur at the centerline, (Figure 3.17). This variation in mean density has to be taken into account for near-wall scalings of turbulence intensities as suggested by Huang *et al.* (1995), although in the outer layer, scaling with wall values still holds. In the light of strong mean property variations, we should now look at local Mach and Reynolds numbers instead of global ones. Figure 3.18 shows \bar{M} and $Re_\tau^* = \bar{\rho} u_\tau^* R / \bar{\mu}$, where $u_\tau^* = \sqrt{\tau_w / \bar{\rho}}$. We see that the local Reynolds number decreases in the supersonic case away from the wall. Near the wall it is higher than that in the subsonic flow. Thus the increased coherence in the near-wall structures is a Mach number effect and is not due to reduced domain size measured in terms of wall units (Coleman *et al.* (1995)).

As noted in previous studies, mean property variations are the only 'compressibility

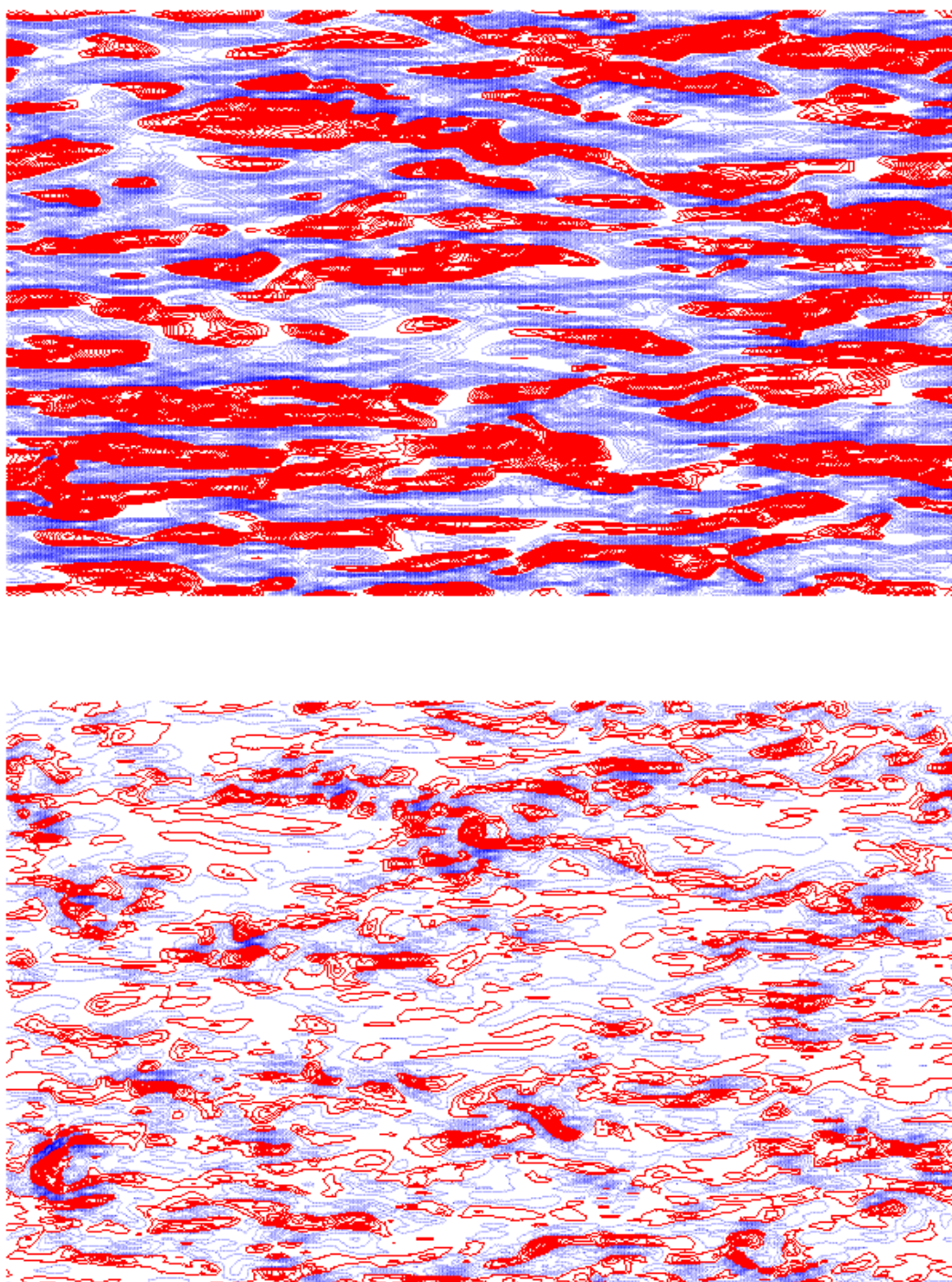


Figure 3.9: Instantaneous axial (top), radial (bottom) velocity fluctuations in a (x, ϕ) -surface for $M = 0.3$ at $y^* = 5$. Red lines show positive fluctuations.

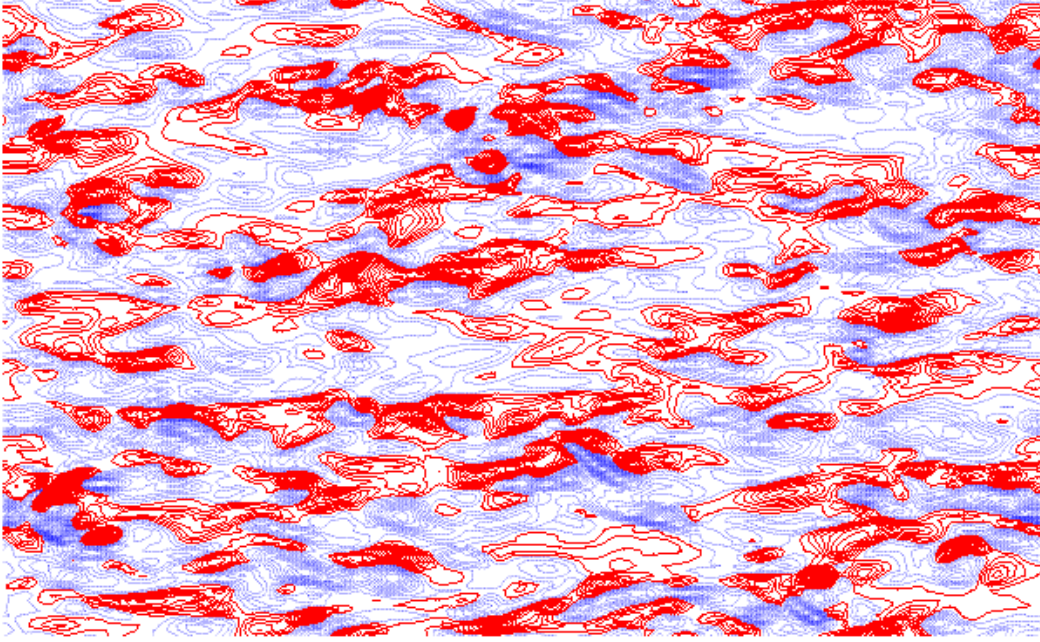


Figure 3.10: Instantaneous azimuthal velocity fluctuations in a (x, ϕ) -surface for $M = 0.3$ at $y^* = 5$. Red lines show positive fluctuations.

effects' to be taken into account in supersonic flows up to $M = 5$, where the turbulent Mach number, M_t and the gradient Mach number, M_g remain subsonic. In the supersonic pipe flow case at $M = 1.5$, both M_t and M_g remain in the low subsonic range (Figure 3.19), so that intrinsic compressibility effects arising from dilatation fluctuations are expected to be negligible. This can be seen in the magnitudes of compressible dissipation rate ($\epsilon_d = 4/3 \overline{\mu u'_{i,l} u'_{k,k}}$) and pressure dilatation correlation, $\overline{p' u'_{i,l}}$ (Figure 3.21) which are less than 0.06% and 1% of the solenoidal dissipation rate ($\epsilon_s = 1/2 \overline{\mu \omega'_k \omega'_k}$) respectively along the pipe radius. However, the mean dilatation plot (Figure 3.20) shows a region of compression near the wall and a weak expansion over most of the pipe radius. Thus weak non-solenoidal effects exist in this flow case which was also observed in supersonic channel flows by Coleman *et al.* (1995).

The mean streamwise momentum equation in cylindrical coordinates after applying streamwise and azimuthal homogeneity reads:

$$-r \frac{\partial \bar{p}}{\partial x} + \frac{\partial r (\bar{\mu} \frac{\partial \bar{u}_x}{\partial r})}{\partial r} - \frac{\partial r \overline{\rho u'_x u'_r}}{\partial r} = 0. \quad (3.1)$$

Integration of (3.1) from 0 to R results in:

$$\frac{\partial \bar{p}}{\partial x} = \frac{2}{R} \mu_w \frac{\partial \bar{u}_x}{\partial r} = \frac{2}{R} (-\tau_w).$$

Integration of (3.1) from 0 to r gives:

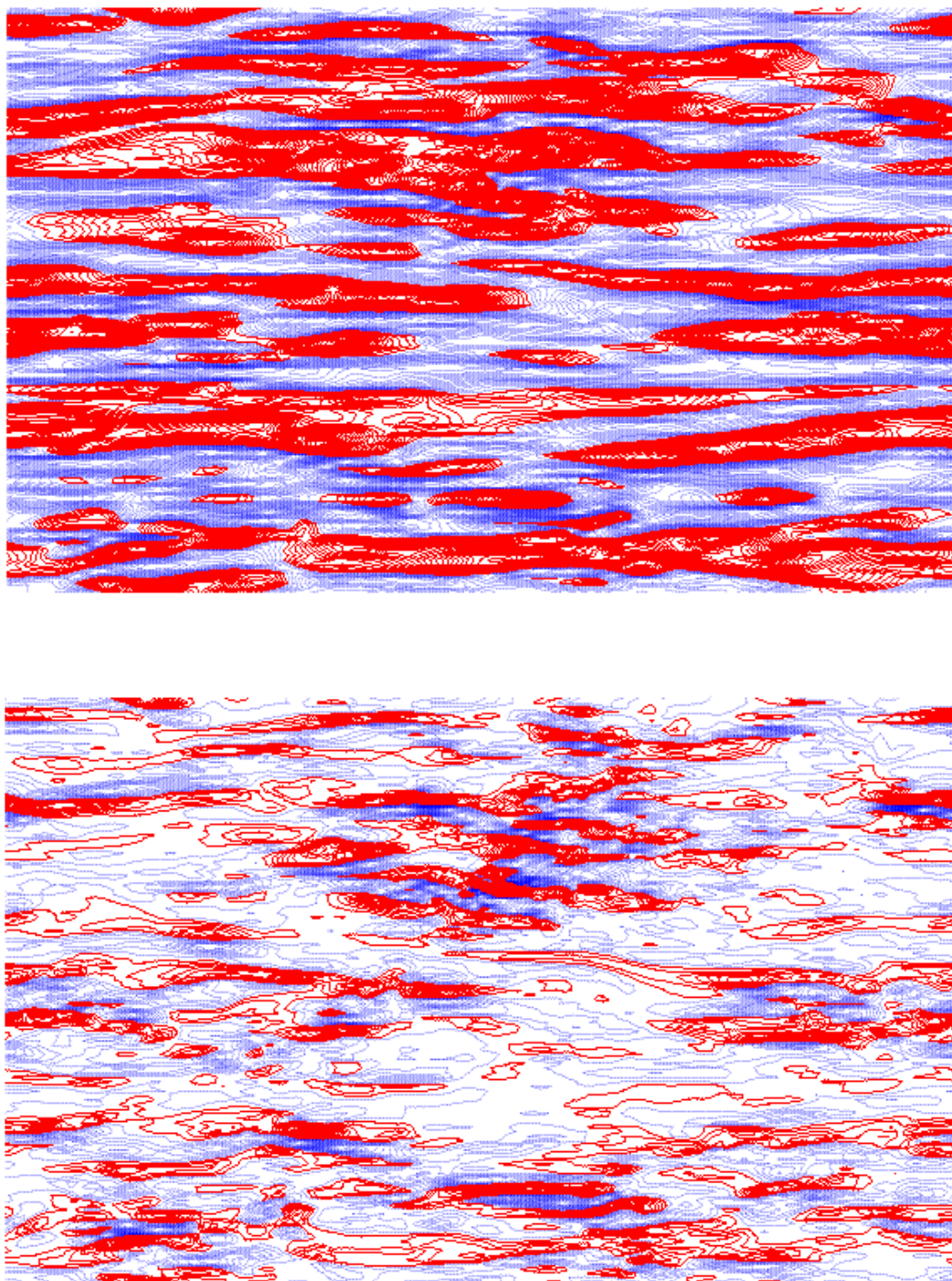


Figure 3.11: Instantaneous axial (top), radial (bottom) velocity fluctuations in a (x, ϕ) -surface, for $M = 1.5$ at $y^* = 5$. Red lines show positive fluctuations.

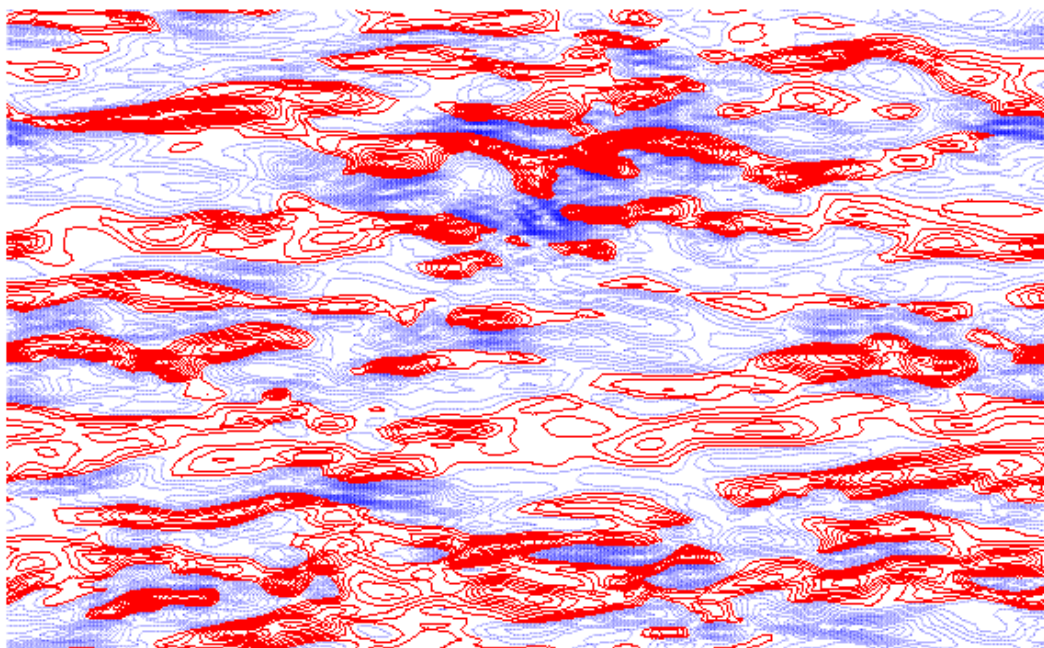


Figure 3.12: Instantaneous azimuthal velocity fluctuations in (x, ϕ) -surface for $M = 1.5$ at $y^* = 5$. Red lines show positive fluctuations

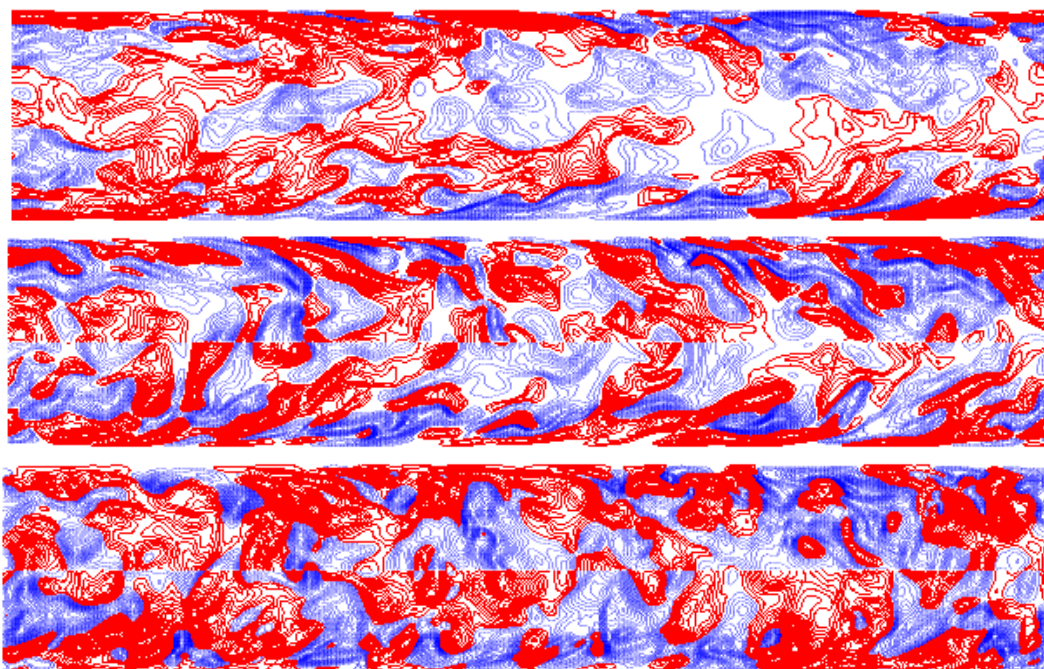


Figure 3.13: Instantaneous axial, azimuthal and radial (top to bottom) velocity fluctuations in a (x, r) -plane for $M = 0.3$. Red lines show positive fluctuations.

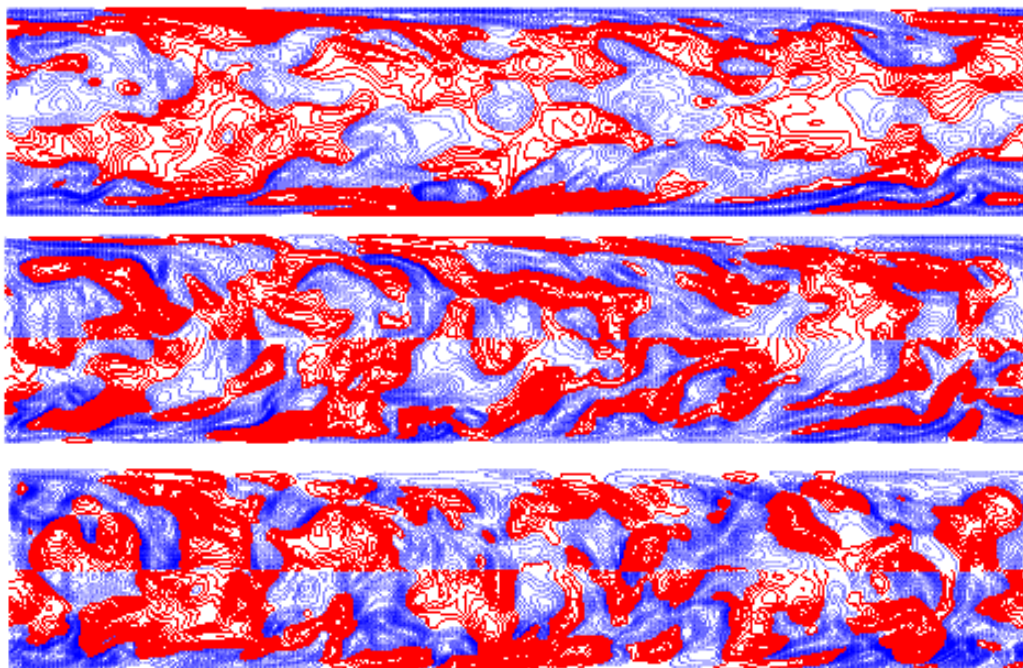


Figure 3.14: Instantaneous axial, azimuthal and radial (top to bottom) velocity fluctuations in a (x, r) -plane for $M = 1.5$. Red lines show positive fluctuations.

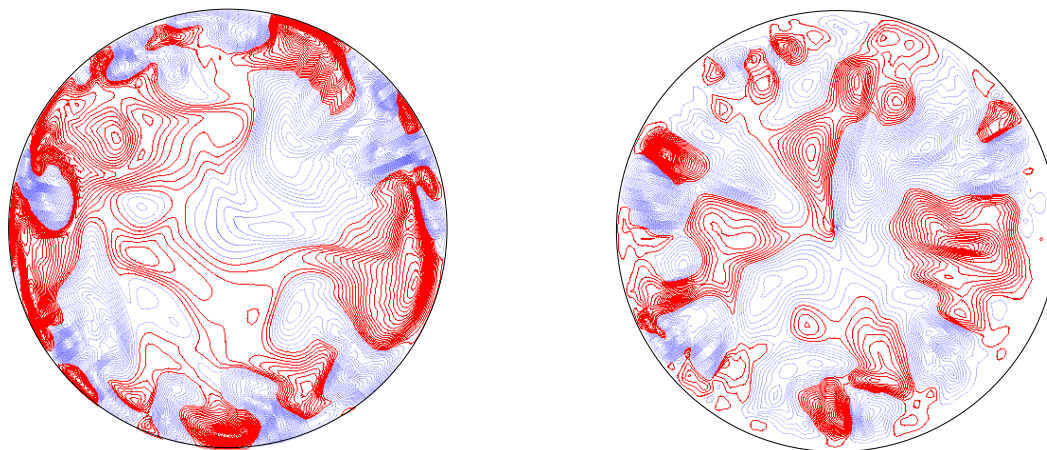


Figure 3.15: Instantaneous axial (left) and radial (right) velocity fluctuations in (ϕ, r) -plane at $x/L_x = 0.5$ for $M = 1.5$. Red lines show positive fluctuations

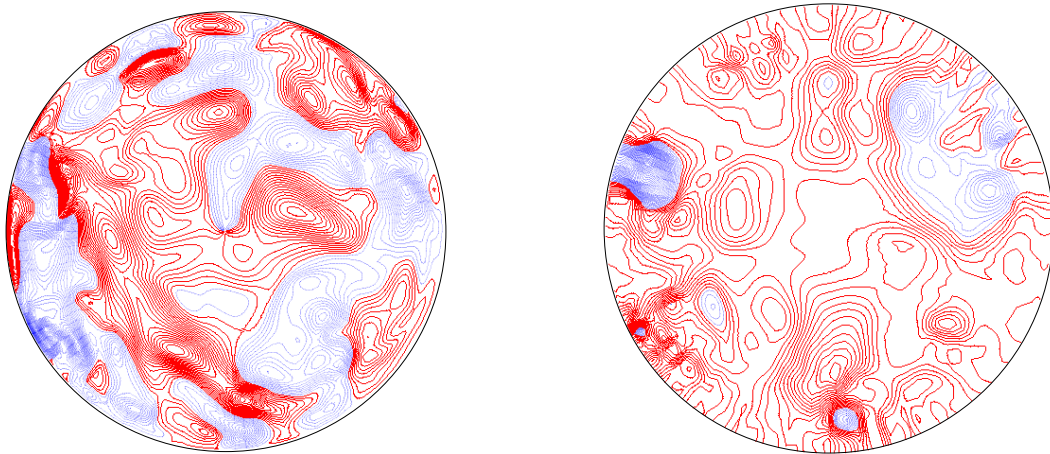


Figure 3.16: Instantaneous azimuthal (left) velocity and pressure (right) fluctuations in (ϕ, r) -plane at $x/L_x = 0.5$ for $M = 1.5$. Red lines show positive fluctuations.

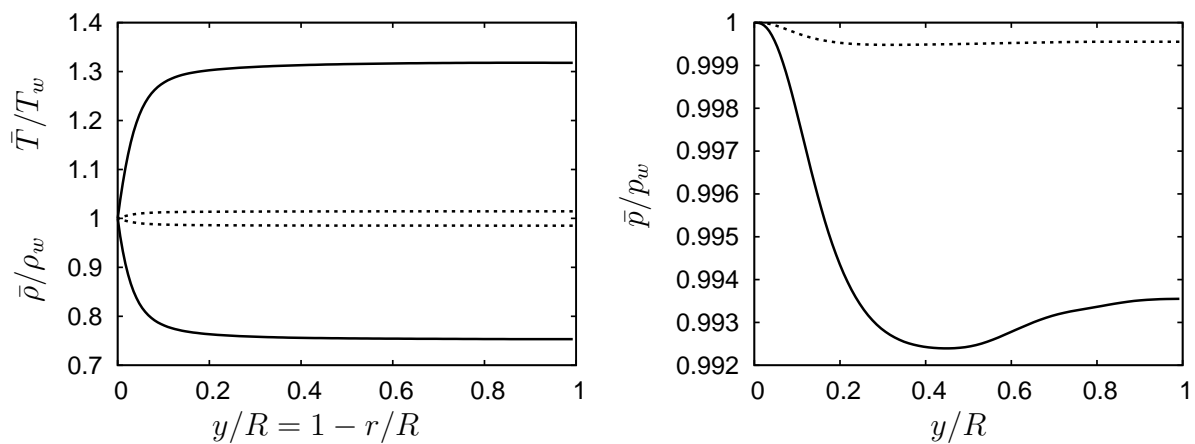


Figure 3.17: Mean temperature, density and pressure normalized with wall values. Solid line: $M=1.5$; Dashed line: $M=0.3$

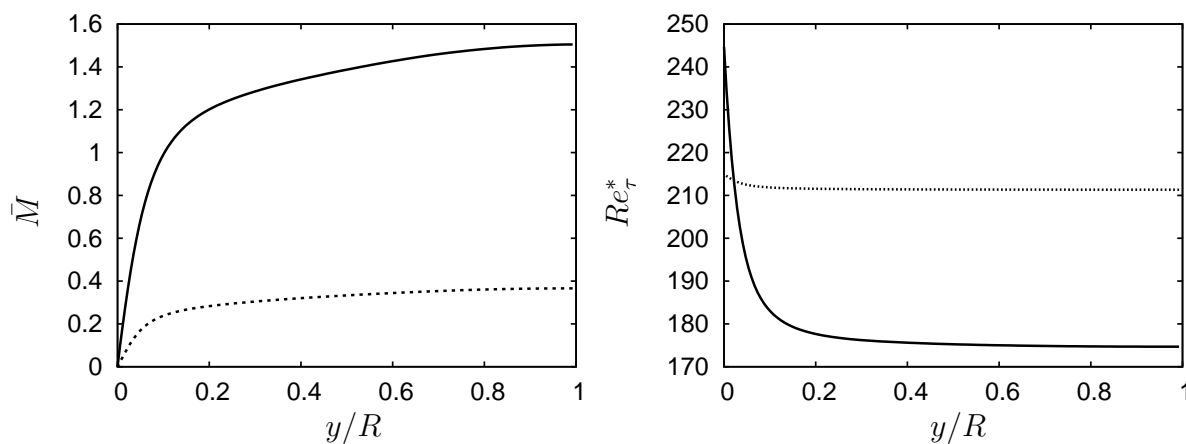


Figure 3.18: Local mean Mach and friction Reynolds numbers. Solid line: $M=1.5$; Dashed line: $M=0.3$

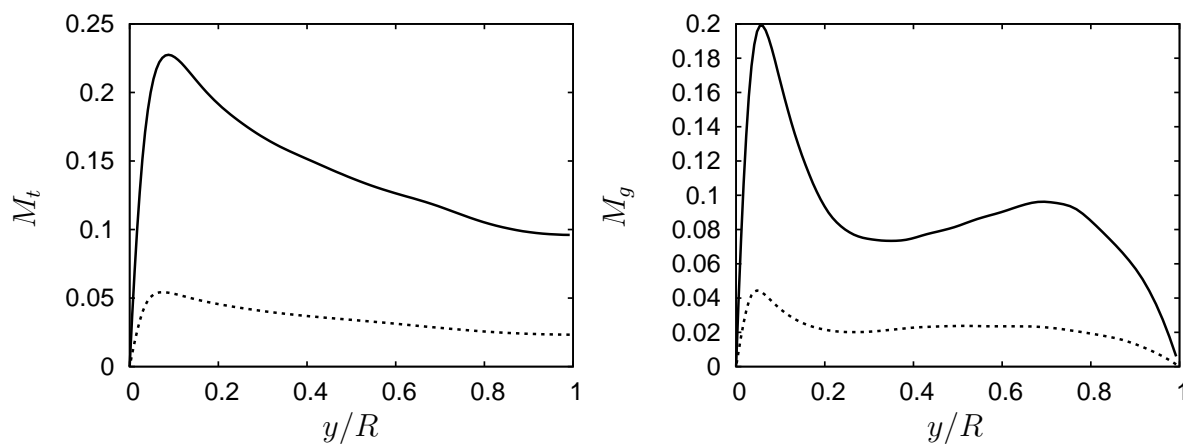


Figure 3.19: Turbulent Mach number (M_t) and gradient Mach number (M_g). Line types as in fig. 3.17

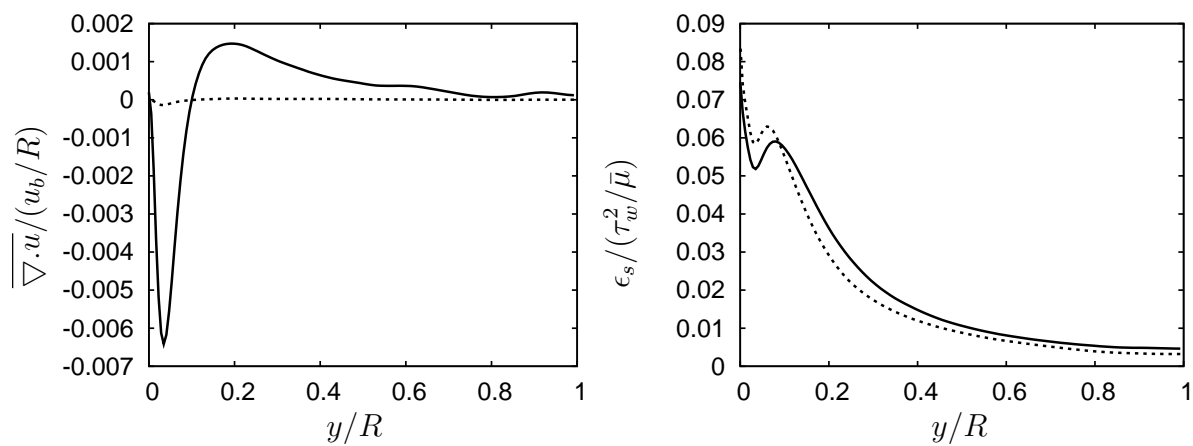


Figure 3.20: Mean dilatation and solenoidal dissipation rate. Line types as in fig. 3.17

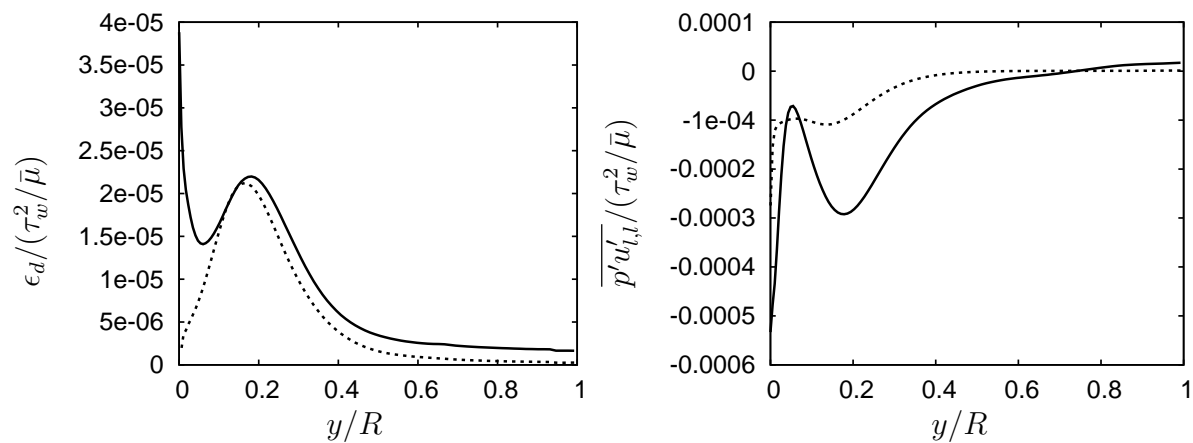


Figure 3.21: Compressible dissipation rate and pressure-dilatation correlation. Line types as in fig. 3.17

$$-\overline{\rho u_x'' u_r''} + \bar{\mu} \frac{\partial \bar{u}_x}{\partial r} = \frac{r}{2} \frac{\partial \bar{p}}{\partial x} = \frac{r}{R} (-\tau_w).$$

Introducing a coordinate $y = (R - r)$ results in:

$$\overline{\rho u_x'' u_r''} + \bar{\mu} \frac{\partial \bar{u}_x}{\partial y} = \left(1 - \frac{y}{R}\right) \tau_w. \quad (3.2)$$

This is the same form of mean momentum equation as in a channel flow with the pipe radius R replacing the channel half-width. It describes the linear relation between the sum of the Reynolds and viscous stresses and the radial (or wall-normal) coordinate.

Equation (3.2) shows that τ_w is a proper scaling parameter for the Reynolds stress $\overline{\rho u_x'' u_r''}$ away from the wall where the viscous effects are small.

Viscous sublayer

This is the region very close to the wall (i.e. $y/R \ll 1$ and $y^+ < 5$) where only viscous effects are important and the Reynolds stress $\overline{\rho u_x'' u_r''}$ is negligibly small. Thus equation (3.2) now becomes:

$$\begin{aligned} \bar{\mu} \frac{\partial \tilde{u}_x}{\partial y} &= \tau_w \\ \text{i.e. } \frac{\bar{\mu}}{\mu_w} \frac{\partial u_x^+}{\partial y^+} &= 1 \end{aligned} \quad (3.3)$$

Integration gives the following scaled velocity for the viscous sublayer:

$$U_\mu^+ : \int_0^{u_x^+} \frac{\bar{\mu}}{\mu_w} d\bar{u}_x^+ = y^+ \quad (3.4)$$

As seen Figure 3.22, this scaling, which takes into account the mean viscosity distribution, collapses the mean velocity profiles in the viscous sublayer ($y^+ < 5$).

Fully turbulent region

Around $y^+ > 25$, the viscous stress becomes negligible in comparison to the Reynolds stress in equation (3.2).

Using mixing length arguments in the buffer layer ($y^+ \gg 1$, $y/R \ll 1$) where Prandtl's linear law and the outer law are usually matched, we can write,

$$\overline{\rho u_x'' u_r''} = \bar{\rho} (\kappa y)^2 \frac{\partial \bar{u}_x}{\partial y} \frac{\partial \bar{u}_x}{\partial y} = \tau_w = \rho_w u_\tau^2$$

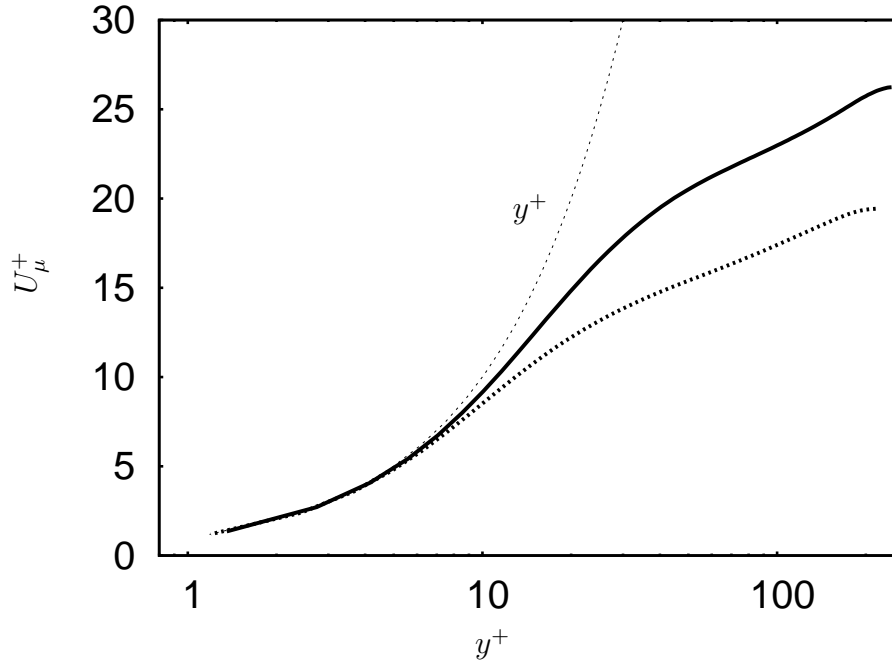


Figure 3.22: Viscosity transformed mean velocity, U_μ^+ for the two Mach numbers. Line types as in fig. 3.17

and obtain,

$$\sqrt{\frac{\bar{\rho}}{\rho_w}} d\bar{u}_x^+ = \frac{1}{\kappa y^+} dy^+. \quad (3.5)$$

Integration gives the Van Driest transformed velocity profile for the buffer layer,

$$U_{VD}^+ : \int_0^{\bar{u}_x^+} \sqrt{\frac{\bar{\rho}}{\rho_w}} d\bar{u}_x^+ = \frac{1}{\kappa} \ln y^+ + C. \quad (3.6)$$

Morkovin's hypothesis is implied in deriving the Van Driest transformed velocity since supersonic boundary layers are assumed to have a similar length scale distribution in the wall-normal direction as subsonic ones. As shown in Figure 3.23 this transform brings the supersonic and subsonic mean velocity profiles closer to each other in the fully turbulent region.

Brun *et al.* (2008) have defined an integral wall-normal coordinate based on equation (3.3) :

$$y^{c+} = \int_0^{y^+} \frac{\mu_w}{\bar{\mu}} dy^+.$$

This coordinate thus includes only near-wall mean viscosity variation and not the mean density variation. In the near-wall region, we can now write:

$$\bar{u}_x^+ = y^{c+}.$$

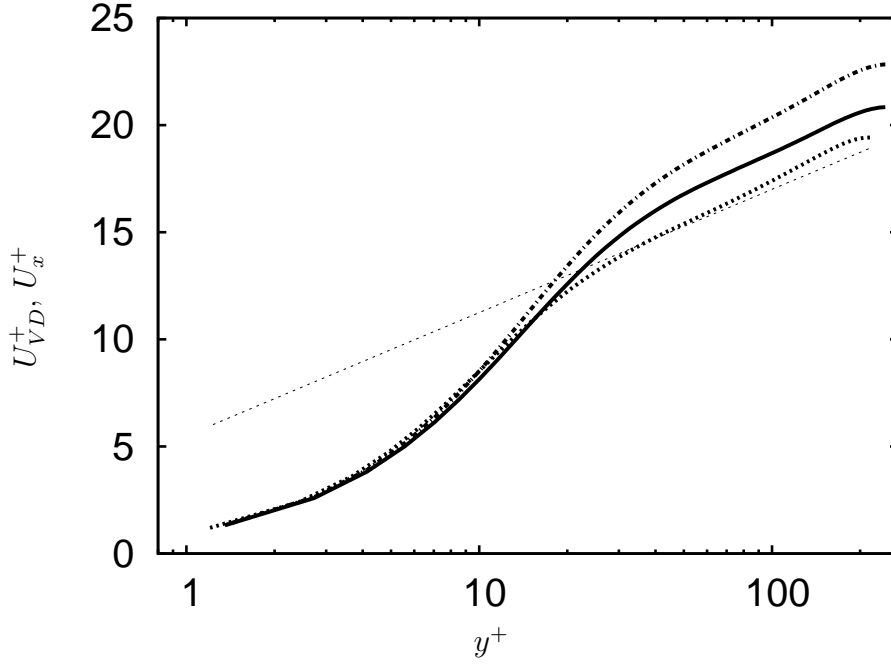


Figure 3.23: Van Driest transformed mean velocity, U_{VD}^+ . Solid line: $M=1.5$; dashed line: $M=0.3$. -.-., U_x^+ at $M=1.5$. Straight line: $u^+ = 2.5 \ln y^+ + 5.5$

In the buffer region, equation (3.5) can be rewritten in the following form which takes into account viscosity variations,

$$d\bar{u}_x^+ = \frac{y^{c^+}}{y^+} \frac{\bar{\mu}}{\mu_w} \sqrt{\frac{\bar{\rho}_w}{\bar{\rho}}} \frac{1}{\kappa y^{c^+}} dy^{c^+}.$$

On integration, we get,

$$U^{c^+} : \int_0^{\bar{u}_x^+} \frac{y^+}{y^{c^+}} \frac{\mu_w}{\bar{\mu}} \sqrt{\frac{\bar{\rho}}{\rho_w}} d\bar{u}_x^+ = \frac{1}{\kappa} \ln y^{c^+} + C_1. \quad (3.7)$$

As seen in Figure 3.24, this transformation works better than the Van Driest transformation in the fully turbulent region.

3.3.5 Turbulence statistics

Rms profiles and Reynolds stresses

Strong gradients in mean temperature and mean density in supersonic pipe flow act as explicit source terms in temperature and density variance transport equations (Hamba, 1999) and lead to increased density and temperature fluctuations in the buffer layer (Figure 3.25). Correlation coefficients between a and b are defined as

$$R_{ab} = \overline{a'b'} / (a_{rms} b_{rms}). \quad (3.8)$$

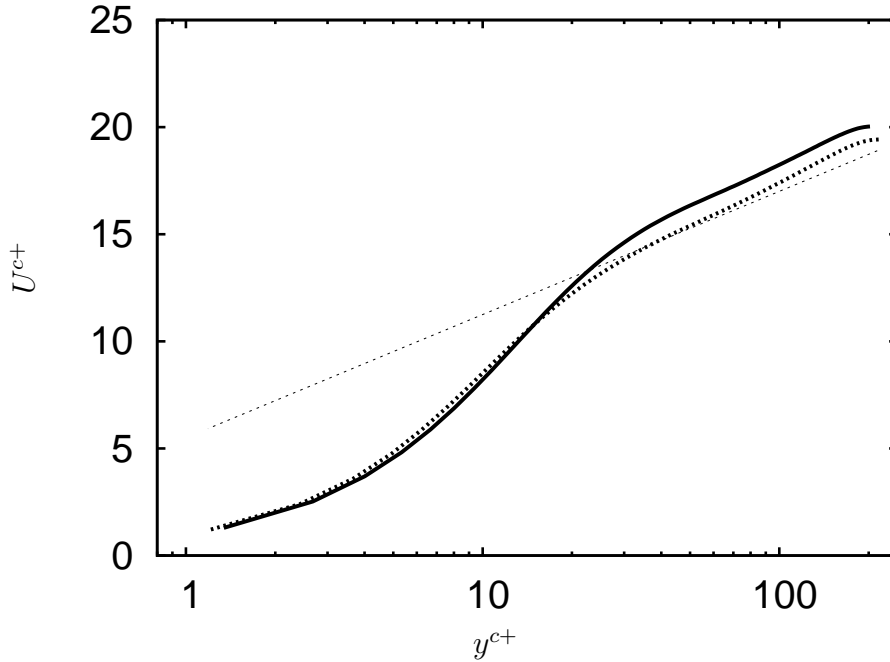


Figure 3.24: Mean velocity using scaling proposed by Brun *et al.* (2008). Solid line: $M=1.5$; dashed line: $M=0.3$. Straight line: $u^+ = 2.5 \ln y^+ + 5.5$

Near the wall, density and temperature show strong negative correlation (≈ -1) which indicates severe non-isentropic effects (in line with the large viscous effects and heat transfer in this region) (Figure 3.27). In the core region there are no mean density and temperature gradients and the positive density-temperature correlation means that acoustic (isentropic) effects are important here (since isentropic conditions imply $T' \approx (\gamma - 1)\rho'$, which means $R_{\rho T}$ would be positive). This is also confirmed by strong (≈ 1) pressure-density correlations in the core and near-zero values near the wall (fig. 3.27). The subsequent increase of $R_{\rho\rho}$ as we approach the wall is a consequence of the isothermal wall boundary condition which suppresses temperature fluctuations and hence gives the pressure-density correlation more weight.

As seen in Figure 3.25 the fluctuations of density and temperature, normalized with the corresponding mean values, are small ($< 5\%$ of the mean values) which is well within the limit of Morkovin's hypothesis. But as discussed in Coleman *et al.* (1995) and Bradshaw (1977), in flows with strong heat transfer at the walls, the ρ' criterion for Morkovin's hypothesis does not hold. Instead, one should revert back to Morkovin's original conjecture, that at non-hypersonic Mach numbers, acoustic pressure fluctuations and variations of total temperature are negligible. Figure 3.26 shows that $p_{rms}/\bar{p} \ll 1$ holds, and $T_{o,rms}$ is about 10% of the mean total temperature. The higher total temperature fluctuations due to strong heat transfer at the wall mean that the 'strong Reynolds analogy (SRA)' relations suggested by Morkovin based on negligible total temperature fluctuations do not hold in these cases. Gaviglio (1987), Rubesin (1990) and Huang *et al.* (1995) have independently derived a 'modified strong Reynolds analogy (MSRA)' for non-adiabatic

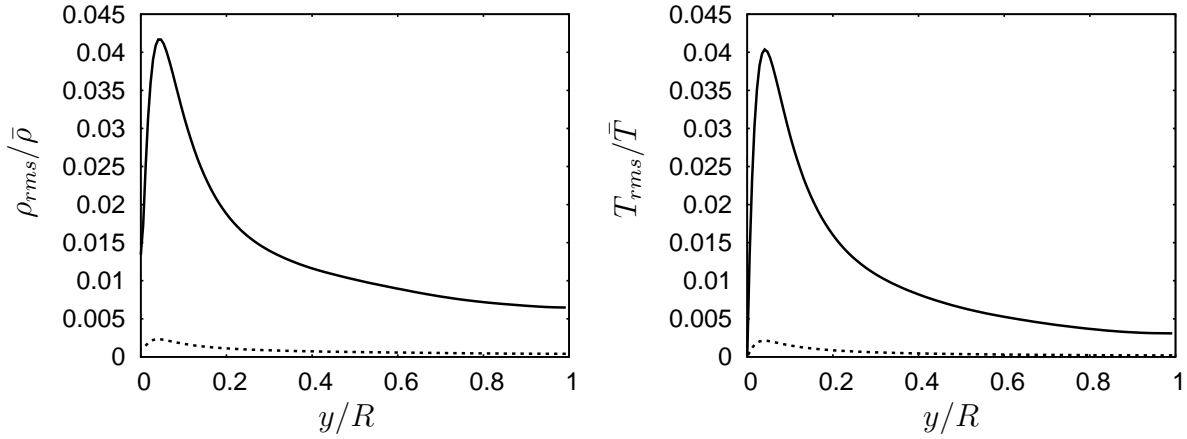


Figure 3.25: Rms density and temperature fluctuations. Line types as in fig. 3.24

cases which has the form:

$$\frac{T'/\bar{T}}{(\gamma - 1)M^2 u'/\bar{u}} \approx \frac{1}{c(\frac{\partial \bar{T}_e}{\partial T} - 1)}. \quad (3.9)$$

Gaviglio chose $c = 1$ and Rubesin $c = 1.34$. Using mixing length arguments and assuming equivalence between Reynolds and Favre averaging, Huang *et al.* (1995) showed that $c \approx Pr_t$, where Pr_t is the turbulent Prandtl number defined as $Pr_t = \overline{\rho u_x'' u_r''} \frac{\partial \bar{T}}{\partial y} / (\overline{\rho u_r'' T''} \frac{\partial \bar{u}}{\partial y})$. Using $c = 1$ already gives a similar trend as the DNS data in the buffer layer where a MSRA is expected to perform well, Figure 3.28 (right). Similar results were also reported by Huang *et al.* (1995). This means that temperature behaves like a passive scalar near the wall, with the temperature fluctuations being strongly correlated with those of stream-wise velocity which is confirmed by high values of velocity-temperature correlations in the near-wall region, Figure 3.28 (left).

Mean property variations near the wall lead to increased inner layer thickness at higher Mach numbers. This has to be taken into account while scaling rms velocity fluctuations near the wall. Huang *et al.* (1995) have introduced a 'semi-local' coordinate $y^* = y u_\tau^* / \bar{\nu}$, where $u_\tau^* = \sqrt{\tau_w / \bar{\rho}}$, to do this.

We can relate y^* and y^+ as follows,

$$y^* = y^+ \sqrt{\frac{\bar{\rho}}{\bar{\rho}_w} \frac{\mu_w}{\bar{\mu}}}.$$

Thus this coordinate includes both near-wall density and viscosity variations unlike y^{c+} used by Brun *et al.* (2008) which only includes viscosity variations.

Huang *et al.* (1995) used u_τ^* to scale rms velocity fluctuations which gives:

$$u_{rms}^* = \sqrt{\frac{\bar{\rho}}{\bar{\rho}_w}} u_{rms}^+.$$

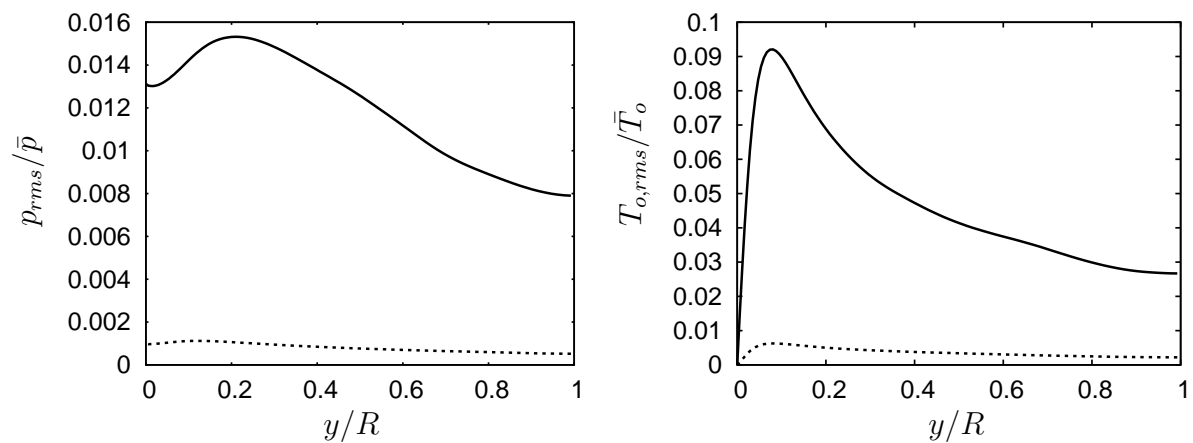


Figure 3.26: Pressure and total temperature fluctuations. Line types as in fig. 3.24

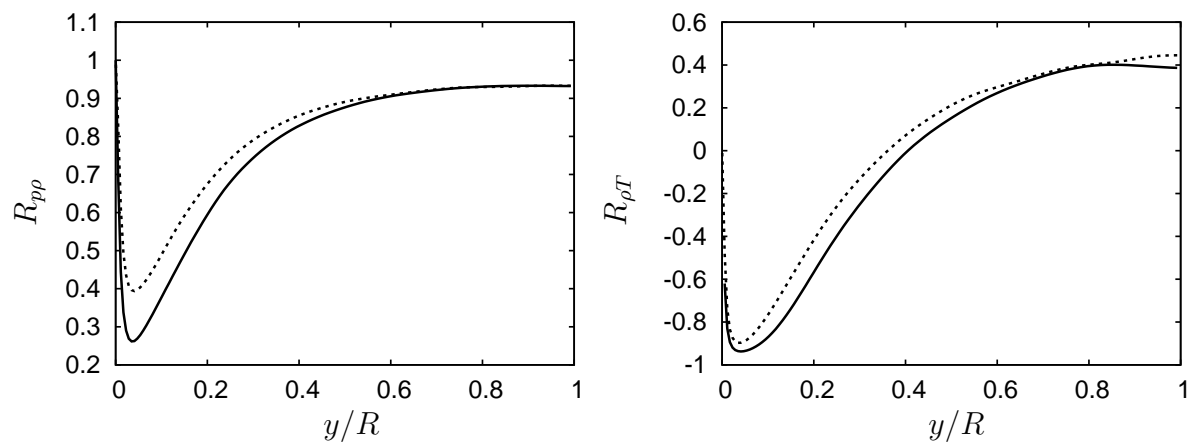


Figure 3.27: Correlations between pressure and density fluctuations; and between density and temperature fluctuations. Line types as in fig. 3.24

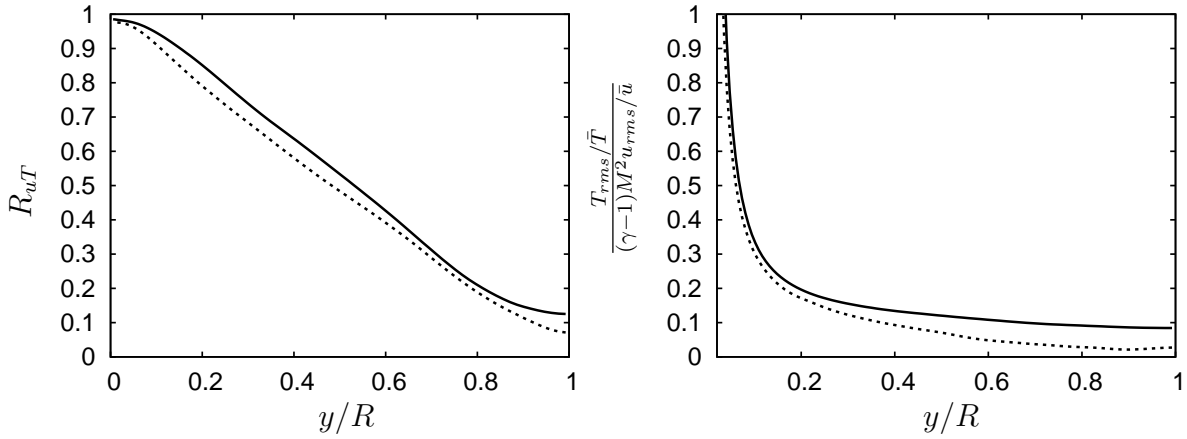


Figure 3.28: Left: Correlations between velocity and temperature fluctuations. Line types as in fig. 3.24; Right: MSRA (Gaviglio (1987)) for $M = 1.5$. solid line: DNS, dashed line: equation 3.9

Figure 3.29 shows $u_{i,rms}^*$ vs y^* where the peaks of the supersonic profiles are close to those of the subsonic ones because of the scaling. However, the peaks themselves show no such collapse. This means that compressibility affects turbulence anisotropy in such a way that streamwise velocity fluctuations increase, while azimuthal and radial fluctuations decrease.

Brun *et al.* (2008) have used the following scaling of the fluctuations analogous to their mean velocity scaling,

$$u_{rms}^{c+} = \frac{y^+}{y^{c+}} \frac{\mu_w}{\bar{\mu}} \sqrt{\frac{\bar{\rho}}{\rho_w}} u_{rms}^+.$$

Figure 3.30 shows $u_{i,rms}^{c+}$ vs y^{c+} nearly collapses the streamwise fluctuations, but not the other components. Moreover, as y^{c+} does not include near-wall density variations, it is unsuitable as a coordinate for inner scaling. Instead we choose to use y^* as an inner scaling coordinate for the Reynolds stresses.

In figures 3.31- 3.34, we combine outer scaling of the Reynolds stresses with the inner scaling of the wall-normal coordinate to show the importance of correcting for the higher viscous layer thickness in the supersonic flow.

As discussed in the previous section, τ_w continues to be the proper 'outer' scaling parameter for the Reynolds stresses away from the wall, where mean property variations are negligible. This is shown by the perfect collapse of the Reynolds stress profiles in the outer layer, i.e. $y > 0.3$, (Figures 3.35 - 3.38).

3.3.6 Reynolds stress budgets

The transport equations of the Reynolds stresses provide a means to understand mechanisms which lead to changes in the turbulence structure. Fully resolved, statistically

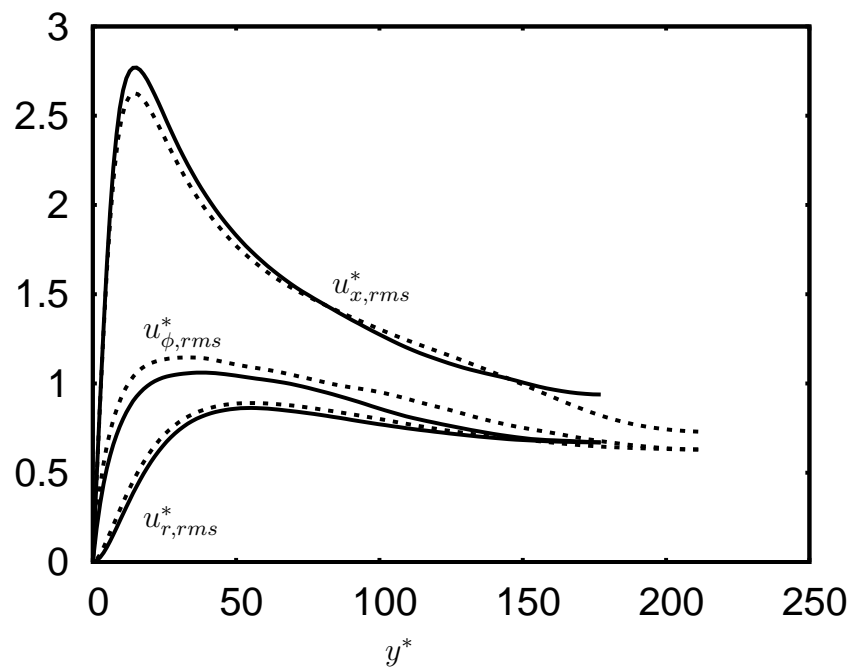


Figure 3.29: Rms velocity fluctuations. Line types as in fig. 3.24

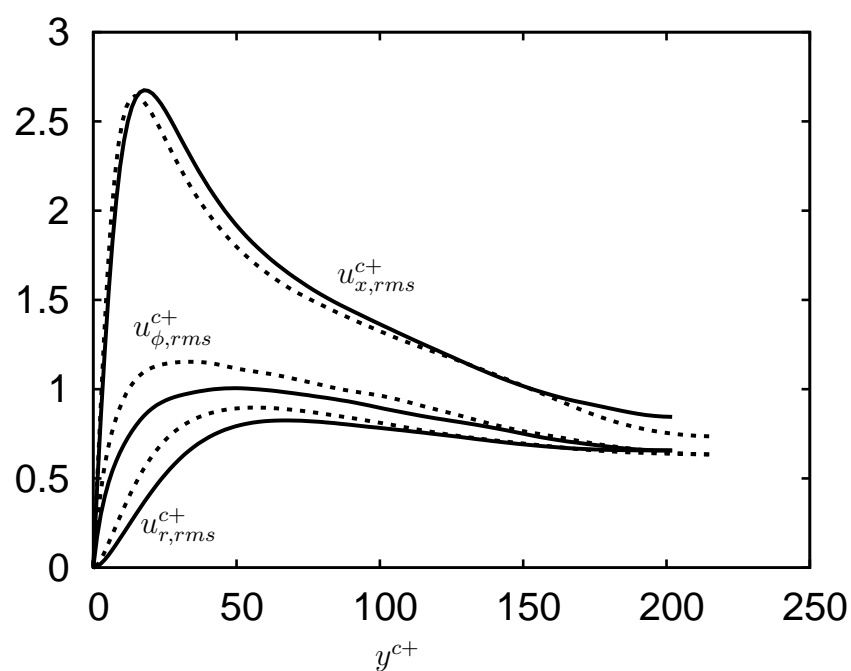


Figure 3.30: Rms velocity fluctuations using the scaling suggested by Brun *et al.* (2008). Line types as in fig. 3.24

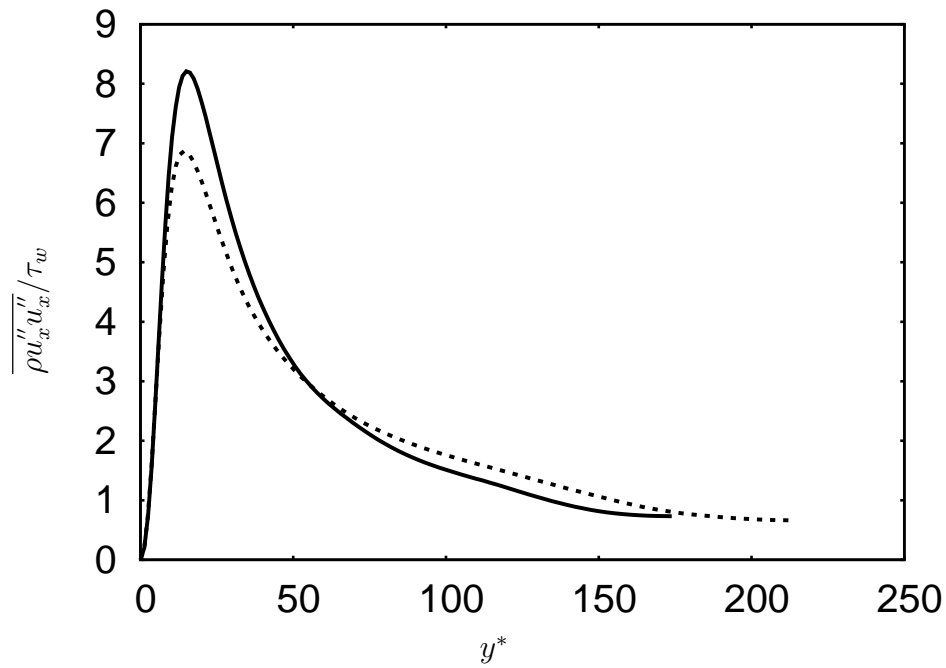


Figure 3.31: Streamwise Reynolds stress plotted against the 'semi-local' wall-normal coordinate. Line types as in fig. 3.24

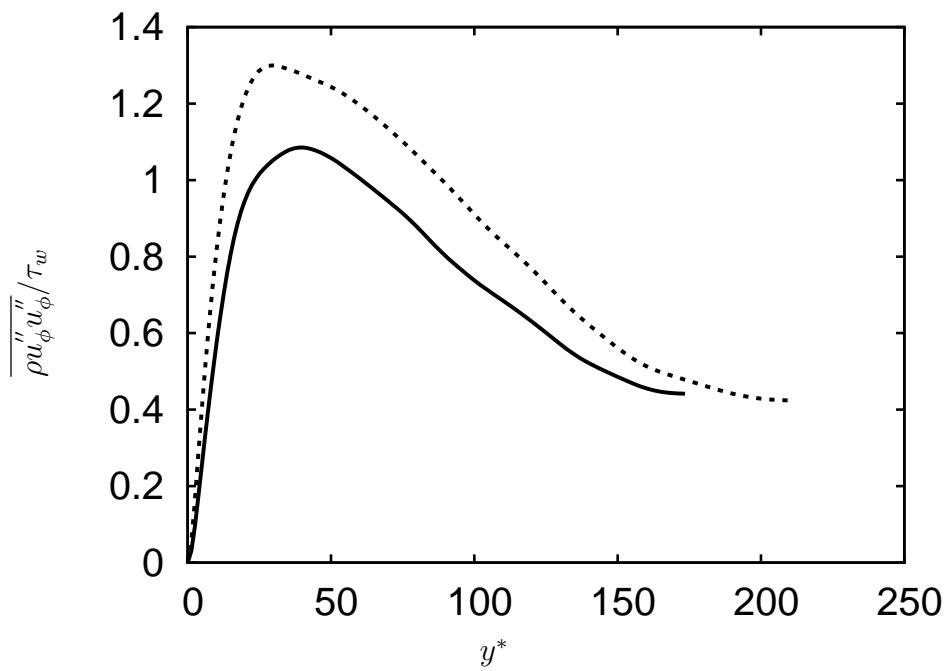


Figure 3.32: Azimuthal Reynolds stress plotted against the 'semi-local' wall-normal coordinate. Line types as in fig. 3.24

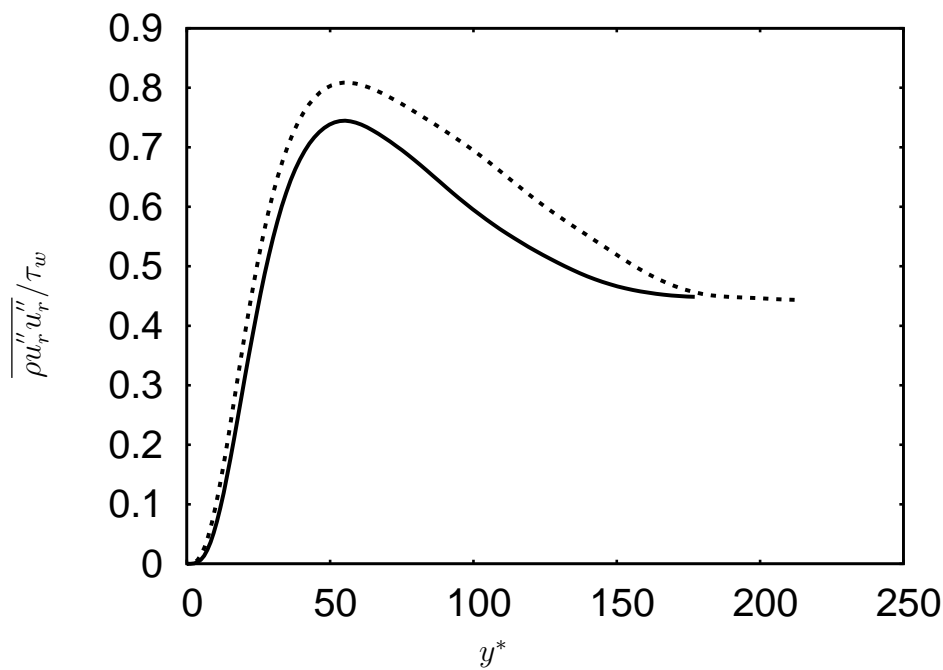


Figure 3.33: Radial Reynolds stress, plotted against the 'semi-local' wall-normal coordinate. Line types as in fig. 3.24

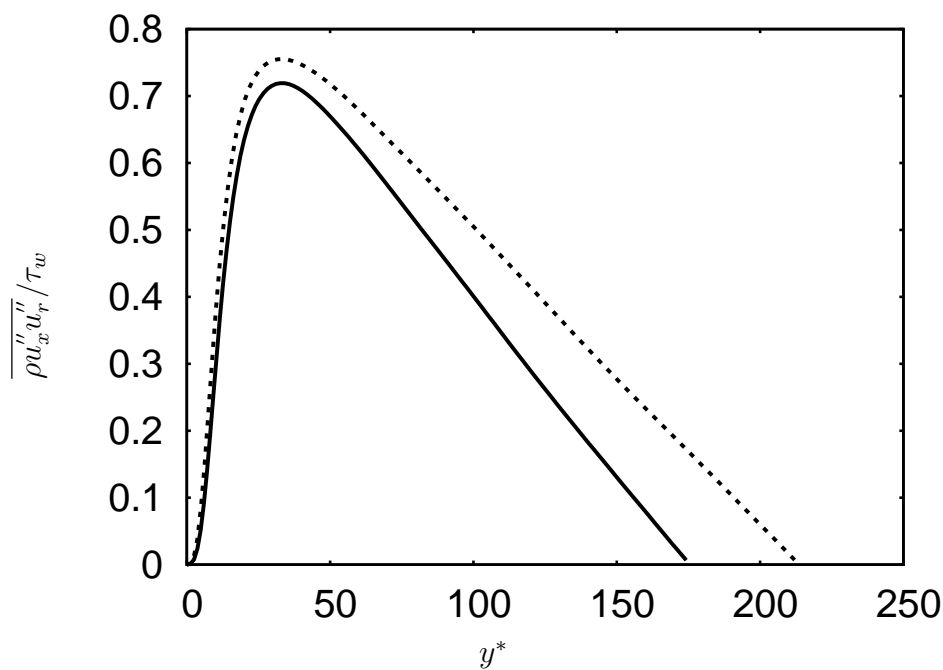


Figure 3.34: Reynolds shear stress, plotted against the 'semi-local' wall-normal coordinate. Line types as in fig. 3.24

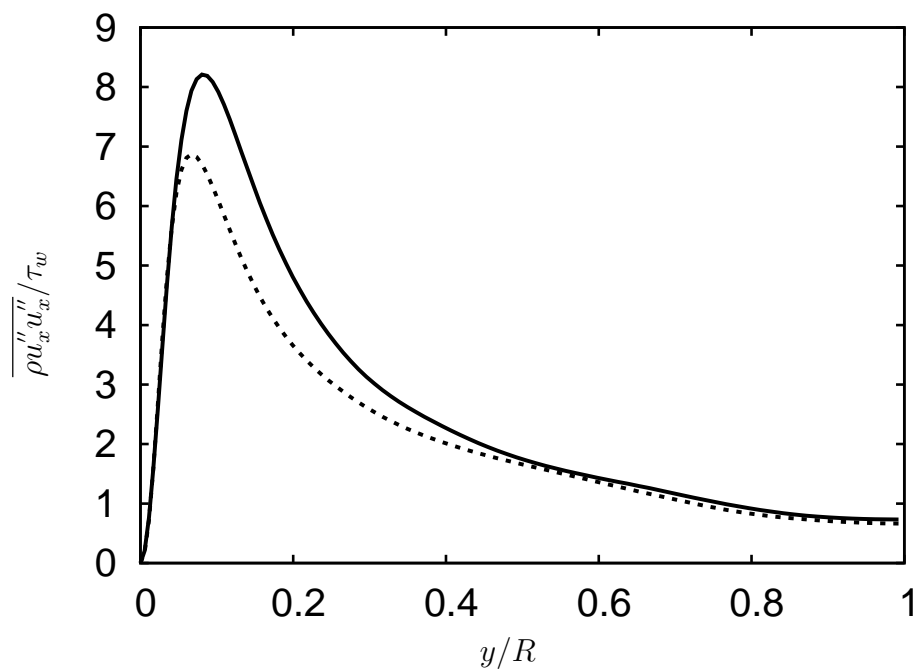


Figure 3.35: Streamwise Reynolds stress, outer scaling. Line types as in fig. 3.24

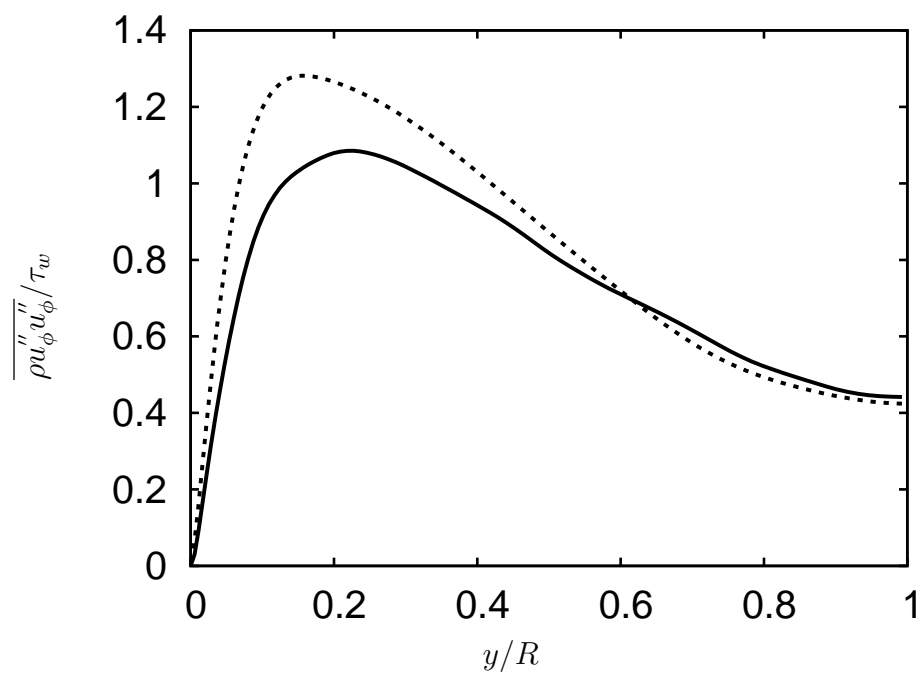


Figure 3.36: Azimuthal Reynolds stress, outer scaling. Line types as in fig. 3.24

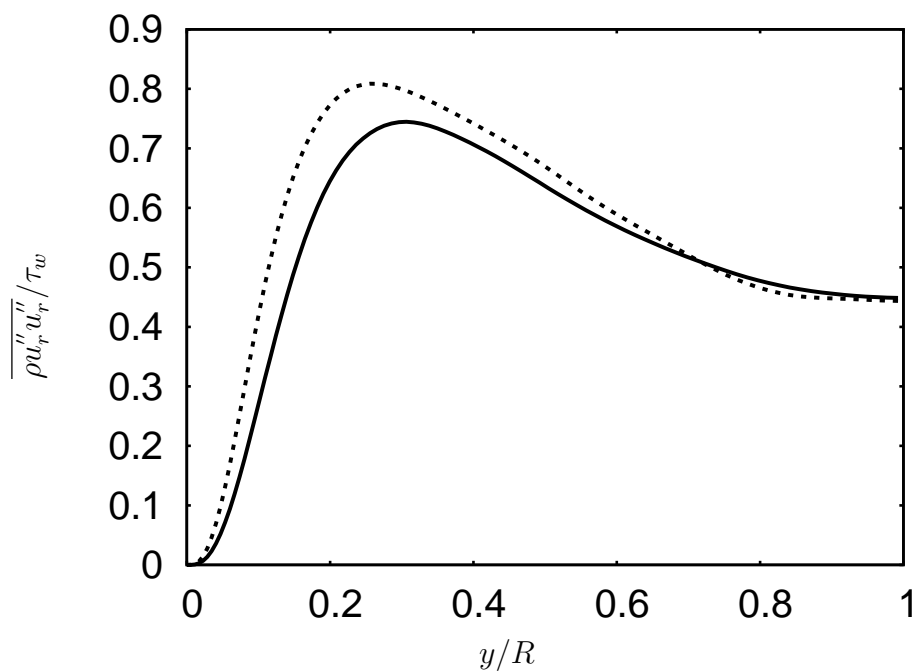


Figure 3.37: Radial Reynolds stress, outer scaling. Line types as in fig. 3.24

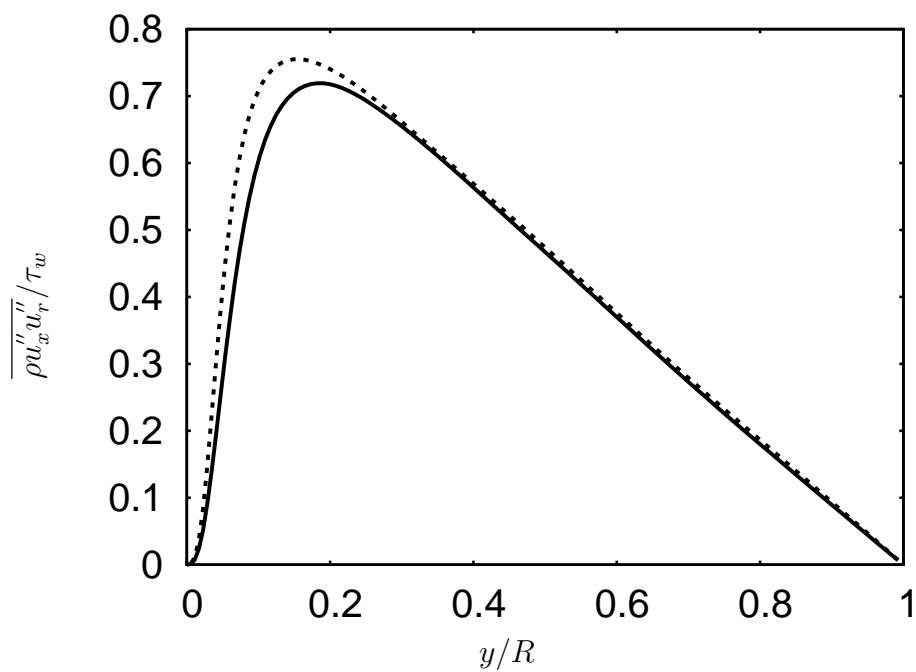


Figure 3.38: Reynolds shear stress, outer scaling. Line types as in fig. 3.24

converged DNS data enables estimation of individual terms in these equations which can be used to develop accurate second order turbulence models and more importantly, to learn new physics. A conservative form of the governing equations in cylindrical coordinates is given below :

$$\begin{aligned}
\frac{\partial \rho}{\partial t} &= -\left(\frac{\partial \rho u_x}{\partial x} + \frac{1}{r} \frac{\partial r \rho u_r}{\partial r} + \frac{1}{r} \frac{\partial \rho u_\theta}{\partial \theta}\right), \\
\frac{\partial \rho u_x}{\partial t} &= -\left(\frac{\partial \rho u_x u_x}{\partial x} + \frac{1}{r} \frac{\partial r \rho u_x u_r}{\partial r} + \frac{1}{r} \frac{\partial \rho u_x u_\theta}{\partial \theta}\right) - \frac{\partial p}{\partial x} + V_x, \\
\frac{\partial \rho u_r}{\partial t} &= -\left(\frac{\partial \rho u_r u_x}{\partial x} + \frac{1}{r} \frac{\partial r \rho u_r u_r}{\partial r} + \frac{1}{r} \frac{\partial \rho u_r u_\theta}{\partial \theta} - \frac{\rho u_\theta^2}{r}\right) - \frac{\partial p}{\partial r} + V_r, \\
\frac{\partial \rho u_\theta}{\partial t} &= -\left(\frac{\partial \rho u_\theta u_x}{\partial x} + \frac{1}{r} \frac{\partial r \rho u_\theta u_r}{\partial r} + \frac{1}{r} \frac{\partial \rho u_\theta u_\theta}{\partial \theta} + \frac{\rho u_r u_\theta}{r}\right) - \frac{1}{r} \frac{\partial p}{\partial \theta} + V_\theta, \\
\frac{\partial e}{\partial t} &= -\left(\frac{\partial(e+p)u_x}{\partial x} + \frac{1}{r} \frac{\partial r(e+p)u_r}{\partial r} + \frac{1}{r} \frac{\partial(e+p)u_\theta}{\partial \theta}\right) \\
&\quad - \frac{\partial q_x}{\partial x} - \frac{1}{r} \frac{\partial r q_r}{\partial r} - \frac{1}{r} \frac{\partial q_\theta}{\partial \theta} \\
&\quad + u_x V_x + u_r V_r + u_\theta V_\theta + \Psi
\end{aligned} \tag{3.10}$$

where the symbols have their usual meanings. e is the total energy per unit volume i.e. the sum of internal and kinetic energies.

Here V_x, V_r, V_θ are the viscous terms in the respective momentum equations given by:

$$\begin{aligned}
V_x &= \frac{\partial \tau_{xx}}{\partial x} + \frac{1}{r} \frac{\partial r \tau_{xr}}{\partial r} + \frac{1}{r} \frac{\partial \tau_{x\theta}}{\partial \theta} \\
V_r &= \frac{\partial \tau_{xr}}{\partial x} + \frac{1}{r} \frac{\partial r \tau_{rr}}{\partial r} + \frac{1}{r} \frac{\partial \tau_{r\theta}}{\partial \theta} - \frac{\tau_{\theta\theta}}{r} \\
V_\theta &= \frac{\partial \tau_{x\theta}}{\partial x} + \frac{1}{r} \frac{\partial r \tau_{r\theta}}{\partial r} + \frac{1}{r} \frac{\partial \tau_{\theta\theta}}{\partial \theta} + \frac{\tau_{r\theta}}{r}
\end{aligned}$$

q_x, q_r, q_θ are the heat fluxes in the respective directions according to Fourier's law. Ψ is the viscous dissipation rate.

The following decomposition of variables into mean and fluctuating parts is used:

$$\begin{aligned}
u &= \tilde{u} + u'' \\
\rho &= \bar{\rho} + \rho' \\
p &= \bar{p} + p' \\
\tau &= \bar{\tau} + \tau'
\end{aligned}$$

where \bar{f} represents Reynolds averaged quantities and the average is taken over homogeneous directions x and θ and time (assuming ergodicity). \tilde{f} represents Favre averaged quantities defined as

$$\bar{\rho} \tilde{f} = \overline{\rho f}$$

The transport equations for the normal and shear Reynolds stress are given below for fully-developed, non-swirling flow. The following symbols are used: P: Production, TD: Turbulent diffusion, VD: Viscous diffusion, DS: Viscous dissipation, PS: Pressure-strain correlations, M: Mass flux variation (Pressure and viscous work), CR: Cylindrical coordinate redistribution, PD: Pressure diffusion.

$$\begin{aligned}
\frac{\partial \overline{\rho u_x'' u_x''}}{\partial t} = & -2\overline{\rho u_x'' u_r''} \frac{\partial \tilde{u}_x}{\partial r} & P \\
& -\frac{1}{r} \frac{\partial r \overline{\rho u_r'' u_x'' u_x''}}{\partial r} & TD \\
& +\frac{2}{r} \frac{\partial r \overline{\tau_{xr}' u_x''}}{\partial r} & VD \\
& -2\overline{\tau_{xx}' \frac{\partial u_x''}{\partial x}} - 2\overline{\tau_{xr}' \frac{\partial u_x''}{\partial r}} - 2\overline{\tau_{x\theta}' \frac{1}{r} \frac{\partial u_x''}{\partial \theta}} & DS \\
& +2\overline{p' \frac{\partial u_x''}{\partial x}} & PS \\
& +2\overline{u_x''} \left(\frac{1}{r} \frac{\partial r \overline{\tau_{xr}}}{\partial r} - \frac{\partial \bar{p}}{\partial x} \right) & M
\end{aligned} \tag{3.11}$$

$$\begin{aligned}
\frac{\partial \overline{\rho u_\theta'' u_\theta''}}{\partial t} = & -\frac{1}{r} \frac{\partial r \overline{\rho u_r'' u_\theta'' u_\theta''}}{\partial r} & TD \\
& +\frac{2}{r} \frac{\partial r \overline{\tau_{r\theta}' u_\theta''}}{\partial r} & VD \\
& -2\overline{\tau_{x\theta}' \frac{\partial u_\theta''}{\partial x}} - 2\overline{\tau_{r\theta}' \frac{\partial u_\theta''}{\partial r}} - 2\overline{\tau_{\theta\theta}' \frac{1}{r} \frac{\partial u_\theta''}{\partial \theta}} + 2\frac{\overline{u_\theta'' \tau_{\theta r}}}{r} & DS \\
& +2\overline{p' \frac{1}{r} \frac{\partial u_\theta''}{\partial \theta}} & PS \\
& -\frac{2}{r} \overline{(\rho u_\theta'' u_\theta'' u_r'')} & CR \\
& +2\overline{u_\theta''} \left(\frac{1}{r} \frac{\partial r \overline{\tau_{\theta r}}}{\partial r} \right) & M
\end{aligned} \tag{3.12}$$

$$\begin{aligned}
\frac{\partial \overline{\rho u_r'' u_r''}}{\partial t} = & -\frac{1}{r} \frac{\partial r \overline{\rho u_r'' u_r'' u_r''}}{\partial r} & TD \\
& -\frac{2}{r} \frac{\partial r \overline{p' u_r''}}{\partial r} + \frac{2}{r} \frac{\partial r \overline{\tau_{rr}' u_r''}}{\partial r} & PD/VD \\
& -2\overline{\tau_{rx}' \frac{\partial u_r''}{\partial x}} - 2\overline{\tau_{rr}' \frac{\partial u_r''}{\partial r}} - 2\overline{\tau_{r\theta}' \frac{1}{r} \frac{\partial u_r''}{\partial \theta}} - 2\frac{\overline{u_r'' \tau_{\theta\theta}}}{r} & DS \\
& +2\overline{p' \frac{1}{r} \frac{\partial u_r''}{\partial r}} & PS \\
& +\frac{2}{r} \overline{(\rho u_\theta'' u_\theta'' u_r'')} & CR \\
& +2\overline{u_r''} \left(\frac{1}{r} \frac{\partial r \overline{\tau_{rr}}}{\partial r} - \frac{\partial \bar{p}}{\partial r} \right) & M
\end{aligned} \tag{3.13}$$

$$\begin{aligned}
\frac{\partial \overline{\rho u_x'' u_r''}}{\partial t} = & -\overline{\rho u_r'' u_r''} \frac{\partial \tilde{u}_x}{\partial r} \quad P \\
& -\frac{1}{r} \overline{\frac{\partial r \rho u_r'' u_x'' u_r''}{\partial r}} \quad TD \\
& -\frac{1}{r} \overline{\frac{\partial r p' u_x''}{\partial r}} \quad PD \\
& +\frac{1}{r} \overline{\frac{\partial (r \tau_{xr}' u_r'' + r \tau_{rr}' u_x'')}{\partial r}} \quad VD \\
& -\tau_{xx}' \frac{\partial u_r''}{\partial x} - \tau_{xr}' \frac{\partial u_r''}{\partial r} - \tau_{x\theta}' \frac{1}{r} \frac{\partial u_r''}{\partial \theta} \\
& -\tau_{rx}' \frac{\partial u_x''}{\partial x} - \tau_{rr}' \frac{\partial u_x''}{\partial r} - \tau_{r\theta}' \frac{1}{r} \frac{\partial u_x''}{\partial \theta} - \frac{u_x'' \tau_{\theta\theta}}{r} \quad DS \\
& +p' \left(\frac{\partial u_r''}{\partial x} + \frac{1}{r} \frac{\partial r u_x''}{\partial r} \right) \quad PS \\
& +\frac{1}{r} \overline{(\rho u_\theta'' u_\theta'' u_x'')} \quad CR \\
& +\tilde{u}_r'' \left(-\frac{\partial \bar{p}}{\partial x} + \frac{1}{r} \frac{\partial r \tau_{xr}^-}{\partial r} \right) + \tilde{u}_x'' \left(\frac{1}{r} \frac{\partial r \tau_{rr}^-}{\partial r} - \frac{\partial \bar{p}}{\partial r} \right) \quad M
\end{aligned} \tag{3.14}$$

We now look at the individual terms of the Reynolds stress balance equations in order to find out the reasons for the observed changes in Reynolds stress anisotropy at the supersonic Mach number. Away from the viscous sublayer, $\overline{\rho u_x'' u_r''} = (1 - \frac{y}{R})\tau_w$ and $\frac{\partial \tilde{u}_x}{\partial y} \approx u_\tau^*/(\kappa y)$, so that the production term, P , in the streamwise momentum equation can be written as

$$P = \frac{\tau_w^2}{\bar{\mu}\kappa} \left(\frac{1}{y^*} - \frac{1}{R^*} \right)$$

This shows that $\tau_w^2/\bar{\mu}$ is an appropriate 'inner' scaling parameter for the terms in the Reynolds stress transport equation and that y^* is the proper wall-normal coordinate. This scaling was used by Foysi *et al.* (2004) in the case of a channel flow.

Huang *et al.* (1995) used $\tau_w u_m/R$ as an 'outer' scaling for the Reynolds stress budgets. They found that q_w could be used as a scaling for the heat flux term in the k budget and since an overall energy balance in the channel requires that $q_w = \tau_w u_m$ (i.e. the heat transfer through the walls is equal to the total pressure work done across the channel.), they applied this scaling. Figures 3.39- 3.42 show the streamwise, azimuthal, radial and shear stress budgets, respectively, for the supersonic case in 'outer' scaling.

Before we discuss the individual terms in the budgets, we should note the differences between these equations in cartesian and cylindrical coordinates. One of these differences stems from the centrifugal and coriolis terms in the u_ϕ and u_r equations which lead to extra redistributive terms in the budgets of $\overline{\rho u_r'' u_r''}$, $\overline{\rho u_\phi'' u_\phi''}$, and $\overline{\rho u_x'' u_r''}$. These are marked as CR (cylindrical coordinate redistribution terms). They are well behaved in the $\overline{\rho u_r'' u_r''}$ and $\overline{\rho u_\phi'' u_\phi''}$ equations, but in the shear stress equation this term asymptotically increases near the centerline. This is compensated in this equation by the turbulent diffusion term (Figure 3.42) which is also not well-behaved near the axis. Similarly, the pressure-strain

and pressure diffusion terms in the shear stress equation are not well-behaved near the axis but their sum which is the velocity pressure gradient is well-behaved and plotted instead. These observations are consistent with those made by Freund *et al.* (1997) in the DNS of a compressible, annular mixing layer using cylindrical coordinates.

In the streamwise balance (figure 3.39), the major source term in the buffer layer ($5 < y^+ < 60$) is the production due to mean shear and the major sink terms are viscous dissipation and pressure-strain correlation. Near the wall, however, viscous effects are dominant as shown by a balance between viscous diffusion and dissipation. The pressure-strain term is redistributive as it acts as a source in both azimuthal and radial equations. Turbulent diffusion, expectedly plays a role only in the buffer layer. The compressible mass flux variation term has a small contribution in a region very close to the wall. It should be noted that the diffusion terms cannot act as a net source or sink since they integrate to zero over the whole domain.

In the azimuthal balance (figure 3.40), there is no explicit production term. The pressure-strain term acts as a source in the buffer layer and the only significant sink term here is the viscous dissipation. Again very close to the wall, viscous diffusion balances viscous dissipation. The cylindrical coordinate redistribution term (CR) is found to be negligible.

The radial budget (figure 3.41) shows the velocity-pressure-gradient (VPG) term, which is the sum of pressure-strain and pressure diffusion terms. The pressure-strain correlation is the only net source here since the pressure diffusion term integrates to zero over the volume. The viscous dissipation term is the only major sink. There is no explicit production due to shear. The turbulent diffusion term has small contributions in the buffer layer and also in the core region. Again, the cylindrical redistribution term (CR) has a negligible contribution.

The shear stress budget (figure 3.42) shows explicit production due to shear which is balanced in the buffer layer by the velocity-pressure gradient term. Turbulent diffusion contributes again primarily in the buffer layer.

Figures 3.43, 3.44 show the streamwise Reynolds stress budget in 'inner' scaling with $\tau_w^2/\bar{\mu}$. It is evident that this scaling collapses the production and viscous dissipation terms for the two Mach numbers, but not the pressure-strain correlation. This means that the observed increase of streamwise Reynolds stress at the supersonic Mach number is a consequence of a decreased pressure-strain correlation Π_{xx} , which leads to decreased redistribution, meaning lower production of the azimuthal and radial stresses. Foysi *et al.* (2004) solved a Poisson equation for the pressure fluctuations, neglecting the acoustic contributions, and using a Green's function approach. Their results show that the changes in pressure-strain correlation at higher Mach number can be properly predicted by taking into account mean density variations.

Figure 3.45 compares the pressure-strain correlations in the streamwise, azimuthal and radial balances. As expected, in the fully turbulent region, Π_{xx} is balanced by $\Pi_{\phi\phi}$ and Π_{rr} . Of particular interest is the region very close to the wall where Π_{rr} acts as a sink in the radial budget, redistributing energy to the azimuthal component which has a positive $\Pi_{\phi\phi}$ in this region. This is due to the 'splatting' or 'impingement' effect which produces a flow pattern similar to a jet impinging on a wall (Moin & Kim, 1982).

The profiles of rms vorticity fluctuations also exhibit this effect, since the wall-normal

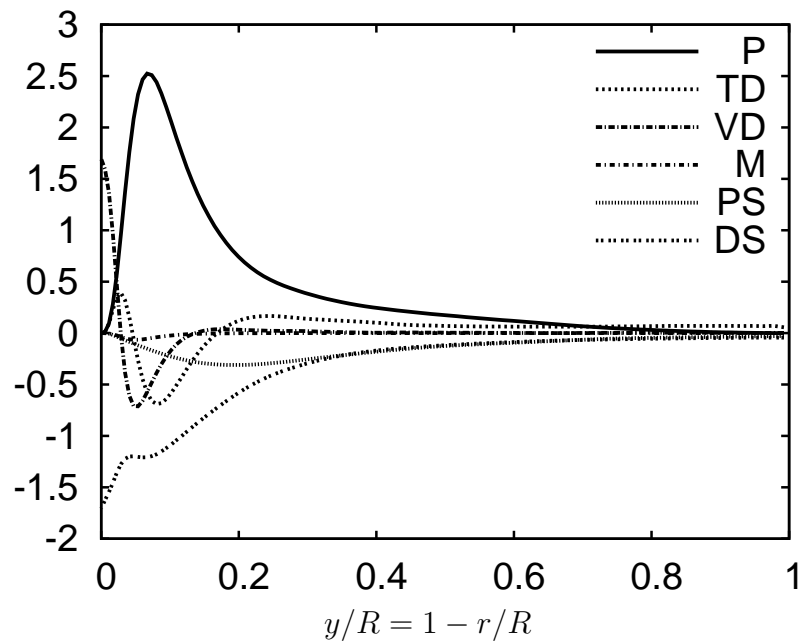


Figure 3.39: Streamwise Reynolds stress balance scaled with $\tau_w u_m / R$ at $M=1.5$

vorticity goes to zero near the wall and the wall-parallel components increase in magnitude, Figure 3.46. Away from the wall, reasonable isotropy is observed. Also note that the radial pressure diffusion term balances the negative Π_{rr} in the radial stress budget close to the wall and hence leads to nearly zero velocity-pressure-gradient term (as shown in the radial budget).

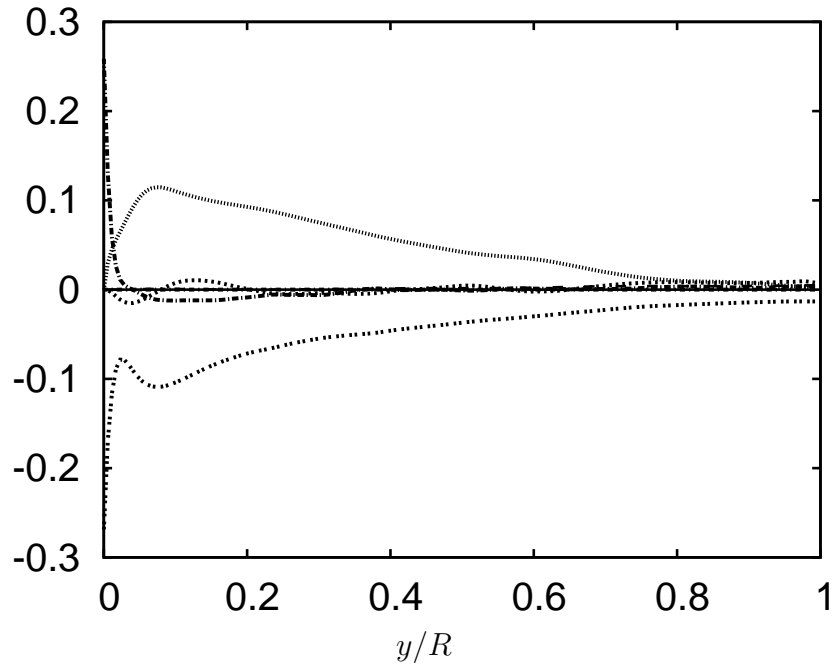


Figure 3.40: Azimuthal Reynolds stress balance scaled with $\tau_w u_m / R$ at $M=1.5$. Line types as in fig. 3.39. Cylindrical coordinates redistribution term (CR) is negligibly small.

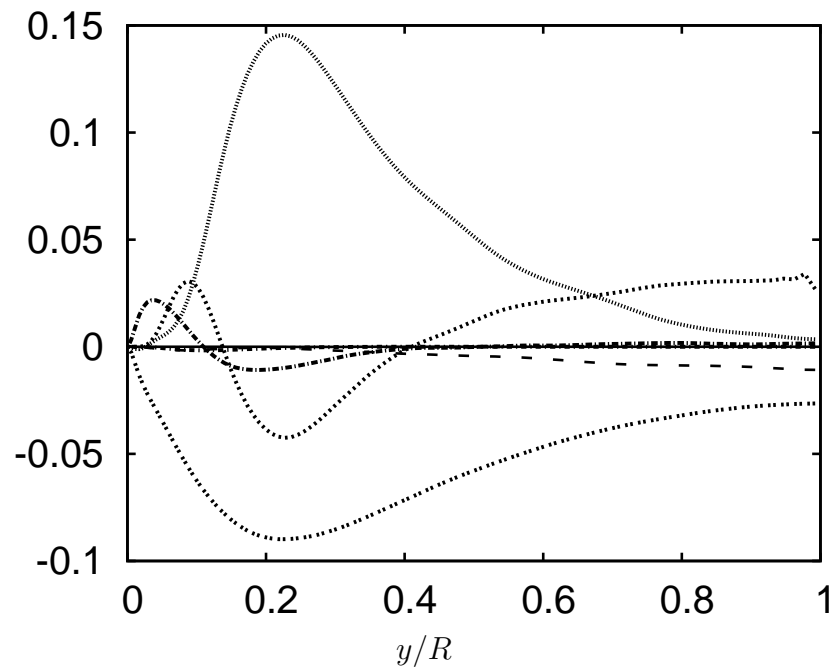


Figure 3.41: Radial Reynolds stress balance scaled with $\tau_w u_m / R$ at $M=1.5$. Line types as in 3.39 but velocity-pressure-gradient term is plotted instead of pressure-strain correlation. Cylindrical coordinates redistribution term (CR) shown by dashed line (- - -)

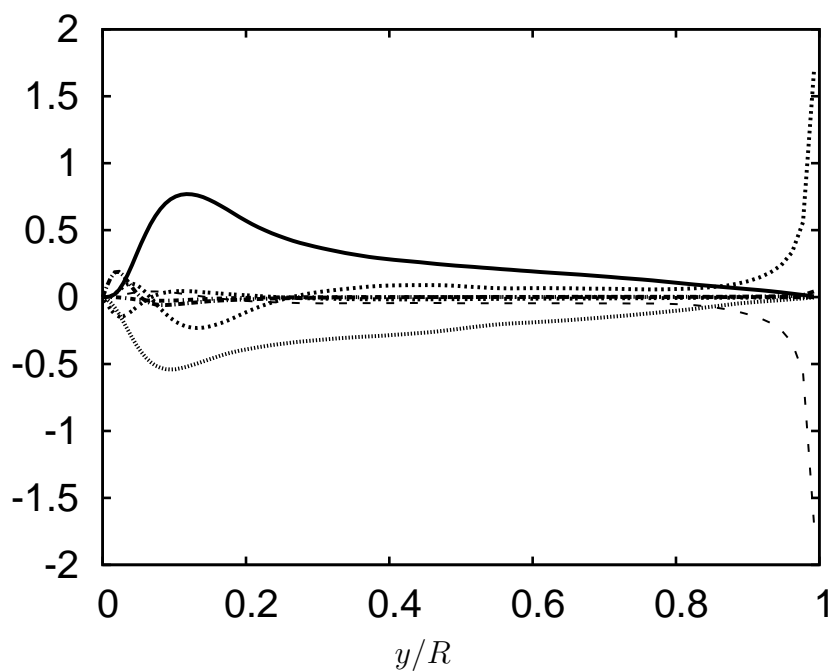


Figure 3.42: Reynolds shear stress balance scaled with $\tau_w u_m / R$ at $M=1.5$. Line types as in 3.39 but velocity-pressure-gradient term is plotted instead of pressure-strain correlation. Cylindrical coordinates redistribution term (CR) shown by dashed line (- -)

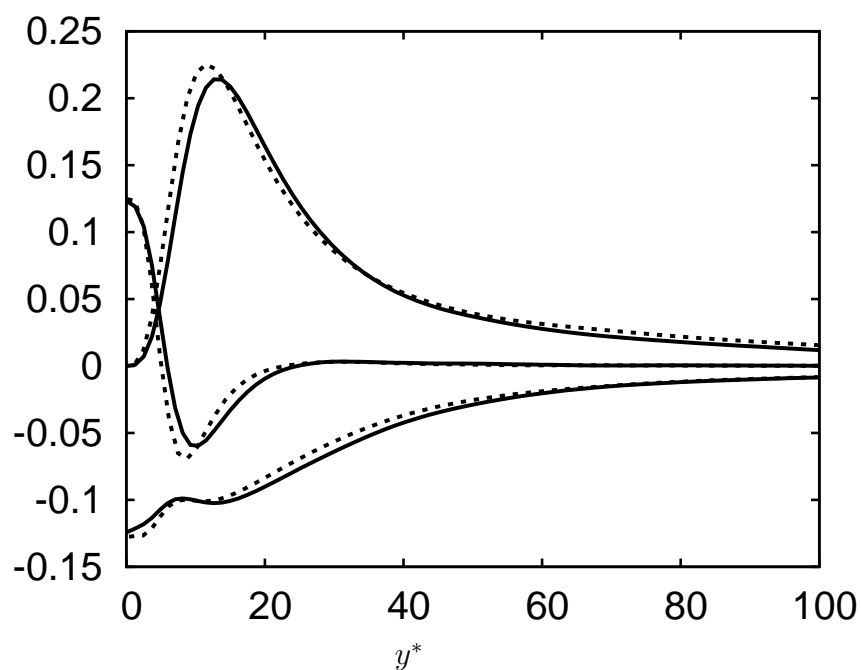


Figure 3.43: Streamwise Reynolds stress production, viscous diffusion and dissipation scaled with $\tau_w^2 / \bar{\mu}$. Solid line $M=1.5$, dashed line $M=0.3$

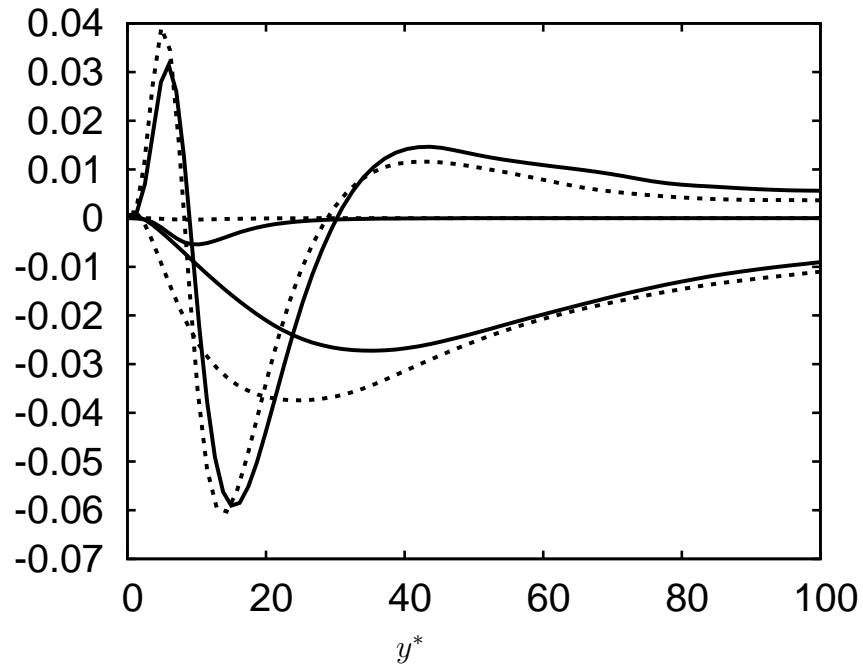


Figure 3.44: Turbulent diffusion, pressure-strain and mass flux variation terms in streamwise Reynolds stress budget, scaled with $\tau_w^2/\bar{\mu}$. Solid line $M=1.5$, dashed line $M=0.3$

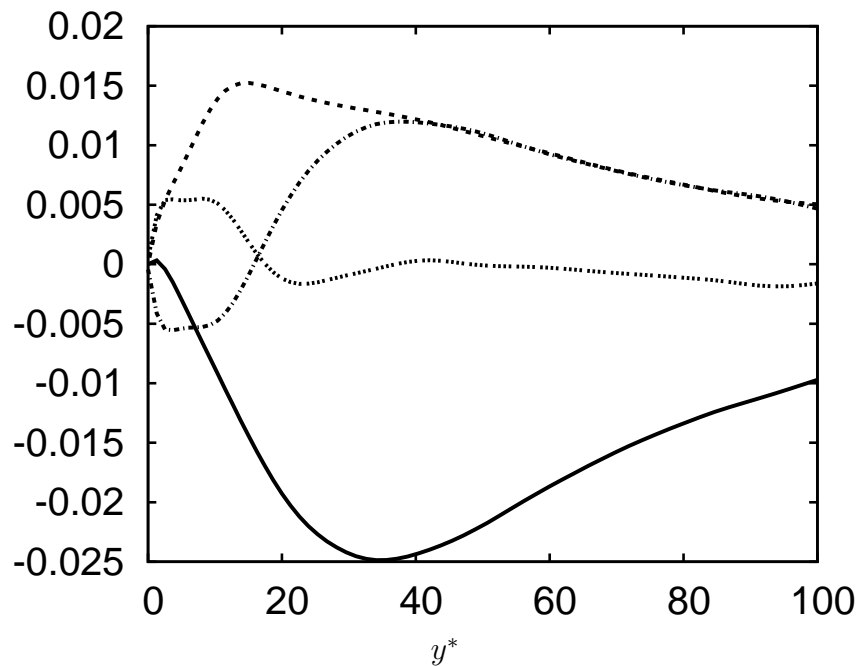


Figure 3.45: Pressure-strain correlations and radial pressure diffusion at $M=1.5$ scaled with $\tau_w^2/\bar{\mu}$. — streamwise; - - - azimuthal; -.- radial; pressure diffusion

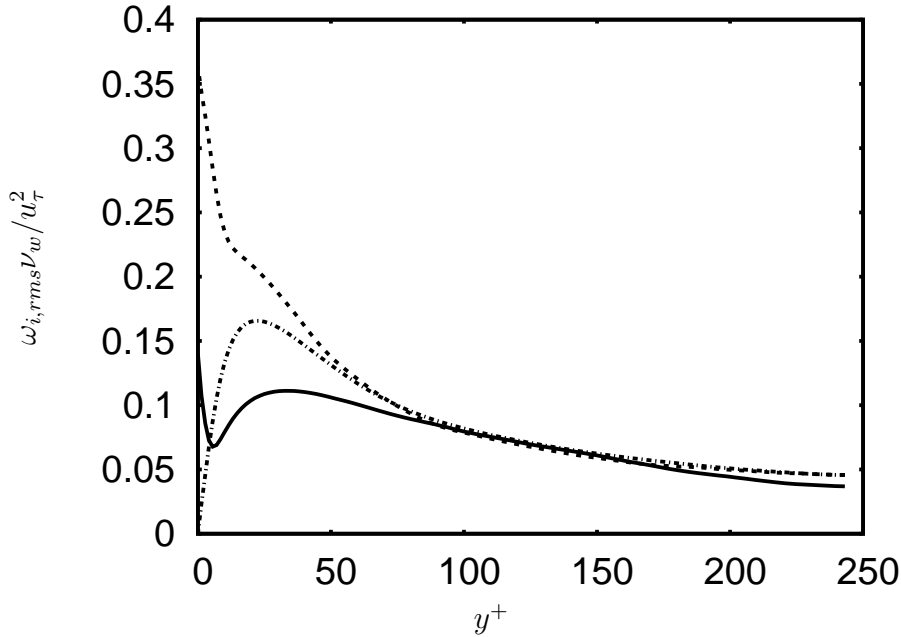


Figure 3.46: Rms vorticity fluctuations at $M=1.5$: — streamwise; -.- radial; - - - azimuthal

3.4 LES of supersonic turbulent pipe flow

LES of compressible flows with implicit SGS models is particularly attractive because there is no need to model the unknown SGS terms separately in the filtered governing equations.

One way of doing this is to use a Leray-type formulation which consists of convection by a smoothed velocity field. For example, Geurts & Holm (2003) have derived such a form of LES equation which is closed by a similarity type model using an explicit filter and its inverse without using eddy viscosity type models.

Explicit filtering is also central to approximate deconvolution approaches applied to shock capturing by Stolz (2000), Loginov *et al.* (2006). Here, the subgrid scales are reconstructed from the resolved fields (like in a scale similarity model) using an approximate inverse of the explicit filter. The approximate inverse is computed using a Van Cittert series expansion approach which gives a linear deconvolution operator. It is to be noted here that the deconvolved variables can only contain scales up to the limit which can be resolved by an LES grid and it is not meant to account for the dissipation scales. The effect of the dissipation scales on the resolved ones has to be accounted for. Additional regularization terms were used to provide extra dissipation to mimic the effects of energy transfer across the cutoff (Stolz, 2000).

A single step explicit filtering variant of the deconvolution approach has been recently used to simulate compressible channel flows (Mathew *et al.*, 2003). Here, the additional regularization is provided by an extra filtering step. This approach is used to obtain the results shown in this section and is detailed in chapter 2. Similar explicit filtering

approaches have been used to predict noise radiated from a round jet by Bogey & Bailly (2006).

Another way to dampen the energy at high wavenumbers is to use the dissipation of numerical schemes. Such approaches originally known as MILES have been applied to high Reynolds number flows by adjusting dissipative, shock capturing schemes (Fureby & Grinstein, 2002) and thereby exploiting the interference between truncation error of a discretization scheme and the SGS stress. Recently, Hickel *et al.* (2006) adapted the linear deconvolution approach of Stolz (2000) in the spirit of MILES to a nonlinear deconvolution procedure using local polynomials for interpolation. However, uncertainties still persist regarding the dampening effects on the resolved scales when shock capturing schemes are used, Garnier *et al.* (1999).

In this section the unfiltered DNS results of the supersonic pipe flow simulations are compared to the corresponding LES data.

Figure 3.50 compares the streamwise and azimuthal spectra of LES and DNS data. The streamwise spectra are shown for all the velocity components and are averaged over the azimuthal and wall normal directions. The azimuthal spectra are shown only for the streamwise velocity component at $y^* = 10$ and are averaged over the streamwise direction. Remarkable agreement between the DNS and LES results are noticed in the resolved wavenumber range for all the velocity components (and hence TKE) for the streamwise spectra. Similar good agreement is also shown by the azimuthal spectra of the streamwise component.

The instantaneous streamwise velocity fluctuations (fig. 3.47) in a plane parallel to the wall at $y^* = 5$ show alternate high and low speed streaks. Thus, physical near-wall dynamics are reflected in the LES data. However, compared with the DNS data only the large structures are found, which is expected, given the general low resolution of an LES. The wall-normal fluctuations show more organisation than in the DNS data which indicates that the LES is not able to predict the anisotropy correctly in this region. Similar observations are made of axial and radial velocity fluctuations in (x, r) - and (ϕ, r) -planes, see figures 3.48 and 3.49.

Mean temperature and density profiles (Figure 3.51) show marginal differences with the DNS data. The LES predicts a lower mean temperature. Mathew *et al.* (2006) presented improved results using no secondary filtering for regularization but a computationally expensive model of the terms in the bracket of equation (2.4). Such a procedure has not been used here because of its computational overhead. The rms temperature and density fluctuations, however, show good agreement with DNS results, Figure 3.52.

A look at the rms velocity fluctuations shows marginal differences between the LES and the DNS data in the buffer layer, Figure 3.53. The streamwise fluctuations are higher than the DNS data and the azimuthal and radial fluctuations are lower. This is also evident in the Reynolds stress profiles, Figure 3.54, 3.55. Here, only the streamwise and shear stresses are compared in outer scaling. Evidently, a form of SGS modelling which automatically takes care of local anisotropy of the flow is required.

The LES provides good predictions of terms in the Reynolds stress budgets, as seen in Figures 3.56, 3.57 for the streamwise component in semi-local, inner scaling. Terms like production due to shear and the pressure-strain correlations, which are largely governed by large-scales, follow the DNS curves closely. This confirms that the large scale flow features

of the LES mimic the DNS properly. Differences are seen only in viscous dissipation, viscous diffusion and turbulent diffusion terms which are controlled by small scales.

3.5 Conclusions

Compressible fully developed flow through a pipe with circular cross-section and with an isothermal wall has been studied in a cylindrical coordinate system by means of DNS and LES using high order finite difference schemes. The Mach numbers for the flows studied are 0.3 and 1.5. These flows thus provide an opportunity to investigate compressibility effects in the absence of complicating effects like those due to shock waves.

Compressibility effects in a pipe flow manifest themselves as changes in turbulence anisotropy. Similar to a plane, compressible channel flow such effects originate from mean property variations caused by increased dissipation in the supersonic flow. Intrinsic compressibility effects are negligible. Morkovin's hypothesis holds for most statistics of the flow and hence the Van Driest transform can be used for the mean velocity. A scaling using local mean density and viscosity nearly collapses the peak locations of the velocity fluctuations but not their peak magnitudes. The supersonic pipe flow shows increased coherence of streaky structures in the near-wall region compared to incompressible flow which has been shown to be an effect of density variations resulting in an increase in turbulence time scales compared to that of the mean shear. Reynolds stress anisotropy is increased in the supersonic pipe flow, which is a result of decreased pressure-strain correlations. As was shown in previous studies on supersonic channel flows, mean density decrease with increasing Mach numbers leads to the decrease of pressure-strain correlations and thus leads to increased Reynolds stress anisotropy.

A further conclusion from this study is the applicability of explicit filtering to compressible pipe flows as has been demonstrated by the good agreement of the LES statistics with those from the DNS. This LES procedure does not properly take into account local anisotropy of the velocity field which is reflected in the streamwise Reynolds stress overshooting the corresponding DNS result. However, terms in the Reynolds stress transport equations like production and pressure-strain which are governed mainly by large scales are predicted properly in the LES. It should also be kept in mind that this LES procedure mimics the effects of unresolved scales by means of regularization by an extra filtering step and hence we see differences in prediction of terms like viscous dissipation and turbulent transport by the LES when compared to DNS data.

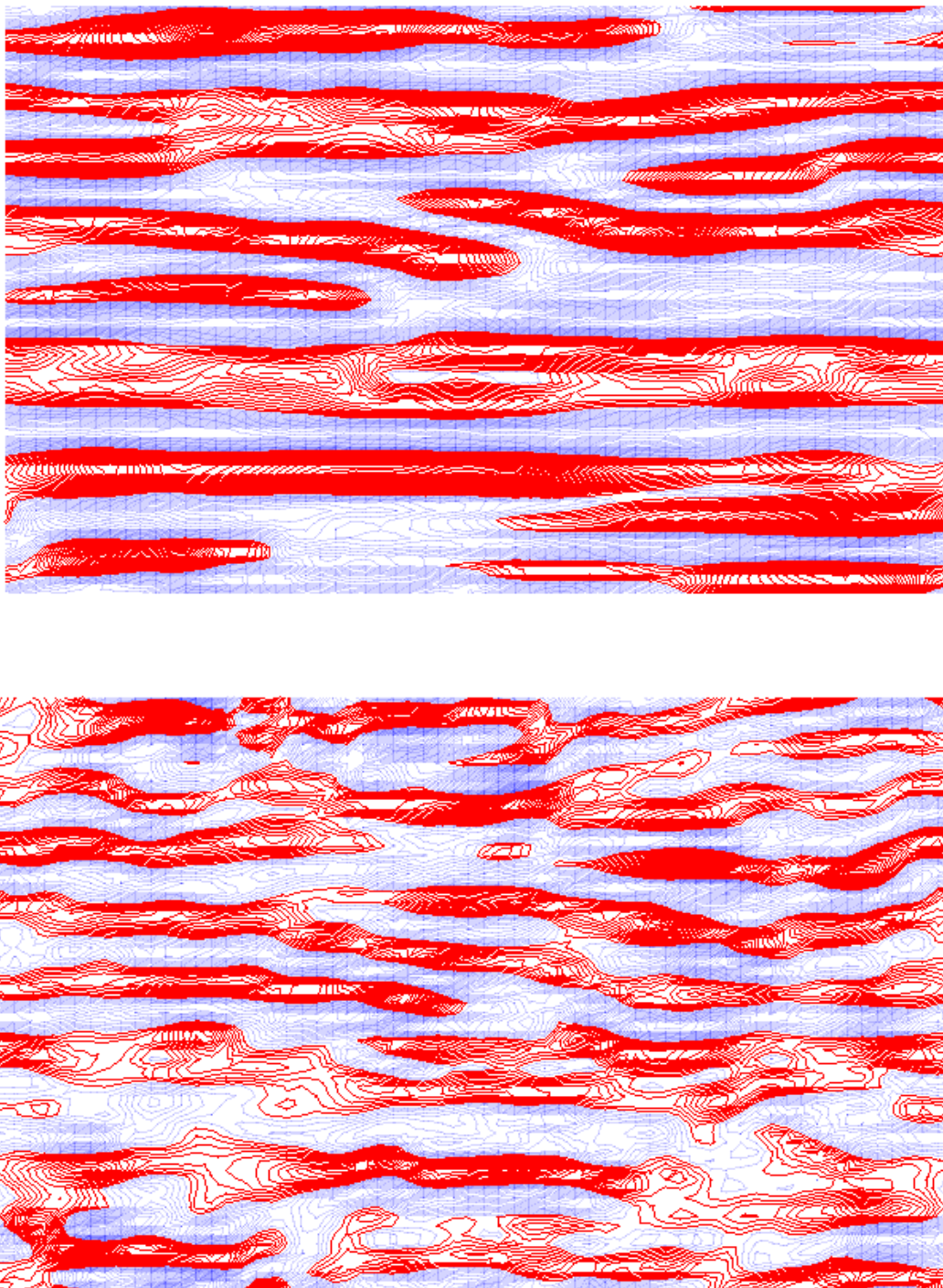


Figure 3.47: Instantaneous axial (top) and radial (bottom) velocity fluctuations in (x, r) plane for $M = 1.5$ at $y^* = 5$. Red lines show positive fluctuations

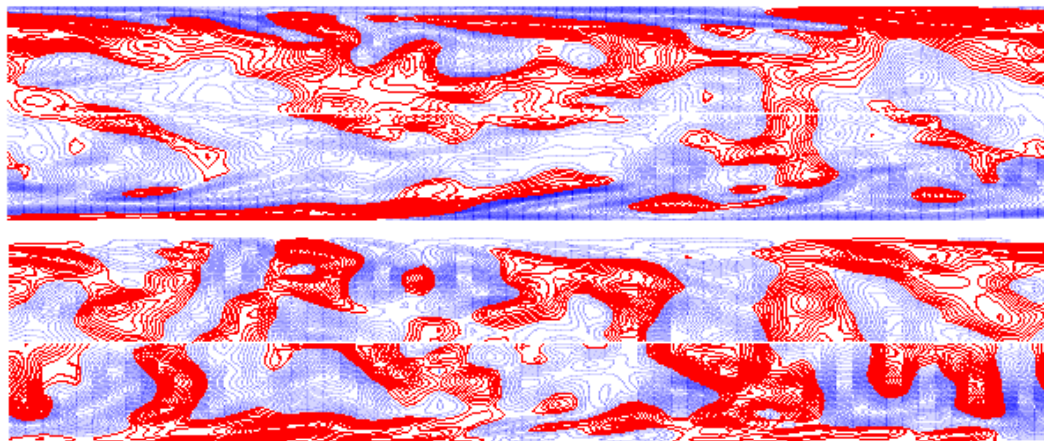


Figure 3.48: Instantaneous axial and radial velocity fluctuations in (x, r) -plane for $M = 1.5$. Red lines show positive fluctuations

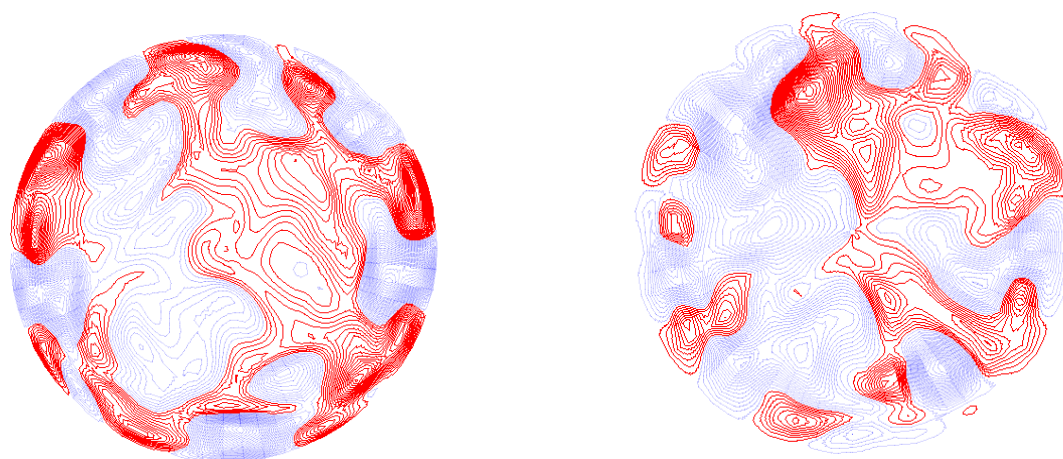


Figure 3.49: Instantaneous axial and radial velocity fluctuations in (ϕ, r) - plane for $M = 1.5$. Red lines show positive fluctuations

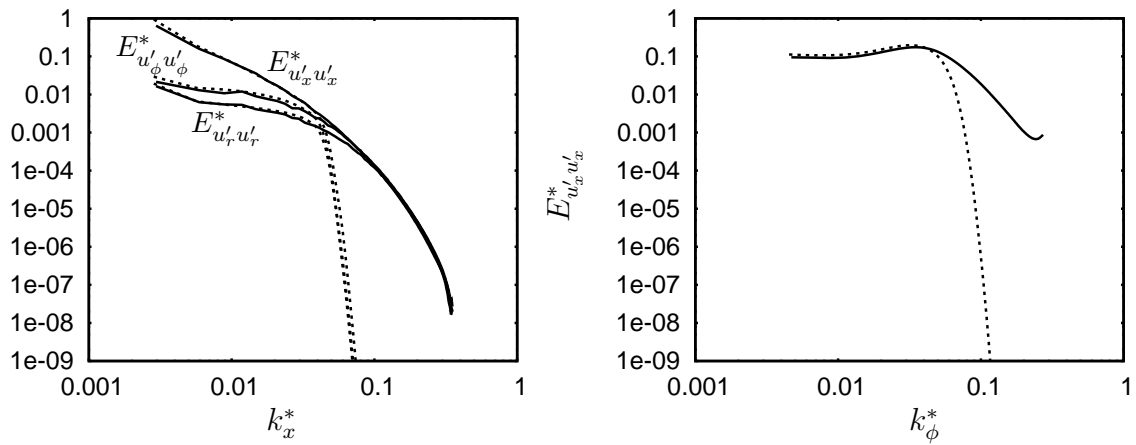


Figure 3.50: Left: Streamwise energy spectra, averaged in the other directions for the three velocity components. Right: azimuthal spectra for the streamwise component, averaged in the streamwise direction at $y^* = 10$. Solid line: DNS, Dashed line: LES

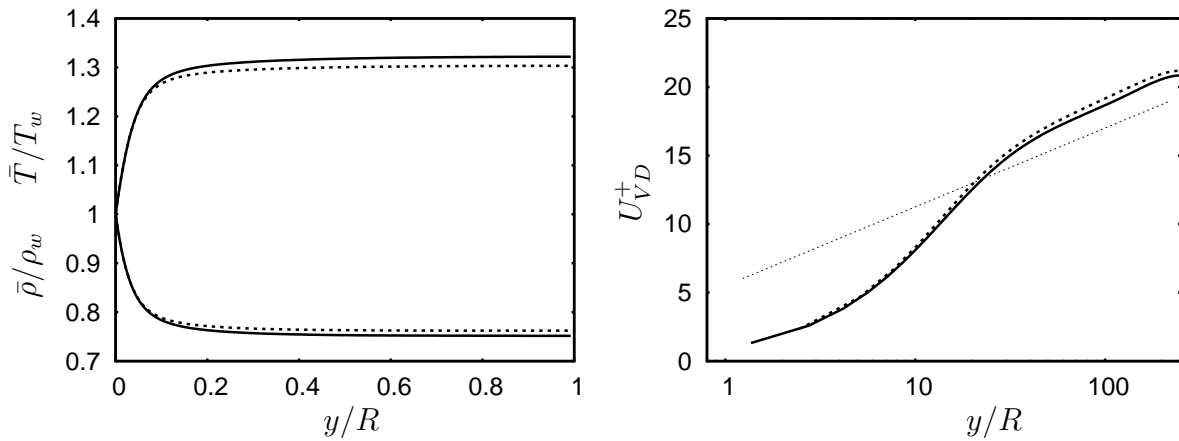


Figure 3.51: Mean temperature, density and Van Driest transformed velocity at $M=1.5$. solid line: DNS; dashed line: LES. Straight line: $u^+ = 2.5 \ln y^+ + 5.5$

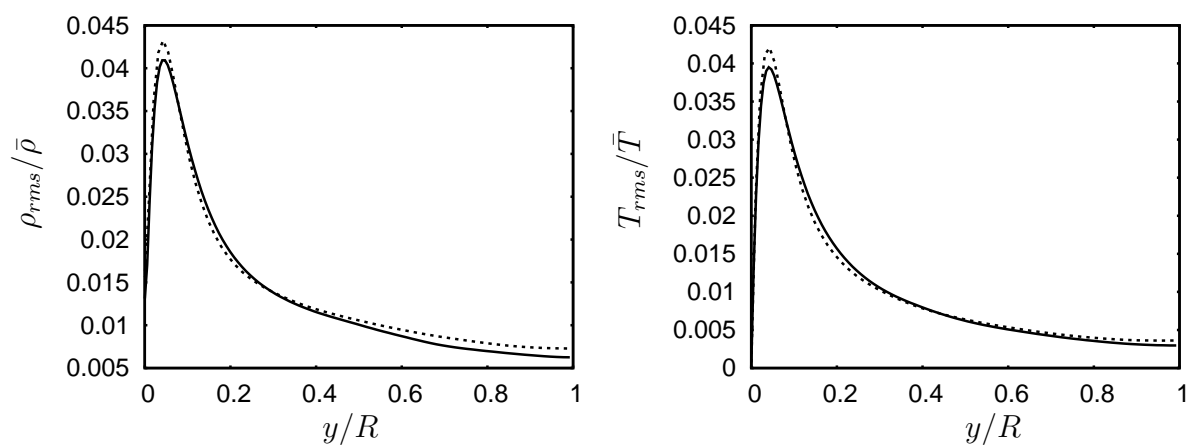


Figure 3.52: Density and temperature fluctuations. Line types as in fig. 3.51

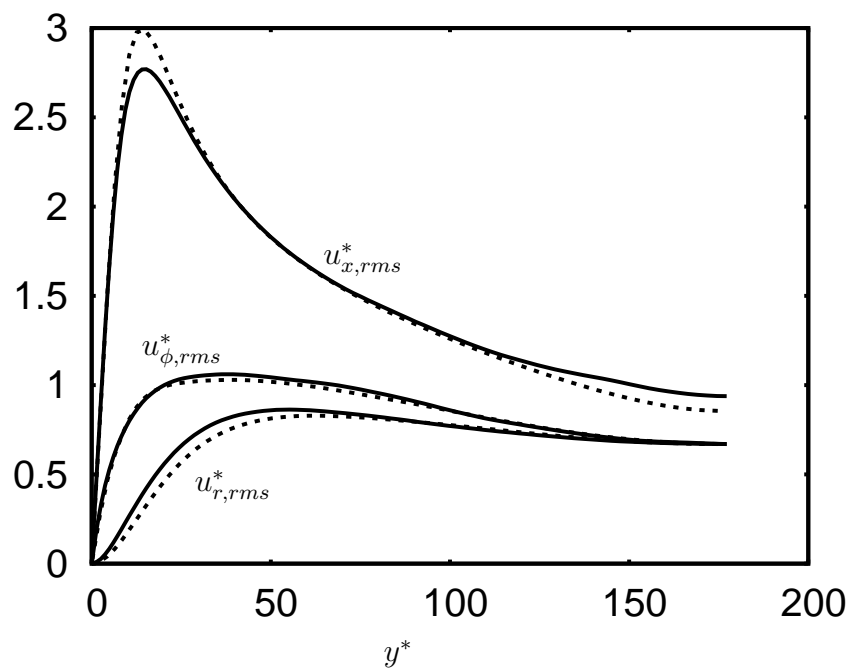


Figure 3.53: Rms velocity fluctuations, semi-local scaling. Line types as in fig. 3.51

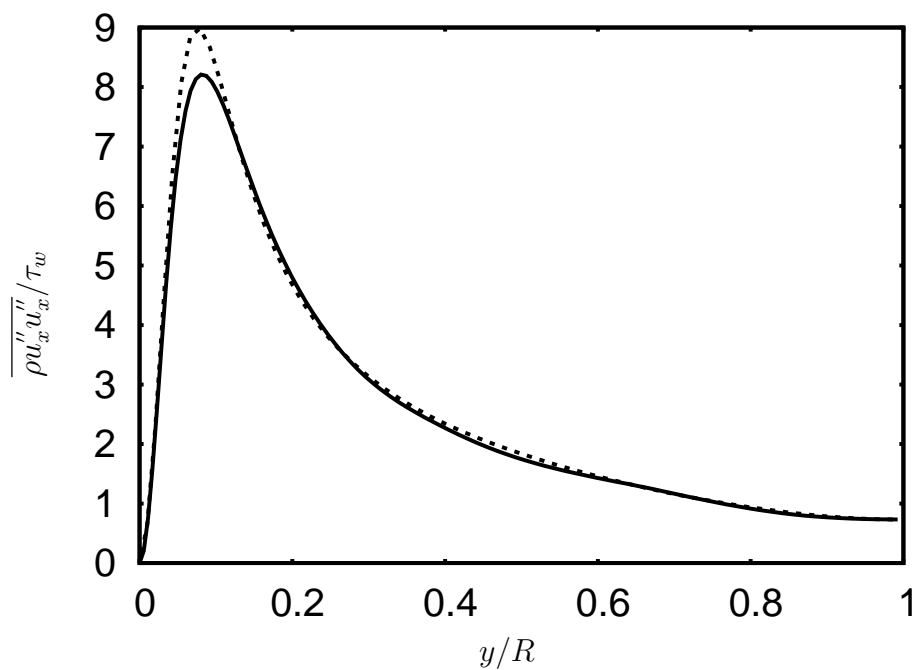


Figure 3.54: Streamwise Reynolds stress in outer scaling. Line types as in fig. 3.51

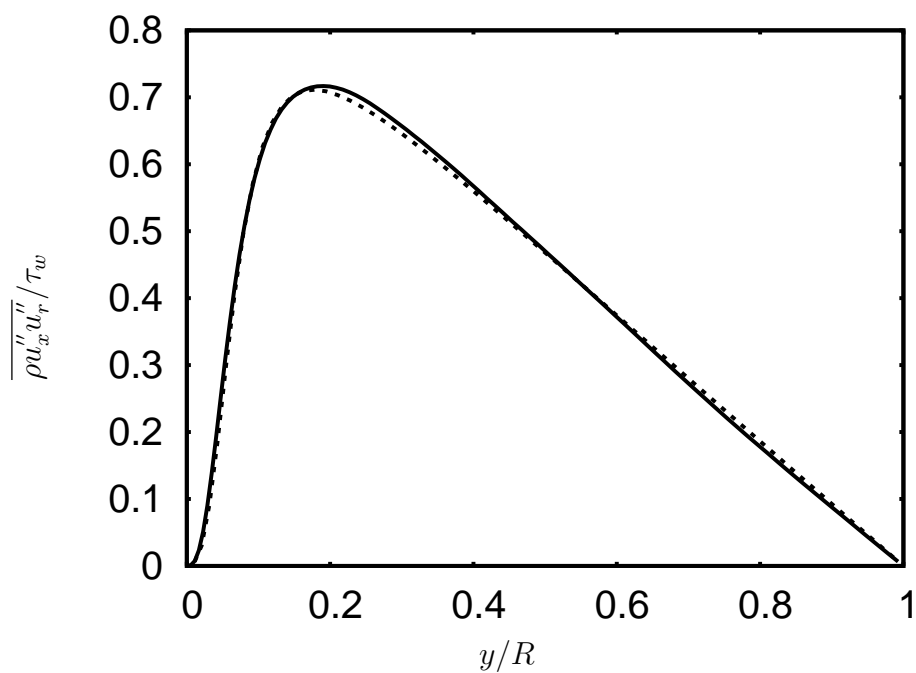


Figure 3.55: Reynolds shear stress in outer scaling. Line types as in fig. 3.51

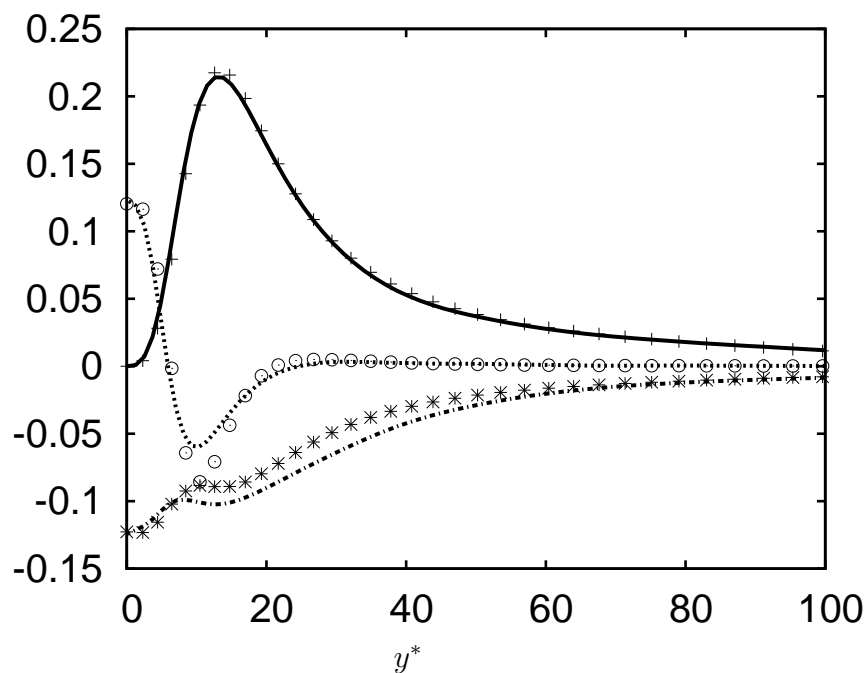


Figure 3.56: Streamwise Reynolds stress production, viscous diffusion and dissipation terms at $M=1.5$, scaled with $\tau_w^2/\bar{\mu}$. Lines: DNS; symbols: LES

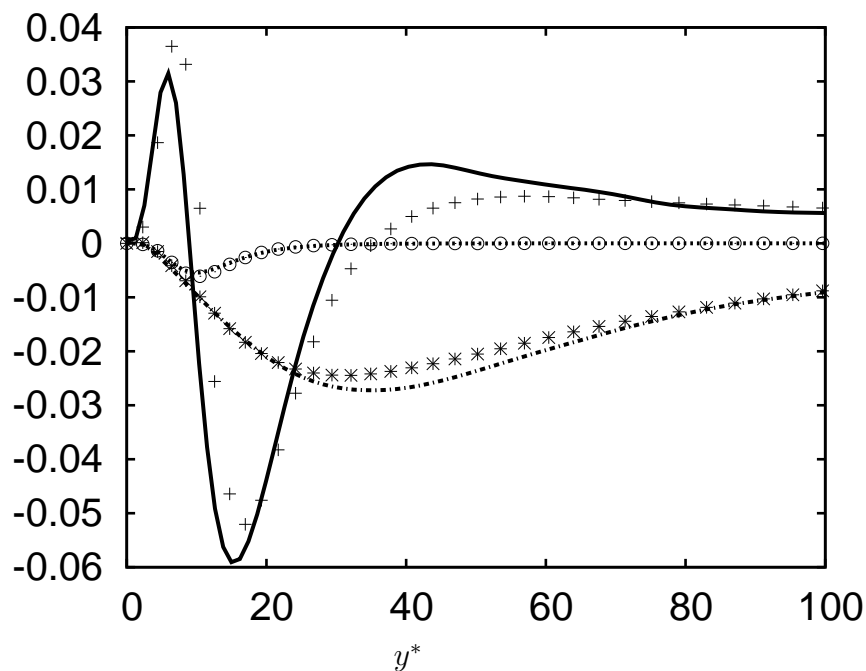


Figure 3.57: Turbulent diffusion, pressure-strain and mass flux variation terms in the streamwise Reynolds stress balance at $M=1.5$, scaled with $\tau_w^2/\bar{\mu}$. Lines: DNS; symbols: LES

Chapter 4

Supersonic turbulent nozzle flow

4.1 Introduction

Compressibility effects in supersonic parallel, wall-bounded flows manifest themselves essentially as strong variations in mean density and temperature (and hence viscosity) normal to the walls, as long as the turbulence intensities remain small compared to the speed of sound. This means that in flows in which M_t is low, Morkovin's hypothesis holds and these flows could be treated like incompressible flows with heat transfer. Intrinsic compressibility effects due to dilatation fluctuations and pressure fluctuations remain negligible in these cases.

However, compressible wall-bounded flows with significant favourable and adverse pressure gradients and extra strain rates are not covered in Morkovin's hypothesis. Mean dilatation or compression in these flows are known to cause effects greater than expected from the magnitude of extra production terms which appear in Reynolds stress equations, as was noted by Bradshaw (1974), who appropriately considered such flows to be complex flows. Particularly interesting in such flows is the role of the pressure-strain correlations which, besides turbulence production due to shear, mean dilatation and extra rate of strain, constitutes another important source/sink mechanism. A recent review of mainly experimental results of supersonic boundary layers under the influence of pressure gradients can be found in Spina *et al.* (1994), where these authors note that favourable pressure gradients cause a decay in turbulence intensities, while adverse pressure gradients cause an increase. They also observe that these kinds of supersonic flows exhibit counterintuitive behaviour when compared to their subsonic counterparts. Changes in density in the longitudinal direction result in variations of skin friction and boundary layer thickness which cannot be predicted based on similar subsonic flows.

Although, bulk expansion leads to decrease in turbulence intensities, the importance of these effects does, of course, depend on the magnitude and rate of expansion. Dussauge & Gaviglio (1987) study a supersonic boundary layer subjected to a rapid expansion and find that the rapid parts of the pressure-strain correlations are modified. The Reynolds stress evolution in the expansion zone is mainly affected by bulk dilatation production terms (i.e. part of kinetic production) and to a lesser extent by mean pressure gradient production terms (enthalpic production). They show that in the case of a rapid distortion with mean dilatation only, the variable $\widetilde{u_i' u_j'} / \bar{\rho}^{2/3}$ remains constant along a mean streamline.

We are, here, interested in flows which are under the influence of nearly constant, weak distributed pressure gradients where the effects of streamline curvature are negligible. These flows which may not fall under the rapid expansion category, however, occur frequently in nature and industry.

Incompressible boundary layers and channel flows also laminarize under the influence of strong, favourable pressure gradients (Narasimha & Sreenivasan, 1973), (Greenblatt & Moss, 2004). However, strictly incompressible flows with no heat transfer do not have density variations and hence no mean dilatation. The decrease in turbulence intensities in this case is due to extra sink terms in the Reynolds stress transport equation containing the acceleration. The vortex stretching mechanism exclusively controls the levels of vorticity in such flows.

High Mach number, accelerated flows will contain explicit mean dilatation effects and mean dilatation and baroclinic terms can become important sources/sinks of vorticity, as already noted in Spina *et al.* (1994). Such flows are analogous to strongly heated low-speed pipe flows which also show mean dilatation effects because of density variation (Bae *et al.* (2006)).

While examining the literature, we noted a lack of time-accurate, high resolution numerical data of compressible channel/pipe flows under the influence of pressure gradients. Hence, it is our aim to report new, useful results from high-order, time accurate simulations of this kind of flows. The flow configurations chosen to achieve this are smoothly contoured nozzles and diffusers with small total divergence and convergence angles.

4.2 Computational details

In this chapter, results are presented from DNS and LES of a fully-developed supersonic pipe flow subjected to a weak, favourable pressure gradient in a nozzle. The incoming flow is at $M = 1.5$ and $Re_\tau = 245$ inside a pipe of constant radius R and length $10R$. The nozzle flow has the same inlet radius as the incoming pipe flow and a length of $10R$. The wall is kept at the same temperature (as the upstream pipe) throughout the expansion in order to focus only on the effects of expansion on the turbulence structure. The resolution used for the DNS is $256 \times 128 \times 91$ and for the LES $64 \times 64 \times 50$ points in the axial (x), azimuthal (ϕ) and radial (r) directions, respectively. The area distribution of the nozzle is generated using isentropic streamtube equations ensuring a region of nearly constant, weak favourable pressure gradient and negligible streamline curvature effects. The maximum divergence angle at the exit of the nozzle is 10 degrees.

The continuity and momentum equations for an isentropic streamtube can be written as:

$$\begin{aligned}\rho V A &= \text{constant}, \\ \rho V \frac{dV}{dx} &= -\frac{1}{\rho} \frac{dp}{dx}.\end{aligned}$$

We specify a static pressure distribution such that $\frac{dp}{dx}$ is constant. Then, using the stagnation conditions at the inflow and assuming isentropic flow, we can get the density

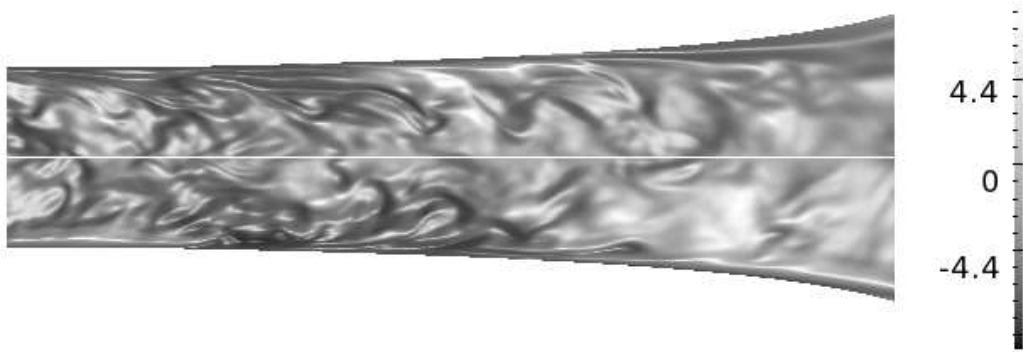


Figure 4.1: Axial velocity fluctuations (DNS), normalized with $u_\tau(x/L = 0)$, in a (x, r) -plane of the nozzle.

distribution. The momentum equation is then solved using a forward Euler finite difference approximation. Finally, the continuity equation is used to get the area distribution.

4.3 Instantaneous fields

Plots of the instantaneous axial velocity fluctuations clearly indicate the reduction in turbulence activity as we go downstream along the nozzle axis. Particularly, in figure 4.1, the near-wall ejection activity is dramatically reduced after about 70% of the nozzle length (L). This plot clearly indicates that the acceleration is gradual which is desired. The plots in a plane normal to the axis, emphasize the changes in the near-wall structure as we move downstream. For example, between $x/L = 0.1$ and $x/L = 0.5$ (figure 4.2) we notice a significant reduction of small-scale activity near the wall. This trend continues at $x/L = 0.88$ (fig. 4.3) where we see only large-scale turbulence activity. Please note that even at $x/L = 0.88$, the flow is not laminar- it shows a state of strongly attenuated turbulence.

4.4 Azimuthal spectra

The spectra of axial velocity fluctuations in the azimuthal direction (Figure 4.4) in the near-wall region show reduced energy at all wavenumbers in the DNS (as we move downstream) which indicates reduced turbulent activity in the buffer layer during the expansion in the nozzle. It should be noted that local density and viscosity are used to non-dimensionalize the spectra and wavenumbers.

4.5 Mean Profiles

The magnitude of acceleration can be judged from the value of the Clauser parameter $\beta = \frac{\delta^*}{\tau_w} \frac{d\bar{p}}{dx}$ which becomes relatively steady at a value of -1.6 after an initial transient

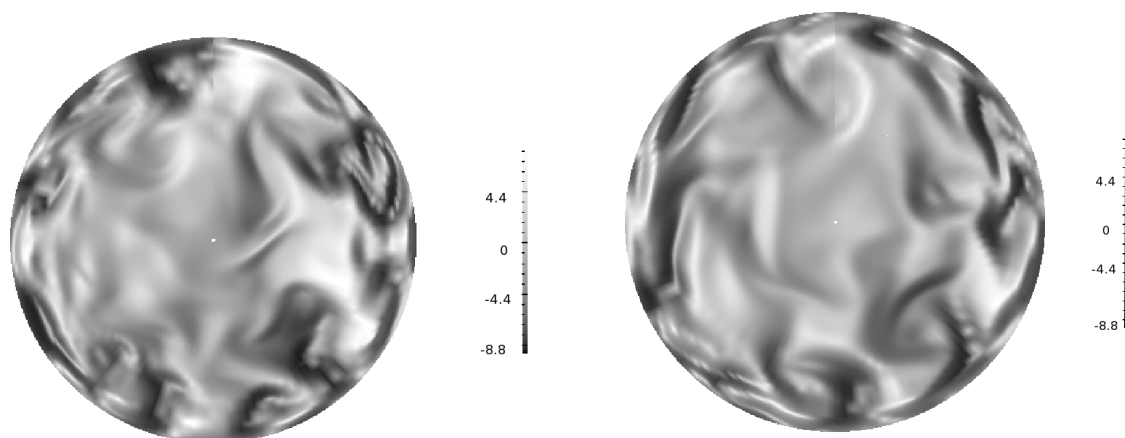


Figure 4.2: Axial velocity fluctuations (DNS), normalized with $u_\tau(x/L = 0)$, in a (r, ϕ) -plane of the nozzle. Left: $x/L = 0.1$, right: $x/L = 0.5$

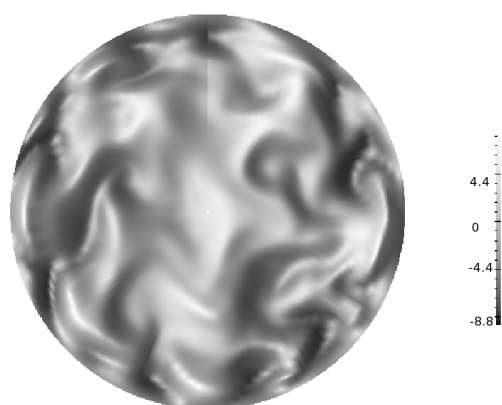


Figure 4.3: Axial velocity fluctuations (DNS), normalized with $u_\tau(x/L = 0)$, in a (r, ϕ) -plane at $x/L = 0.88$

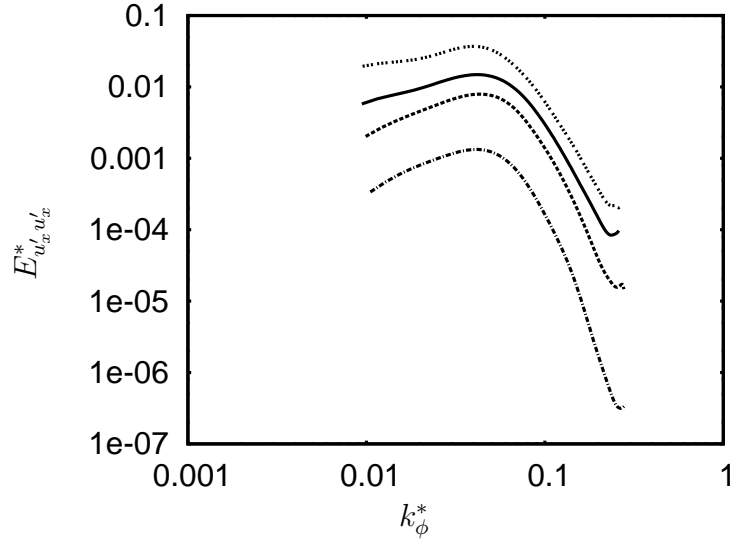


Figure 4.4: Energy spectra (DNS) of axial velocity fluctuations in the near-wall region ($y^* = 10$) in the azimuthal direction. $x/L = \dots \dots 0.0$; — 0.25; — — — 0.5; -.-.- 0.8

(Figure 4.5). This weak acceleration leads to a gradual increase of bulk velocity up to about 40% of the incoming value.

Centerline distributions of mean pressure, local Mach number, mean density and temperature show close agreement with the solutions of isentropic streamtube equations (Figure 4.6). This means that as expected from one dimensional, inviscid analysis of flows dominated by expansion, non-isentropic effects are negligible in regions where frictional effects are small, like in the core region of this flow. The flow accelerates from a local Mach number of 1.5 to around 2.3 (at the end of the nearly constant acceleration region). Figure 4.6 also shows the axial variation of the nozzle cross-section.

Radial pressure gradients remain small in this flow as in the incoming supersonic pipe flow. This is clearly evident from the plots of wall and centerline pressure, in which the wall pressure profile follows closely that of the centerline (figure 4.7). The weak oscillations which appear in the centerline pressure profile when the flow first encounters the expansion are damped in the near-wall region. The wall shear stress first increases at the beginning of the acceleration and then shows a slow decrease (figure 4.7). The displacement thickness δ^* increases in the region where the wall shear decreases (figure 4.8). Such behaviour has also been reported in supersonic boundary layers by Spina *et al.* (1994). They attribute this counterintuitive behaviour to the axial variation of near-wall density. The momentum thickness θ remains more or less unaltered which means that the shape factor $H = \delta^*/\theta$ follows the behaviour of δ^* . These quantities clearly bring out the non-equilibrium nature of the flow.

Figure 4.9 shows radial profiles of mean density and temperature. It is clear that acceleration leads to nearly isentropic cooling of the flow in the core region, where effects of viscous dissipation by the mean flow are negligibly small. Since the radial pressure gradient is small, the decrease in T leads to an increase in the mean density ratio, $\bar{\rho}/\bar{\rho}_w$. In

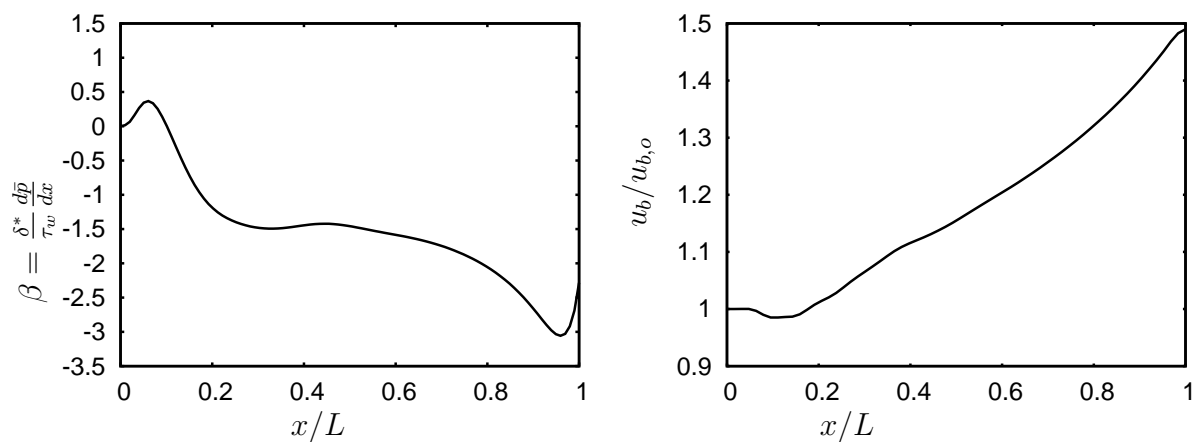


Figure 4.5: Axial variation of Clauser parameter (β) and bulk velocity. $u_{b,o}$: bulk velocity at $x/L = 0$ (LES)

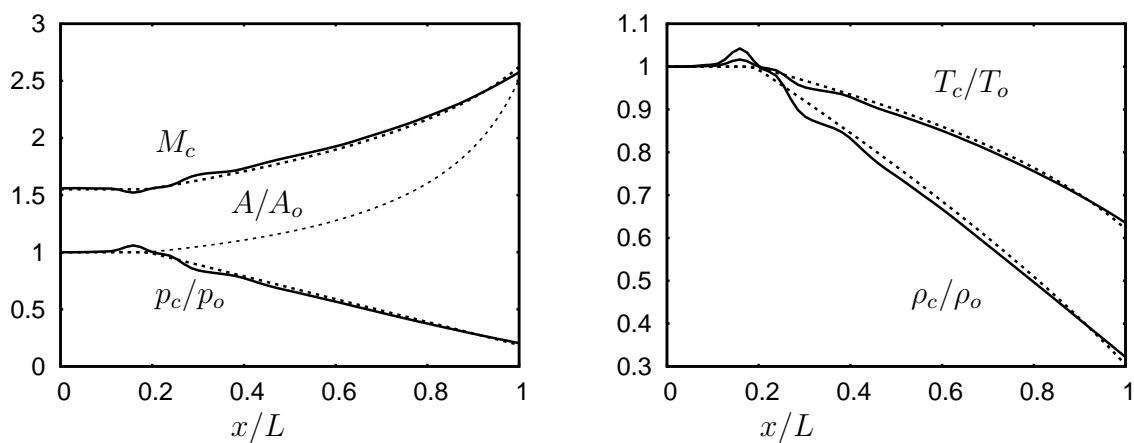


Figure 4.6: Centerline pressure, local Mach number, area distributions; Centerline density and temperature distributions from the LES. Subscript 'o' denotes values at $x/L = 0$. Dashed lines are the solutions of isentropic streamtube equations.

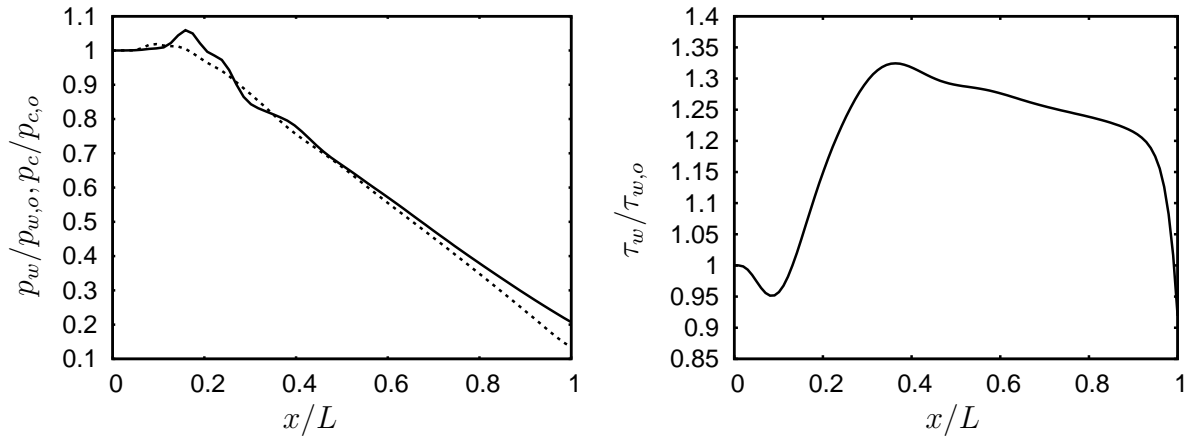


Figure 4.7: Centerline (solid line) and wall (dashed line) pressure and wall shear stress (LES) profiles.

the near-wall region, heating due to viscous dissipation causes an increase in temperature and a corresponding decrease in density and hence typical peaks appear in these profiles near the wall in the later stages of expansion. Figure 4.9 also shows good agreement between DNS (symbols) and LES data (lines) for mean density and temperature profiles for this flow case.

Due to acceleration, dissipation of the mean flow goes down marginally (figure 4.9), but the effect on turbulent dissipation is more spectacular as seen in the profiles of solenoidal dissipation rate in the TKE equation (figure 4.10). Nevertheless, the reduction in mean temperature in the near-wall region of the nozzle is largely due to reduced dissipation of the mean flow. It is to be noted here that we did not notice substantial baroclinic effects in the solenoidal dissipation rate equation, when we checked our DNS data. Such effects have been investigated and modelled by Kreuzinger *et al.* (2006). So, the reduction of solenoidal dissipation is an effect of mean dilatation in accelerated flow, which appears in production terms in the solenoidal dissipation rate equation.

The mean dilatation produced in this nozzle is seen in figure 4.10, where it increases strongly in the wall layer. The effects of mean dilatation on turbulence structure will be shown when we analyse the production terms in the individual Reynolds stress equations (Section 4.9).

The extra strain rate $\frac{\partial \tilde{u}_x}{\partial x}$ in this flow case is still limited to about 6% of the wall shear rate $\frac{\partial \tilde{u}_x}{\partial r}|_w$ in the peak production zone $y/R = 0.1$ (figure 4.11).

The radial Mach number profiles show the gradual acceleration occurring in the flow and also that the mean sonic line shifts towards the wall (figure 4.11) as we move downstream.

The strong mean density variation in the axial direction coupled with the variation in wall shear stress leads to the failure of the Van Driest transformation for mean axial velocity in the fully turbulent region (figure 4.12). The profiles show a collapse in the near-wall region since we used local values of density and viscosity for the scaling. Similar

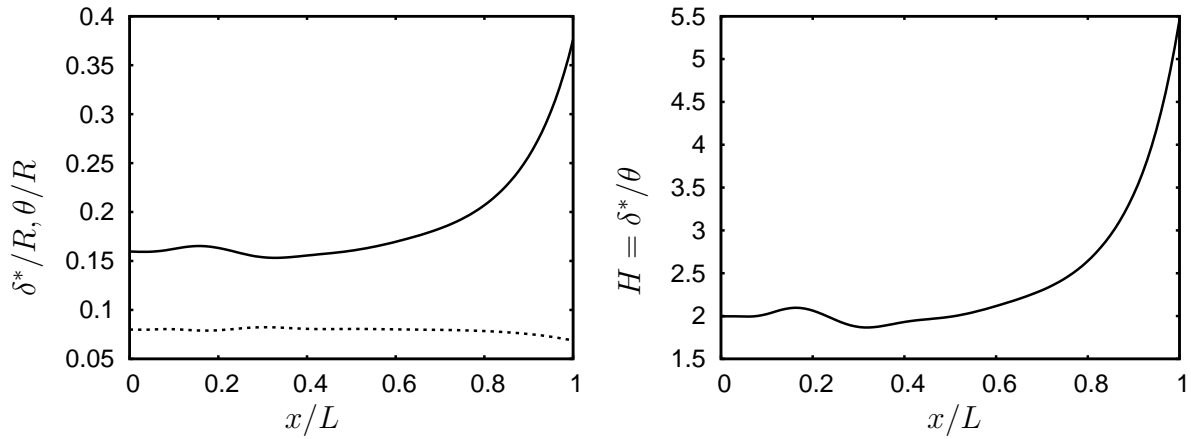


Figure 4.8: Displacement (solid line), momentum thickness (dashed line) and Shape factor

effects have been observed in DNS of strongly heated, accelerated incompressible pipe flows by Bae *et al.* (2006).

4.6 Rms profiles

The acceleration in the nozzle also causes a strong decrease in density and temperature and a weaker decrease in pressure fluctuations (figures 4.12, 4.13). The decay in temperature fluctuations is a result of the reduced mean temperature gradient. The reduced density fluctuations could be due to the reduced mean density gradient and due to the mean dilatation which appear as explicit source terms in the density variance equation (Hamba, 1999). The reduction in pressure fluctuations is difficult to analyse, since pressure fluctuations cannot be unambiguously split into thermodynamic and hydrodynamic parts, where the latter is due to velocity fluctuations. A clear answer can only be given based on an equation for the pressure fluctuations, derived from the divergence of the momentum equation and the continuity equation. Further studies in this direction involving the analysis of a Poisson equation for the pressure fluctuations are part of future work.

The near wall density-temperature correlation is weakly affected (figure 4.14) by the expansion. $R_{\rho T}$ now shows marginally lower negative values than in the supersonic pipe flow. However, the pressure-density correlation, $R_{p\rho}$, shows higher positive values in the near-wall region. This means that near-wall non-isentropic effects are somewhat lower under acceleration, as already confirmed by the reduced turbulent dissipation rate.

An interesting feature is noticed in the profiles of velocity-temperature correlation, R_{uT} which show a strong decay in the near-wall region during the later stages of acceleration (figure 4.15). This is expected from the mean temperature profiles in the near-wall region. Thus modified strong Reynolds analogies (MSRA) which have been shown to work for isothermal channel and pipe flows would not work in this case. It will be shown in the next chapter on diffusers, that near-wall temperature and velocity fluctuations continue to be correlated in that case and MSRAs might be used there.

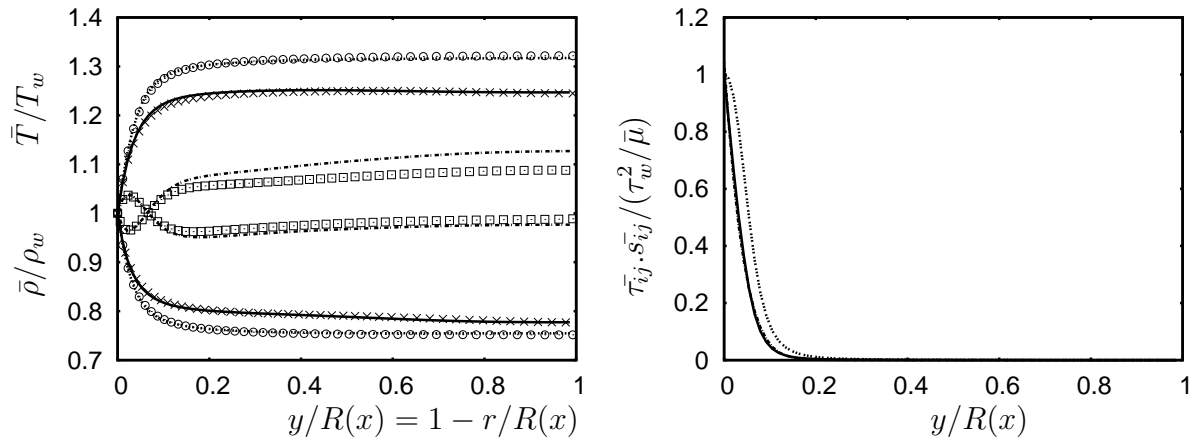


Figure 4.9: Profiles of mean density, temperature, normalized with values at the wall, and dissipation rate of the mean flow. $x/L = \dots \dots 0.0$; — 0.45, -.-.- 0.8. Symbols represent DNS results at the corresponding x/L locations.

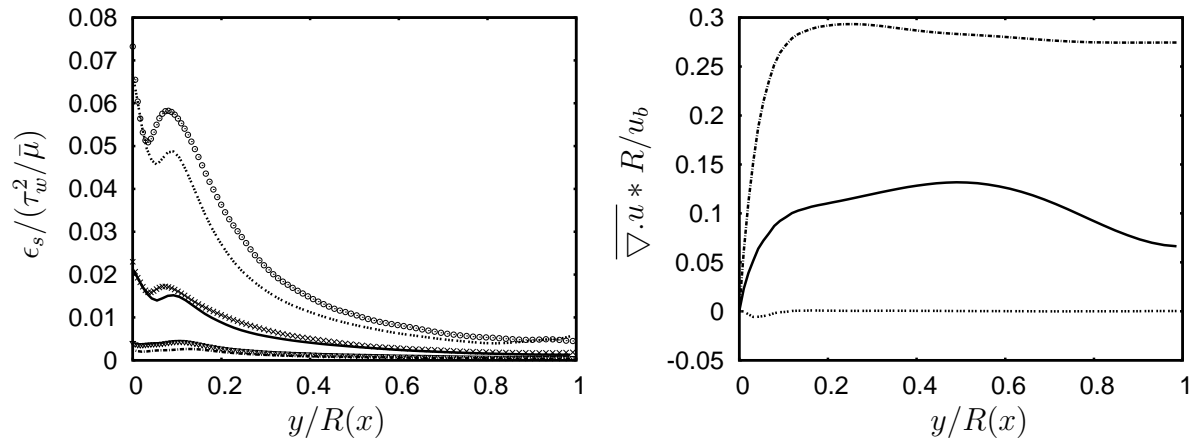


Figure 4.10: Solenoidal dissipation rate and mean dilatation. Line types as in fig. 4.9. Symbols represent DNS results at the corresponding x/L locations.

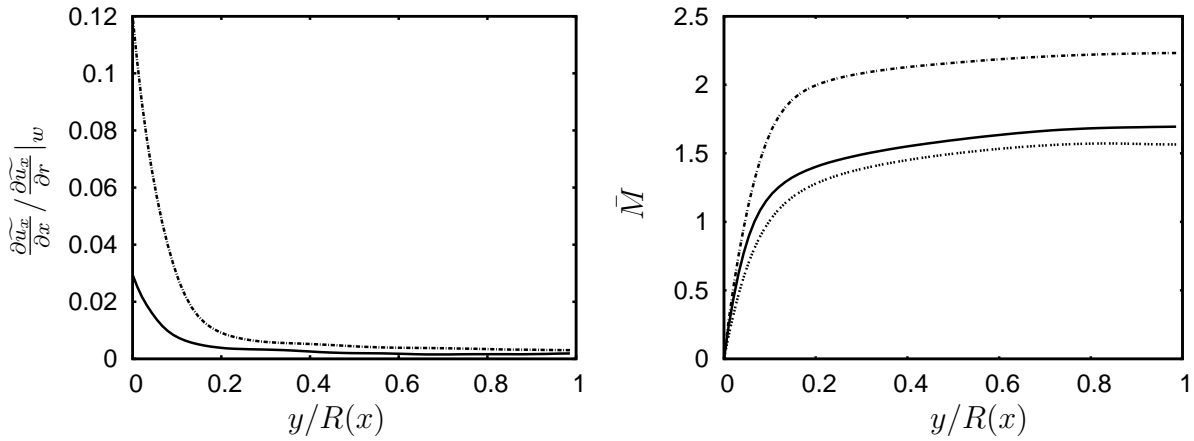


Figure 4.11: Extra strain rate versus wall shear rate and local Mach number. Line types as in fig. 4.9

The turbulent Mach number, M_t , decreases in this flow case which is due to the lower turbulence activity as a result of acceleration of the flow (figure 4.15). Now, since M_t has a low subsonic value, effects due to dilatational fluctuations are negligible. This is confirmed by the peak values of the dilatational dissipation rate (ϵ_d) which is limited to 0.2% of the solenoidal dissipation rate (ϵ_s) in the peak production region. ϵ_d , normalized with $\tau_w^2/\bar{\mu}$ (figure 4.16), decays consistently along the nozzle, reflecting the decaying velocity fluctuations. The pressure dilatation correlation ($\overline{p'u'_{i,i}}$) is limited to less than 4% of ϵ_s in the near-wall region and remains less than 0.01% of $\tau_w^2/\bar{\mu}$ at $x/L = 0.45$ and 0.8 . Hence, intrinsic compressibility effects due to dilatational fluctuations can be neglected in this flow case.

Acceleration of the flow results in a reduction of fluctuations of all velocity components. The 'inner', semi-local scaling which was shown to work well for the supersonic pipe flow, fails in this case as can be seen in figures 4.17 and 4.18 since the scaling does not take care of acceleration effects. The peak locations show a collapse, but their magnitudes differ widely. Thus the effects of mean dilatation (or a negative pressure gradient) are indeed substantial on the turbulence structure near the wall.

4.7 Reynolds stresses

The normal and shear components of the Reynolds stress tensor are now shown in 'outer scaling' where the stresses are normalized using wall shear stress (figures 4.19-4.22). Such a scaling is justified in case of incompressible and compressible parallel flows, as was shown using the streamwise momentum equation in Chapter 3. In flows where axial pressure gradients exist, such a scaling cannot work, even if the axial inhomogeneity is small. This is verified here for the Reynolds stress profiles. All components show strong decay in the nozzle flow, both in near-wall and core regions. The overshoot of the LES profiles for $\overline{\rho u_x'' u_x''}$ over those of DNS in the near-wall region is a result of the LES procedure applied

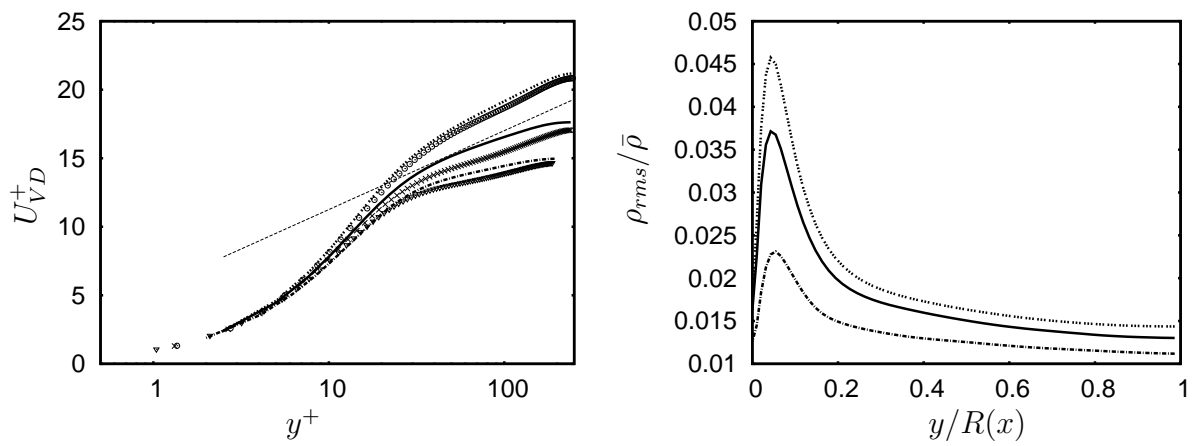


Figure 4.12: Van Driest transformed mean velocity, rms density fluctuations. Line types as in fig. 4.9. Symbols represent DNS results at the corresponding x/L locations.

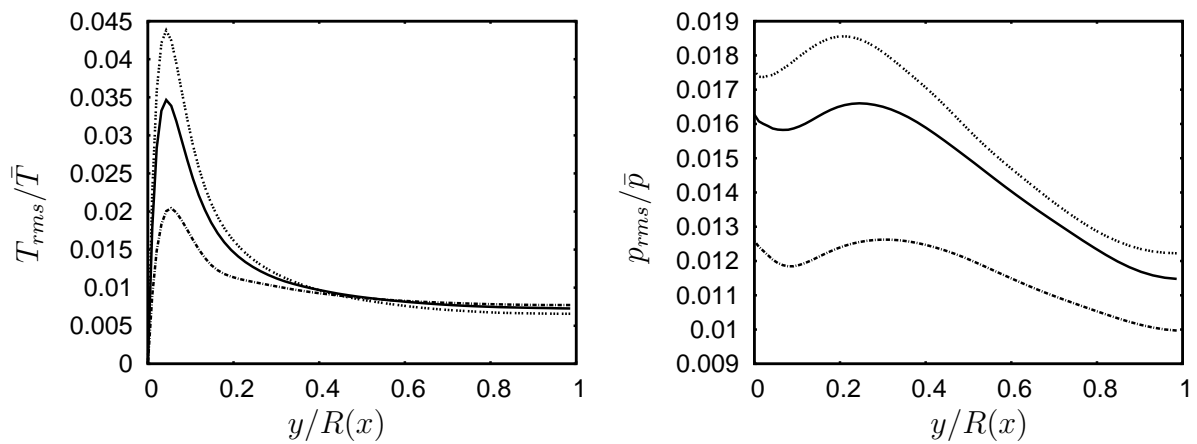


Figure 4.13: Rms temperature and pressure fluctuations. Line types as in fig. 4.9

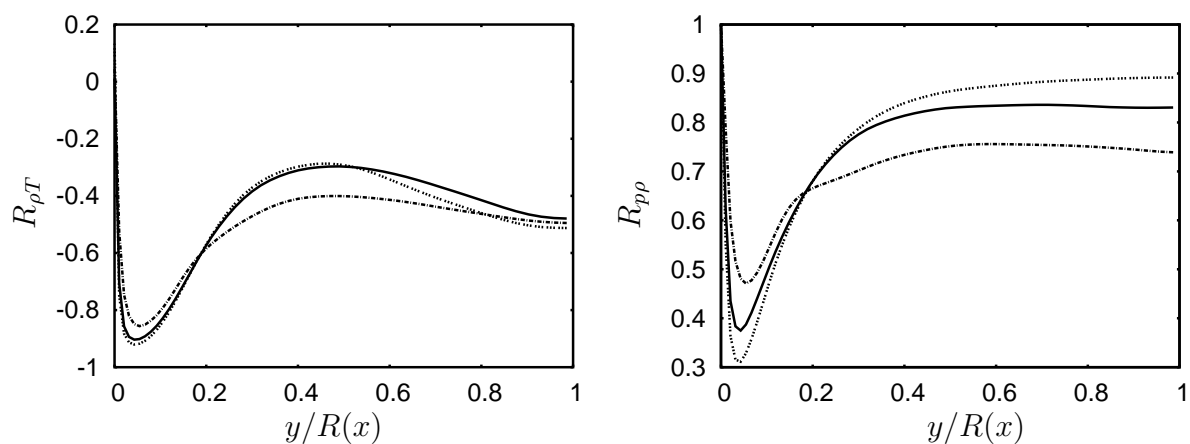


Figure 4.14: Density-temperature and pressure-density correlations. Line types as in fig. 4.9

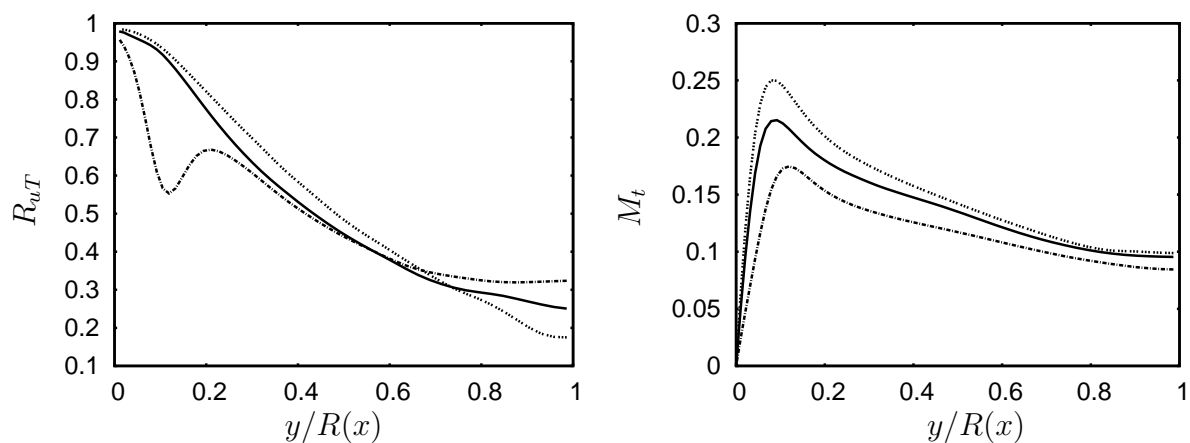


Figure 4.15: Velocity-temperature correlations, Turbulent Mach number. Line types as in fig. 4.9

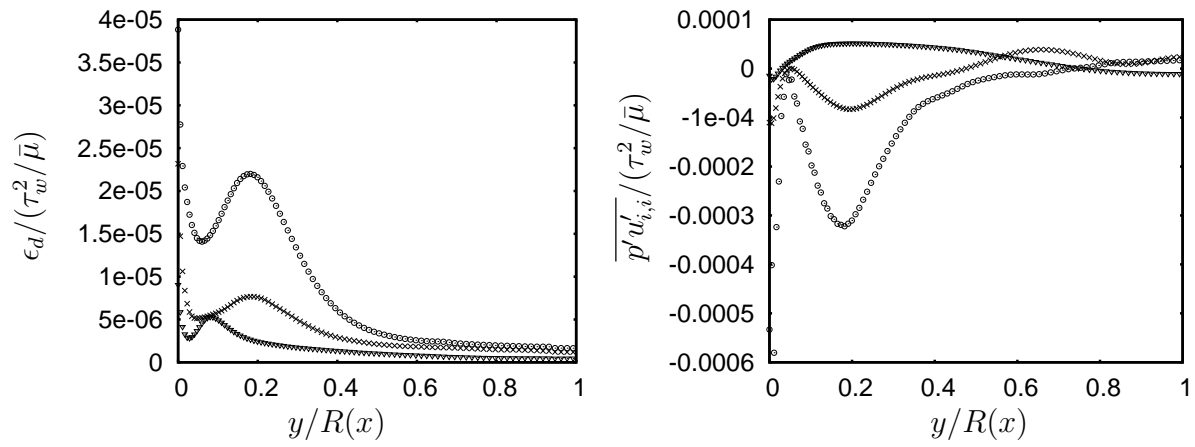


Figure 4.16: Compressible dissipation rate and pressure-dilatation correlation (DNS).
 \odot , $x/L = 0$; \times , $x/L = 0.5$; ∇ , $x/L = 0.8$

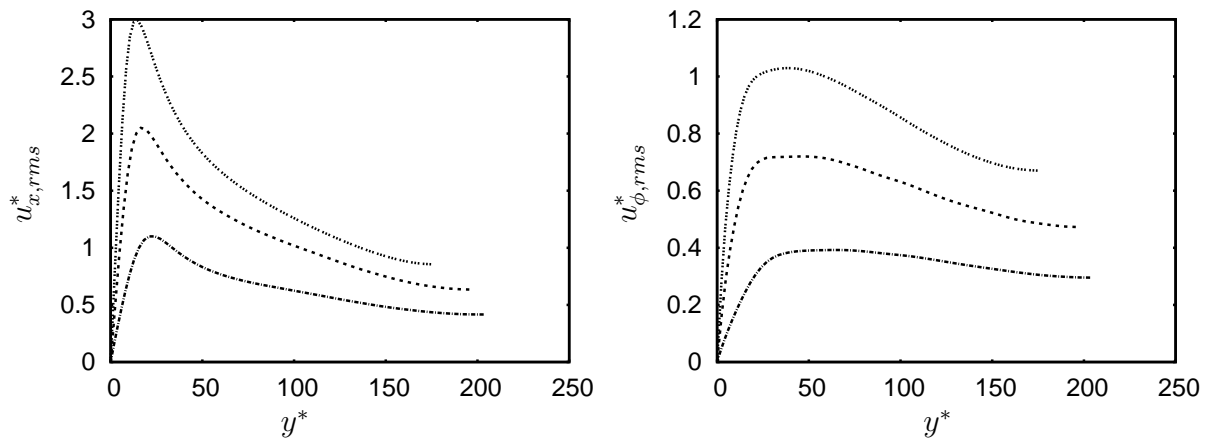


Figure 4.17: Rms velocity fluctuations in 'semi-local', inner scaling. Line types as in fig. 4.9

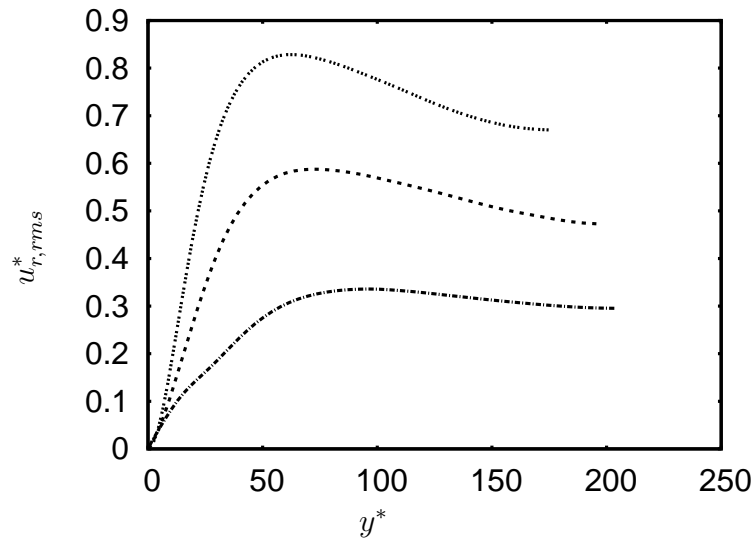


Figure 4.18: Rms velocity fluctuations, 'semi-local', inner scaling. Line types as in fig. 4.9

here which has no provision to take care of local strong anisotropies in the flow.

We now analyse the Reynolds stress transport equations to find out the reasons which lead to such strong decay of all components of the Reynolds stress tensor.

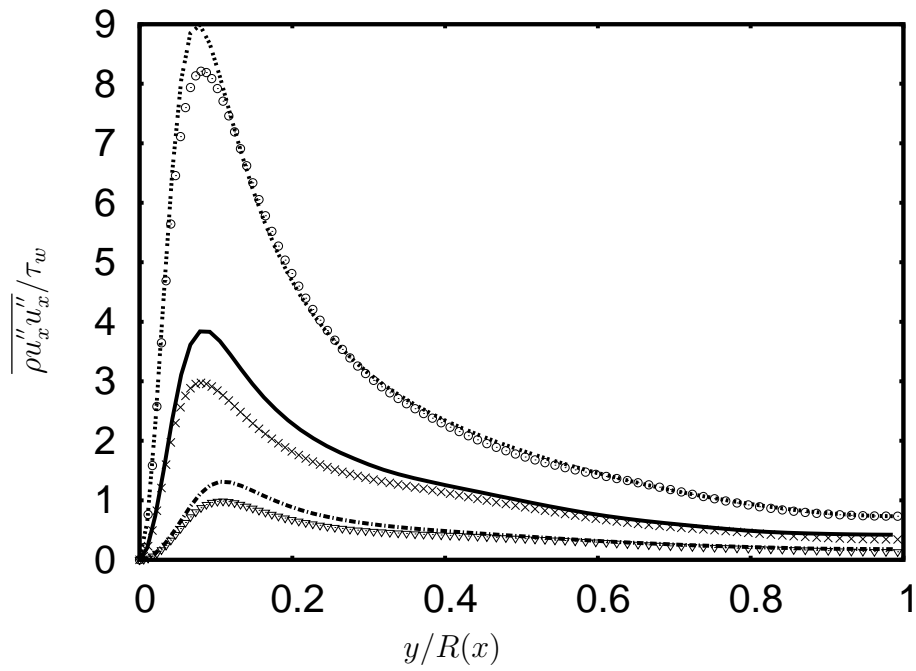


Figure 4.19: Axial Reynolds stress in outer scaling. Line types as in fig. 4.9. Symbols represent DNS results.

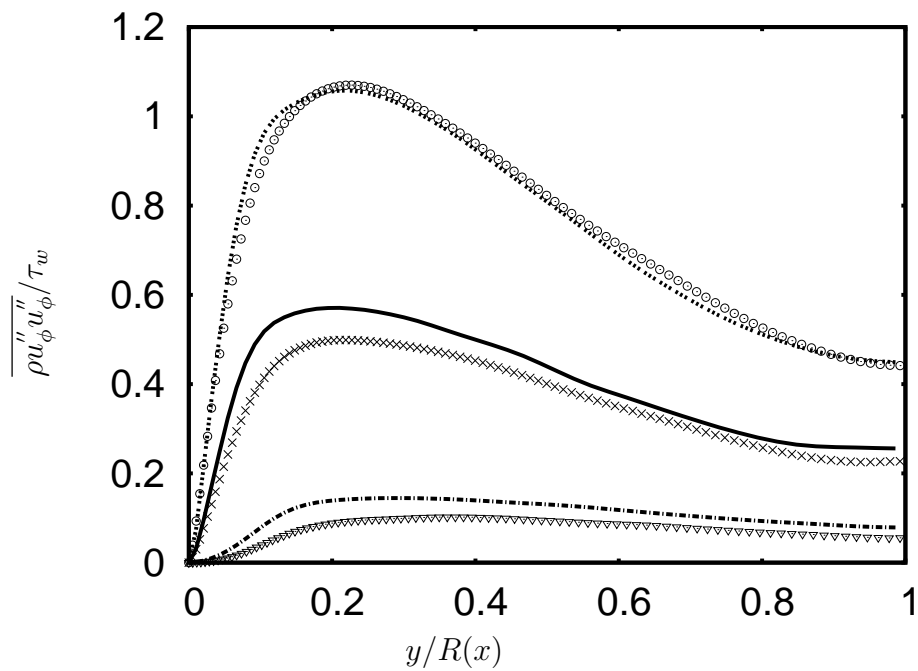


Figure 4.20: Azimuthal Reynolds stress in outer scaling. Line types as in fig. 4.9. Symbols represent DNS results.

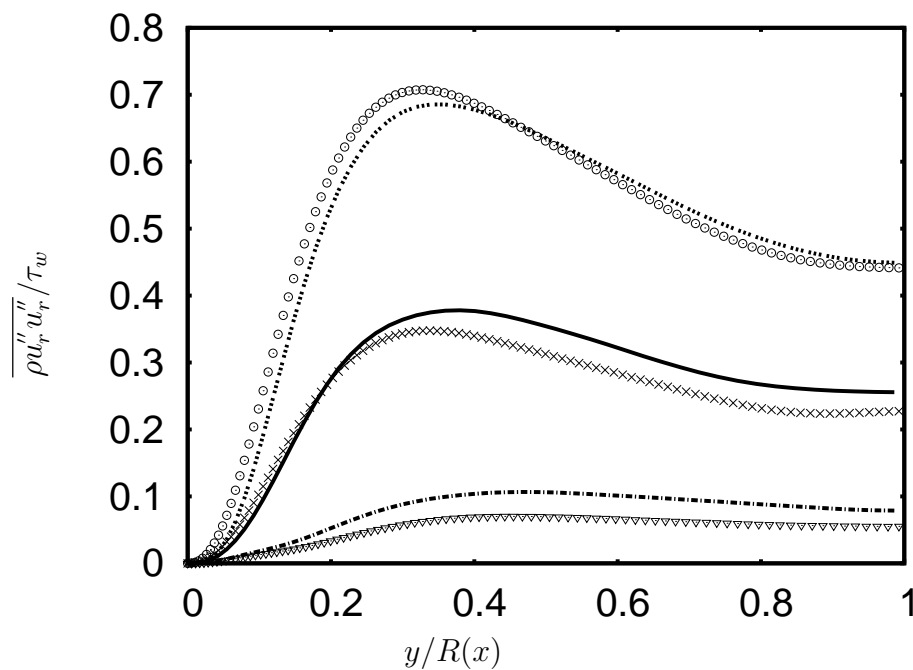


Figure 4.21: Radial Reynolds stress in outer scaling. Line types as in fig. 4.9. Symbols: DNS

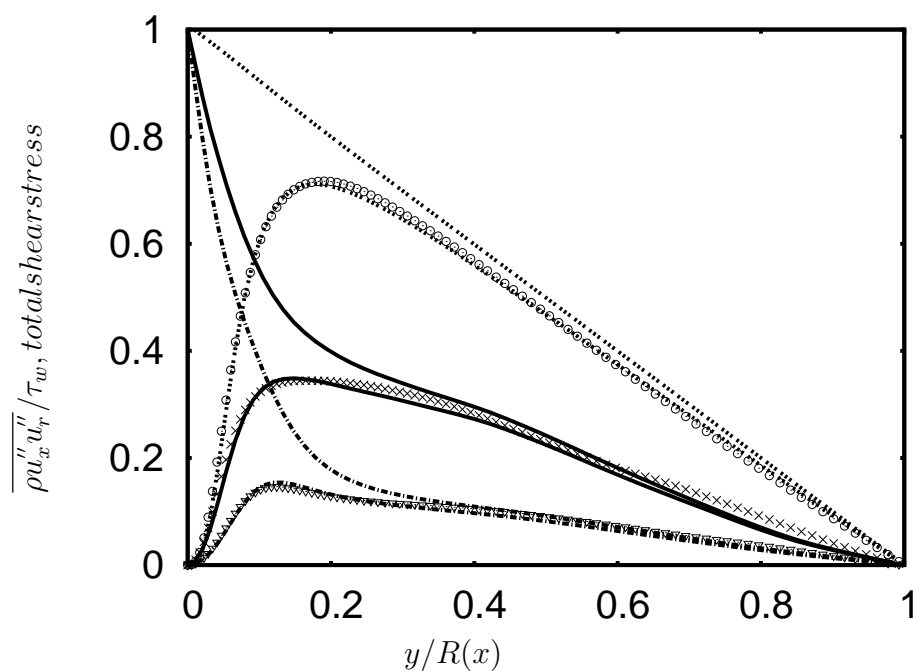


Figure 4.22: Reynolds shear stress and total shear stress, outer scaling. Line types as in fig. 4.9. Symbols: DNS

4.8 Reynolds stress budgets

The Reynolds stress transport equations are now written in a cylindrical coordinate system, allowing for axial inhomogeneity of the flow. This coordinate system differs weakly from our computational coordinate system which is non-orthogonal. Since the angle of divergence is small (max 10 degrees near the nozzle outlet), a discussion of transport mechanisms in an (x, ϕ, r) -coordinate system makes sense. The equations for the normal and shear Reynolds stress components are:

$$\begin{aligned}
\frac{\partial \bar{\rho} \widetilde{u_x'' u_x''}}{\partial t} = & -2\bar{\rho} \widetilde{u_x'' u_r''} \frac{\partial \widetilde{u_x}}{\partial r} - 2\bar{\rho} \widetilde{u_x'' u_x''} \frac{\partial \widetilde{u_x}}{\partial x} & P \\
& -\frac{1}{r} \frac{\partial r \overline{\rho u_r'' u_x'' u_x''}}{\partial r} - \frac{\overline{\partial \rho u_x'' u_x'' u_x''}}{\partial x} & TD \\
& -\frac{1}{r} \frac{\partial r \widetilde{u_r} \overline{\rho u_x'' u_x''}}{\partial r} - \frac{\partial \widetilde{u_x} \overline{\rho u_x'' u_x''}}{\partial x} & MT \\
& +\frac{2}{r} \frac{\partial r \overline{\tau'_{xr} u_x''}}{\partial r} + 2 \frac{\partial \overline{\tau'_{xx} u_x''}}{\partial x} & VD \\
& -2\overline{\tau'_{xx} \frac{\partial u_x''}{\partial x}} - 2\overline{\tau'_{xr} \frac{\partial u_x''}{\partial r}} - 2\overline{\tau'_{x\theta} \frac{1}{r} \frac{\partial u_x''}{\partial \theta}} & DS \\
& +2\overline{p' \frac{\partial u_x''}{\partial x}} & PS \\
& -2 \frac{\partial \overline{p' u_x''}}{\partial x} & PD \\
& +2\overline{u_x''} \left(\frac{1}{r} \frac{\partial r \overline{\tau_{xr}}}{\partial r} - \frac{\partial \bar{p}}{\partial x} + \frac{\partial \overline{\tau_{xx}}}{\partial x} \right) & M
\end{aligned} \tag{4.1}$$

$$\begin{aligned}
\frac{\partial \bar{\rho} \widetilde{u_\theta'' u_\theta''}}{\partial t} = & -\frac{2}{r} \widetilde{u_r} \overline{\rho u_\theta'' u_\theta''} & P \\
& -\frac{1}{r} \frac{\partial r \overline{\rho u_r'' u_\theta'' u_\theta''}}{\partial r} - \frac{\overline{\partial \rho u_x'' u_\theta'' u_\theta''}}{\partial x} & TD \\
& -\frac{1}{r} \frac{\partial r \widetilde{u_r} \overline{\rho u_\theta'' u_\theta''}}{\partial r} - \frac{\partial \widetilde{u_x} \overline{\rho u_\theta'' u_\theta''}}{\partial x} & MT \\
& +\frac{2}{r} \frac{\partial r \overline{\tau'_{r\theta} u_\theta''}}{\partial r} + \frac{\partial \overline{\tau'_{x\theta} u_\theta''}}{\partial x} & VD \\
& -2\overline{\tau'_{x\theta} \frac{\partial u_\theta''}{\partial x}} - 2\overline{\tau'_{r\theta} \frac{\partial u_\theta''}{\partial r}} - 2\overline{\tau'_{\theta\theta} \frac{1}{r} \frac{\partial u_\theta''}{\partial \theta}} + 2 \frac{\overline{u_\theta'' \tau_{\theta r}}}{r} & DS \\
& +2\overline{p' \frac{1}{r} \frac{\partial u_\theta''}{\partial \theta}} & PS \\
& -\frac{2}{r} \overline{(\rho u_\theta'' u_\theta'' u_r'')} & CR \\
& +2\overline{u_\theta''} \left(\frac{1}{r} \frac{\partial r \overline{\tau_{\theta r}}}{\partial r} + \frac{\partial \overline{\tau_{\theta x}}}{\partial x} \right) & M
\end{aligned} \tag{4.2}$$

$$\begin{aligned}
\frac{\partial \bar{\rho} \widetilde{u_r'' u_r''}}{\partial t} = & -2 \bar{\rho} \widetilde{u_r'' u_r''} \frac{\partial \widetilde{u_r}}{\partial r} - 2 \bar{\rho} \widetilde{u_r'' u_x''} \frac{\partial \widetilde{u_r}}{\partial x} & P \\
& - \frac{1}{r} \frac{\partial r \overline{\rho u_r'' u_r'' u_r''}}{\partial r} - \frac{\partial \overline{\rho u_r'' u_r'' u_x''}}{\partial x} & TD \\
& - \frac{1}{r} \frac{\partial r \widetilde{u_r} \overline{\rho u_r'' u_r''}}{\partial r} - \frac{\partial \widetilde{u_x} \overline{\rho u_r'' u_r''}}{\partial x} & MT \\
& - \frac{2}{r} \frac{\partial r p' u_r''}{\partial r} + \frac{2}{r} \frac{\partial r \tau_{rr}' u_r''}{\partial r} + \frac{\partial \tau_{xr}' u_r''}{\partial x} & PD/VD \\
& - 2 \tau_{rx}' \frac{\partial u_r''}{\partial x} - 2 \tau_{rr}' \frac{\partial u_r''}{\partial r} - 2 \tau_{r\theta}' \frac{1}{r} \frac{\partial u_r''}{\partial \theta} - 2 \frac{\overline{u_r'' \tau_{\theta\theta}}}{r} & DS \\
& + 2 p' \frac{1}{r} \frac{\partial r u_r''}{\partial r} & PS \\
& + \frac{2}{r} \overline{(\rho u_\theta'' u_\theta'' u_r'')} & CR \\
& + 2 \bar{u}_r'' \left(\frac{1}{r} \frac{\partial r \tau_{rr}^-}{\partial r} - \frac{\partial \bar{p}}{\partial r} + \frac{\partial \tau_{xr}^-}{\partial x} \right) & M
\end{aligned} \tag{4.3}$$

$$\begin{aligned}
\frac{\partial \bar{\rho} \widetilde{u_x'' u_r''}}{\partial t} = & - \bar{\rho} \widetilde{u_x'' u_x''} \frac{\partial \widetilde{u_r}}{\partial x} - \bar{\rho} \widetilde{u_x'' u_r''} \frac{\partial \widetilde{u_x}}{\partial x} - \bar{\rho} \widetilde{u_x'' u_r''} \frac{\partial \widetilde{u_r}}{\partial r} - \bar{\rho} \widetilde{u_r'' u_r''} \frac{\partial \widetilde{u_x}}{\partial r} & P \\
& - \frac{\partial \overline{\rho u_x'' u_x'' u_r''}}{\partial x} - \frac{1}{r} \frac{\partial r \overline{\rho u_r'' u_x'' u_r''}}{\partial r} & TD \\
& - \frac{\partial \widetilde{u_x} \overline{\rho u_x'' u_r''}}{\partial x} - \frac{1}{r} \frac{\partial r \widetilde{u_r} \overline{\rho u_x'' u_r''}}{\partial r} & MT \\
& - \frac{1}{r} \frac{\partial r p' u_x''}{\partial r} - \frac{\partial p' u_r''}{\partial x} & PD \\
& + \frac{\partial (\tau_{xx}' u_r'' + \tau_{xr}' u_x'')}{\partial x} + \frac{1}{r} \frac{\partial (r \tau_{xr}' u_r'' + r \tau_{rr}' u_x'')}{\partial r} & VD \\
& - \tau_{xx}' \frac{\partial u_r''}{\partial x} - \tau_{xr}' \frac{\partial u_r''}{\partial r} - \tau_{x\theta}' \frac{1}{r} \frac{\partial u_r''}{\partial \theta} \\
& - \tau_{rx}' \frac{\partial u_x''}{\partial x} - \tau_{rr}' \frac{\partial u_x''}{\partial r} - \tau_{r\theta}' \frac{1}{r} \frac{\partial u_x''}{\partial \theta} - \frac{\overline{u_x'' \tau_{\theta\theta}}}{r} & DS \\
& + p' \left(\frac{\partial u_r''}{\partial x} + \frac{1}{r} \frac{\partial r u_x''}{\partial r} \right) & PS \\
& + \frac{1}{r} \overline{(\rho u_\theta'' u_\theta'' u_x'')} & CR \\
& + \bar{u}_r'' \left(- \frac{\partial \bar{p}}{\partial x} + \frac{\partial \tau_{xx}^-}{\partial x} + \frac{1}{r} \frac{\partial r \tau_{xr}^-}{\partial r} \right) + \bar{u}_x'' \left(\frac{1}{r} \frac{\partial r \tau_{rr}^-}{\partial r} + \frac{\partial \tau_{xr}^-}{\partial x} - \frac{\partial \bar{p}}{\partial r} \right) & M
\end{aligned} \tag{4.4}$$

The following abbreviations have been used to name the terms on the right hand side.

P: Production
TD: Turbulent diffusion
MT: Mean convection

VD : Viscous diffusion
 PD : Pressure diffusion
 PS : Pressure-strain correlations
 CR : Cylindrical coordinate redistribution
 DS : Viscous dissipation
 M : Mass flux variation

Figures 4.23- 4.26 show the individual terms in the axial stress transport equation using local $\tau_w^2/\bar{\mu}$ as a scaling at four locations along the nozzle. We notice a strong decrease in the production term in the near-wall region. This is accompanied by decays in viscous dissipation and the pressure-strain correlations. The viscous diffusion terms naturally balance the dissipation at the wall. At all locations we notice reasonable balance between the major source and sink terms, except beyond $x/L = 0.8$. The mean convection term (MT) which was absent in the fully developed pipe flow is small but non-negligible in this flow case. Its magnitude increases marginally during the beginning of expansion and then gradually decreases from its increased upstream levels. It might be noted that the production term in the core region becomes negative during the later stages of expansion. We will explain this later in this chapter (Section 4.9).

A look at major source/sink contributions in the turbulent kinetic energy (TKE) budget at two axial locations $x/L = 0.4, 0.65$ reveals a lack of local equilibrium of the flow at these locations, in the sense that the production terms are not balanced by the corresponding dissipation terms (figures 4.27, 4.28). This is a consequence of the acceleration. The pressure-dilatation correlations and compressible dissipation rates are negligible at all positions.

4.9 Analysis of production terms

In the nozzle flow under investigation, enthalpic production $\overline{u'' \frac{\partial \bar{p}}{\partial x}}$ which appears in the axial Reynolds stress budget, is found to be negligible (not shown) when compared to kinetic production. We now analyse the kinetic production term in order to explain the reduction of turbulence in this flow. The production term of the axial Reynolds stress budget which is also the dominant production term in the TKE budget, is now shown in the local $\tau_w^2/\bar{\mu}$ scaling (figure 4.29). A large, abrupt decrease can be seen at the beginning of the expansion and then the profiles show a continuous reduction. One reason for the abrupt decrease at the beginning is the scaling using local τ_w which increases sharply in that region. This has been noted by Coleman *et al.* (2003) in their study of decelerated channel flow where they use the values at the channel inlet for the scaling. Another reason is the sudden decrease in Reynolds stresses when flow acceleration sets in. The production terms in the axial, radial and shear stress transport equations are now decomposed into parts showing explicit contributions of shear, extra rate of strain and mean dilatation:

$$P_{xx} = \underbrace{-\rho u_x'' u_r'' \frac{\partial \tilde{u}_x}{\partial r}}_{\text{shear}} - \underbrace{\frac{1}{3} \rho u_x'' u_x'' \frac{\partial \tilde{u}_l}{\partial x_l}}_{\text{mean dilatation}} - \underbrace{\rho u_x'' u_x'' \left(\frac{\partial \tilde{u}_x}{\partial x} - \frac{1}{3} \frac{\partial \tilde{u}_l}{\partial x_l} \right)}_{\text{extra rate of strain}}, \quad (4.5)$$

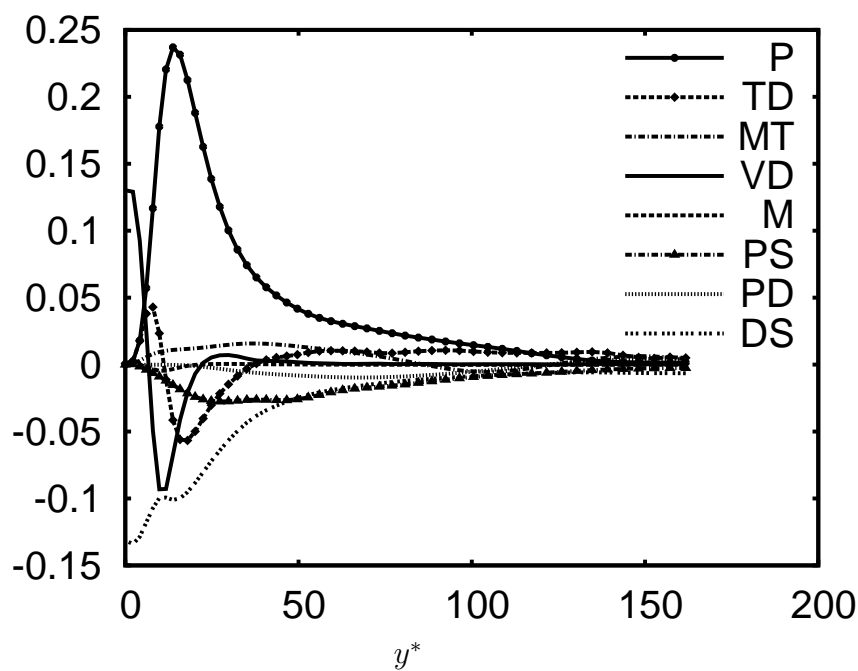


Figure 4.23: Axial Reynolds stress budget (LES) at $x/L = 0.1$, scaled with local $\tau_w^2/\bar{\mu}$.

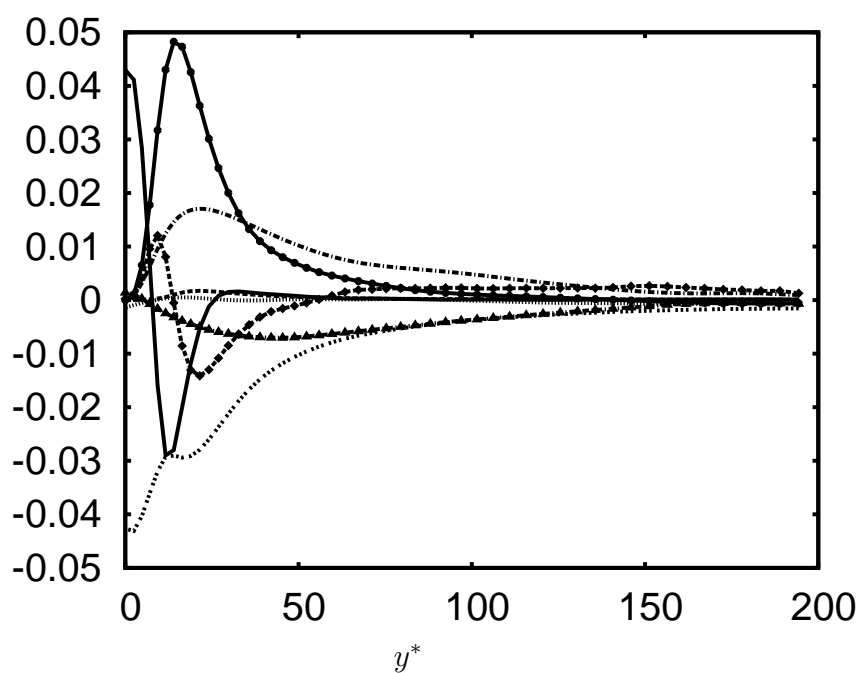


Figure 4.24: Axial Reynolds stress budget at $x/L = 0.4$, scaled with local $\tau_w^2/\bar{\mu}$. Line types as in fig. 4.23

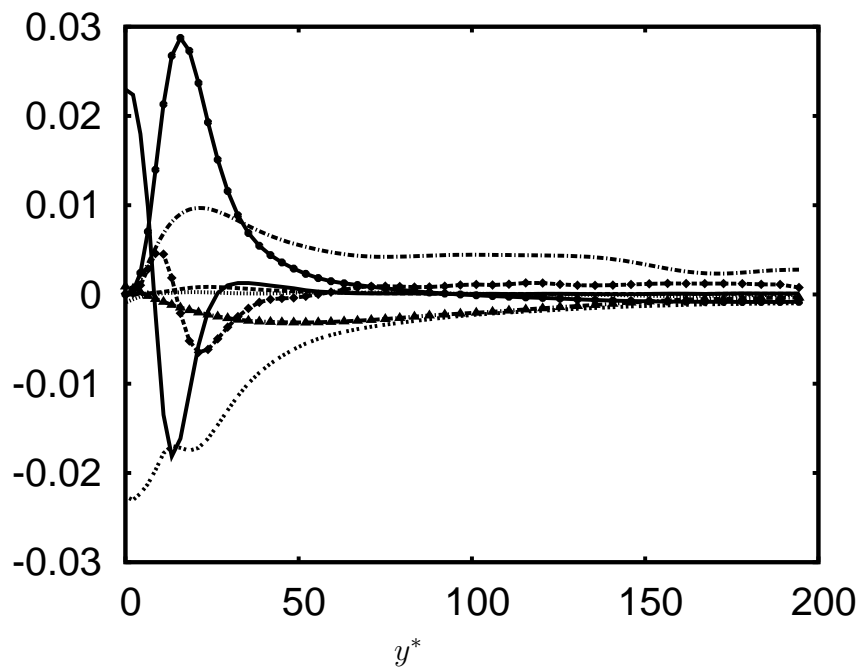


Figure 4.25: Axial Reynolds stress budget (LES) at $x/L = 0.65$, scaled with local $\tau_w^2/\bar{\mu}$. Line types as in fig. 4.23

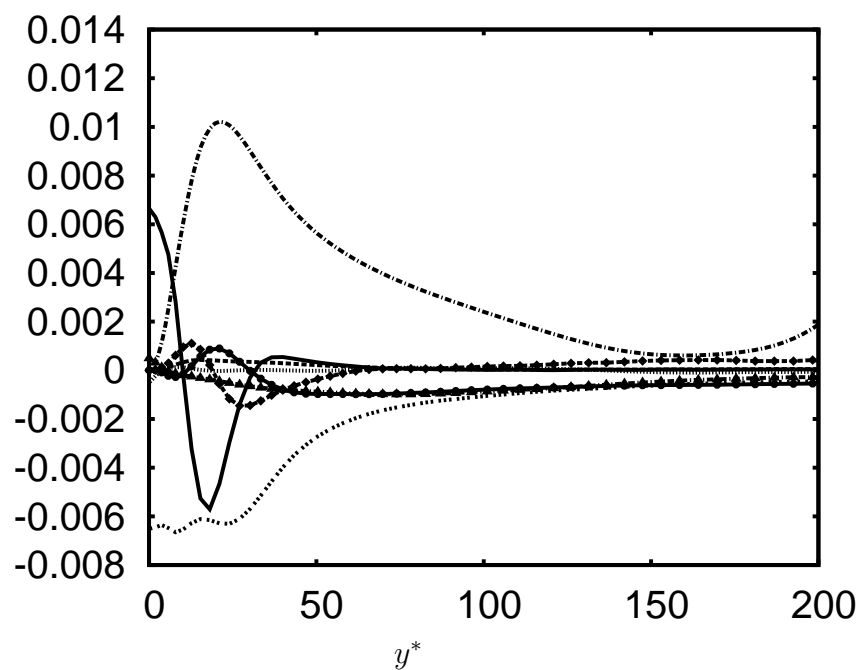


Figure 4.26: Axial Reynolds stress budget (LES) at $x/L = 0.8$, scaled with local $\tau_w^2/\bar{\mu}$. Line types as in fig. 4.23

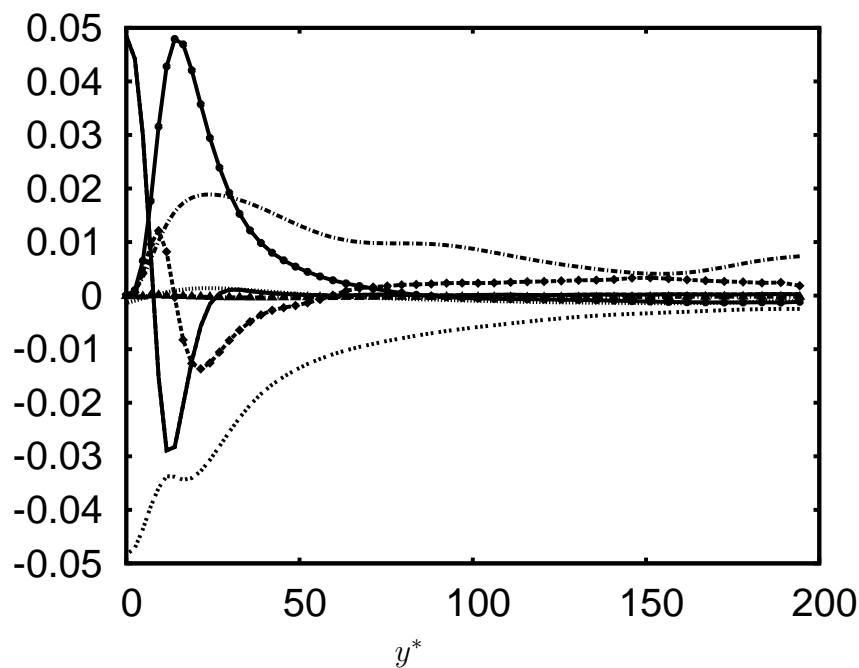


Figure 4.27: Terms in the TKE budget (LES) at $x/L = 0.4$, scaled with local $\tau_w^2/\bar{\mu}$. All line types as in fig. 4.23 except that for pressure-strain which here denotes pressure-dilatation correlations.

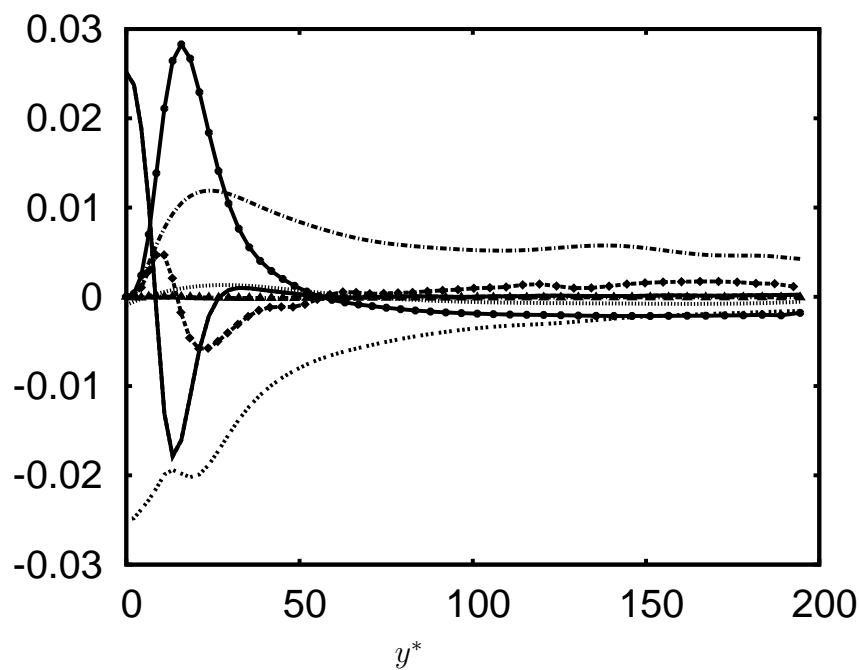


Figure 4.28: Terms in the TKE budget (LES) at $x/L = 0.65$, scaled with local $\tau_w^2/\bar{\mu}$. Line types as in fig. 4.27.

$$P_{xr} = \underbrace{-\overline{\rho u_r'' u_r''} \frac{\partial \tilde{u}_x}{\partial r}}_{shear1} - \underbrace{\overline{\rho u_x'' u_x''} \frac{\partial \tilde{u}_r}{\partial x}}_{shear2} - \underbrace{\frac{2}{3} \overline{\rho u_x'' u_r''} \frac{\partial \tilde{u}_l}{\partial x_l}}_{mean\ dilatation} - \underbrace{\overline{\rho u_x'' u_r''} \left(\frac{\partial \tilde{u}_x}{\partial x} + \frac{\partial \tilde{u}_r}{\partial r} - \frac{2}{3} \frac{\partial \tilde{u}_l}{\partial x_l} \right)}_{extra\ rate\ of\ strain}, \quad (4.6)$$

$$P_{rr} = \underbrace{-\overline{\rho u_x'' u_r''} \frac{\partial \tilde{u}_r}{\partial x}}_{shear} - \underbrace{\frac{1}{3} \overline{\rho u_r'' u_r''} \frac{\partial \tilde{u}_l}{\partial x_l}}_{mean\ dilatation} - \underbrace{\overline{\rho u_r'' u_r''} \left(\frac{\partial \tilde{u}_r}{\partial r} - \frac{1}{3} \frac{\partial \tilde{u}_l}{\partial x_l} \right)}_{extra\ rate\ of\ strain}. \quad (4.7)$$

As seen in figure 4.30 where we have plotted the contributions to P_{xx} at $x/L = 0$ and 0.45, the shear part is the dominant axial stress production mechanism, which is counteracted in the nozzle flow by the parts containing extra rate of strain and mean dilatation. The extra rate of strain has a larger negative contribution at $x/L = 0.45$ than the mean dilatation part. It is clear that the large changes in the shear part is primarily responsible for the changes in the axial production term.

In figures 4.32 and 4.33, we show the decomposition of the axial production term at $x/L = 0.65, 0.8$ to clarify that the small negative values of the total production term in the core region, seen in the axial stress budgets, is due to the dilatation part since in the core the extra strain and shear parts nearly balance each other. This effect is larger at $x/L = 0.8$ since the mean dilatation is larger there.

A detailed look at the shear part of P_{xx} is now necessary because of its dominant effect on production of the axial Reynolds stress. As seen in figure 4.34, changes in the normalized mean shear $\frac{\partial \tilde{u}_x}{\partial r}$ in the axial direction are negligible. So, the changes in $\overline{\rho u_x'' u_r''}$ are clearly responsible for the changes in the shear part of P_{xx} .

The decomposition of the production term in the shear stress transport equation (figure 4.31) shows that the first part (*shear1, sh1*) is dominant. The changes of $\overline{\rho u_x'' u_r''}$ term affect the evolution of $\overline{\rho u_x'' u_r''}$. Now, this term is controlled only by changes in $\overline{\rho u_r'' u_r''}$ since the mean shear was shown to remain nearly unchanged.

The dominant source mechanism in the radial stress budget is the redistributive pressure-strain correlation term. The production terms appearing in this equation remain negligible compared to the pressure-strain term. As seen in figures 4.35 and 4.36, the decrease in axial and hence, in radial pressure-strain correlations is drastic which brings about the decay in the radial stress and hence in the shear stress and ultimately in the axial stress. Thus, the pressure-strain term is clearly identified as the dominant agent which causes such drastic changes in the Reynolds stresses. Large decays are observed both in pressure fluctuations and velocity gradient fluctuations. It remains to be shown whether the pressure fluctuations are affected by the longitudinal density gradient, the mean dilatation or both.

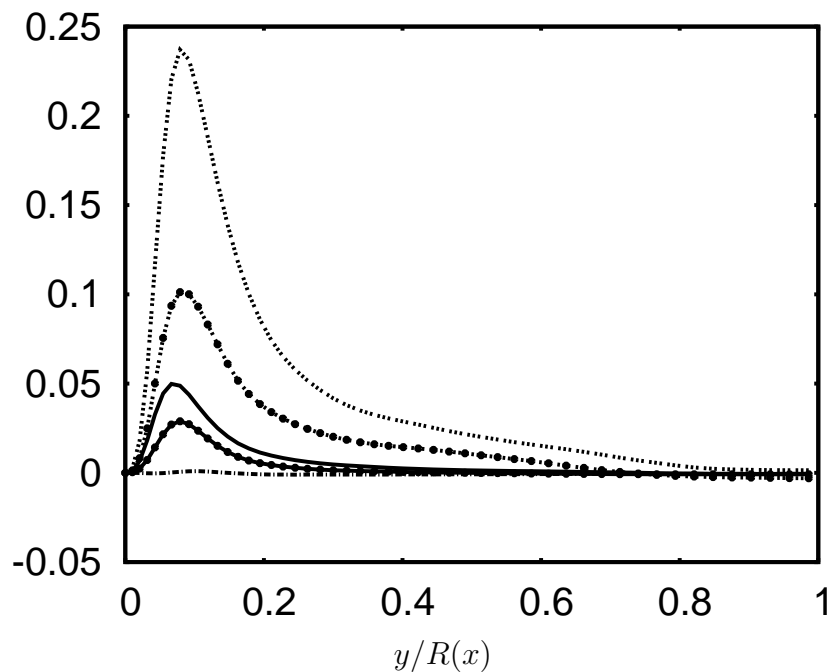


Figure 4.29: Production term of the axial Reynolds stress budget at $x/L = 0.1, 0.15, 0.45, 0.65, 0.8$ (from top to bottom of the figure) scaled by local $\tau_w^2/\bar{\mu}$ (LES)

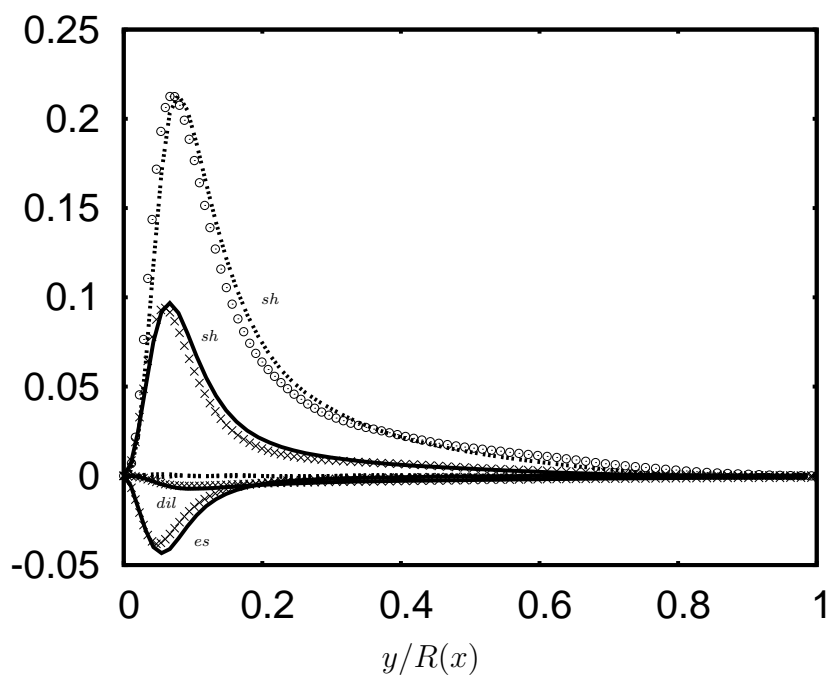


Figure 4.30: Contributions to the production of the axial Reynolds stress in the nozzle at stations $x/L = 0.0$ (dashed line) and 0.45 (solid line). sh : mean shear, dil: mean dilatation, es: extra rate of strain. Lines: LES, symbols: DNS. All terms are normalized by $\tau_w^2/\bar{\mu}$.

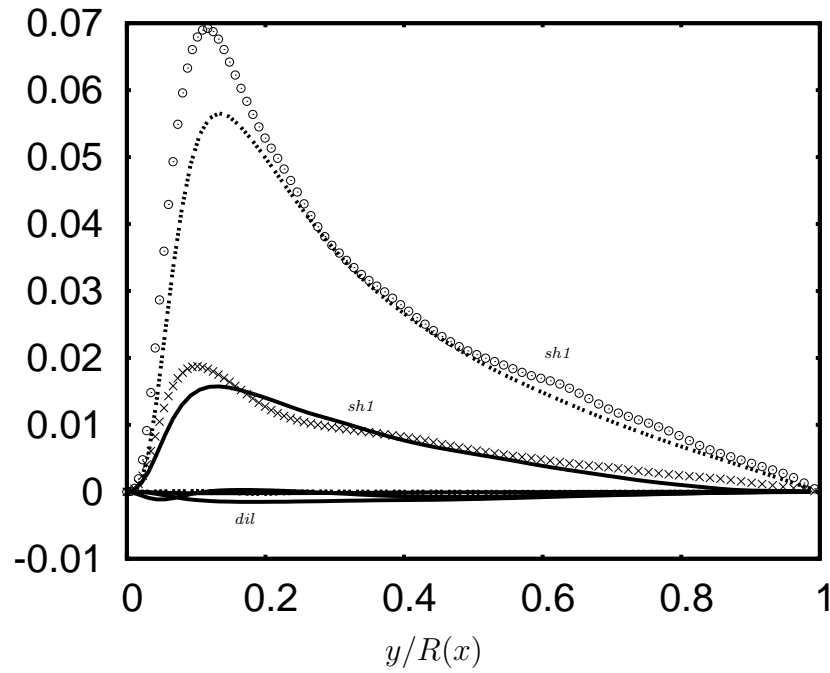


Figure 4.31: Contributions to the production of the Reynolds shear stress in the nozzle at stations $x/L = 0.0$ (dashed line), 0.45 (solid line). sh1: mean shear (*shear1*), dil: mean dilatation. Lines: LES, symbols: DNS. All terms are normalized by $\tau_w^2/\bar{\mu}$.

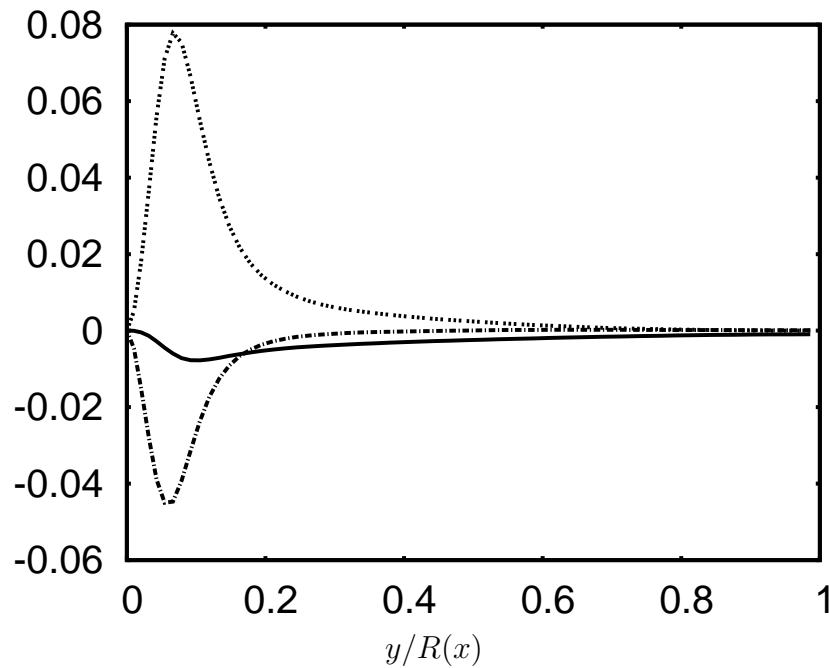


Figure 4.32: Decomposition of the axial production terms at $x/L = 0.65$, mean shear; — mean dilatation; -.- extra strain rate (LES). All terms are normalized by $\tau_w^2/\bar{\mu}$.

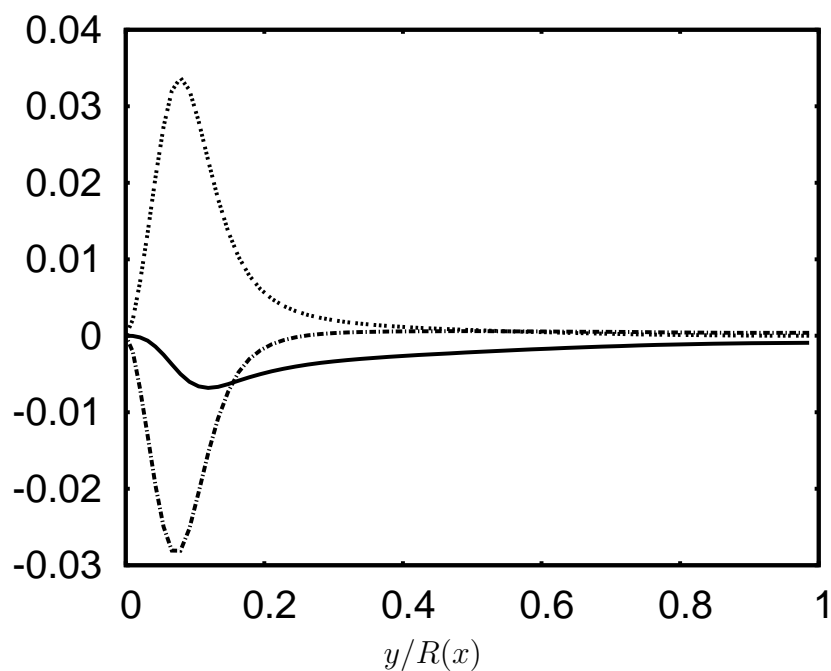


Figure 4.33: Decomposition of the axial production terms at $x/L = 0.8$, mean shear; — mean dilatation; -.- extra strain rate (LES). All terms are normalized by $\tau_w^2/\bar{\mu}$.

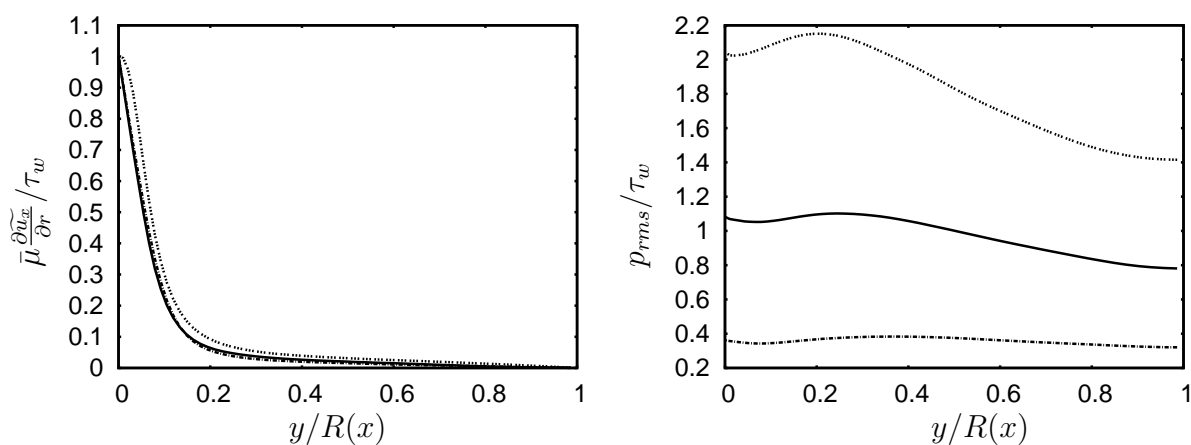


Figure 4.34: Mean shear, rms pressure fluctuations. $x/L = \dots \dots 0.0$; — 0.45, -.- 0.8 (LES)

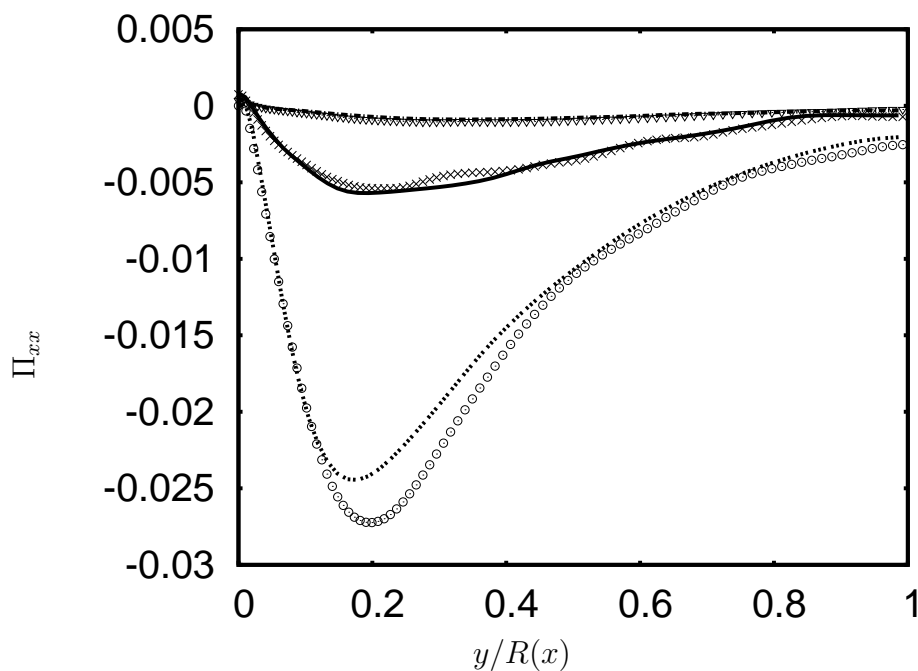


Figure 4.35: Pressure-strain correlation Π_{xx} in the nozzle, x/L stations as in Figure 4.9. Lines: LES. Symbols: DNS. Terms are normalized by $\tau_w^2/\bar{\mu}$.

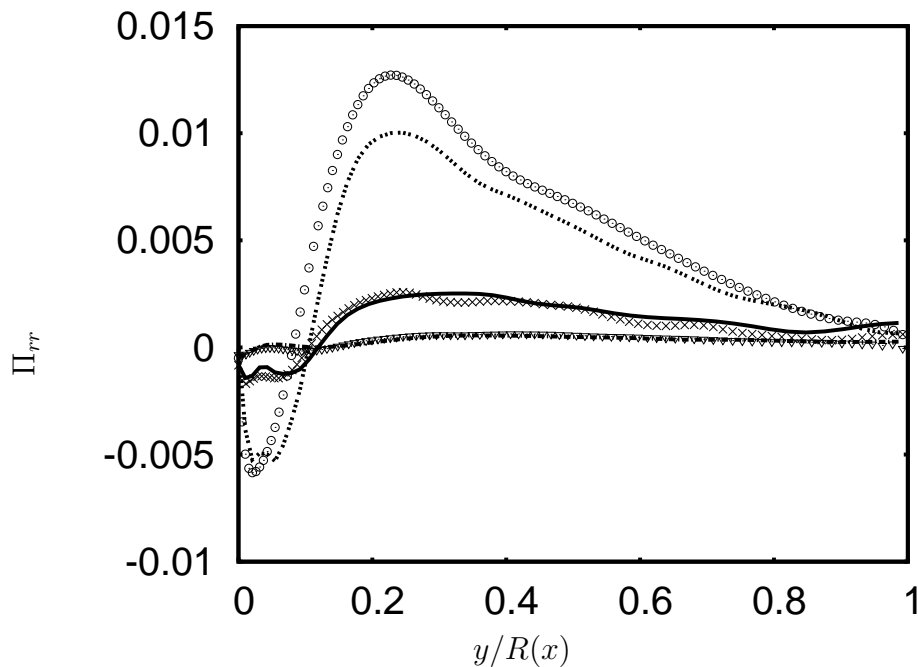


Figure 4.36: Pressure-strain correlation Π_{rr} in the nozzle x/L stations as in Figure 4.9. Lines: LES. Symbols: DNS. Terms are normalized by $\tau_w^2/\bar{\mu}$.

4.10 Conclusions

DNS and LES of supersonic turbulent flow through a weakly diverging axisymmetric nozzle with fully developed supersonic pipe flow as inflow reveals interesting effects of mean dilatation and extra rates of strain on the turbulence structure. The effects are dramatic even though the effective acceleration is small. The flow remains nearly isentropic in the core. Dilatation fluctuations in this flow are negligible as in the incoming pipe flow. Weak mean expansion of the flow leads to a drastic decay of all turbulence intensities. Turbulence production is reduced significantly. A decomposition of the production terms in the transport equations of the Reynolds stresses into mean shear, extra strain rate and mean dilatation contributions shows their individual importance. While mean dilatation and extra strain rates reduce streamwise production to some extent, the decay of production due to shear is the most significant effect. This decay of shear production is shown to be due to the reduced Reynolds shear stress, the mean shear remaining nearly constant. Decay of pressure-strain correlations leads to the decay in radial stress and hence in shear stress. There is a decrease in pressure fluctuations as well as in strain rate fluctuations. The decay in pressure fluctuations could be due to the axial density gradient, the mean dilatation or both. Further studies in this direction will be undertaken.

Thus this study provides adequate support that effects of mean dilatation on the turbulent structure are indeed indirect. They cannot be solely estimated from the extra production terms in the Reynolds stress transport equations. This large indirect effect had already been mentioned by Bradshaw (1974).

Chapter 5

Supersonic turbulent diffuser flow

5.1 Introduction

A supersonic diffuser is a device which reduces the incoming supersonic flow velocity to a lower supersonic or a subsonic value and thereby achieves static pressure recovery. The aim of design of such a device is to keep stagnation pressure losses to a minimum. The deceleration of a supersonic flow in industrial diffuser configurations mostly occurs through a shock train which consists of a series of weak shocks instead of a single strong normal shock. The shape and number of individual shocks in a shock train depends on the incoming flow Mach number and a flow confinement parameter defined as the ratio of upstream boundary layer thickness to the radius (for a pipe). This phenomenon has been confirmed by numerous experiments and RANS computations, see Matsuo *et al.* (1999). However, RANS is not the most suitable tool to predict such complex flows with complicated shock-wall layer interaction.

To the best of the author's knowledge, no time-accurate simulation data are available for flows with shock trains. Thus, as a compromise between computational cost and more complete knowledge of the flow physics, LES of such flows (rather than DNS) seems to be logical.

Supersonic flows can be decelerated without shocks when the incoming viscous layer is relatively thin (i.e. at higher Reynolds and Mach numbers) and the APG is weak so that the flow near the wall has high momentum relative to the APG. In such cases, the thickness of the viscous region will not be sufficiently enhanced so as to cause shocks to appear. Such a flow case is of interest for us, since effects opposite to the nozzle flow case (detailed in the previous chapter) on the turbulence structure are expected. However, flows undergoing deceleration show more complicating flow features than those undergoing acceleration as we will show below. For example, when the incoming Mach number is at a low supersonic value, (as in one of our flow cases with $M_{in} = 1.8$), substantial transonic regions can develop during the later stages of deceleration and can lead to local flow acceleration.

Here, we would like to refer to the review of Spina *et al.* (1994) on experimental studies of supersonic boundary layers subjected to adverse pressure gradients. In particular, Fernando & Smits (1990) study the effects of APGs on such flows and find that turbulence intensities are amplified due to deceleration. Incompressible, temporal APG channel flow

DNS of Coleman *et al.* (2003) explore different inner and outer layer characteristics of these flows. Using LES of incompressible flow in a planar diffuser, Wu *et al.* (2006) report on internal layers in flows subjected to strong APG. Although in our flow cases, we have strong mean axial density gradients due to compression, the incompressible flow results should provide some pointers to interpret our results.

Coleman & Mansour (1993) study effects of rapid spherical compression on compressible isotropic turbulence and observe high pressure-dilatation correlation at large compression rates. Effects of rapid, axial compression on compressible, homogeneous turbulence have been studied by Cambon *et al.* (1993) using DNS. They found increased pressure-dilatation correlation at large compression speeds. However, its relative importance compared to TKE production was reduced with increasing compressibility (i.e. with increasing M_t). On the other hand, the pressure-strain correlation, which modifies the Reynolds stress anisotropy and hence TKE production, was found to be larger than the pressure-dilatation correlation. Both studies provide comparisons of DNS with rapid distortion theory (RDT).

5.2 Flow cases

We study the effects of weak, distributed APGs on an incoming fully developed supersonic turbulent pipe flow retarded in a diffuser using LES. The wall is kept at constant temperature to avoid further complications due to modified thermal boundary conditions.

Two flow cases without shocks are computed with incoming flow conditions, $M = 1.8, 2.5$ and $Re_\tau = 280, 550$, respectively. These flows have relatively high momentum in the near-wall region and hence no shocks appear and the deceleration occurs through non-isentropic compression waves. For the lower Mach number case we found a noticeable transonic region after about 2/3 of the diffuser length which results in marginal acceleration of the flow and this has an effect on the turbulence structure in that region. Hence, we decided to simulate a higher incoming Mach number case to more convincingly isolate the effects of bulk compression on the turbulence structure.

Additionally, one flow case with incoming $M = 1.5$ and $Re_\tau = 245$ is reported here where the interaction of the marginally thicker viscous layer with the APG leads to the formation of shock trains. This flow thus shows intrinsic compressibility effects due to increased dilatation fluctuations.

For all the computations the length of the domain in the axial direction is $10R$ where R is the radius of the incoming pipe flow. $64 \times 64 \times 50$ points are used for the LES with $Re_\tau = 214, 280$ and $128 \times 64 \times 60$ points are used for the LES with $Re_\tau = 550$ in the axial, azimuthal and radial directions, respectively.

5.3 Supersonic diffuser without shock train ($M_{in} = 1.8$)

The incoming Mach and Reynolds numbers for this case are $M = 1.8$ and $Re_\tau = 280$ where shocks do not occur because of the low incoming viscous layer thickness. The

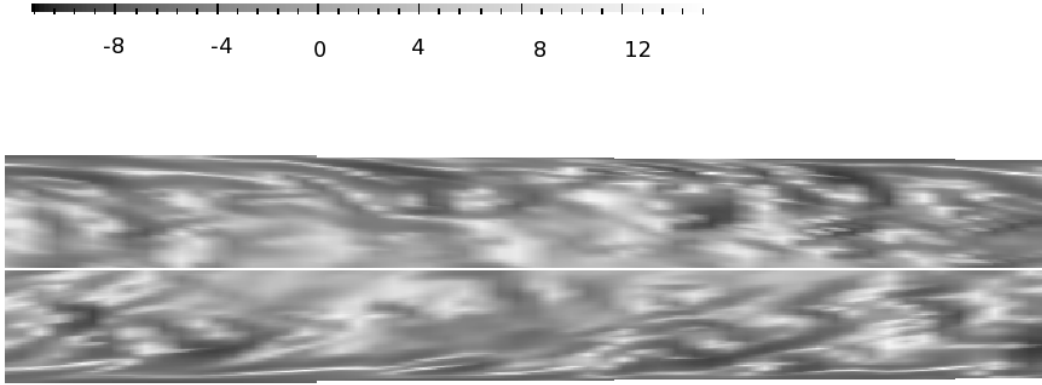


Figure 5.1: Axial velocity fluctuations (LES), normalized with $u_\tau(x/L = 0)$, in a (x, r) -plane. Flow is from left to right.

non-dimensional pressure gradient expressed as the Clauser parameter $\beta = \frac{\delta^*}{\tau_w} \frac{d\bar{p}}{dx}$ is nearly constant at 1.6 after an initial smooth transient (figure 5.3). This flow thus shows the effects of mean compression which are in many ways exactly opposite to those of mean dilatation in a nozzle as described in the previous chapter. An instantaneous plot of axial velocity fluctuations (figure 5.1) shows increased turbulence activity in the near-wall region when the flow is decelerated.

5.3.1 Azimuthal spectra

The spectra of axial velocity fluctuations in the azimuthal direction (figure 5.2) in the near-wall region show increased energy content at all resolved wavenumbers which indicates enhanced turbulence activity in the buffer layer during the compression in the diffuser. The small changes in non-dimensional wavenumber are due to changes in the local friction Reynolds number in the flow which is used for normalization.

5.3.2 Mean flow features

This flow, however, shows noticeable non-isentropic effects in the core region as compared to the flow in the nozzle which was found to follow the isentropic streamtube predictions very closely. This is seen in centerline pressure, density and temperature profiles which are compared to the isentropic profiles in figure 5.4. The centerline Mach number is reduced from 1.8 to nearly 1.45. The bulk velocity, u_b , is reduced to about 80% of its incoming value, $u_{b,o}$. The short region of acceleration near the end of the diffuser is the consequence of a growing transonic region as the flow decelerates. Alternate regions of compression and expansion could be noticed at the beginning of compression near $x/L = 0.2$ in all the profiles which lead to steeper static pressure (as well as density and temperature) rise compared to an isentropic compression. These regions of alternate compression and expansion waves are localized only in the core region, since near the wall these waves are damped due to viscosity. The result is a smoother static pressure profile near the wall as

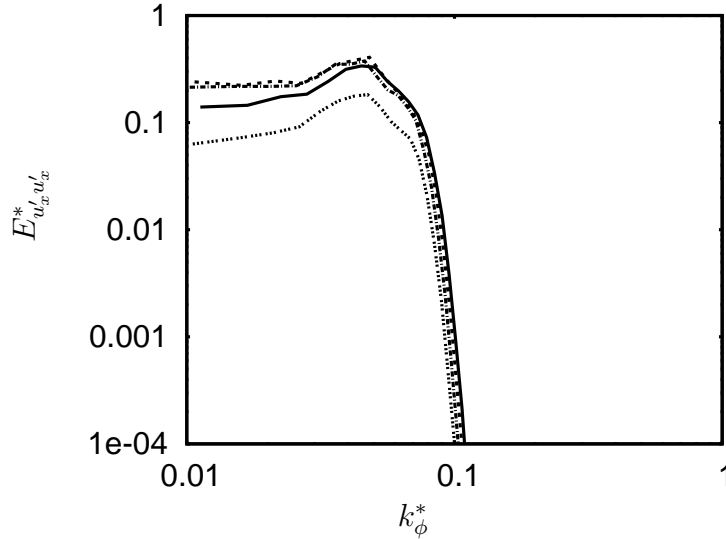


Figure 5.2: Energy spectra (LES) of axial velocity fluctuations in the near-wall region ($y^* = 10$) in the azimuthal direction. $x/L = \dots \dots 0.0$; — 0.25; - - - 0.5; -.-.- 0.65

compared to that in the core (figure 5.5). This figure also shows that the radial variation of mean pressure remains negligible in this diffuser flow case.

The wall shear stress (figure 5.5) decreases substantially at the beginning of compression, reaches a minimum, and then increases monotonically throughout the region of nearly constant adverse pressure gradient. This is the combined effect of density increase, velocity decrease and weak area decrease which leads to changes in the viscous layer thickness. The displacement thickness δ^* (fig. 5.6) first increases in the region where the wall shear stress decreases and then shows a slow decrease with a corresponding increase in wall shear stress. The momentum thickness θ increases continuously throughout the adverse pressure gradient region. The relative variations of δ^* and θ lead to an initial increase and a subsequent decrease in the shape factor H (figure 5.6).

Marginally increased mean dissipation and substantially increased turbulent dissipation rates produce higher temperature levels (figure 5.7 (left)) in the diffuser compared to the incoming supersonic pipe. Figure 5.7 (right) shows an increase in mean dissipation levels of the order of 20%, while the increase in turbulent dissipation, the solenoidal part of which is shown in figure 5.8, is comparatively large, namely a factor of nearly three larger than the upstream value. The turbulent dissipation rate is increased primarily by mean compression acting as a source term in the solenoidal dissipation rate transport equation. Baroclinic effects in this transport equation are found to be negligible in the present flow case since the axial pressure gradient is still sufficiently weak not to cause significant source effects when coupled with the wall-normal density gradient.

Fig. 5.8 shows the mean compression in the diffuser along with that in the upstream pipe flow normalized with local radius and local bulk velocity. The compression increases abruptly, especially in the core region, near $x/L = 0.22$ where the flow experiences the first effects of the adverse pressure gradient, and then settles to lower values further

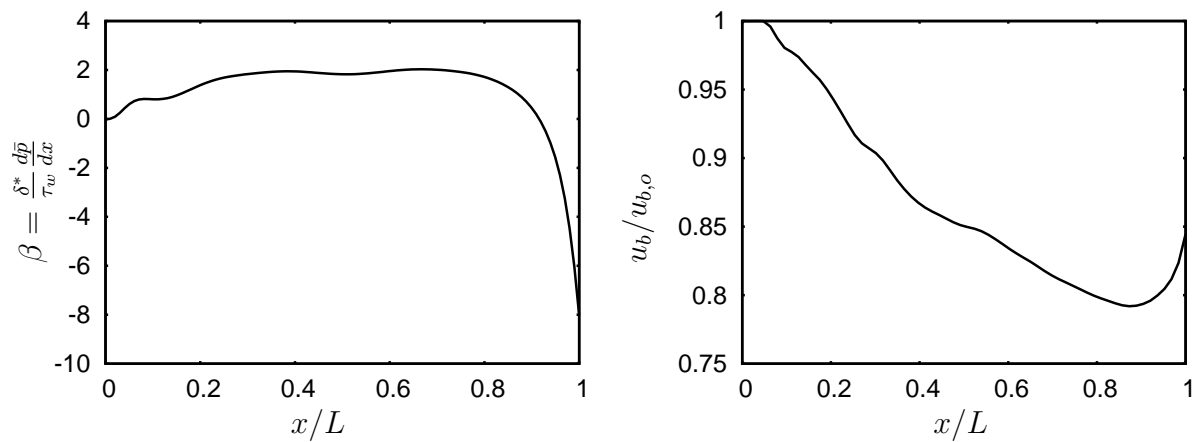


Figure 5.3: Axial variation of Clauser parameter (β) and bulk velocity. $u_{b,o}$: bulk velocity at $x/L = 0$.

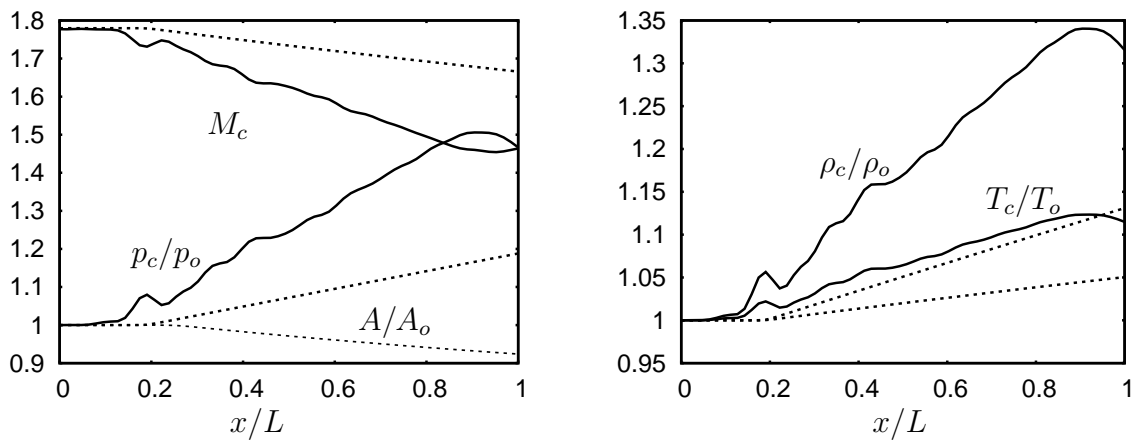


Figure 5.4: Left: Centerline pressure, local Mach number, and area distribution; Right: centerline density and temperature. Dashed lines are the solutions of isentropic stream-tube equations. Subscript 'o' denotes values at $x/L = 0$.

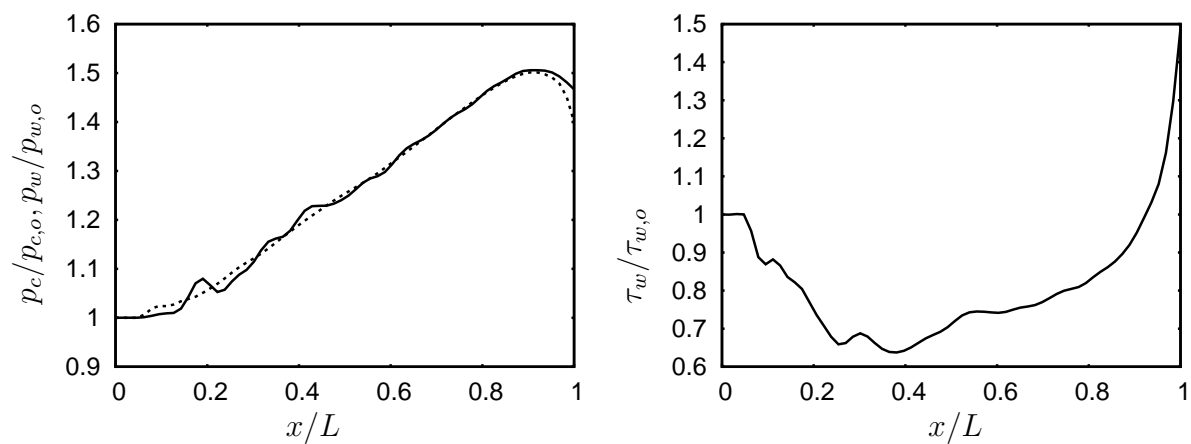


Figure 5.5: Left: Centerline (solid line) and wall (dashed line) pressure distribution. Right: Wall shear stress

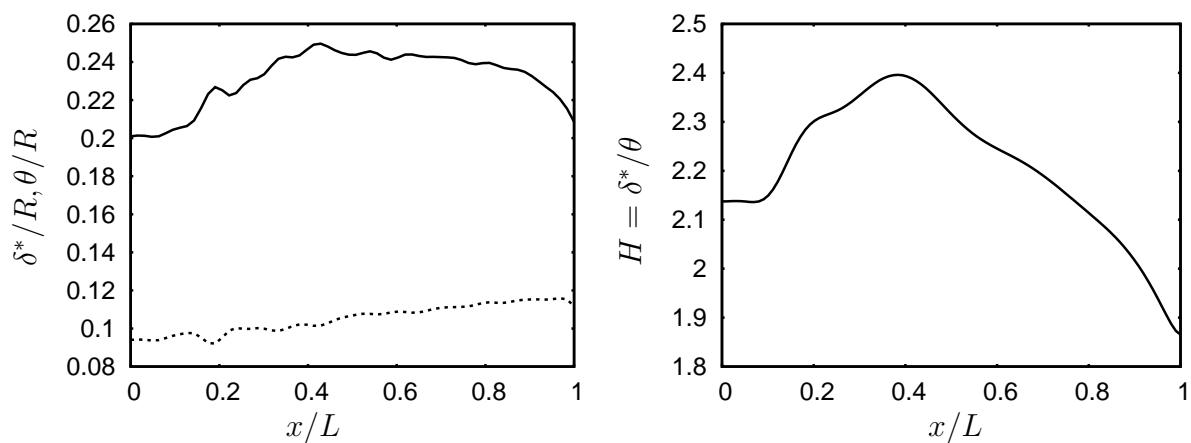


Figure 5.6: Left: Displacement (solid line) and momentum thickness (dashed line). Right: Shape factor

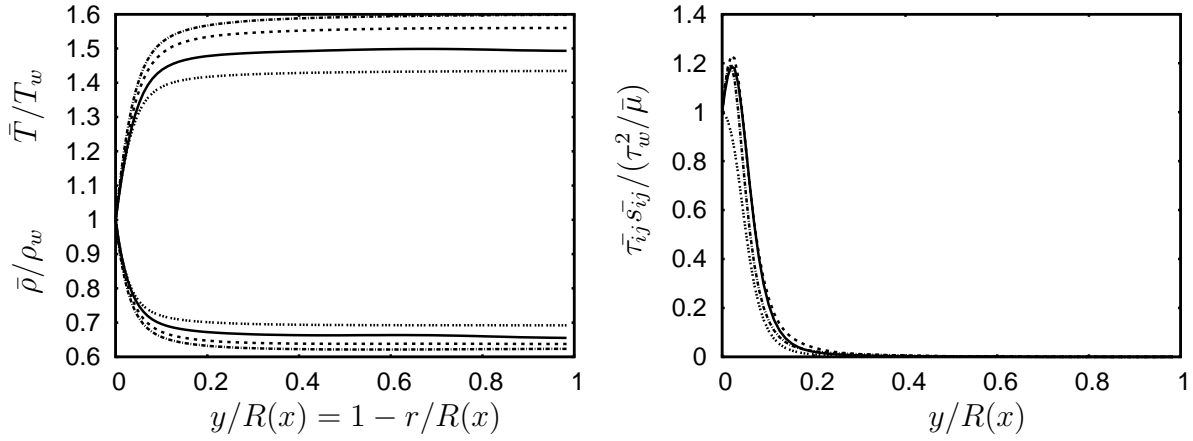


Figure 5.7: Left: Mean density, temperature profiles. Right: Dissipation of the mean flow. $x/L = \dots \dots 0.0$; $-\ - \ - 0.25$; $- \cdot \cdot \cdot 0.5$; $- \cdot \cdot \cdot 0.65$

downstream. In a small region near the exit, after $x/L = 0.8$ positive values of dilatation are noticed (not shown) where the flow becomes transonic. This region is thus subjected to weak acceleration as evident from the plots of centerline pressure and Mach number, fig. 5.4.

The relative magnitude of the extra strain rate $\frac{\partial \widetilde{u_x}}{\partial x}$ in the buffer layer where Reynolds stresses have their maxima, is less than 0.5% of the wall shear rate, figure 5.9. The effect of such a small magnitude of extra strain on the turbulence structure (to be discussed later) is, however, found to be dramatic.

The local Mach number profiles (fig. 5.9) reflect the growing transonic region in the diffuser as seen by the shift of the sonic line away from the wall. At around $x/L = 0.7$ the peak production region is already in the subsonic region which has direct consequences on the turbulence structure to be shown below.

Variations in wall shear stress in the axial direction and the increase in density due to compression lead to failure of the Van Driest transform for the mean velocity. As seen in fig. 5.10, the profiles in the fully turbulent region are always above that of the fully-developed pipe flow. Only in the viscous region very close to the wall, we see some sort of a collapse of the profiles because we use local values of the friction velocity as a scale for the mean velocity.

5.3.3 Rms profiles

The increase in mean density and temperature gradients in the diffuser leads to stronger density and temperature fluctuations. But, these rms values are less than 10% of their corresponding mean values, fig. 5.10, 5.11. The rms pressure fluctuations still remain negligible in this flow case, although there is an increase when compared to the levels in fully-developed pipe flow.

Acoustics are still important in the core region where mean density and temperature

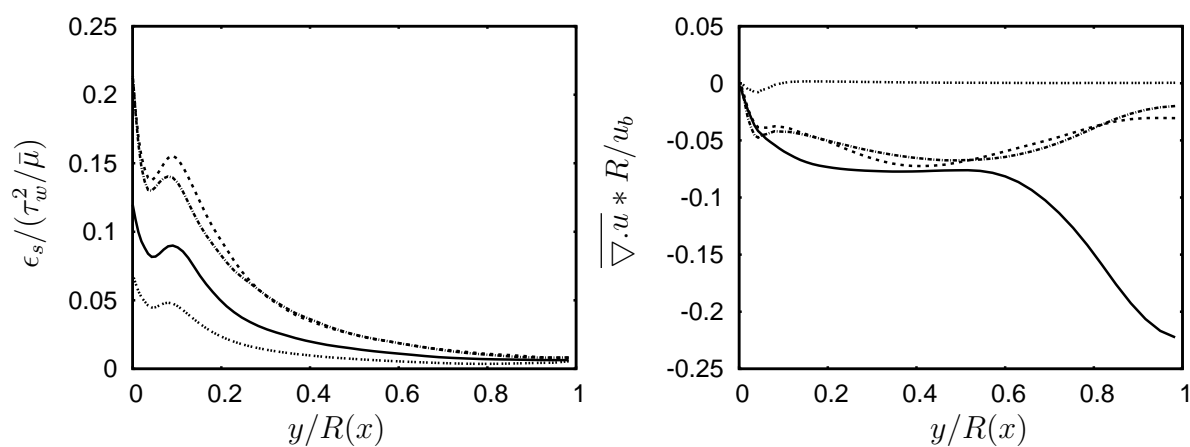


Figure 5.8: Solenoidal dissipation rate and mean dilatation. Line types as in fig. 5.7

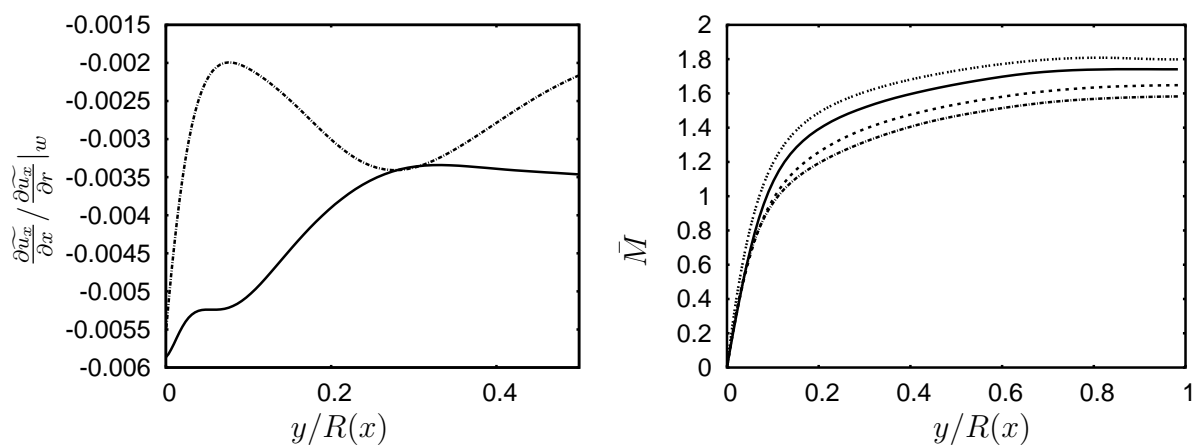


Figure 5.9: Left: Extra strain rate normalized with wall shear at $x/L = -0.3$; -.- 0.5. Right: Local Mach number. Line types as in fig. 5.7

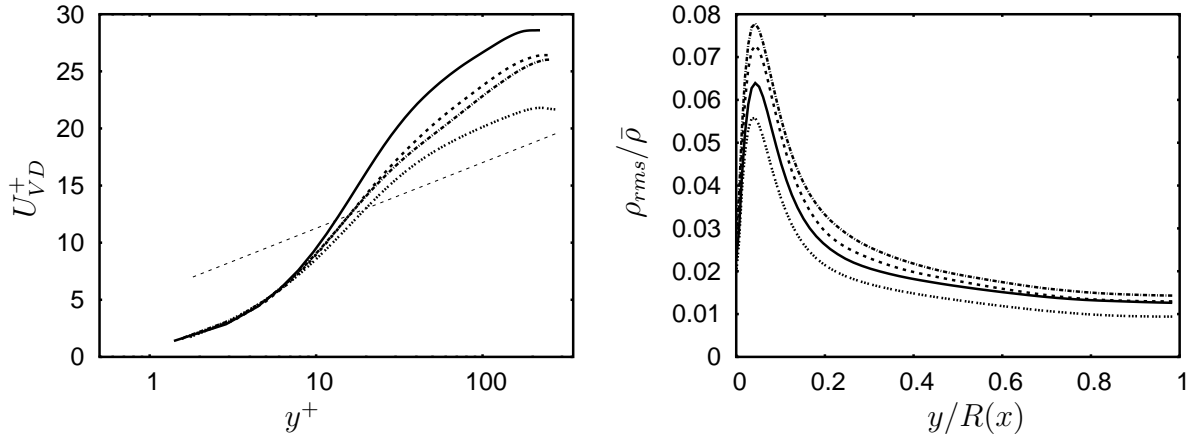


Figure 5.10: Van Driest transformed mean velocity, rms density fluctuations. Line types as in fig. 5.7. Dashed line in left figure: $u^+ = 2.5 \ln y^+ + 5.5$

gradients are negligible. This is indicated by the positive density-temperature correlations and the strong pressure-density correlations in the core, fig. 5.12.

The values of these correlations near the wall reflect the strong heat transfer because of the cooled wall. Indeed, $R_{\rho T}$ is close to -1 and naturally, R_{pp} drops nearly to zero in this region.

The velocity-temperature correlations do not show any major changes in this diffuser (fig. 5.12) compared to the incoming pipe flow. They remain very close to unity in the near-wall viscous region, unlike in the nozzle (in previous chapter) where they show large reductions. This might indicate that modified SRAs which have been shown by Huang *et al.* (1995) and in this work to be suitable for supersonic channel and pipe flows may also be applicable in this case. In this context, it is also of interest to note that the behaviour of the single-point correlation coefficients $R_{\rho T}$, R_{pp} is practically the same as that in fully-developed pipe flow, as a result of weak mean compression.

Intrinsic compressibility effects are expected to be negligible, since the turbulent Mach number M_t was found to increase only weakly from around 0.27 to about 0.33, fig. 5.12. It is to be noted that beyond $x/L = 0.65$ there is a decrease in the turbulence intensities in the inner viscous layer, and an increase in the outer layer. This difference in effects of adverse pressure gradients on inner and outer layers has been observed in incompressible, APG channel flow by Coleman *et al.* (2003). Evidence of different inner and outer layer dynamics in incompressible, APG flows has been found in studies of incompressible diffusers (see Wu *et al.* (2006)).

Although we expect appreciable dilatation fluctuations when the flow is compressed, the rate of compression in this flow case is too small to cause significant intrinsic compressibility effects ($|D|q^2/\epsilon = 0.7$ in the buffer layer, where $D = \frac{\partial \bar{u}}{\partial x}$ is the mean deformation rate, q^2/ϵ is the 'eddy-turnover' time). The compressible dissipation rate is limited to less than 0.1% of the solenoidal dissipation rate in the near-wall region. It is a negligible fraction of $\tau_w^2/\bar{\mu}$ as seen in figure 5.14 where we also notice a marginal increase of ϵ_d from

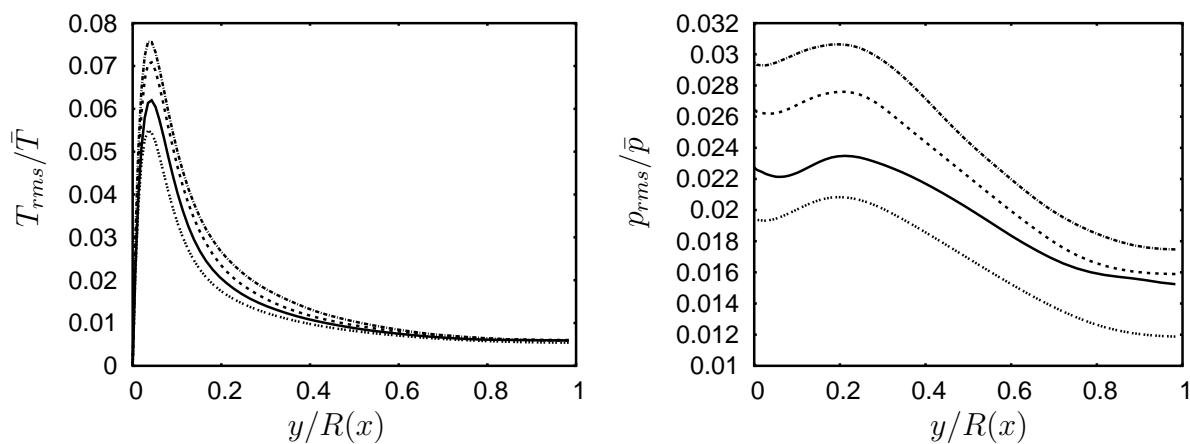


Figure 5.11: Rms temperature and pressure fluctuations. Line types as in fig. 5.7

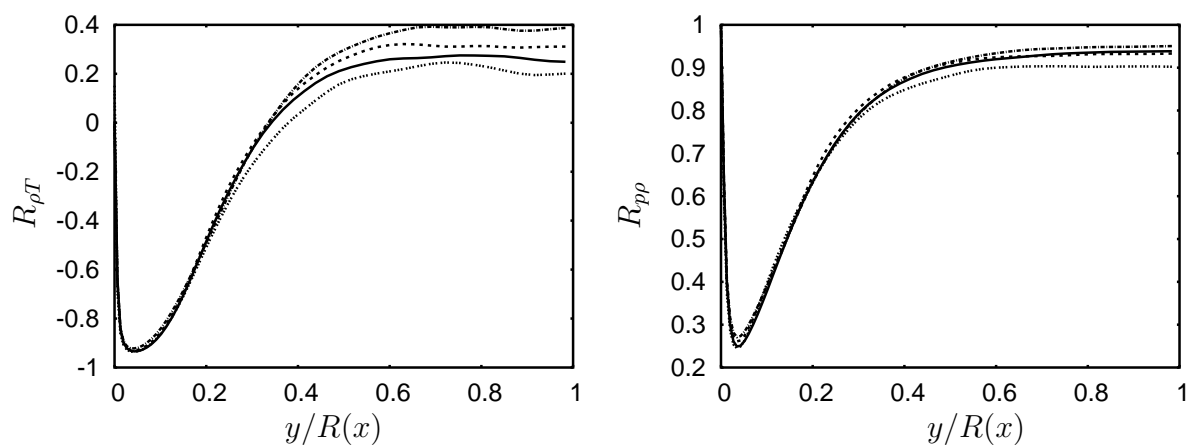


Figure 5.12: Density-temperature and pressure-density correlations. Line types as in fig. 5.7

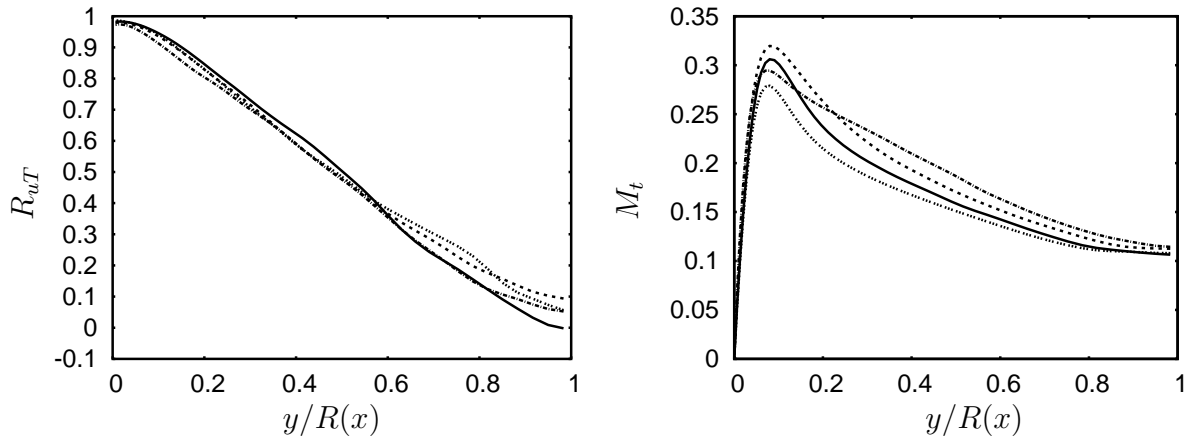


Figure 5.13: Velocity-temperature correlations, Turbulent Mach number. Line types as in fig. 5.7

its incoming pipe flow levels. This is caused by higher velocity fluctuations. The pressure-dilatation correlation also rises to about 1% of $\tau_w^2/\bar{\mu}$ and approximately to 10% of the solenoidal dissipation rate in the peak production region. Coleman & Mansour (1993), from their studies of homogeneous turbulence subjected to rapid spherical compression, show that $\overline{p'u'_{i,i}}$ strongly increases with the rate of compression. Their results show that $\overline{p'u'_{i,i}}$ rises to about 6 times the TKE dissipation rate when the initial spherical compression rate, $S_o q^2/\epsilon$ (S_o denotes spherical compression) has a magnitude of 47, which is more than a factor of 50 larger than our compression rate.

Rms velocity fluctuations are presented in semi-local, inner scaling with local u_τ^* and \bar{v} in figures 5.15 and 5.16. The axial velocity fluctuations show a monotonic increase in the axial direction up to about $x/L = 0.6$ at all radial locations. Then there is a drop in intensity in the inner, viscous layer although the intensities in the outer layer continue to increase. This phenomenon has been noted in incompressible APG channel flow studies of Coleman *et al.* (1995), where they attribute the near-wall decrease to a decrease in axial production caused by reduced mean shear only. We will look into this while analysing the production terms. Although, the axial rms profiles show distinct inner and outer layer behaviour, the azimuthal and radial intensities do not reflect this. These components reveal a monotonic increase all along the axis. Distinct differences in inner and outer layer dynamics would be expected only when the APG is high and rapid changes in skin friction occurs leading to flow separation. Wu *et al.* (2006) have investigated such effects in a planar diffuser and we refer to that paper for other references.

5.3.4 Reynolds stresses

The normal components of the Reynolds stress tensor are shown in figures 5.17- 5.19 using the outer scaling τ_w which is valid for channel and pipe flows with streamwise mean flow homogeneity. The deceleration of the flow is clearly evident from the failure of this outer

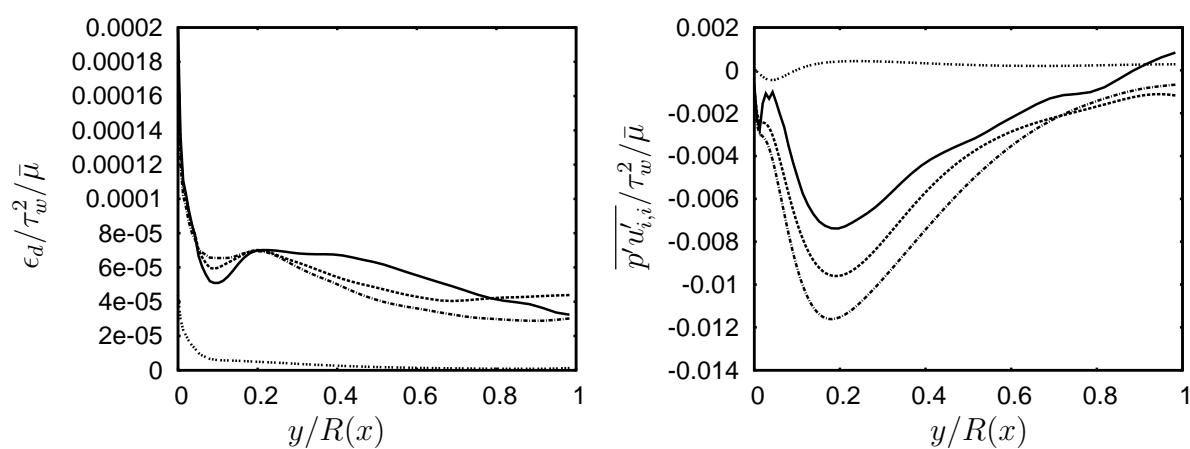


Figure 5.14: Compressible dissipation rate and pressure-dilatation correlation. Line types as in fig. 5.7

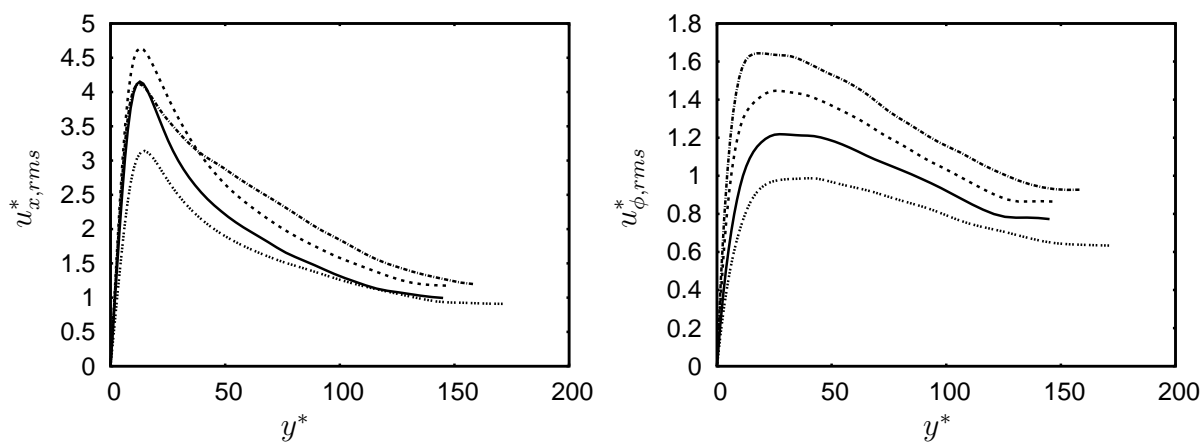


Figure 5.15: Rms velocity fluctuations, 'semi-local', inner scaling. $x/L = \dots \dots 0.0$; — 0.25; - - - 0.5; -.-.- 0.75

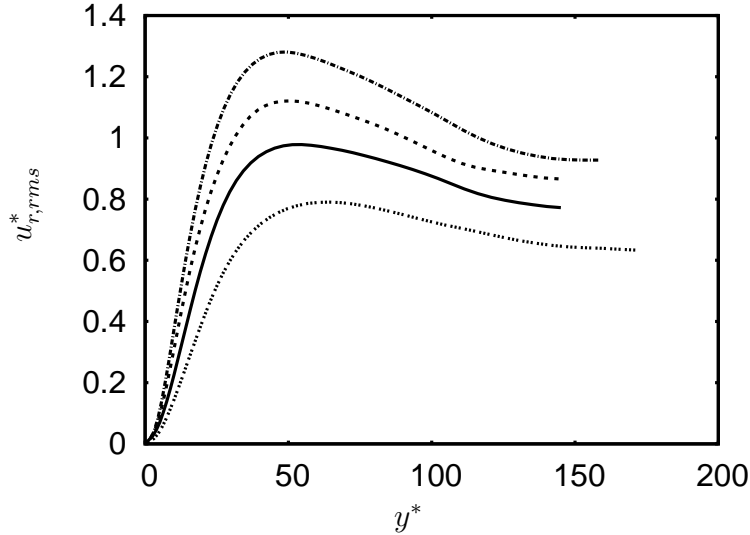


Figure 5.16: Rms velocity fluctuations, inner scaling. Line types as in fig. 5.15

scaling. Distinct inner and outer layer behaviour of the axial component after $x/L = 0.6$ is observed. No such effects are seen in azimuthal and radial components. The Reynolds shear stress profiles increase monotonically in axial direction at all radial locations, figure 5.20. The peaks of the profiles shift away from the wall throughout the region of adverse pressure gradient. The increase in the radial Reynolds stress and the Reynolds shear stress are primarily responsible for the increased axial production.

5.3.5 Reynolds stress budgets

The terms in the axial Reynolds stress transport equation are shown in figures 5.21- 5.23 at three axial locations, using semi-local, inner scaling $\tau_w^2/\bar{\mu}$.

At $x/L = 0.25$, i.e. just after the beginning of compression, the production term increases sharply from its value in fully-developed pipe flow. This is accompanied by an increase in viscous dissipation. In the wall layer, where the production term peaks, production is balanced by the viscous dissipation, viscous diffusion, turbulent diffusion, pressure-strain correlation and mean transport terms. The mean transport term only appears in these flow cases with axial inhomogeneity and is non-negligible at all axial positions. The pressure diffusion term is negligibly small.

At $x/L = 0.5$, there is a further increase in production, viscous dissipation and the pressure-strain correlations. There is a balance between the various terms of the budget, which is maintained further downstream at $x/L = 0.75$. At this location, however, a small decrease in production from its high upstream levels is observed. Unfortunately, the balance of terms is not perfectly achieved in the diffuser core region. This is due to the lack of statistical samples. It is also seen in the following TKE budgets. In contrast to this, the turbulence statistics are much more stable close to the wall.

Figures 5.24, 5.25 and 5.26 show the production, viscous diffusion, pressure diffusion,

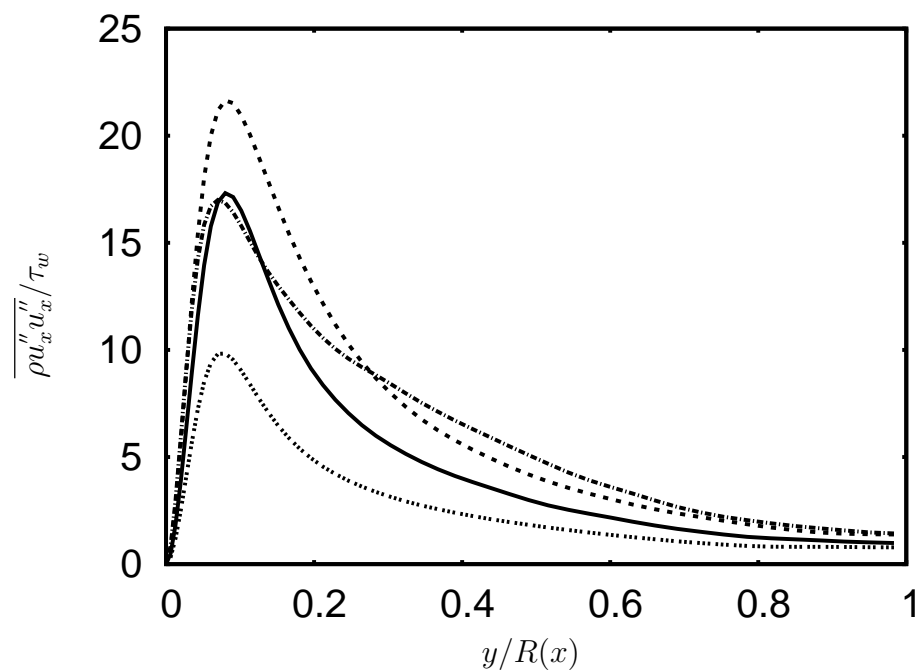


Figure 5.17: Axial Reynolds stress, outer scaling. Line types as in fig. 5.15

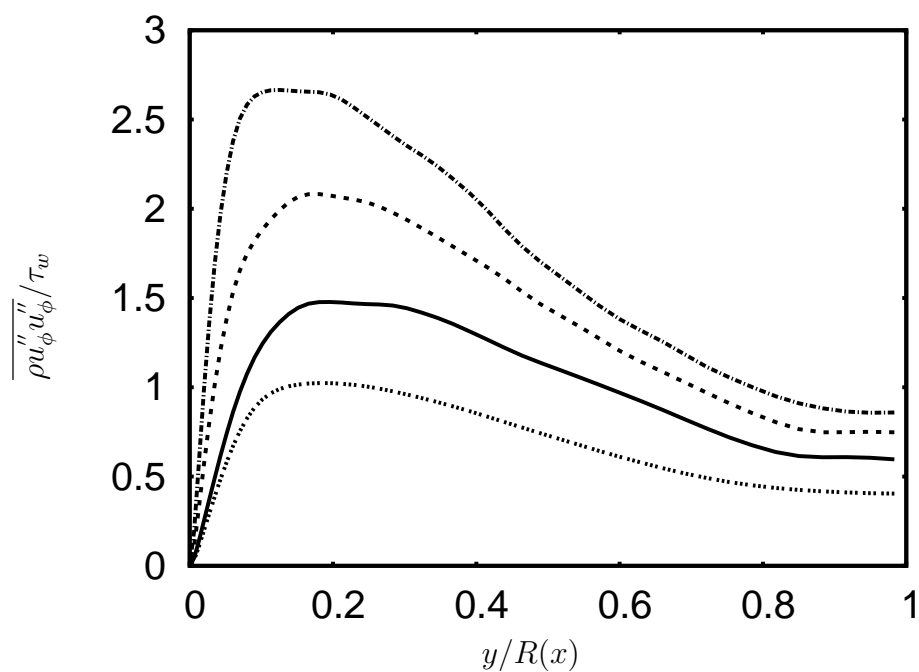


Figure 5.18: Azimuthal Reynolds stress, outer scaling. Line types as in fig. 5.15

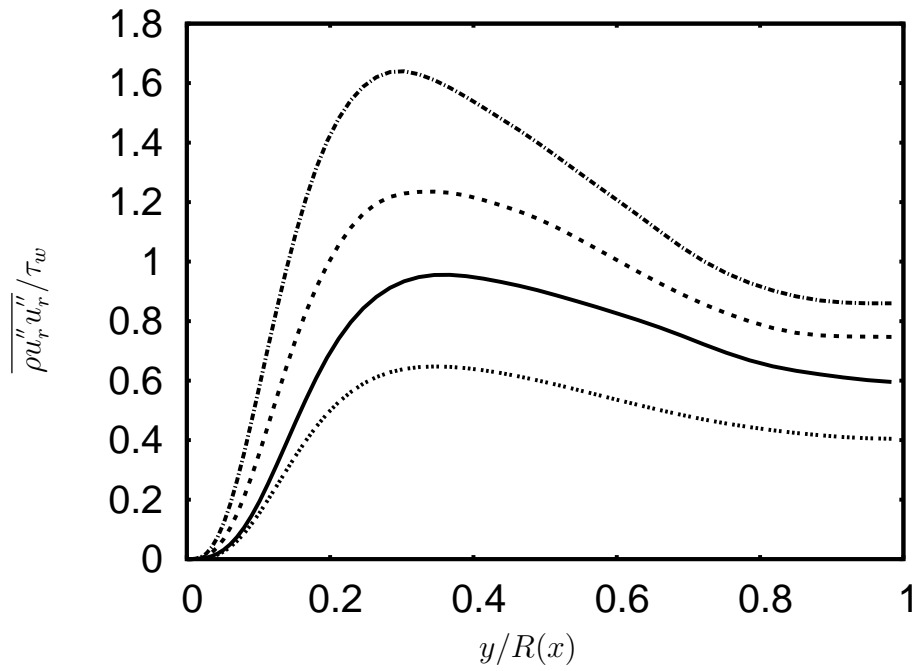


Figure 5.19: Radial Reynolds stress, outer scaling. Line types as in fig. 5.15

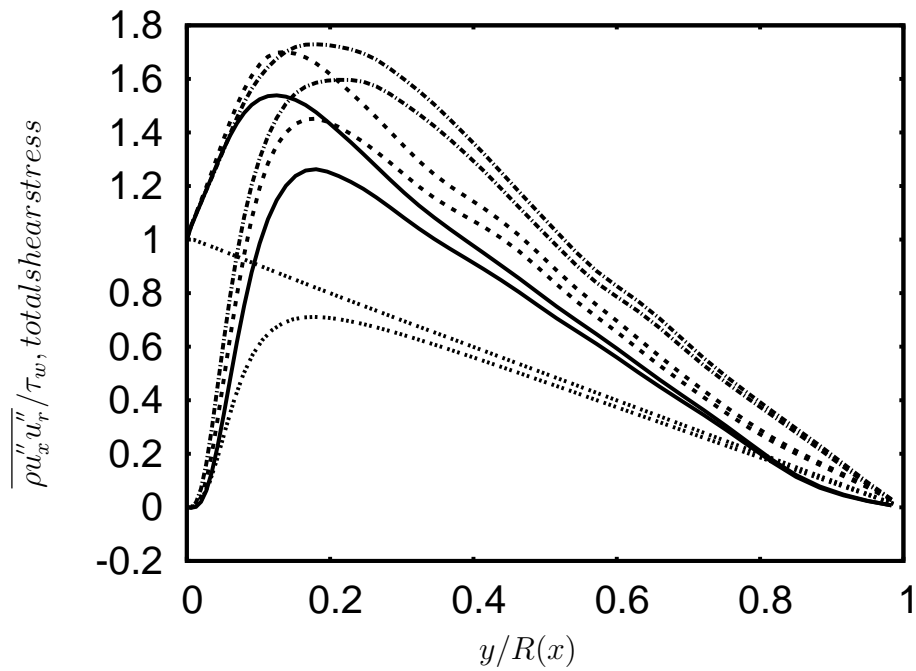


Figure 5.20: Reynolds shear stress and total shear stress, outer scaling. Line types as in fig. 5.15

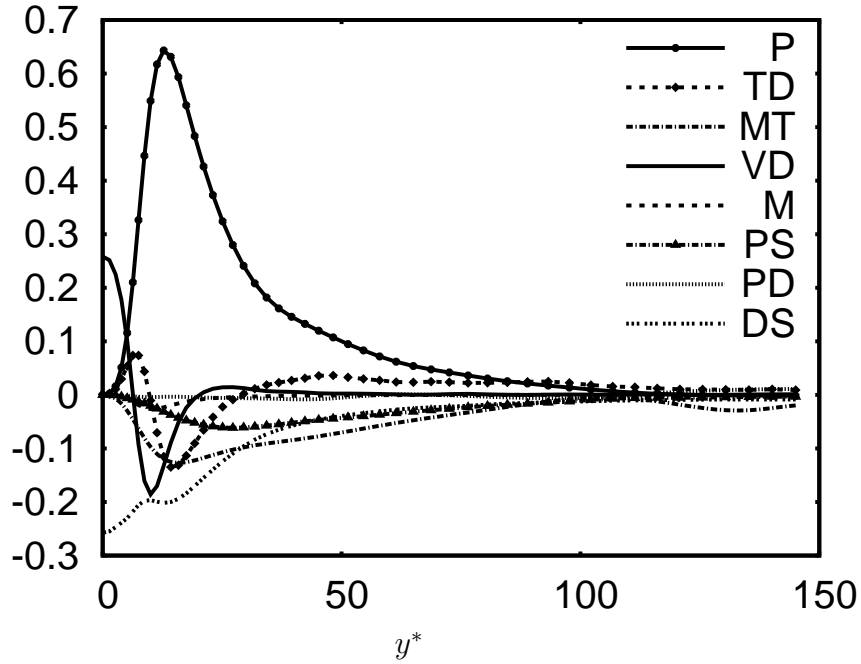


Figure 5.21: Axial Reynolds stress budget at $x/L = 0.25$ scaled with local $\tau_w^2/\bar{\mu}$. P: Production TD: turbulent diffusion, MT: mean convection, VD: viscous diffusion, M: Mass flux variation, PS: Pressure-strain correlations, PD: Pressure diffusion, DS:viscous dissipation

viscous dissipation and the pressure-dilatation correlation terms in the TKE budget at $x/L = 0.25, 0.5$ and 0.75 . As expected in this flow without shocks and at low turbulent Mach number, the pressure-dilatation term is negligible at all locations compared to the viscous dissipation and, of course, to the production term.

Figure 5.27 compares the axial production term which increases in the inner layer at the beginning of compression up to about $x/L = 0.6$ and then starts decreasing. This accounts for the similar behaviour of the axial intensities.

The individual production terms are now decomposed into shear, dilatation and extra rate of strain parts in the same way as discussed in the case of nozzle flow so that the influence of each part on the evolution of the turbulence structure under compression can be ascertained.

In the axial production (figure 5.28), shear contributions are dominant and mean dilatation and extra rates of strain act as small source terms. The shear component first increases drastically and then shows a decrease in the inner layer, while in the outer layer it still shows a marginal increase. The mean dilatation part has a small positive contribution in the inner layer and does not vary appreciably along the diffuser. The extra strain rate term in the near-wall viscous layer first increases and then decreases remarkably to the levels of the mean dilatation term. Thus, the large variations of the shear part combined with the variations of the extra strain parts contribute to the changes in production of axial stresses. Now, the increase in the shear production term $\overline{\rho u_x'' u_r'' \frac{\partial \bar{u}}{\partial r}}$ up to $x/L = 0.6$ is mainly due to changes in $\overline{\rho u_r'' u_r''}$ since the change in the mean shear in the buffer layer is

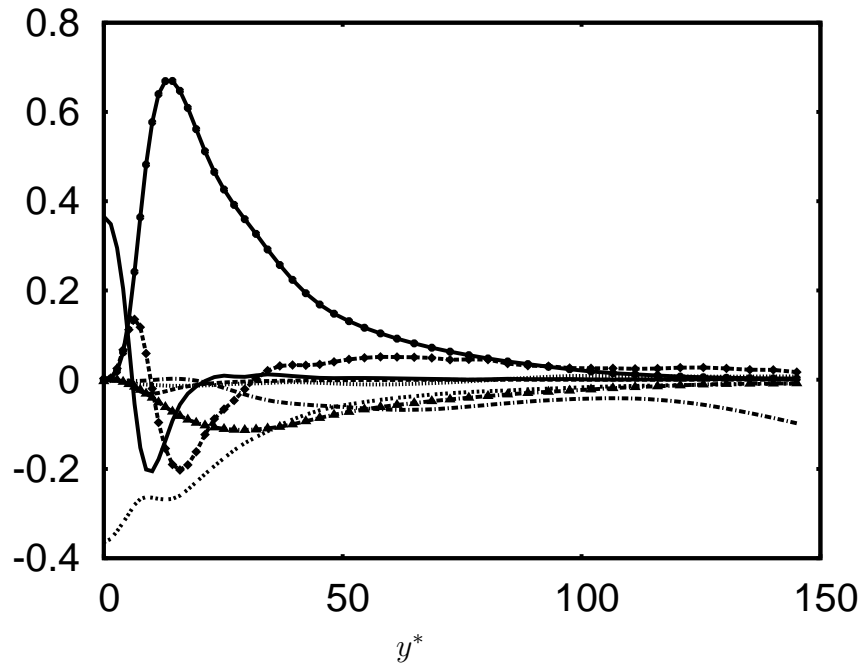


Figure 5.22: Axial Reynolds stress budget at $x/L = 0.5$ scaled with local $\tau_w^2/\bar{\mu}$. Line types and abbreviations as in fig. 5.21

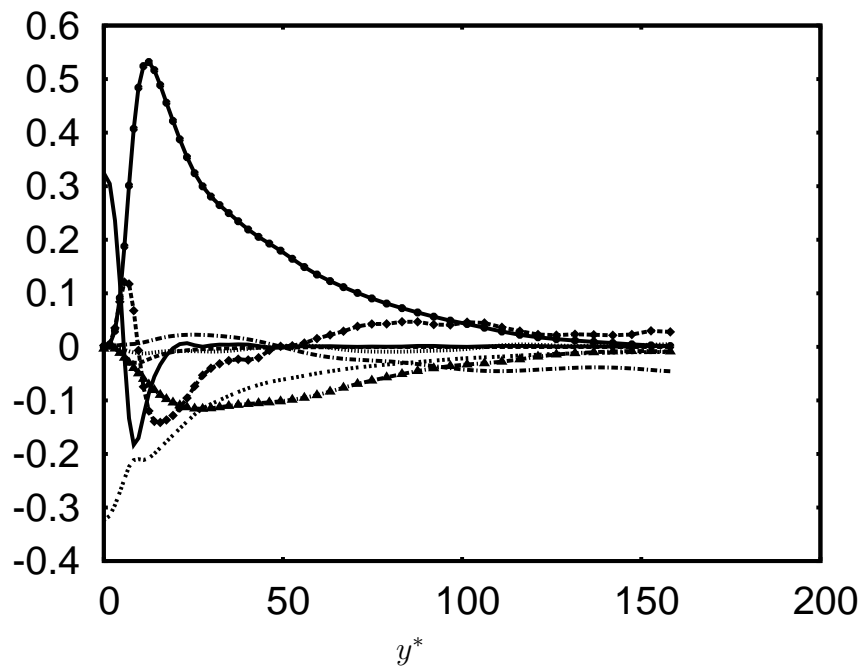


Figure 5.23: Axial Reynolds stress budget at $x/L = 0.75$ scaled with local $\tau_w^2/\bar{\mu}$. Line types and abbreviations as in fig. 5.21

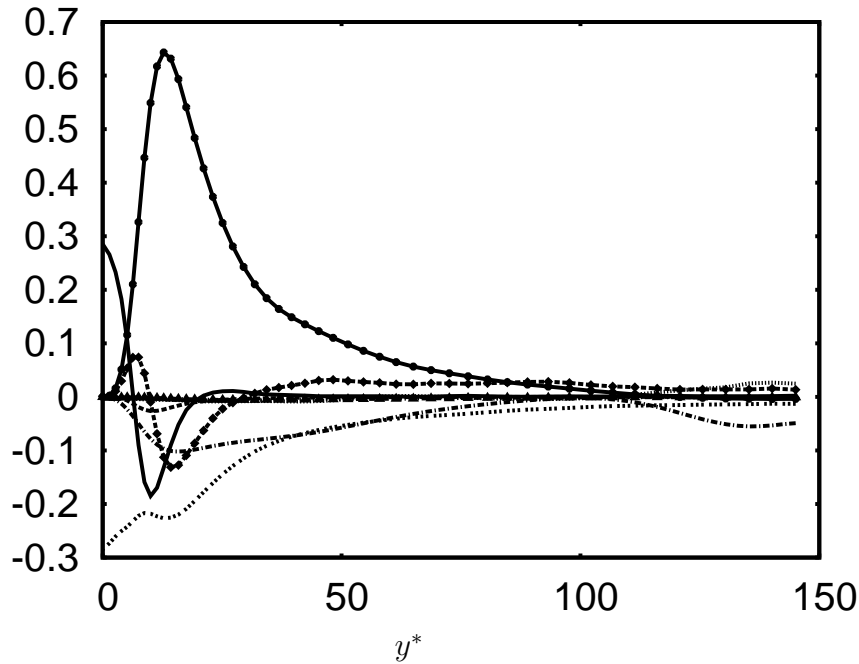


Figure 5.24: Terms in the TKE budget at $x/L = 0.25$ scaled with local $\tau_w^2/\bar{\mu}$. All line types as in fig. 5.21 except that for pressure-strain which here denotes pressure-dilatation correlation.

comparatively small, figure 5.29. But interestingly, after this region, the decrease in shear production is due to decrease in mean shear since the Reynolds shear stress in this region keeps on increasing. This phenomenon of decreasing production due to decrease in mean shear has been observed in some studies of incompressible boundary layers subjected to adverse pressure gradients, Coleman *et al.* (2003). The marginal increase of the shear production term in the outer layer is due to an increase in Reynolds shear stresses since in this region the mean shear rate does not play any role.

The production terms in the shear stress transport equation are now decomposed into terms containing mean dilatation, extra rates of strain and mean shear, figure 5.30. The major shear contribution (term sh1) increases drastically from its value in the pipe flow and then does not change in the region between $x/L = 0.5$ to $x/L = 0.75$. In this region, there is a decrease of the second shear part which had a small negative contribution at $x/L = 0.5$. At $x/L = 0.75$ this negative contribution is even smaller. And, hence this explains the small increase in the shear stress in this zone. The contributions of the mean dilatation and extra strain rates in this production term are negligible. The change in the sh1 term is brought about by changes in the stress $\overline{\rho u_r'' u_r''}$.

The transport equation (4.3) for $\overline{\rho u_r'' u_r''}$ contains production terms for this flow case with axial inhomogeneity. Although they could be decomposed in the same manner as the axial and shear components, their contribution remains negligible compared to the pressure-strain correlation term which is the major source for this stress, figure 5.31. Finally, the pressure-strain-correlations increase drastically in the diffuser during the early

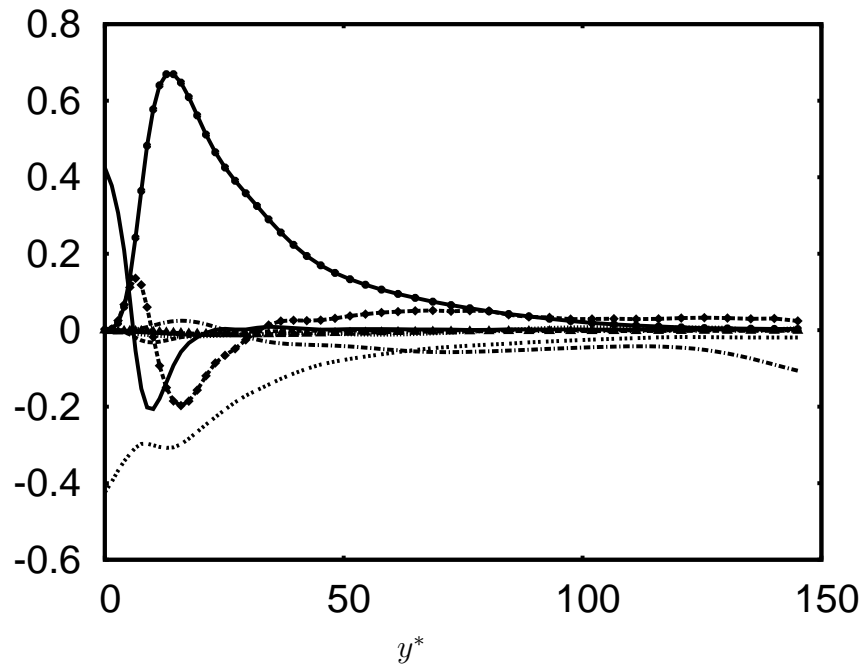


Figure 5.25: Terms in the TKE budget at $x/L = 0.5$ scaled with local $\tau_w^2/\bar{\mu}$. All line types as in fig. 5.21 except that for pressure-strain which here denotes pressure-dilatation correlation.

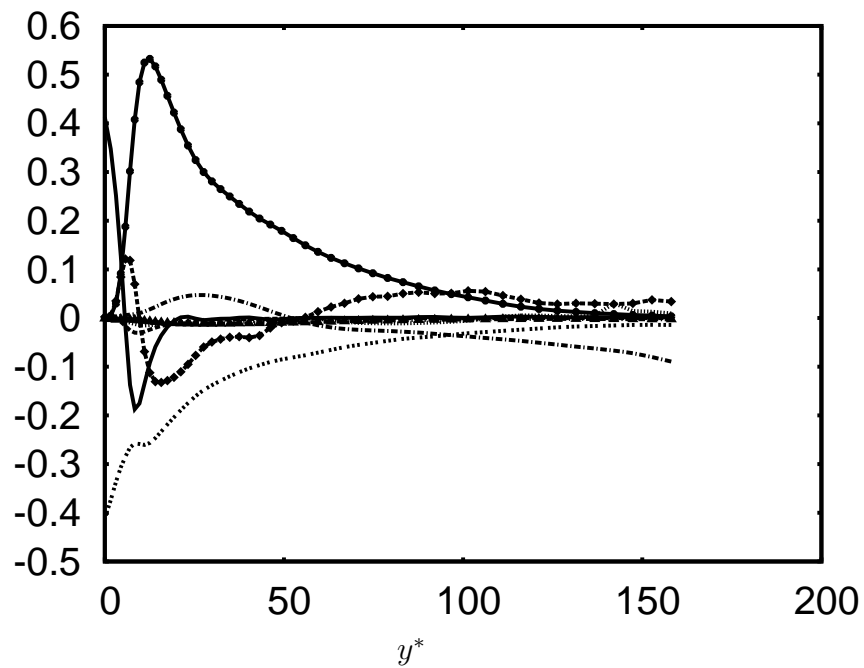


Figure 5.26: Terms in the TKE budget at $x/L = 0.75$ scaled with local $\tau_w^2/\bar{\mu}$. Line types as in 5.24.

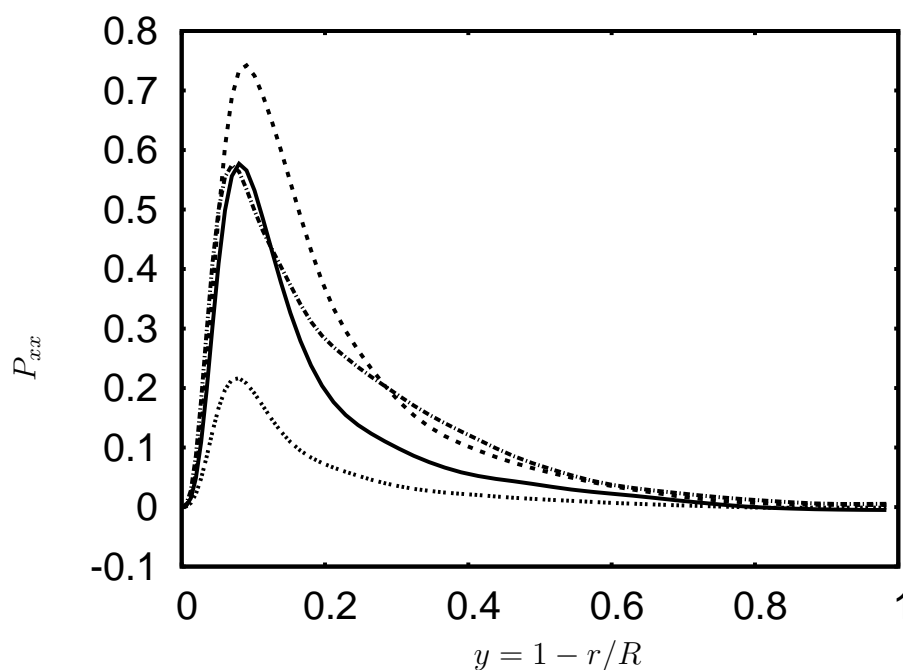


Figure 5.27: Axial production term scaled with local $\tau_w^2/\bar{\mu}$. Line types as in fig. 5.15

stages of compression to bring about increase in the radial stresses, which in turn causes the increase in shear stress and hence, the increase in axial intensities in this region, figures 5.33 and 5.34. The strong increase in pressure fluctuations is demonstrated in figure 5.32.

So, the increase in axial Reynolds stress during the compression up to $x/L = 0.6$ is exclusively controlled by the redistributive pressure-strain correlations, which increase rapidly in this region thereby increasing the radial and shear stresses. Although the radial stress continues to increase after this region owing to the increasing pressure-strain term, the axial stress decreases in the inner layer due to a reduction of mean shear. The shear stress in the region after $x/L = 0.6$ continues to increase slowly due to the combined effects of increasing radial stresses and decreasing mean shear in its production term.

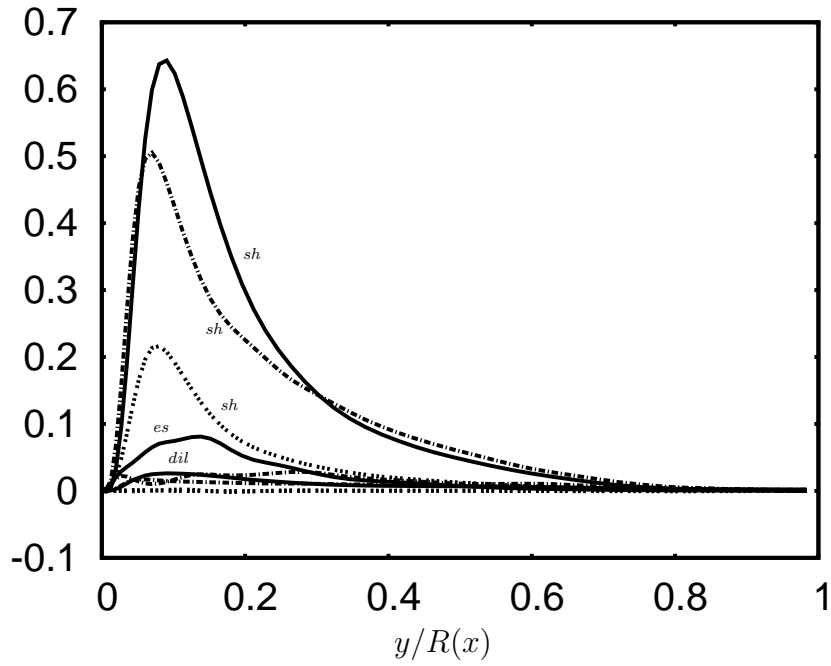


Figure 5.28: Decomposition of axial production term. $x/L = \dots \dots 0.0$; $—$ 0.5; $-.-.-$ 0.75. sh: mean shear term; es: extra strain rate term; dil: mean dilatation term. All terms normalized with $\tau_w^2/\bar{\mu}$

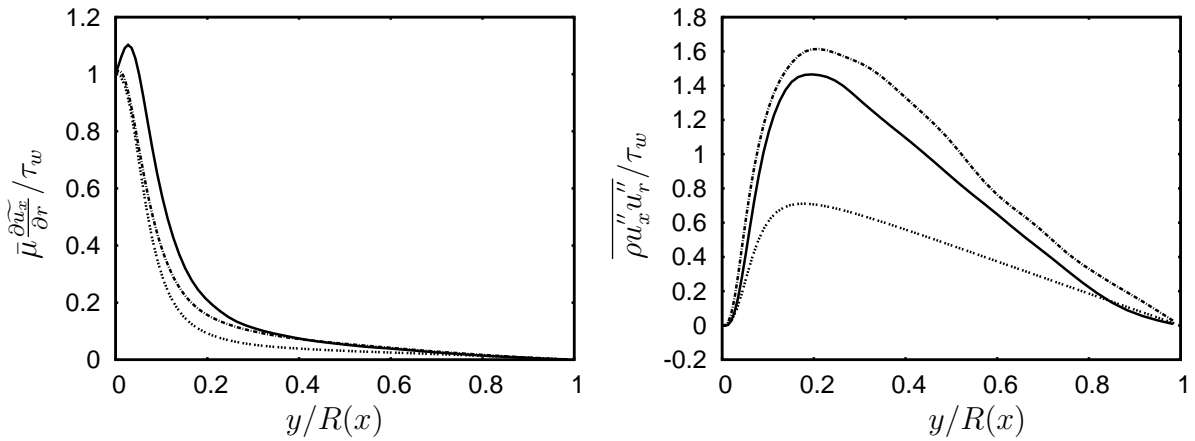


Figure 5.29: Mean shear rate and Reynolds shear stress. $x/L = \dots \dots 0.0$; $—$ 0.5; $-.-.-$ 0.75

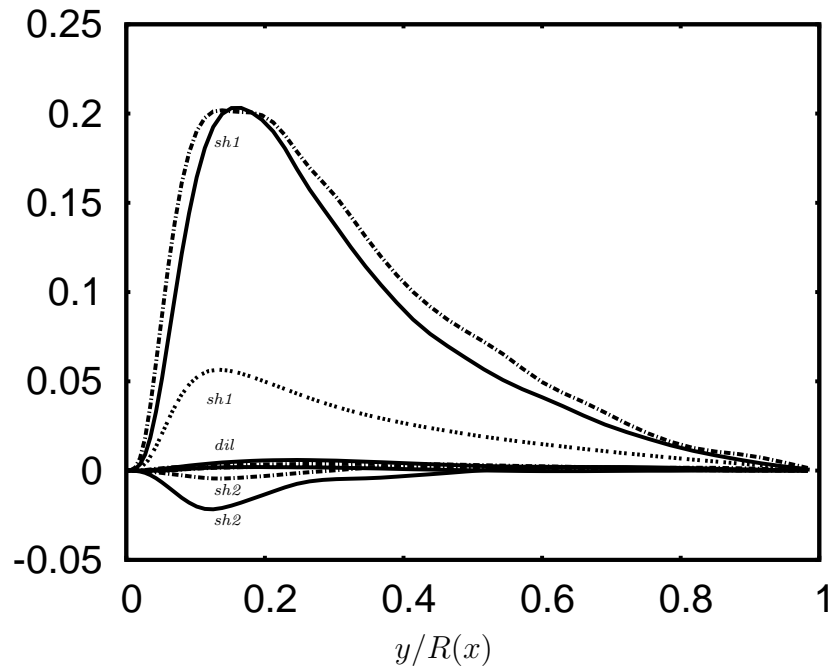


Figure 5.30: Decomposition of production terms in the Reynolds shear stress transport. $x/L = \dots \dots 0.0$; $-$ 0.5; $-.-.$ 0.75. All terms are normalized with $\tau_w^2/\bar{\mu}$.

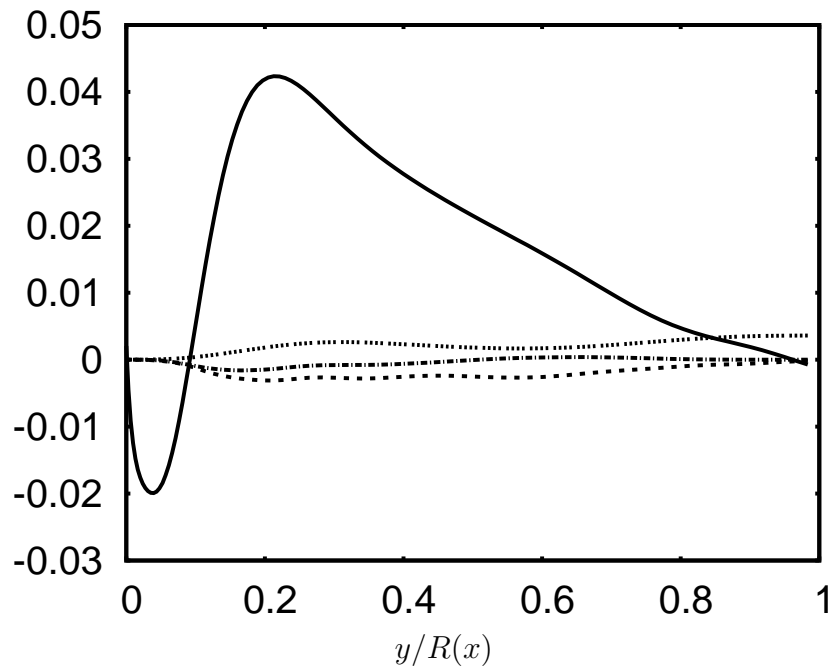


Figure 5.31: Comparison of pressure-strain correlation (PS) and decomposed production term in the radial Reynolds stress budget at $x/L = 0.5$. $-$ PS; $- - -$ extra strain; $-.-.$ shear; $\dots \dots$ dilatation. All terms are normalized with $\tau_w^2/\bar{\mu}$.

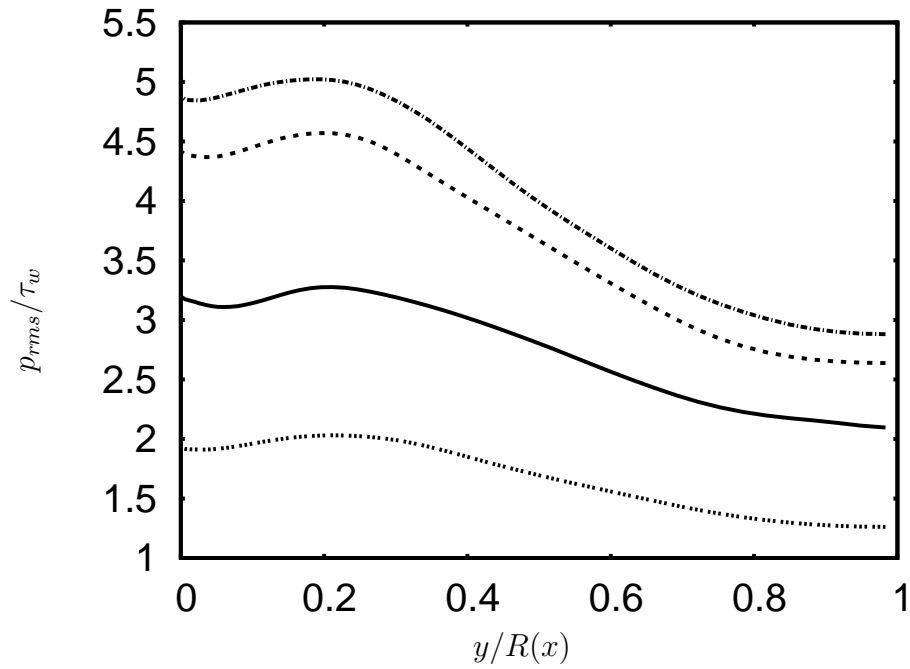


Figure 5.32: Rms pressure fluctuations. Line types as in 5.29

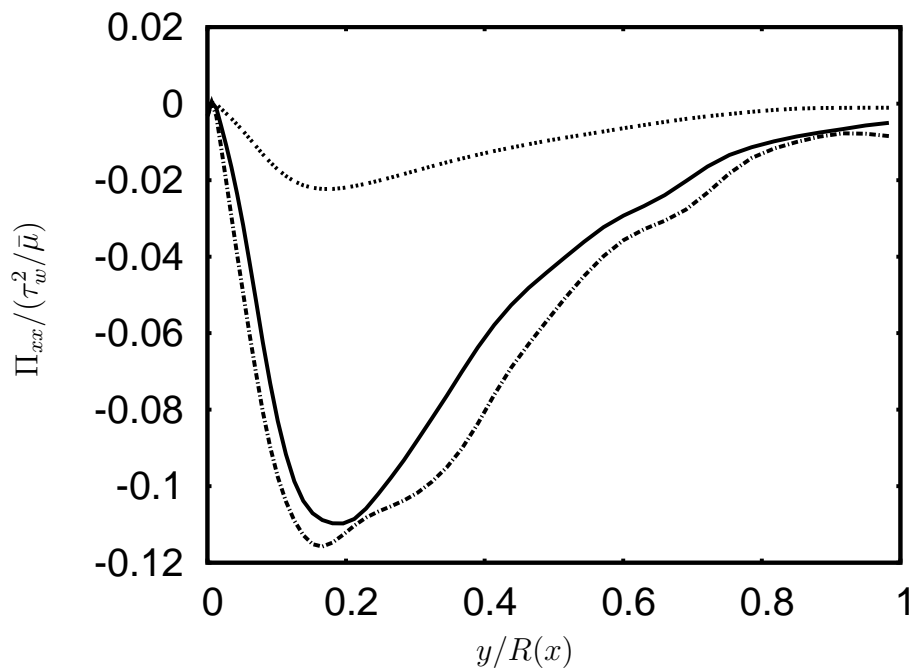


Figure 5.33: Axial pressure-strain correlations. Line types as in fig. 5.29. Terms are normalized with $\tau_w^2/\bar{\mu}$.

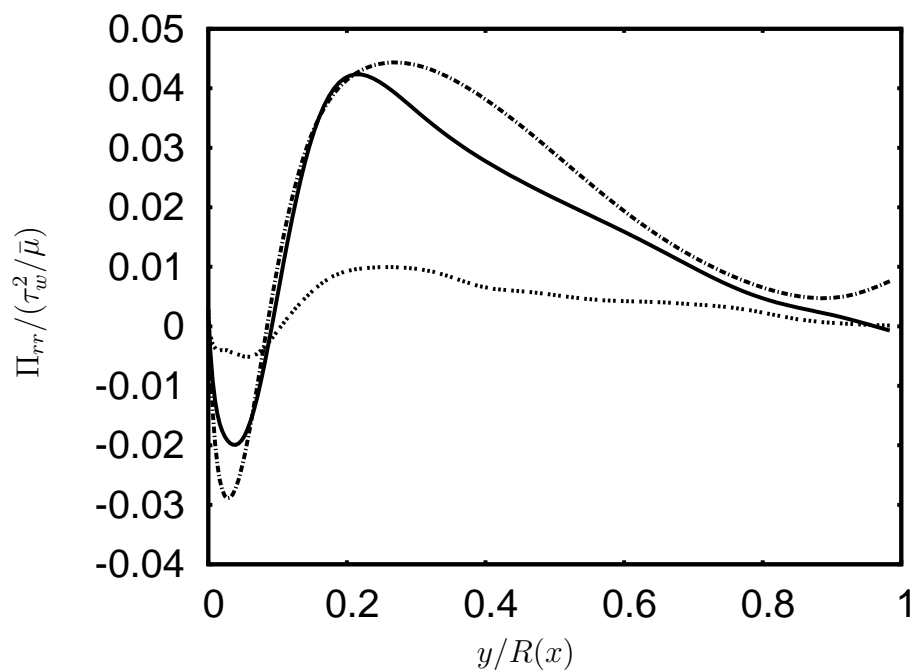


Figure 5.34: Radial pressure-strain correlations. Line types as in fig. 5.29. Terms are normalized with $\tau_w^2/\bar{\mu}$.

5.4 Supersonic diffuser without shock train ($M_{in} = 2.5$)

The objective of this section is to report results from the higher incoming Mach and Reynolds number LES. The incoming flow has a centerline Mach number of 2.5 and a Reynolds number, $Re_\tau = 550$. The area distribution is kept identical to the lower Mach number case which leads to $\beta = 0.5$. This low deceleration along with the high incoming Mach number avoids the appearance of transonic regions near the outflow.

5.4.1 Mean flow features

The flow uniformly decelerates from a Mach number of 2.5 at inflow to 2.25 at exit, figure 5.35. As in the low Mach number diffuser flow, the relative axial increase of pressure and density is stronger than that of the temperature. We do not see local acceleration of the flow near the outflow because of the higher incoming Mach number so that no substantial transonic region appears near the outflow. The wall shear stress shows a decrease at the beginning of deceleration and then a slow increase (fig. 5.36). The displacement thickness shows a corresponding increase, and then a slow decrease.

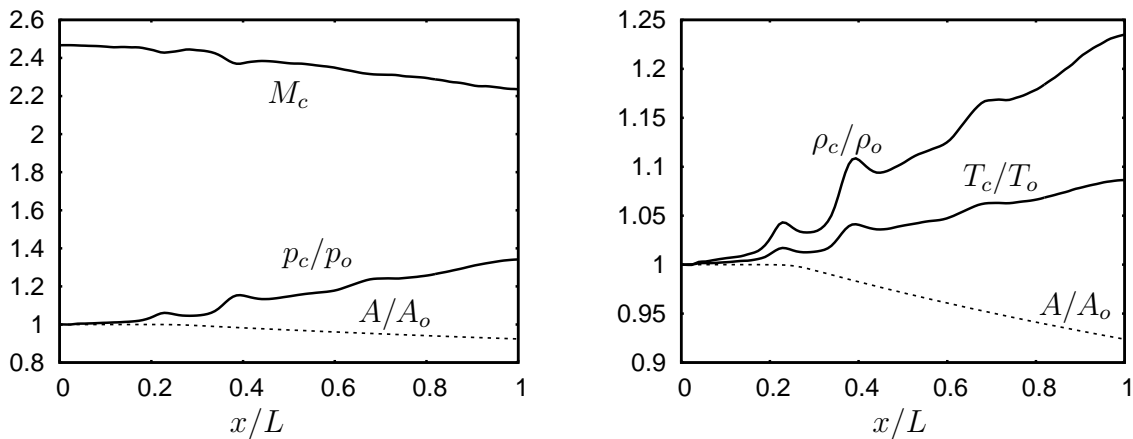


Figure 5.35: Centerline pressure, local Mach number and area; centerline density and temperature.

It must be noted that the relative deceleration is lower in this flow case than in the diffuser at the lower Mach number. The extra strain $\frac{\partial \tilde{u}_x}{\partial x}$ is about 2% of the mean shear, $\frac{\partial \tilde{u}_x}{\partial r}$ (the principal strain) in the peak production zone. Thus, the increase in mean temperature is lower in this case as seen in figure 5.37. In fact, the density profiles normalized with their local wall values show nearly no change at the various axial locations. The small rise in temperature is a result of increased turbulent dissipation, the solenoidal part of which is shown here, fig. 5.37. The dissipation of the mean flow remains nearly unchanged in axial direction. The local Mach number profiles (fig. 5.38) further confirm the weak

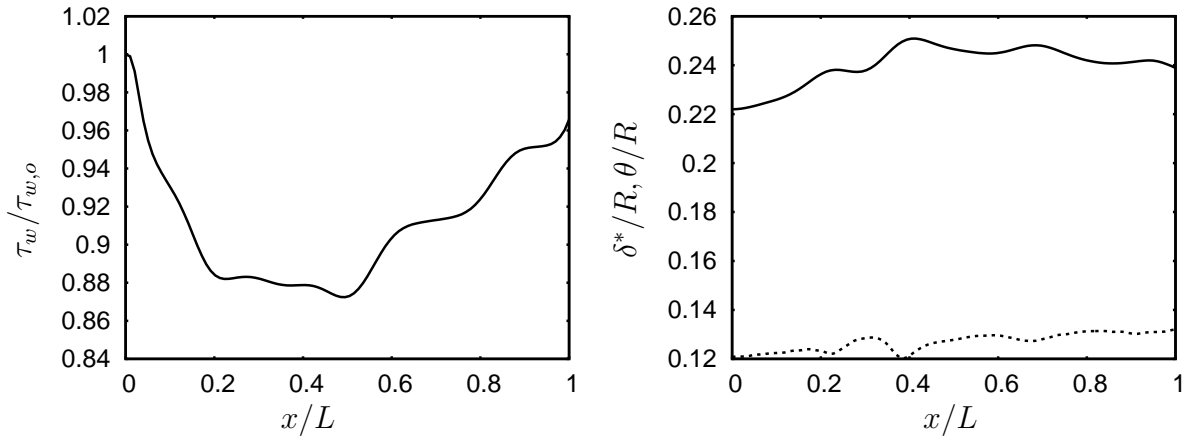


Figure 5.36: Left: Wall shear stress, Right: Displacement (solid line) and momentum thickness (dashed line).

deceleration of the flow. The Van Driest transformed mean velocity profiles (fig. 5.38) show an overshoot above the incoming pipe flow profile in the fully-turbulent region.

5.4.2 Turbulence statistics

The fluctuations of density and temperature which are dictated by the gradients of their mean values, show small increase, figure 5.39. Effects due to dilatation fluctuations are negligible in this diffuser. The axial Reynolds stress is amplified almost uniformly throughout the region of deceleration, figure 5.40. The increase in the axial production is shown in figure 5.41. The decomposition of the axial production term (fig. 5.43) reveals the strong increase of the shear part. The extra strain rate part also shows an increase. The mean dilatation part has a small positive contribution. The axial pressure-strain correlation (and hence the radial pressure-strain correlation) steadily increases in the diffuser (Figure 5.42), which leads to the steady increase in shear production of axial stresses as discussed before.

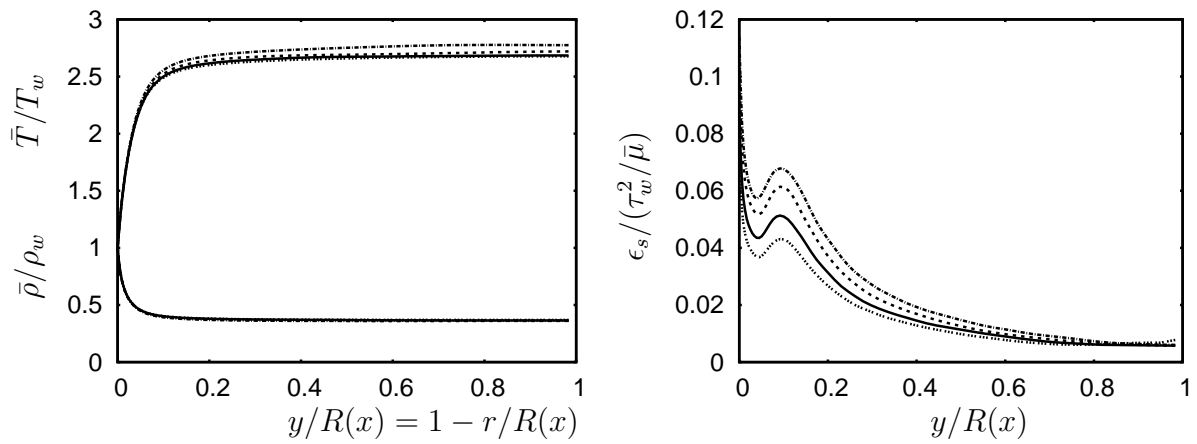


Figure 5.37: Left: Mean density, temperature profiles. Right: Solenoidal dissipation rate. $x/L = \dots \dots 0.0$; $— 0.25$; $--- 0.5$; $-.-.- 0.8$

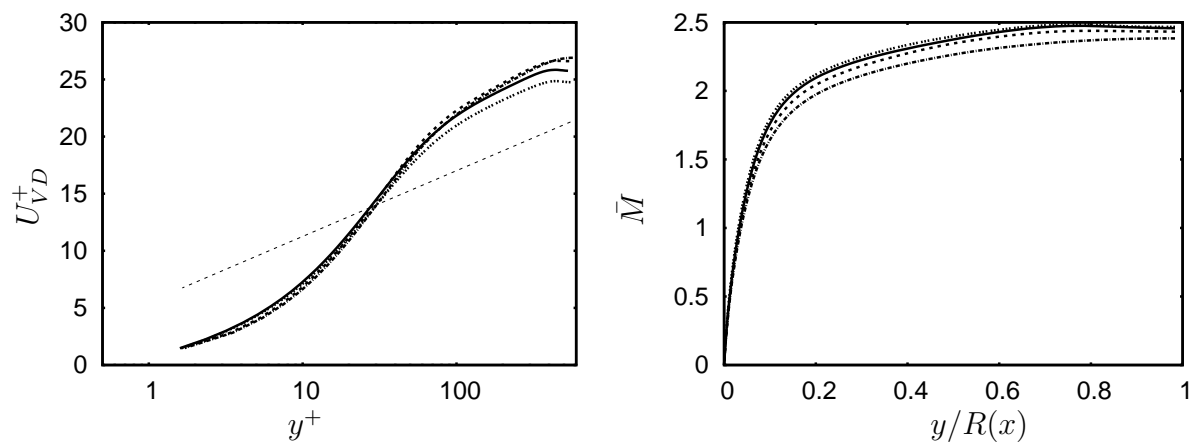


Figure 5.38: Left: Van Driest transformed mean velocity. Right: Local Mach number. Line types as in fig. 5.37. Dashed line in left figure: $u^+ = 2.5 \ln y^+ + 5.5$

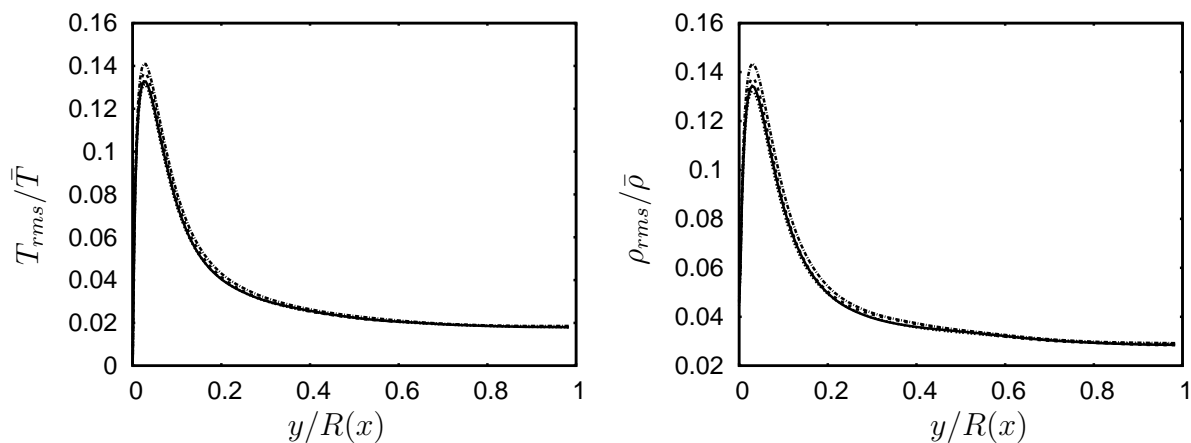


Figure 5.39: Rms temperature and density fluctuations. Line types as in fig. 5.37

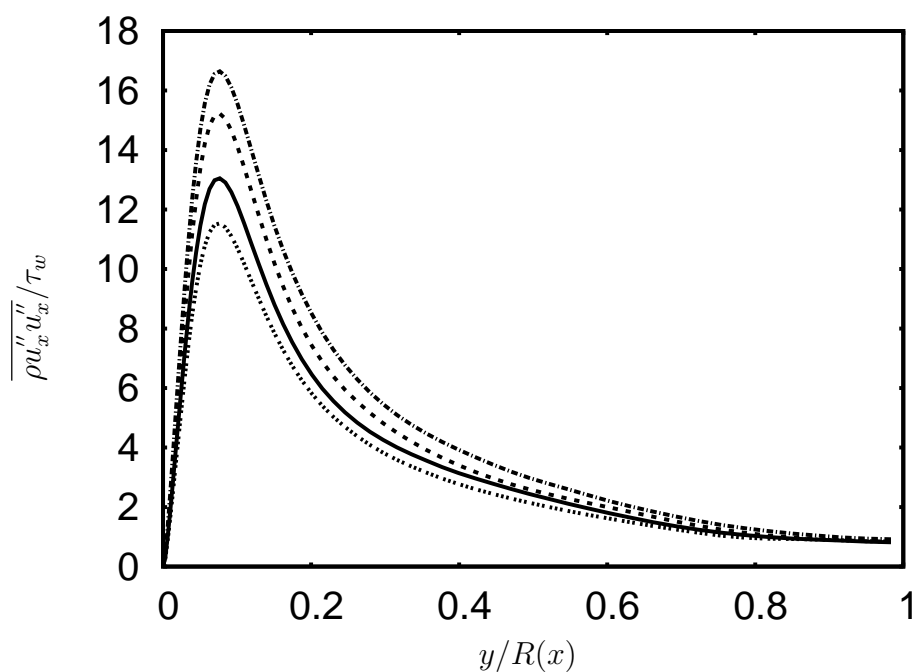


Figure 5.40: Axial Reynolds stress, outer scaling. Line types as in fig. 5.37

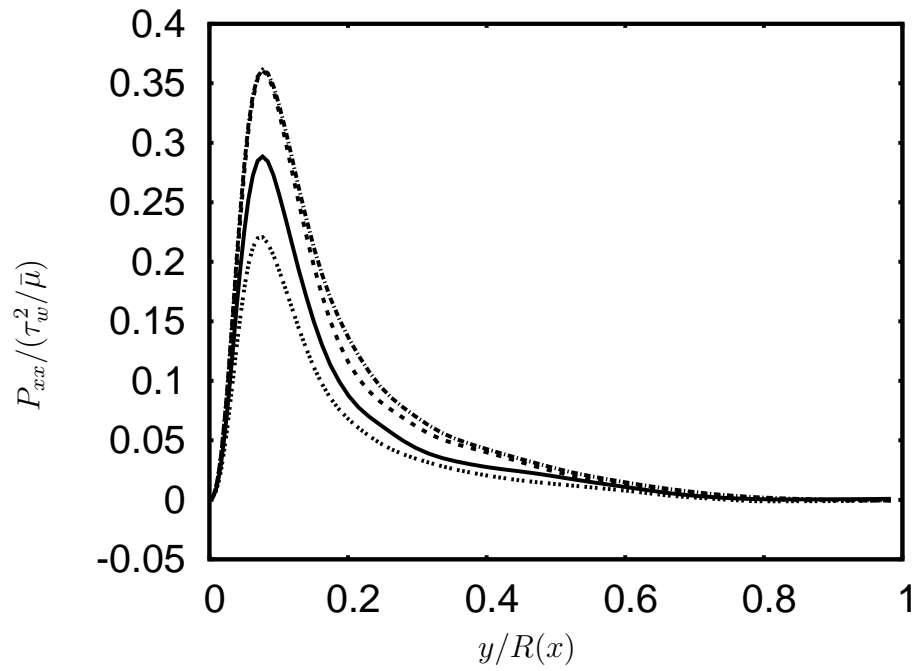


Figure 5.41: Axial production scaled with local $\tau_w^2/\bar{\mu}$. Line types as in fig. 5.37

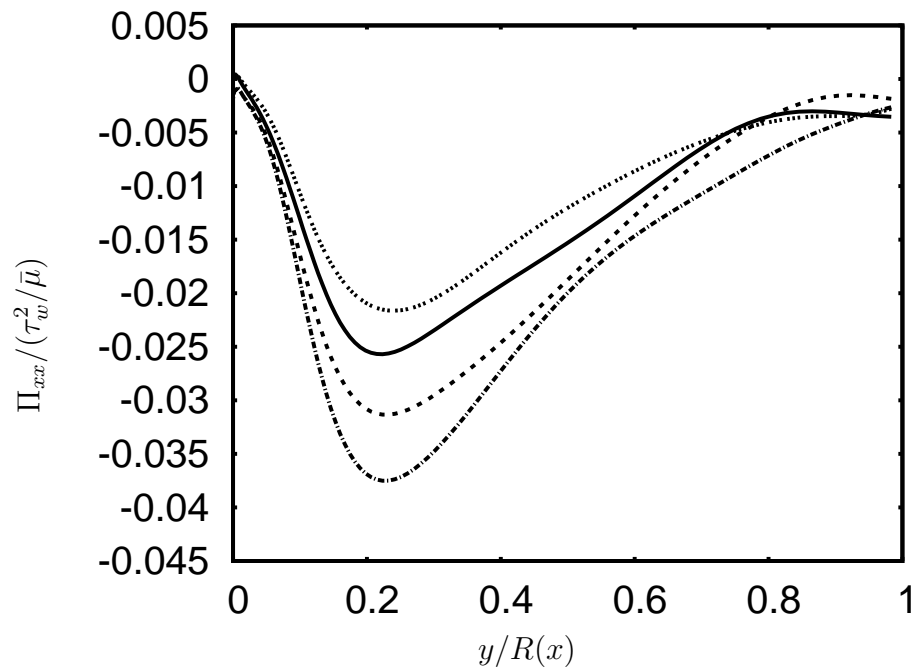


Figure 5.42: Pressure-strain correlation scaled with local $\tau_w^2/\bar{\mu}$. Line types as in fig. 5.37

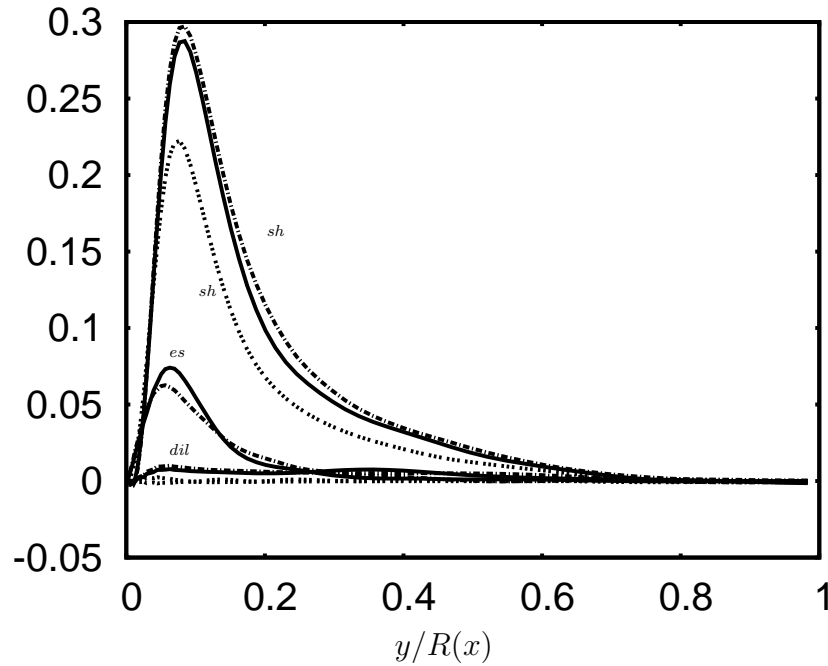


Figure 5.43: Decomposition of axial production term. $x/L = \dots \dots 0.0$; — 0.5; -.- 0.8. sh: mean shear term; es: extra strain rate term; dil: mean dilatation term. Terms are normalized with $\tau_w^2/\bar{\mu}$.

5.5 Supersonic diffuser with shock train ($M_{in} = 1.5$)

The expression 'shock train' refers to a series of shocks which appear when a supersonic flow in a duct is decelerated. The deceleration from supersonic to subsonic flow mostly occurs through a complex pattern of shock-viscous layer interactions and the overall pressure rise occurs over a finite length of the duct. Such a region is called a "pseudo shock" as opposed to a single normal shock. The pseudo shock is generally composed of a "shock train" region consisting of a series of shocks and a "mixing region" without shocks. The occurrence of the mixing region where static pressure rise occurs without shocks depends on the length of the duct. These phenomena are very important in flow devices operating at supersonic speeds. Although, there have been many experimental and RANS investigations of these phenomena, (see Matsuo *et al.* (1999) for an extensive review) time accurate computations have not been extensively performed. To the best of the author's knowledge, there is no high order accurate LES data of flows in which shock trains occur. Such computations are expected to provide more insight into the details of this kind of shock-viscous layer interactions, in which mean dilatation and dilatation fluctuations affect the turbulence structure.

LES of shock-boundary layer interaction studies in case of a compression corner and a compression-expansion corner have been performed by Stolz (2000) and Loginov *et al.* (2006), respectively, using explicit filtering and additional regularization which provides sufficient dissipation to capture the shock and the shocklets that arise.

However, shock-viscous layer interactions in internal flows have not received much attention in the past, mainly because compressible duct flows are expensive to compute even as an LES, especially when one wishes to achieve high Reynolds numbers for comparison with experimental results. This section aims to report new, interesting results regarding shock trains, albeit at low Reynolds numbers. We investigate the effects of a distributed adverse pressure gradient on an incoming fully-developed supersonic pipe flow with $M = 1.5$ and $Re_\tau = 245$ in a diffuser. The shocks that arise in such a case are weak in nature, but the flow features are still expected to be analogous to cases with strong shocks. The resolution for the LES is $64 \times 64 \times 50$ which was found to be sufficient (each shock peak region spans over 6 gridpoints in the axial direction) to capture these weak shocks using explicit filtering.

5.5.1 Instantaneous fields

The structure of the pseudo-shock is clearly visible in the instantaneous pressure field (figure 5.44). Alternate peaks and valleys can be noticed within the shock train indicating regions of alternate expansion and compression. The strength of each individual shock decreases in the direction of the flow. After approximately 65% of the domain length, the flow in the core region becomes transonic and hence no shocks appear there. The shock system shows no appreciable translatory motion.

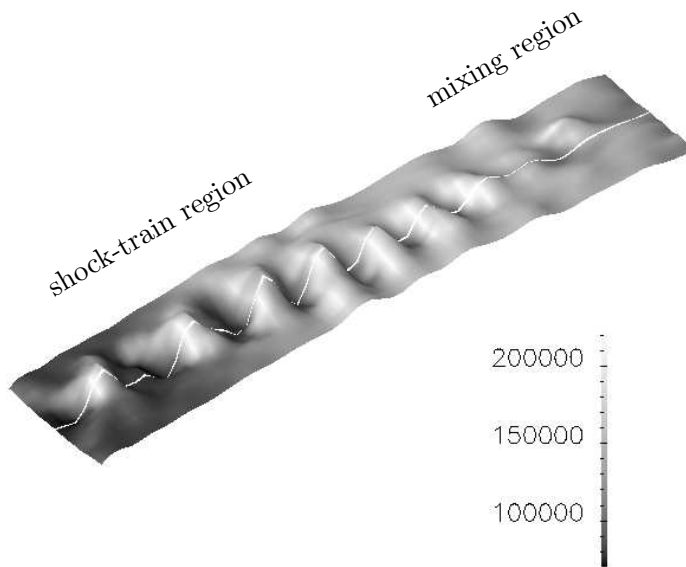


Figure 5.44: Instantaneous pressure in an (x, r) -plane containing the axis. Flow is from left to right.

Time traces of azimuthally averaged wall pressure, instantaneous centerline pressure and centerline Mach number are shown in figures 5.45- 5.47 after the first shock (at $x/L = 0.2$) and in the mixing region ($x/L = 0.75$). The objective is to detect translatory motion

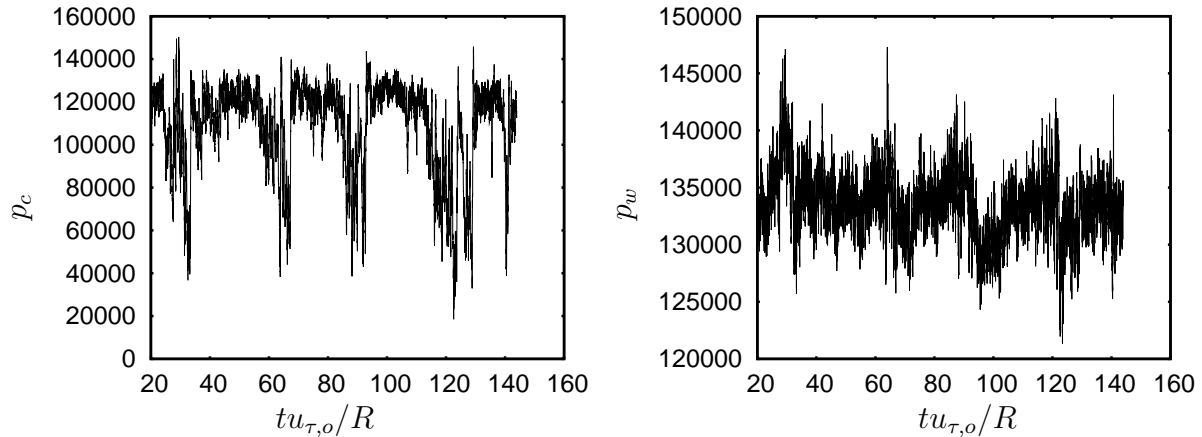


Figure 5.45: Time trace of centerline and wall pressure at $x/L = 0.2$, downstream of the first shock. $u_{\tau,o}$ is the friction velocity at inlet to the diffuser, R is the radius at inlet.

of the shock or its oscillatory nature in the core region. The oscillatory incursions of the shock into the viscous layer near the wall are well-known and have been studied extensively in the past (Adams (2000)). This, however, is beyond the scope of the present work. At this low Reynolds number and due to the APG, the viscous sublayer is thick enough so that the effects of the shock train are small in the wall pressure trace at $x/L = 0.2$, fig. 5.45. Downstream of the first shock ($x/L = 0.2$), strong expansion waves having a time period (in terms of $tu_{\tau,o}/R$, where $u_{\tau,o}$, R are the friction velocity and radius at inlet) of 30 appear in the centerline pressure and Mach number profiles. The quasi-periodic downward excursions of the centerline pressure in Fig. 5.45 (left) must be due to expansion waves, since as seen in fig. 5.48 (left), the position $x/L = 0.2$ corresponds to a low-pressure zone (close to 1 bar) between two pressure peaks and this zone undergoes expansions to pressures below 0.6 bar. These expansion waves demonstrate the low frequency, oscillatory nature of the shock train. It is clear that no major translatory motion occurs since we do not see shocks in these time traces. The centerline pressure trace (and the wall pressure) in the mixing region (fig. 5.46) is close to that of a flow without shock and expansion waves although we can still detect some large oscillations. They could be due to the presence of shocklets. The Mach number trace in the mixing region ($x/L = 0.75$) shows the flow to be transonic (fig. 5.47).

5.5.2 Mean Profiles

The pressure rise, p_2/p_1 , across a normal shock with incoming $M = 1.5$ is estimated to be around 2.45 from one-dimensional equations without friction. The actual pressure rise is lower where pseudo shocks instead of a single normal shock occur as seen from the centerline pressure distribution, figure 5.48. This was also observed in experiments (Matsuo *et al.* (1999)). Alternate compression and expansion zones are visible. The overall pressure rise which is lower than that caused by a single discontinuity occurs over

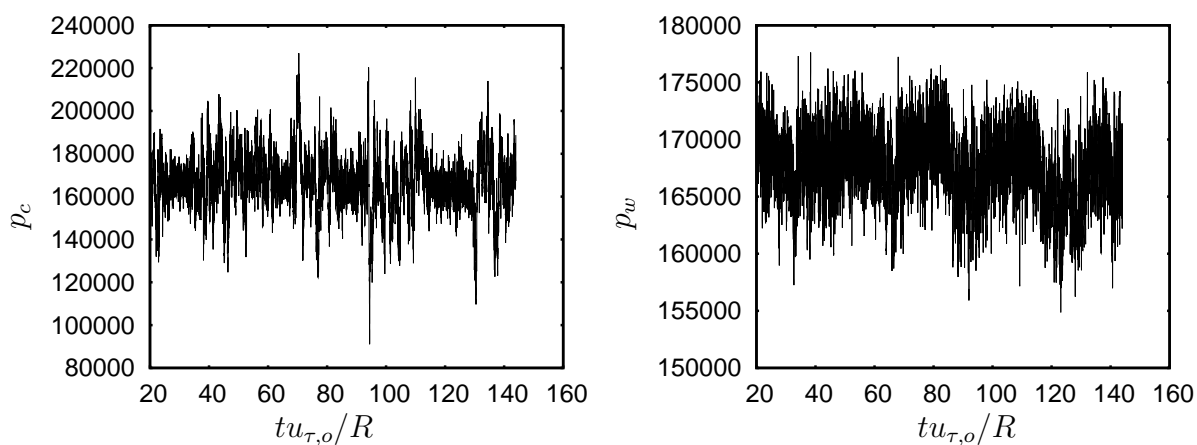


Figure 5.46: Time trace of centerline and azimuthally averaged wall pressure at $x/L = 0.75$, in the mixing region.

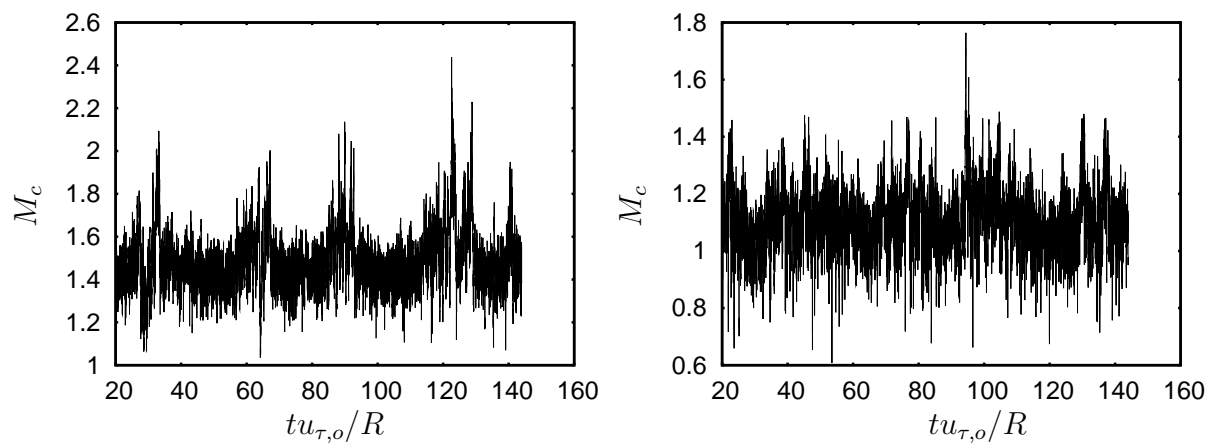


Figure 5.47: Time trace of centerline Mach number $x/L = 0.2$ (left) and $x/L = 0.75$

nearly 70% of the diffuser length in our flow case. The pressure distribution at the wall is predictably smooth, as no shocks can occur in the viscous sublayer. It is interesting to note that the mean centerline pressure fluctuates around values which are nearly equal to the wall pressure. These fluctuations confirm the presence of alternate compression and expansion zones within the shock train.

The local mean centerline Mach number profile (figure 5.49) shows that the shocks are weak since M never reaches subsonic values. However, away from the centerline, where the incoming Mach number is lower, alternate regions of subsonic and supersonic flows are observed.

The axial profile of the centerline density closely resembles that of the centerline pressure. The increase in density is of the same order as that of the pressure. The overall increase in the centerline temperature is found to be lower than that of the density, figure 5.49.

The profiles of mean pressure and density reveal a region where the flow is accelerated in this diffuser after the deceleration through the shock train. This occurs after $x/L = 0.6$ in this transonic flow where the cross-sectional area continues to decrease. The centerline Mach number profile also shows this acceleration region.

The wall shear stress profile along the axial direction (figure 5.48) indicates a region of local flow separation below the first shock ($x/L = 0.15$) which is the strongest of all the shocks in the shock train. The thickening of the incoming viscous layer under the influence of the APG is the reason why a shock train occurs. Whether or not local separation occurs depends on the strength of the shock relative to the momentum of the incoming viscous layer. Control techniques like boundary layer suction and vortex generators have been employed to prevent pseudo-shock occurrence or to restrict it to a single normal shock by decreasing the viscous layer thickness or by injecting more momentum into this layer, Matsuo *et al.* (1999).

The higher incoming displacement and momentum thicknesses in this flow case relative to the case with no shocks at the incoming Mach number 1.8 are shown in figure 5.50. The higher mass and momentum defects in the near-wall viscous region are the reasons for the occurrence of the pseudo shock phenomenon due to further thickening of this region under the influence of the adverse pressure gradient.

We now investigate the evolution of mean flow quantities along the diffuser. Radial distributions of mean density and temperature show that the shocks not only affect the local dissipation near the centerline but also have significant influence in the buffer layer, figure 5.51. This follows from the effects seen in the wall shear stress profiles, fig. 5.48. The local Mach number profiles again show the regions of compression and expansion that characterize this flow. One notices a large transonic region in the profiles after about $x/L = 0.7$.

We now look at Van Driest transformed mean velocity profiles, where the friction velocity u_τ at the entrance is used as a velocity scale, instead of the local value which vanishes in the regions of separation. The profiles show no collapse even very close to the wall, figure 5.52 because we do not use the local quantities for the scaling. After about $x/L = 0.45$, the mean velocity profile shows two different slopes in the logarithmic region. This has also been observed by Wu *et al.* (2006) in their strong APG plane diffuser flow and is interpreted as the signature of an internal layer emerging when the flow is subjected

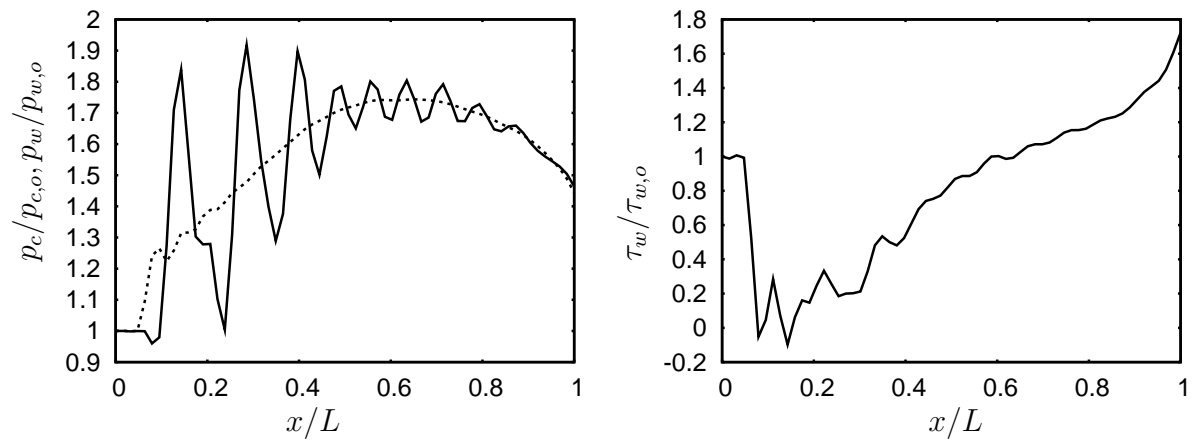


Figure 5.48: Axial distribution of wall (dashed line), centerline (solid line) pressure and wall shear stress.

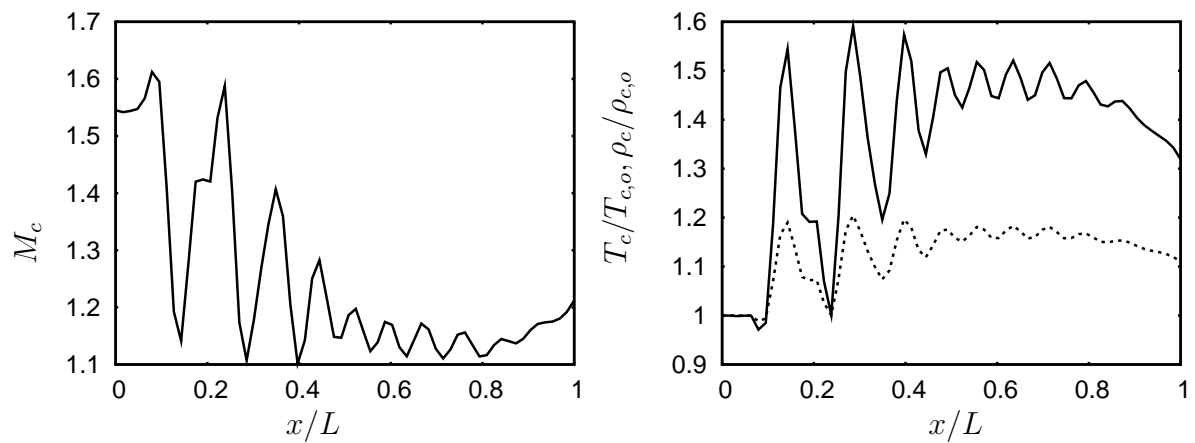


Figure 5.49: Axial distribution of centerline local Mach number, density and temperature. In the figure on the right, the solid line shows density and the dashed line shows temperature distributions.

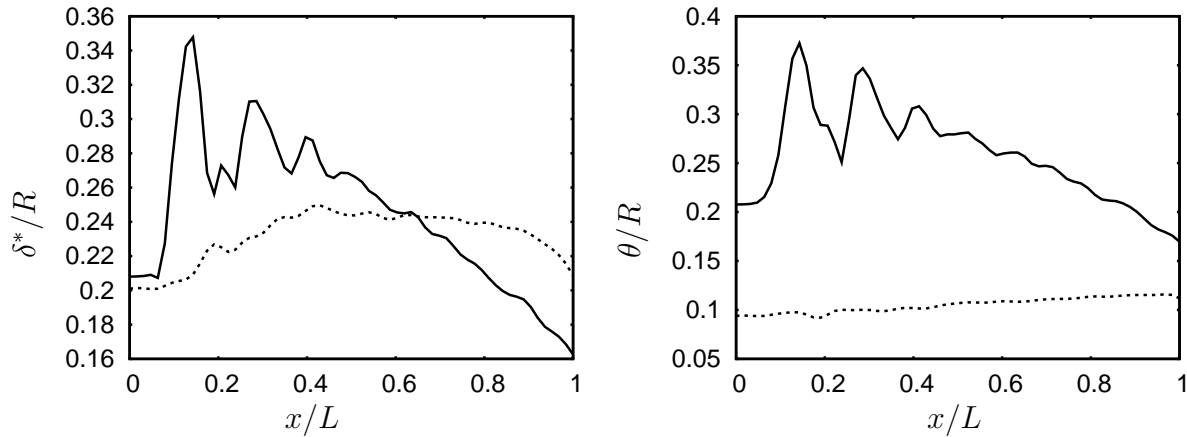


Figure 5.50: Displacement and momentum thicknesses. Solid line: Shock train case; Dashed line: No shock train case (section 5.3)

to strong pressure gradient perturbations. Although we observed distinct inner and outer layer dynamics in the flow case with no shocks (section 5.3), such effects are much more dominant in this flow case with stronger effective APG. We will see further evidences of different inner and outer layer behaviour when we look at the Reynolds stress profiles.

5.5.3 Rms profiles

Turbulent Mach numbers in this flow never increase beyond levels at which intrinsic compressibility effects due to dilatational fluctuations could be expected, figure 5.53. The levels are locally increased near the centerline where the shocks lead to increased turbulent fluctuations. Near $x/L = 0.6$, a second peak in the profile is seen which is a characteristic of an emerging internal layer in flows subjected to large adverse pressure gradients.

The rms pressure fluctuations reach about 25% of the mean pressure in the core near the shocks, which means that this flow is not covered by Morkovin's hypothesis, even though the turbulent Mach number is not significantly high, fig. 5.53. From this point of view we might expect intrinsic compressibility effects due to dilatation fluctuations.

Non-negligible mean temperature and density gradients in the core region lead to significant density fluctuations there, the levels of which are nearly equal and even higher than the peak which occurs in the buffer region. These fluctuations, however, remain within 10% of their respective mean values.

Significant intrinsic compressibility effects are observed in this flow case which is reflected in the peak values of the normalized pressure-dilatation correlation in the core region which are nearly 3 to 4 times the solenoidal dissipation rate in the buffer layer (figure 5.56). Typical non-dimensional deformation rates ($|D|q^2/\epsilon$) estimated in the vicinity of the first and second shocks of this weak shock system lie between 3 to 4 which are much smaller than those in the studies of Cambon *et al.* (1993) and Coleman & Mansour (1993). We used the values of q^2/ϵ in the buffer layer to calculate the deformation rates.

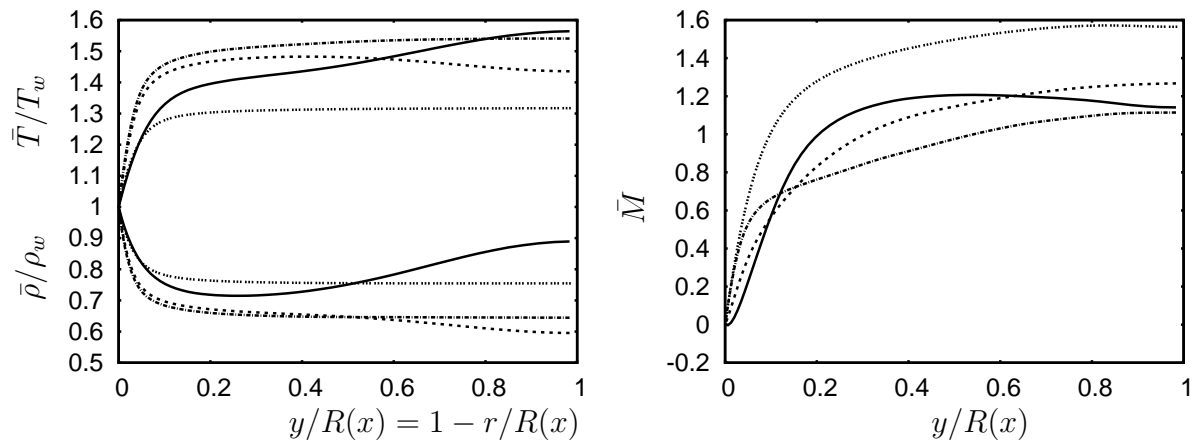


Figure 5.51: Radial density, temperature and local Mach number distribution. $x/L = \dots$
 \dots 0.0, — 0.15, - - - 0.4, -.- 0.6

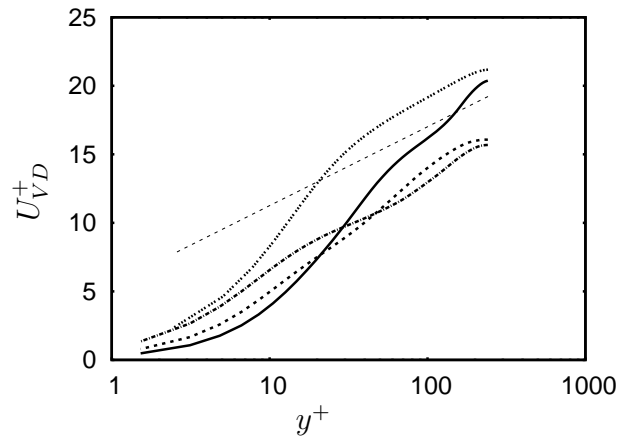


Figure 5.52: Van Driest transformed mean velocity. Line types as in fig. 5.51

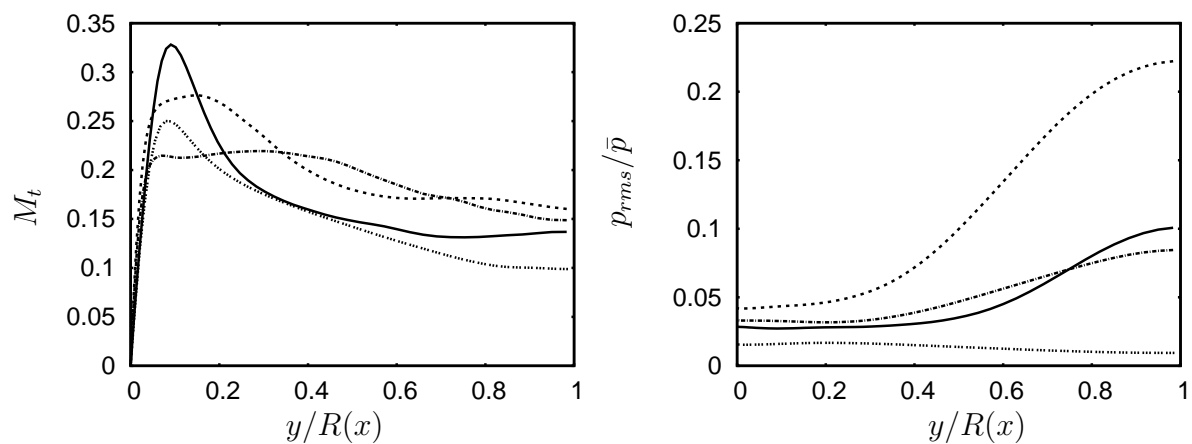


Figure 5.53: Turbulent Mach number and rms pressure fluctuations. Line types as in fig. 5.51

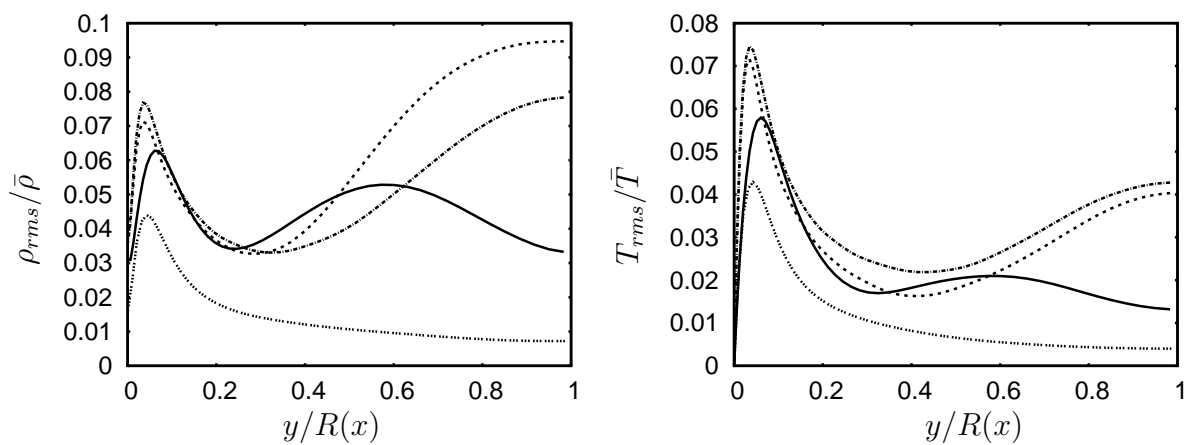


Figure 5.54: Rms density and temperature fluctuations. Line types as in fig. 5.51

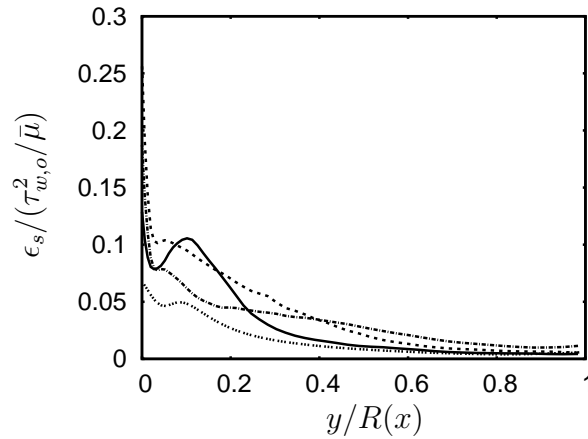


Figure 5.55: Solenoidal dissipation rate. Line types as in fig. 5.51

The solenoidal dissipation rate itself shows an increase in the buffer layer (fig. 5.55). It is to be noted that we used the value of τ_w at the inlet and the local $\bar{\mu}$ to non-dimensionalize ϵ_s . So, only changes in dynamic viscosity is taken into account in the scaling.

From the results, it is evident that the pressure-dilatation correlation plays a significant role in the TKE budget, because turbulence interacts with shocks or zones of strong compression.

5.5.4 Reynolds stresses

The Reynolds stresses are now shown using τ_w at the inlet as a scaling. A look at the individual components reveals a fairly complicated behaviour which needs careful analysis.

The axial component (figure 5.57) shows a drastic increase in the inner viscous layer near the entrance to the diffuser where the first shock occurs. The peaks in the inner layer then go down as we move further downstream. A clear signature of the emergence of an internal layer is shown by the second peak in the stress profiles after around $x/L = 0.4$. This was also observed in the axial mean velocity profiles. The drastic changes in skin friction caused by the shock train results in a new internal layer emerging near the wall after reattachment occurs and the flow outside this layer develops differently. A recent study by Wu *et al.* (2006) reports similar findings for the flow in an incompressible diffuser.

The behaviour of the axial stress in the core region reveals the significant effects of the individual shocks on the turbulence structure. Peaks occur in the profiles near the axial locations where the compression due to shocks takes place. The alternate expansion and compression regions in the shock train result in increase and decrease in the levels of these peaks in the core region. Concerning the amplification of turbulence due to shocks, the reader is referred to the work of Lee *et al.* (1993) and Hannappel & Friedrich (1995). The situation here is more complex since zones of compression (amplification of TKE) are followed by zones of expansion (damping of TKE).

The azimuthal stress profiles (figure 5.58) reveal the internal layer characteristics once

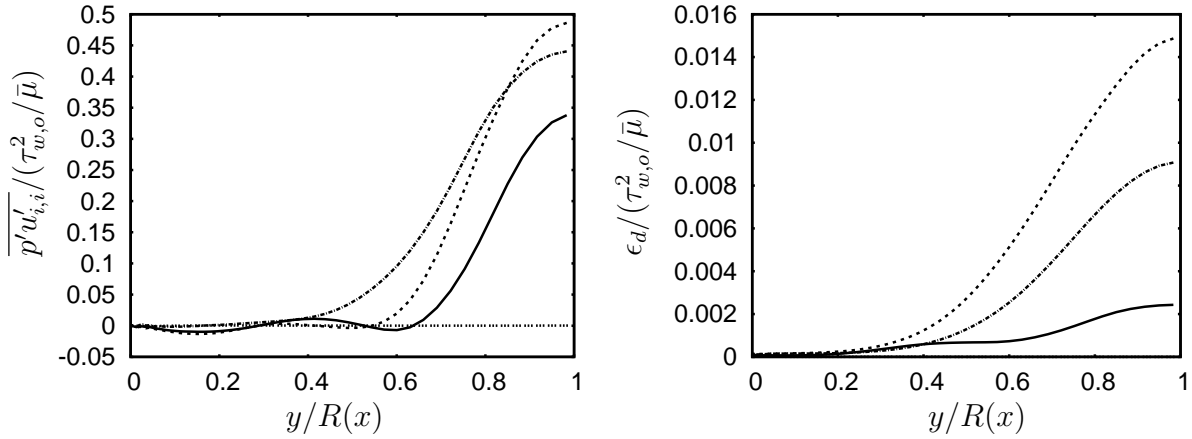


Figure 5.56: Pressure-dilatation correlation and compressible dissipation rate. Line types as in fig. 5.51

again. But the effect of shocks on this component is not as strong as that on the axial component. Only at the location of the first shock we can see a peak in the profile in the core region. The peak levels in the viscous layer increase monotonically up to about $x/L = 0.6$ and then we find a marginal decrease. The two-layer behaviour is especially evident downstream of this location as seen by the increase in stress levels in the outer layer and the simultaneous decrease in the inner layer.

The radial stress (figure 5.59) increases monotonically in the viscous, inner layer up to an axial location of about $x/L = 0.6$. Although, we do not see appreciable evidence of a two-layer behaviour for this stress component, we certainly observe the effects of the shocks on the stress levels in the core region.

5.5.5 Aspects of TKE and Reynolds stress budgets

We finally investigate the production, viscous dissipation and pressure-dilatation correlation terms. The latter act as major source/sink terms in the TKE transport equation in this flow case. The terms are scaled with $\tau_{w,o}^2/\bar{\mu}$, where $\tau_{w,o}$ is the wall shear stress at inlet.

The levels of TKE in the inner, viscous layer are exclusively controlled by the production term, more specifically the axial production term, the peak magnitude of which changes radically in the compression and expansion regions as seen in the figures 5.60-5.63.

In the core region, the pressure-dilatation correlation term is the most important source/sink (for compression/expansion respectively), whose magnitude becomes comparable to that of peak production in the buffer layer. Thus, intrinsic compressibility effects are dominant in this flow case, as was expected. The production term also contributes appreciably in the core region at some axial locations.

Distinct internal layer characteristics, manifested as second peaks in the production

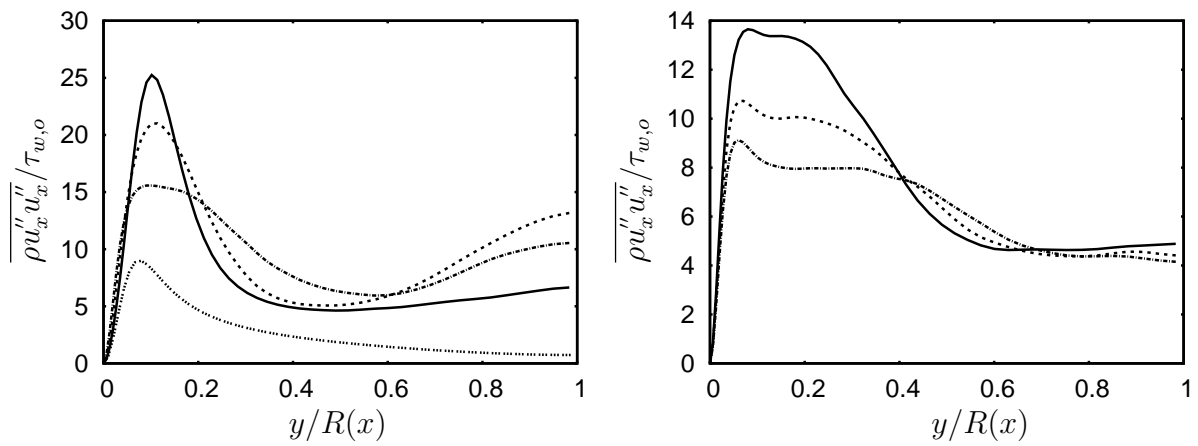


Figure 5.57: Axial Reynolds stress. Left: $x/L = \dots \dots 0.0$; $—$ 0.15; $- - -$ 0.25; $- \cdot -$ 0.3
 Right: $x/L = - - -$ 0.4; $- \cdot -$ 0.55; \dots 0.6

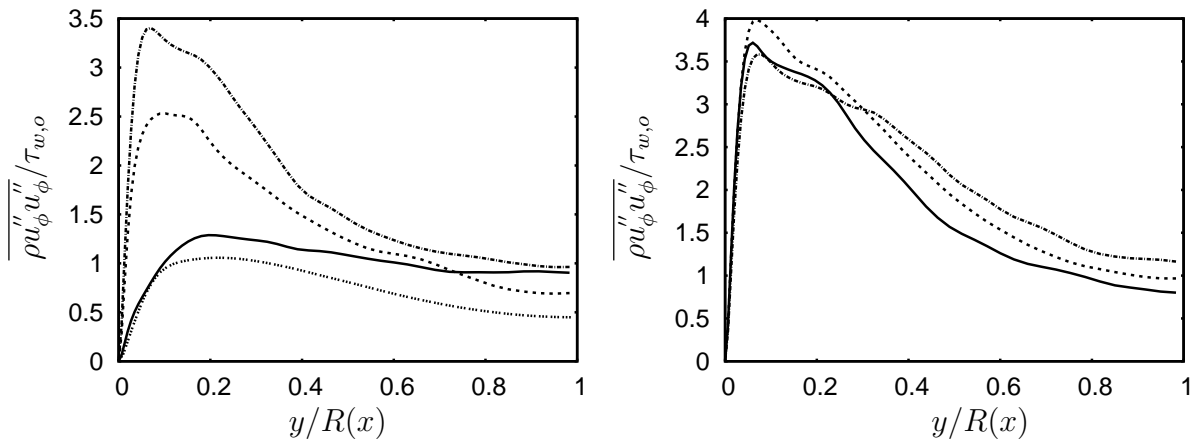


Figure 5.58: Azimuthal Reynolds stress. Line types as in fig. 5.57

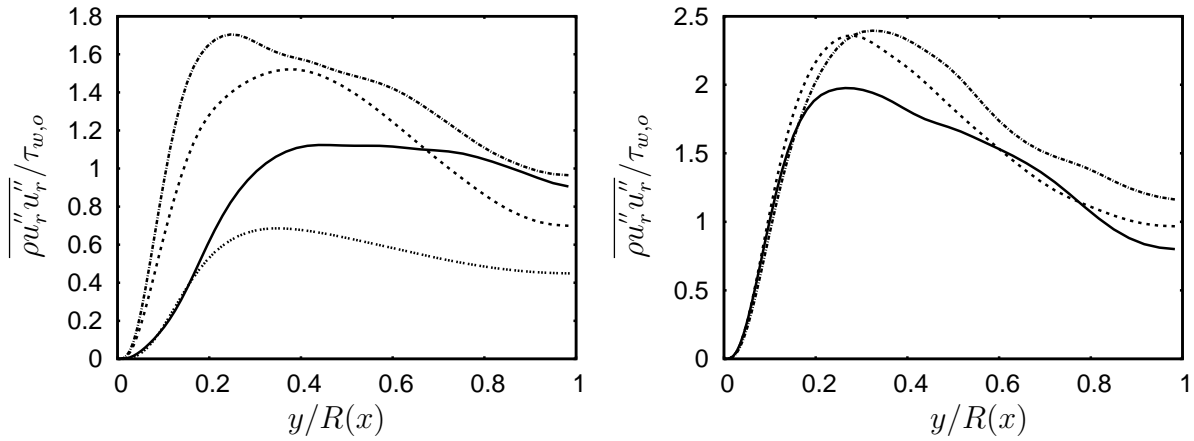


Figure 5.59: Radial Reynolds stress. Line types as in fig. 5.57

profiles, appear after $x/L = 0.5$.

A detailed look at the axial production term which is the dominant term in TKE production is necessary now. The profiles of the term at different axial locations are shown in figure 5.64. The peaks in the inner layer show an initial increase in the region near the first shock (around $x/L = 0.15$). The peak magnitudes then show a decrease as we go downstream. The levels in the core region increase and decrease in the axial direction as the flow experiences alternate compression and expansion regions.

The axial production term is now decomposed into mean shear, extra rate of strain and mean dilatation parts (as in the previous chapters), so as to determine the causes leading to its changes, figures 5.65- 5.67. The extra strain rate term is the dominant source near the first shock location ($x/L = 0.15$) both in the core region as well as in the buffer layer, where production due to shear is expected to be dominant. The source effect of this term in the buffer layer however decreases as we move downstream. The effect in the core region diminishes after the second shock ($x/L = 0.25$). The mean dilatation term has a small source effect in the buffer layer near both the first and second shocks and a much enhanced source effect in the core region at these axial locations. We notice opposing effects of mean dilatation and extra strain rate in the inner, viscous layer after $x/L = 0.25$. The mean shear production term increases up to around $x/L = 0.45$ and then begins to decay as we approach the transonic region. The two-peak behaviour indicating emergence of an internal layer is also observed. These changes are dictated primarily by the changes in Reynolds shear stress i.e. by the redistributive pressure-strain correlation term, fig. 5.68. Changes in mean shear in the peak production region (fig. 5.67) are seen to be a minor contribution to the changes in production due to mean shear.

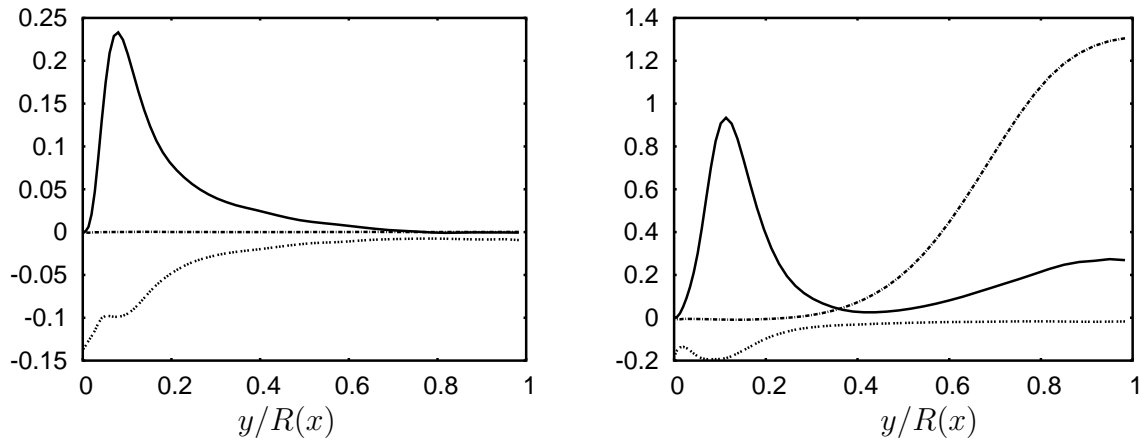


Figure 5.60: Comparison of production (—), dissipation (... ..), pressure dilatation (-.-.-) terms in the TKE budget at $x/L=0$ (left), 0.15 (right). Terms are normalized with $\tau_{w,o}^2/\bar{\mu}$.

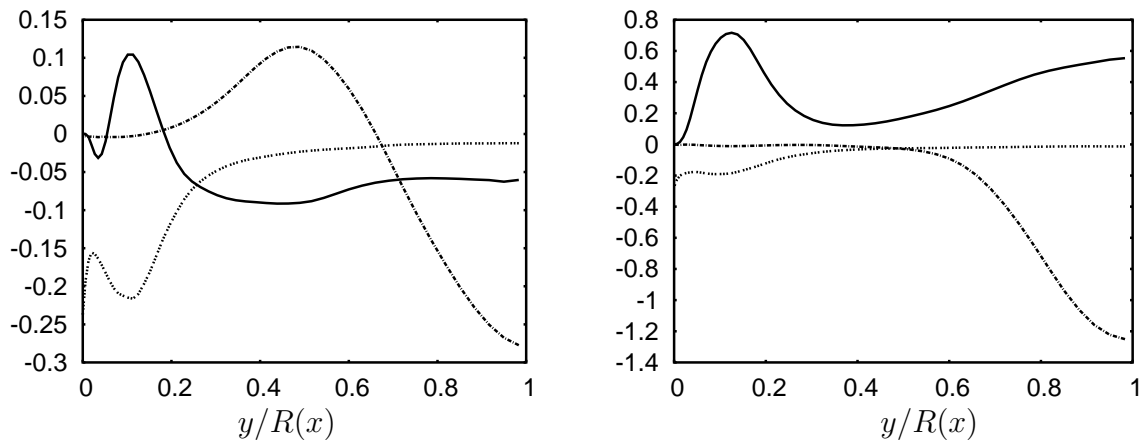


Figure 5.61: Comparison of production (—), dissipation (... ..), pressure dilatation (-.-.-) terms in the TKE budget at $x/L=0.2$ (left), 0.25 (right). Terms are normalized with $\tau_{w,o}^2/\bar{\mu}$.

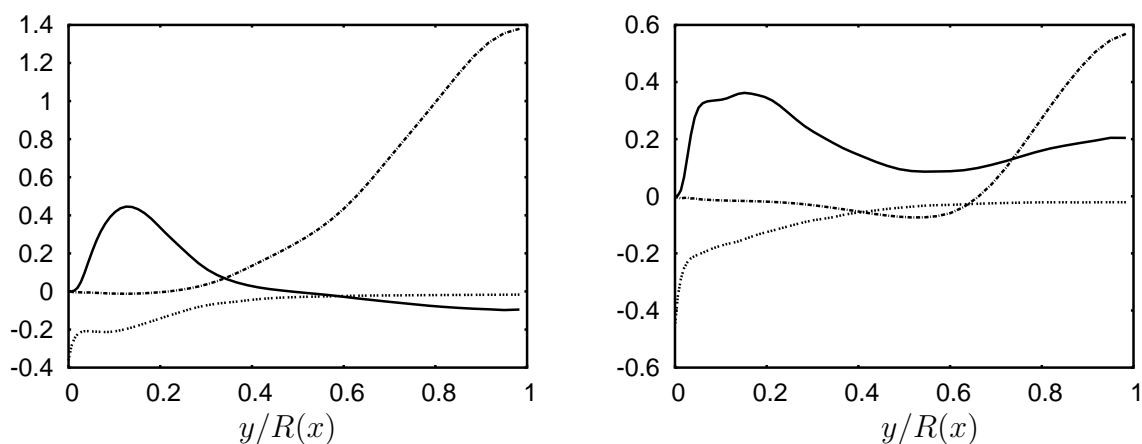


Figure 5.62: Comparison of production (—), dissipation (... ..), pressure dilatation (-.-.-) terms in the TKE budget at $x/L = 0.3$ (left), 0.4 (right). Terms are normalized with $\tau_{w,o}^2/\bar{\mu}$.

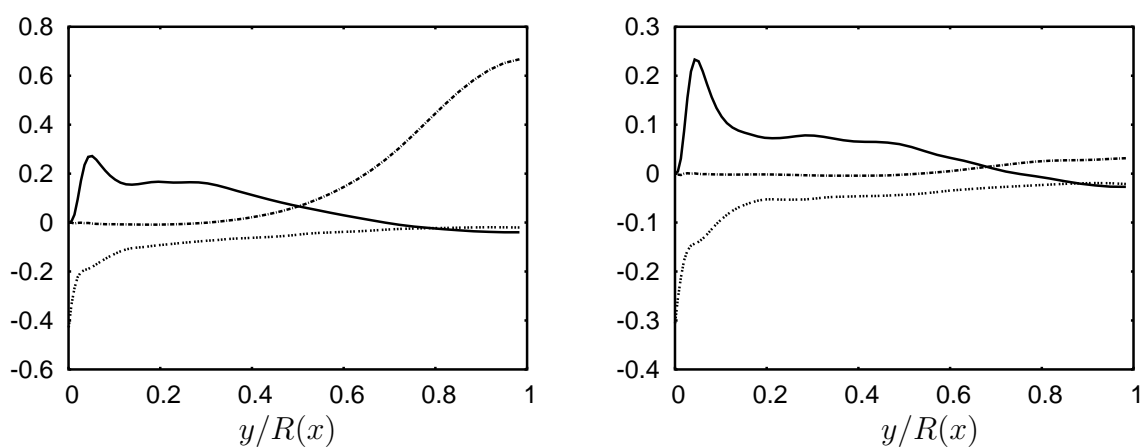


Figure 5.63: Comparison of production (—), dissipation (... ..), pressure dilatation (-.-.-) terms in the TKE budget at $x/L = 0.6$ (left), 0.75 (right). Terms are normalized with $\tau_{w,o}^2/\bar{\mu}$.

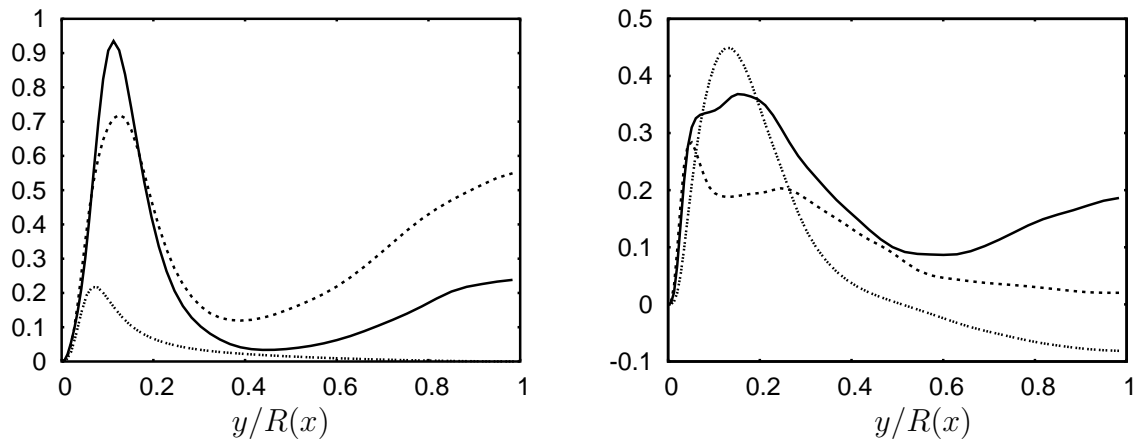


Figure 5.64: Axial production term : $x/L = \dots \dots 0.0$, $—$ 0.15 , $- - -$ 0.25 for the figure on the left and $x/L = \dots \dots 0.3$, $—$ 0.4 , $- - -$ 0.5 for the one on the right. Terms are normalized with $\tau_{w,o}^2/\bar{\mu}$.

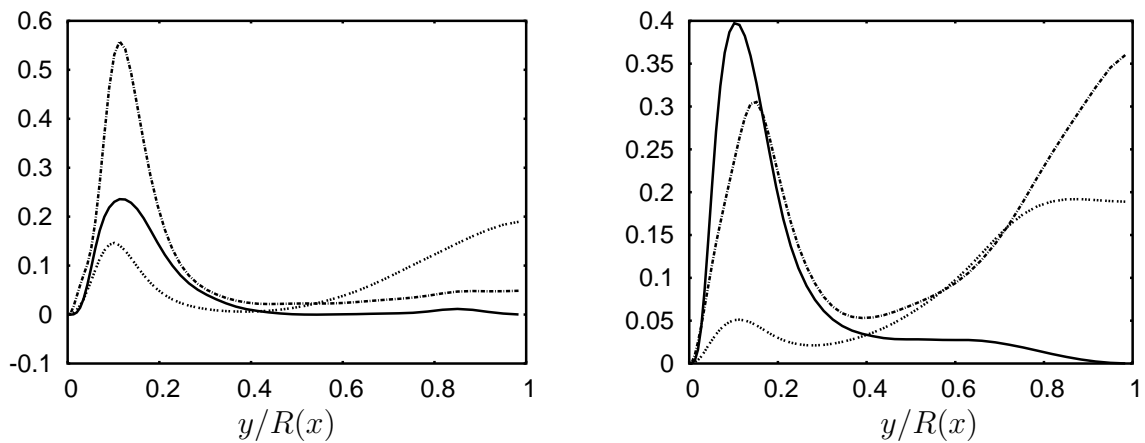


Figure 5.65: Decomposition of axial production term at $x/L = 0.15$ (left), 0.25 (right). $—$, mean shear; $\dots \dots$ mean dilatation; $-.-.-$ extra strain rate. Terms are normalized with $\tau_{w,o}^2/\bar{\mu}$.

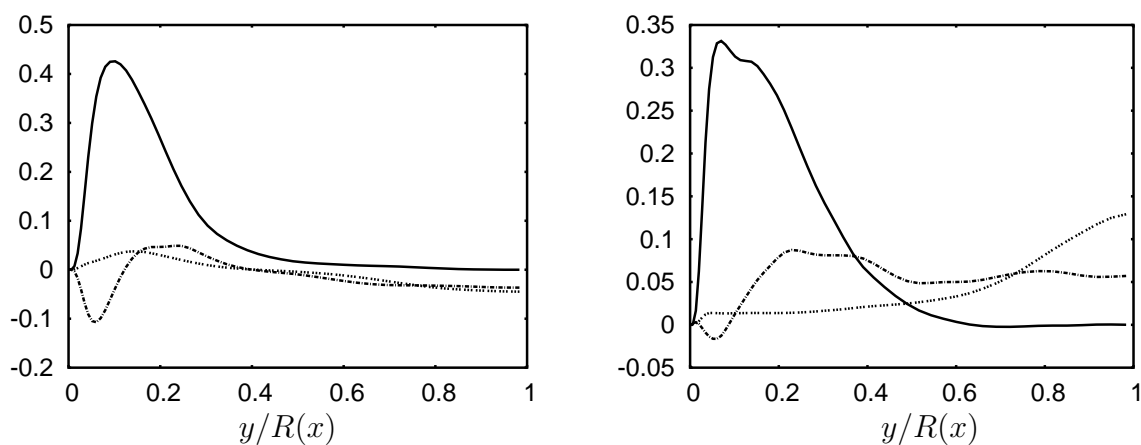


Figure 5.66: Decomposition of axial production term at $x/L = 0.3$ (left), 0.4 (right). Line types as in figure 5.65. Terms are normalized with $\tau_{w,o}^2/\bar{\mu}$.

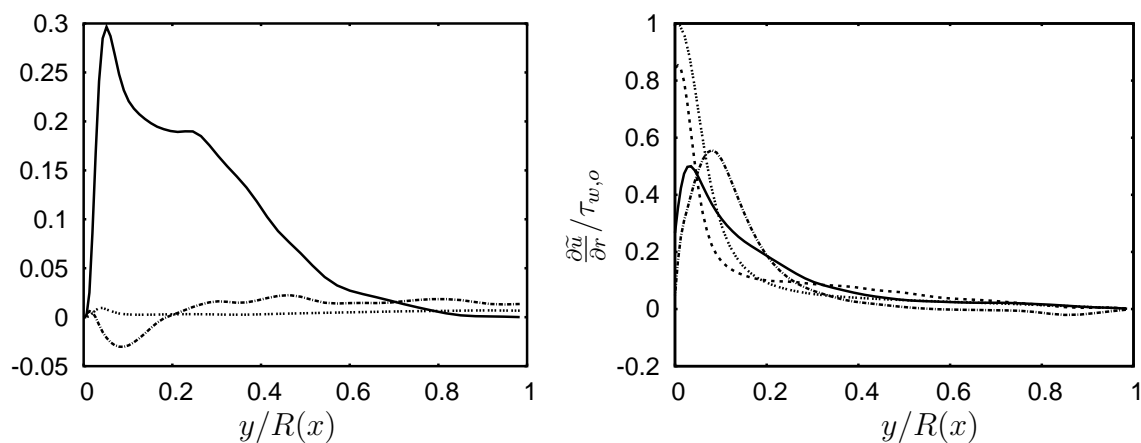


Figure 5.67: Left: Decomposition of axial production term at $x/L = 0.5$. Line types as in figure 5.65. Terms are normalized with $\tau_{w,o}^2/\bar{\mu}$. Right: Mean shear at $x/L = \dots$, 0.0; --- 0.15; — 0.25; - - - 0.5

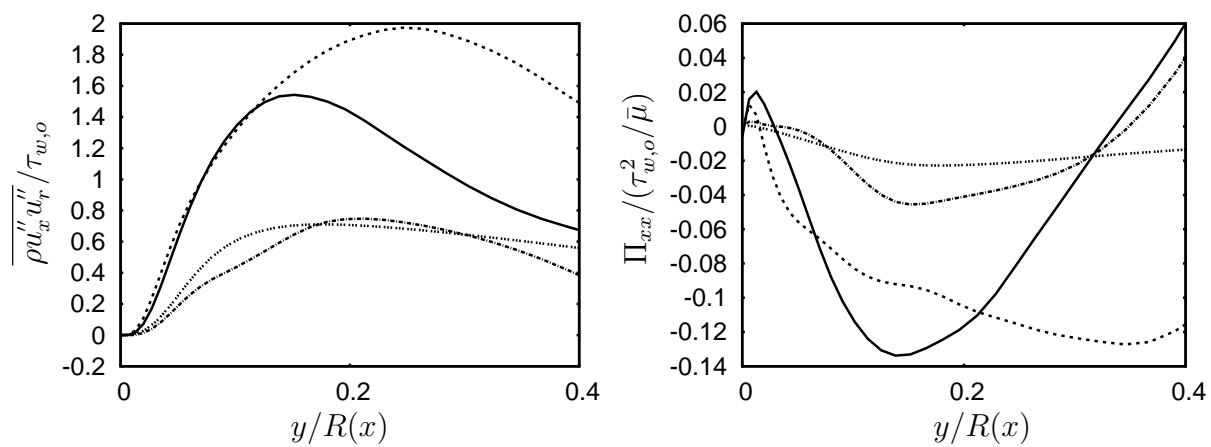


Figure 5.68: Reynolds shear stress (left); Pressure-strain correlations (right). Line types as in figure 5.67 (right)

5.6 Conclusions

Supersonic turbulent flow in weakly converging axisymmetric diffusers with fully-developed supersonic pipe flow at inlet is investigated by means of LES. Although the deceleration is not strong, its effects on the flow depend on the characteristics of the incoming flow when the same diffuser geometry is used.

At incoming Mach numbers 1.8 and 2.5, the flow shows effects of mean compression on the turbulence structure, which are qualitatively opposite to those of mean expansion. However, the degree and spatial variation of these effects on the turbulence structure are dictated by the incoming flow. These flows show considerable nonisentropic effects in the core region. The turbulence intensities are amplified substantially especially in the near-wall region as the flow is compressed. However, in the $M = 1.8$ case, the flow becomes transonic in a substantial region near the outflow which leads to local acceleration and partial decay of turbulence intensities in the buffer layer from their upstream amplified values. This is not the case when the incoming Mach number is 2.5. Here, the turbulence intensities are amplified throughout the length of the diffuser. The effects of weak compression on the turbulence structure appear to be dramatic. Turbulence production is strongly enhanced throughout the region of compression. Extra rates of strain and mean dilatation have small source effects on turbulence production. The major effect of mean compression appear as enhancement of pressure-strain correlations which leads to increased turbulence production by shear. Thus the effects of mean compression on the turbulence structure appear indirectly through the variations of the pressure-strain correlations, as was observed by Bradshaw (1974).

An additional interesting effect is found in the flow with incoming Mach number 1.8. The increase in the thickness of the subsonic region after approximately 65% of the diffuser length leads to distinct inner and outer layer effects as in incompressible APG boundary layers of Coleman *et al.* (2003). Here, the decrease of the mean shear in the inner layer is greater than the increase in shear stress and hence the production by shear goes down marginally from its increased levels. In the flow through the same diffuser geometry at the higher incoming Mach number of 2.5, no transonic zone appears and we find no distinct inner and outer layer behaviour in the turbulence statistics. This again confirms that relatively high APG is required for internal layers to emerge.

When the inflow Mach number is 1.5 (same as the nozzle inflow) and the diffuser geometry is kept the same, shock trains appear in the flow because this flow has a relatively thick viscous layer which thickens further under the APG (the flow locally separates below the first shock). At this Mach number, the shocks are weak, and oscillate about their mean positions at a low frequency. After approximately 50% of the diffuser length, the mean axial velocity profile shows two different slopes in the logarithmic region which is an indication of an internal layer emerging due to strong, local APG in this flow. This is also indicated by second peaks in the axial Reynolds stress profiles and in the axial production term. Intrinsic compressibility effects in the form of high pressure-dilatation correlation in the vicinity of the shock waves act as major source/sink terms in TKE production in the core region. Mean dilatation, extra rates of strain also play a role in the core region as a source/sink of turbulence. The source effect of extra strain rate in the buffer layer at the beginning of compression is large. Mean dilatation causes small source effects in

the buffer region. The production due to shear (and the pressure-strain correlation) is drastically increased throughout the compression region. Large transonic regions after about 50% of the diffuser length lead to partial decrease of turbulence intensities through mechanisms discussed earlier.

The complicated nature of compressible wall-bounded flows subjected to deceleration is obvious from this study and all the abovementioned effects provide sufficient motivation for future work.

Chapter 6

Summary and outlook

With increasing supercomputing power it is now possible to simulate compressible wall-bounded flows at reasonable Reynolds numbers directly. Flow cases simulated in the past are mostly boundary layers and plane channel flows in the supersonic Mach number range. These studies provided sufficient evidence that Morkovin’s hypothesis formulated in his strong Reynolds analogy and referring to nearly negligible total temperature variations, holds only in flows with adiabatic walls. Internal supersonic flows, however need wall cooling to avoid choking. However even in these flows pressure fluctuations are negligible and do not affect the turbulence structure. In channel flows with cooled walls, for example, increasing Mach numbers lead to increased viscous dissipation and finally produce strong temperature (and density, viscosity) gradients in the near-wall region. These variations in mean properties are the only “compressibility effects” found in these flows and need to be taken into account for modelling purposes.

The first part of this thesis examines these effects in the context of supersonic pipe flows. DNS and LES of these flows with isothermal wall at a subsonic ($M = 0.3$) and a supersonic Mach number ($M = 1.5$) have been performed to assess compressibility effects. The computations are performed in cylindrical coordinates using high order compact schemes in a finite difference mode. The axis singularity is removed by placing no gridpoint on the axis by means of suitable staggering (Mohseni & Colonius (2000)) which provides physical instantaneous fields and statistics. As in plane channel flows, the “compressibility” effects in supersonic pipe flows originate from the mean property variations in the near-wall region which change the structure of turbulence. A Van Driest transformation involving a mean density scaling brings the supersonic streamwise mean velocity profile close to the subsonic one. A new scaling proposed by Brun *et al.* (2008) which modifies the Van Driest transform by taking into account near-wall viscosity variations works better in the fully turbulent region. The rms velocity fluctuations, however, show a better collapse with their nearly incompressible counterparts in the near-wall region when semi-local scaling (Huang *et al.* (1995)) involving local mean density is used instead of the wall values. Although their near-wall peaks appear in the same radial locations their magnitudes do not collapse. We also used the scalings proposed by Brun *et al.* (2008) and found that there is no appreciable improvement over the scalings of Huang *et al.* (1995). The outer scaling of the Reynolds stresses using τ_w works away from the wall where viscous effects are small. In this scaling the increased anisotropy in the supersonic pipe flow

is distinctly visible in the near-wall region. The streamwise stresses are increased and radial, azimuthal and shear stresses are decreased. The reason for this increased anisotropy is the reduction in the redistributive pressure-strain term in the supersonic case. This is seen when the streamwise budget terms are scaled using $\tau_w^2/\bar{\mu}$. Among the net source and sink terms, production and dissipation show a collapse but the pressure-strain correlations do not. The observed reduction in pressure-strain correlations results in the increase of streamwise stress and decrease in the other components. In channel flows it was shown by Foyi *et al.* (2004) that the reduction in pressure-strain correlations is due to the reduced density in the supersonic flow. Similar arguments also apply for supersonic pipe flows.

Large-eddy simulations (LES) have also been performed to predict supersonic pipe flow using a single-step explicit filtering version of the Approximate Deconvolution Method. The LES provides proper prediction of the production and pressure strain terms which are governed mainly by large scales. Predictions of terms governed by small scales like turbulent dissipation have to be handled with caution. At least the trends provided by the LES results of turbulent dissipation e.g. due to increasing Mach number can be used with confidence.

The second part of the thesis contains DNS and LES results of supersonic nozzle and diffuser flows with incoming fully-developed supersonic pipe flow. Here we intend to observe the effects of weak acceleration or deceleration on the turbulence structure. Such flows are not covered by Morkovin's hypothesis and their behaviour cannot be predicted from knowledge of their incompressible counterparts. The area distribution in these flow cases is such that there is a substantial region of constant weak, mean axial pressure gradient.

First we focus on the flow features in the nozzle with incoming pipe flow at $M = 1.5$ based on DNS and LES data. The extra strain rate in the peak production region is about 15% of the mean shear. The expansion in the core of the nozzle is essentially isentropic as seen in the centerline pressure and density profiles. Radial pressure gradients are small and the mean temperature and density remain coupled radially. The strong axial density variation leads to a failure of the Van Driest transformation for the axial velocity in the fully turbulent region. This effect was also noticed in strongly heated low-speed pipe flows (Bae *et al.* (2006)). Dilatation fluctuations are negligible in this case. The weak acceleration in the nozzle leads to strong decay in all turbulence intensities. Decomposition of the production terms in the individual Reynolds stress equations is performed in order to explain the decay of turbulence in this flow case. It is found that both extra rates of strain and mean dilatation act as small sinks in the axial production but the major cause of decay in axial production is due to the reduction of production due to shear. Since the mean shear remains essentially constant along the nozzle, the reduced Reynolds shear stress is the cause of reduced production due to shear. Production of the Reynolds shear stress is again found to decrease due to reduction in production due to shear. This is caused by the decay of the radial stress which is primarily produced by the redistributive pressure-strain term. So, finally, the decay in turbulence in this nozzle is essentially due to a decay in pressure-strain correlations. Both pressure fluctuations and strain rate fluctuations decay.

Decelerated wall-bounded flows show more complicating features as compared to the accelerated ones. Strong adverse pressure gradients are known to cause appearance of

internal layers as already reported for incompressible diffuser flows (Wu *et al.* (2006)). If the flow is compressible additional complications due to appearance of shocks may occur. We report LES results of two flow cases, one in which only mean compression effects appear and the other where we have strong dilatation fluctuations due to shocks.

We have looked at two diffuser flow cases having incoming Mach numbers 1.8 and 2.5 where only mean compression effects are important and dilatation fluctuations are negligible. The higher incoming Mach numbers at the inlet are required to avoid large transonic regions near the diffuser outflow. These flows show deviations from the isentropic streamtube equations in the core. The turbulence intensities are strongly amplified throughout the region of compression. Decomposition of the production terms as in the nozzle flow case show that although extra rates of strain and mean dilatation act as small sources, the main reason for the increased turbulence production is the amplification of pressure-strain correlations. Distinct inner and outer layer behaviour (as in Coleman *et al.* (2003)) is observed for the flow with incoming $M = 1.8$ in the Reynolds stress profiles during the final stages of compression after about 65% of the diffuser length. It should be noted that the flow is transonic in this region.

Thus, our DNS and LES of nozzle and diffuser flows with weak mean dilatation provide support to the observations of Bradshaw (1974) that the effects of mean dilatation on the Reynolds stresses are far greater than those predicted by the extra production terms in their transport equations. Indeed, the modification of pressure-strain correlations plays the most significant role in modifying the turbulence structure in these flows.

As an appropriate closure to this work, LES of a diffuser flow at incoming $M = 1.5$ has been performed where shock trains appear. This is because at this Mach (and Reynolds) number, the APG resulting from the geometry of the diffuser is strong enough to cause substantial thickening of the viscous layer. The pressure rise in such a flow occurs through a region of weak shocks instead of a single normal shock. This is the direct consequence of a thickened viscous region. Alternating regions of strong compression and expansion appear and the flow is highly nonisentropic. These weak shocks subsequently bring the flow to a transonic state. The overall pressure rise occurs in a distributed manner as opposed to that through a single discontinuity. The region over which the pressure rise occurs is called a “pseudo-shock region” in the literature (Matsuo *et al.*, 1999). The individual shocks oscillate about their mean positions, but no translatory motion is observed. Appreciable values of pressure-dilatation correlations are observed in the core region in the vicinity of the shocks. The turbulence production here is also increased directly by mean dilatation and extra strain rates. Near the wall extra strain rates now have a larger effect on turbulence production compared to the no-shock case. Emergence of an internal layer indicated by the dual slope behaviour in the log-region of mean axial velocity and the second peaks in the Reynolds stress profiles is noticed in this flow. Further research is aimed at investigating the causes of the oscillatory shock motion and the detailed effects of shock trains including flow separation on the turbulence structure.

The flows investigated in this study form a generic class of internal, compressible flows with circular cross-section. Especially, the spatially developing nozzle and diffuser flows provide interesting canonical test cases for modelling purposes. Future work should focus on flow cases with longer sections where the pipe radius is constant before it increases or decreases downstream and on longer nozzles and diffusers in order to minimize inflow

and outflow effects. There is also a strong interest in performing direct simulations of supersonic diffusers operating in the shock-train mode, since they will allow for a detailed and unambiguous study of all flow phenomena.

Bibliography

- ADAMS, N. A. 2000 Direct simulation of turbulent boundary layer along a compression ramp at $M = 3$ and $Re_\theta = 1685$. *Journal of Fluid Mechanics* **420**, 47–83.
- ADAMS, N. A. & LEONARD, A. 1999 Deconvolution of subgrid scales for the simulation of shock-turbulence interaction. In *Direct and Large-Eddy simulation III* (ed. P. Voke, N. D. Sandham & L. Kleiser), p. 201.
- ADAMS, N. A. & SHARIFF, K. 1996 A high-resolution hybrid compact-ENO scheme for shock-turbulence interaction problems. *Journal of Computational Physics* **127**, 27–51.
- BAE, J. H., YOO, J. Y., CHOI, H. & MCELIGOT, D. M. 2006 Effects of large density variation on strongly heated internal air flows. *Physics of fluids* **18**, 075102–1.
- BLAISDELL, G. A., MANSOUR, N. N. & REYNOLDS, W. C. 1993 Compressibility effects on the growth and structure of homogeneous turbulent shear flow. *Journal of Fluid Mechanics* **256**, 443–485.
- BOGEY, C. & BAILLY, C. 2006 Computation of a high Reynolds number jet and its radiated noise using large eddy simulation based on explicit filtering. *Computers and fluids* **35**, 1344–1358.
- BRADSHAW, P. 1974 The effect of mean compression or dilatation on the turbulence structure of supersonic boundary layers. *Journal of Fluid Mechanics* **63**, 449–464.
- BRADSHAW, P. 1977 Compressible turbulent shear layers. *Annual Rev. Fluid Mech.* **9**, 33–52.
- BRUN, C., BOIARCIUC, M., HABERKORN, M. & COMTE, P. 2008 Large eddy simulation of compressible channel flow. *Theoretical and computational fluid dynamics*, DOI: [10.1007/s00162-007-0073-y](https://doi.org/10.1007/s00162-007-0073-y).
- CAMBON, C., COLEMAN, G. N. & MANSOUR, N. N. 1993 Rapid distortion analysis and direct simulation of compressible homogeneous turbulence at finite Mach numbers. *Journal of Fluid Mechanics* **257**, 641–665.
- COLEMAN, G. N., KIM, J. & MOSER, R. D. 1995 A numerical study of turbulent supersonic isothermal-wall channel flow. *Journal of Fluid Mechanics* **305**, 159–183.
- COLEMAN, G. N., KIM, J. & SPALART, P. R. 2003 Direct numerical simulation of a decelerated wall-bounded turbulent shear flow. *Journal of Fluid Mechanics* **495**, 1–18.

- COLEMAN, G. N. & MANSOUR, N. N. 1993 Simulation and modelling of homogeneous compressible turbulence under isotropic mean compression. *Turbulent Shear Flows*, vol. 8, ed. F. Durst et al. p. 269.
- CONSTANTINESCU, G. & LELE, S. K. 2002 A highly accurate technique for the treatment of flow equations at the polar axis in cylindrical coordinates using series expansions. *Journal of Computational Physics* **183** (1), 165–186.
- DUSSAUGE, J. P. & GAVIGLIO, J. 1987 The rapid expansion of a supersonic turbulent flow: role of bulk dilatation. *Journal of Fluid Mechanics* **174**, 81–112.
- EGGELS, J. G. M., UNGER, F., WEISS, M. H., WESTERWEEL, J., ADRIAN, R. J., FRIEDRICH, R. & NIEUWSTADT, F. T. M. 1994 Fully developed turbulent pipe flow: A comparison between direct numerical simulation and experiment. *Journal of Fluid Mechanics* **268**, 175–209.
- FERNANDO, E. M. & SMITS, A. J. 1990 A supersonic turbulent boundary layer in an adverse pressure gradient. *Journal of Fluid Mechanics* **211**, 285–307.
- FOYSI, H. 2005 Transport passiver Skalare in wandgebundener und isotroper kompressibler Turbulenz. PhD thesis, Technische Universitaet, Muenchen.
- FOYSI, H., SARKAR, S. & FRIEDRICH, R. 2004 Compressibility effects and turbulence scalings in supersonic channel flow. *Journal of Fluid Mechanics* **509**, 207–216.
- FREUND, J. B., MOIN, P. & LELE, S. K. 1997 Compressibility effects in a turbulent annular mixing layer. *Tech. Report TF-72, Stanford Univ., Mechanical Engg. Dept.* .
- FUREBY, C. & GRINSTEIN, F. F. 2002 Large eddy simulation of high reynolds number free and wall-bounded shear flows. *Journal of Computational Physics* **181**, 68–97.
- GARNIER, E., MOSSI, M., SAGAUT, P., COMTE, P. & DEVILLE, M. 1999 On the use of shock-capturing schemes for large-eddy simulation. *Journal of Computational Physics* **153**, 273–311.
- GAVIGLIO, J. 1987 Reynolds analogies and experimental study of heat transfer in the supersonic boundary layer. *International J. of Heat and Mass Transfer* **30**, 911–926.
- GEURTS, B. J. & HOLM, D. D. 2003 Regularization modelling for large-eddy simulation. *Physics of Fluids* **15** (1), L13.
- GREENBLATT, D. & MOSS, E. A. 2004 Rapid temporal acceleration of a turbulent pipe flow. *Journal of Fluid Mechanics* **514**, 65–75.
- HAMBA, F. 1999 Effects of pressure fluctuations on turbulence growth in compressible flows. *Physics of Fluids* **11** (6), 1623–1635.
- HANNAPPEL, R. & FRIEDRICH, R. 1995 Direct numerical simulation of a Mach 2 shock interacting with isotropic turbulence. *Applied scientific research* **54**, 205–221.

- HICKEL, S., ADAMS, N. A. & DOMARADZKI, J. A. 2006 An adaptive local deconvolution method for implicit LES. *Journal of Computational Physics* **213** (1), 413–436.
- HU, F. Q. 2004 Absorbing boundary conditions. *International Journal of Computational Fluid Dynamics* **18** (6), 513–522.
- HUANG, P. G., COLEMAN, G. N. & BRADSHAW, P. 1995 Compressible turbulent channel flows: DNS results and modelling. *Journal of Fluid Mechanics* **305**, 185–218.
- KIM, J., MOIN, P. & MOSER, R. 1987 Turbulence statistics in fully developed channel flow at low Reynolds number. *Journal of Fluid Mechanics* **177**, 133–166.
- KOVASZNAV, L. S. G. 1953 Turbulence in supersonic flow. *J. Aeronaut. Sci.* **20**, 657–682.
- KREUZINGER, J., FRIEDRICH, R. & GATSKI, T. B. 2006 Compressibility effects in the solenoidal dissipation rate equation: A priori assessment and modeling. *International J. of Heat and Fluid Flow* **27**, 696–706.
- LECHNER, R., SESTERHENN, J. & FRIEDRICH, R. 2001 Compressibility effects and turbulence scalings in supersonic channel flow. *J. of Turbulence* **2**, 1–25.
- LEE, M. J., KIM, J. & MOIN, P. 1990 Structure of turbulence at high shear rate. *Journal of Fluid Mechanics* **216**, 561–583.
- LEE, S., LELE, S. K. & MOIN, P. 1993 Direct numerical simulation of isotropic turbulence interacting with a weak shock wave. *Journal of Fluid Mechanics* **251**, 533–562.
- LELE, S.K. 1992 Compact finite difference schemes with spectral-like resolution. *Journal of Computational Physics* **103**, 16–42.
- LOGINOV, M. S., ADAMS, N. A. & ZHELTOVODOV, A. A. 2006 Large-eddy simulation of shock-wave/turbulent-boundary-layer interaction. *Journal of Fluid Mechanics* **565**, 135–169.
- LOW, M-M. MAC & KLESSEN, R. S. 2004 Control of star formation by supersonic turbulence. *Rev. Mod. Phys.* **76**, 125–194.
- MAHESH, K., MOIN, P. & LELE, S. K. 1996 The interaction of a shock wave with a turbulent shear flow. *Tech. Report TF-69, Stanford Univ., Mechanical Engg. Dept.* .
- MATHEW, J., FOYSI, H. & FRIEDRICH, R. 2006 A new approach to LES based on explicit filtering. *International J. of Heat and Fluid Flow* **27**, 594–602.
- MATHEW, J., LECHNER, R., FOYSI, H., SESTERHENN, J. & FRIEDRICH, R. 2003 An explicit filtering method for large eddy simulation of compressible flows. *Physics of Fluids* **15**, 2279–2289.
- MATSUO, K., MIYAZATO, Y. & KIM, H.D. 1999 Shock train and pseudo-shock phenomena in internal gas flows. *Progress in Aerospace Sciences* **35**, 33–100.

- MOHSENI, K. & COLONIUS, T. 2000 Numerical treatment of polar coordinate singularities. *Journal of Computational Physics* **157**, 787–795.
- MOIN, P. & KIM, J. 1982 Numerical investigation of turbulent channel flow. *Journal of Fluid Mechanics* **118**, 341–377.
- MORKOVIN, M. V. 1964 Effects of compressibility on turbulent flows. *Mechanique de la turbulence* (ed. A. Favre) pp. 367–380.
- NARASIMHA, R. & SREENIVASAN, K. R. 1973 Relaminarization of highly accelerated turbulent boundary layers. *Journal of Fluid Mechanics* **61**, 417–447.
- PANTANO, C. & SARKAR, S. 2002 A study of compressibility effects in the high-speed turbulent shear layer using direct simulation. *Journal of Fluid Mechanics* **451**, 329–371.
- PATEL, V. C. & HEAD, M. R. 1969 Some observations on skin friction and velocity profiles in fully developed pipe and channel flows. *Journal of Fluid Mechanics* **38**, 181–201.
- POINSOT, T. J. & LELE, S. K. 1992 Boundary conditions for direct simulations of compressible viscous flows. *Journal of Computational Physics* **101**, 104–129.
- RUBESIN, M. W. 1990 Extra compressibility terms for favre-averaged two-equation models of inhomogeneous turbulent flows. *NASA CR-177556* .
- SARKAR, S. 1995 The stabilizing effect of compressibility in turbulent shear flow. *Journal of Fluid Mechanics* **282**, 163–186.
- SARKAR, S., ERLEBACHER, G., HUSSAINI, M. Y. & KREISS, H. O. 1991 The analysis and modelling of dilatational terms in compressible turbulence. *Journal of Fluid Mechanics* **227**, 473–493.
- SATAKE, S., KUNUGI, T., SNEHATA, A. M. & MCELIGOT, D. M. 2000 Direct numerical simulation for laminarization of turbulent forced gas flows in circular tubes with strong heating. *International J. of Heat and Fluid Flow* **21**, 526.
- SCHLUETER, J. U., SHANKARAN, S., KIM, S., PITSCH, H. & ALONSO, J. J. 2002 Integration of RANS and LES flow solvers: interface validation. *Annual research briefs, CTR, Stanford* pp. 155–166.
- SESTERHENN, J. 2001 A characteristic-type formulation of the Navier-Stokes equations for high order upwind schemes. *Computers and Fluids* **30**, 37–67.
- SPINA, E. F., SMITS, A. J. & ROBINSON, S. K. 1994 The physics of supersonic turbulent boundary layers. *Annual Rev. Fluid Mech.* **26**, 287–319.
- STOLZ, S. 2000 Large eddy simulation of complex shear flows using an approximate deconvolution model. PhD thesis, ETH, Zurich.

- STOLZ, S., ADAMS, N. A. & KLEISER, L. 2001 An approximate deconvolution model for large-eddy simulation with application to incompressible flows. *Physics of Fluids* **13**, 997–1015.
- UNGER, F. 1994 Numerische Simulation Turbulenter Rohrstroemungen. PhD thesis, Technische Universitaet, Muenchen.
- VREMAN, A. W., SANDHAM, N. D. & LUO, K. H. 1996 Compressible mixing layer growth rate and turbulence characteristics. *Journal of Fluid Mechanics* **320**, 235–258.
- WALSHAW, C. & FARR, S. J. 1993 A two-way parallel partition method for solving tridiagonal systems. *Tech. Rep.* 93.25. School of Computer Studies, Univ. of Leeds.
- WILLIAMSON, J. K. 1980 Low-storage Runge-Kutta schemes. *Journal of Computational Physics* **35**, 48–56.
- WU, X., SCHLUETER, J., MOIN, P., PITSCH, H., IACARRINO, G. & HAM, F. 2006 Computational study on the internal layer in a diffuser. *Journal of Fluid Mechanics* **550**, 391–412.
- XU, X., LEE, J. S., R. H. PLETCHER, A. M. SNEHATA & MCELIGOT, D. M. 2004 Large eddy simulation of turbulent forced gas flows in vertical pipes with high heat transfer rates. *International J. of Heat and Mass Transfer* **47**, 4113.
- ZAMAN, K. B. M. Q. 1999 Spreading characteristics of compressible jets from nozzles of various geometries. *Journal of Fluid Mechanics* **383**, 197–228.